SPRAY FORMING OF Si-Al ALLOYS FOR THERMAL MANAGEMENT APPLICATIONS

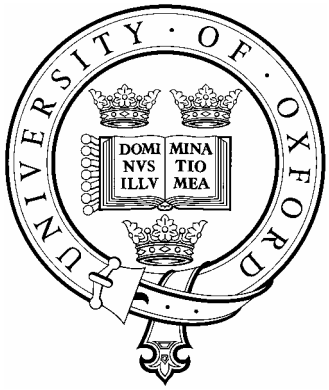

Alexis Lambourne
Department of Materials Science
Queen's College, Oxford
Trinity 2007

SPRAY FORMING OF Si-Al ALLOYS FOR THERMAL MANAGEMENT APPLICATIONS

Alexis Lambourne

Queen's College, Oxford

A thesis submitted for the degree of Doctor of Philosophy

at the University of Oxford

Trinity term 2007

Department of Materials

Parks Road

Oxford

OX1 3PH

United Kingdom

Abstract

Spray Forming of Si-Al Alloys for Thermal Management Applications

A. Lambourne **D.Phil Thesis**
The Queen's College **Trinity Term 2007**

This thesis describes the processing and characterisation of Al-70Si alloys manufactured by gas atomised spray forming at Sandvik-Osprey (Neath, UK) and Oxford University using a newly commissioned spray forming pilot-plant facility. Spray formed Al-70Si (CE7) provides an attractive balance of thermophysical properties making it suitable for thermal management applications. Microstructural characterisation of CE7 was conducted using optical microscopy, image analysis, electron probe micro analysis (EPMA) and electron backscatter diffraction (EBSD). Microscopy revealed an interpenetrating network microstructure consisting of fine, randomly oriented polycrystalline primary Si interpenetrated by large, α-Al grains devoid of eutectic Si. Mechanical testing and thermal cycling simulated a service environment and revealed for the first time crack initiation, growth and blunting mechanisms, the effect of intermetallic phases on the bulk mechanical properties, and anisotropy effects resulting from macrosegregation of Al during solidification.

A relationship between the inter-phase interface length and the fracture toughness has been proposed and methods of interface length refinement have been investigated, including chill casting and spray forming. Spray formed CE7 modified with separate additions of B, P, P+Ce and Sr have been microstructurally and mechanically characterised and compared with binary CE7. While alloy additions were effective in refining primary and eutectic Si in chill cast alloys, spray formed alloys showed little change in interface length. Particle injection of Si-Al powder was effective in refining the scale of the spray formed microstructure, and improving mechanical properties. The deleterious effect of intermetallic phases on bulk mechanical properties has been demonstrated and highlighted the importance of melt cleanliness and materials control during manufacturing.

Acknowledgements

I would like to thank my supervisor Prof. P S Grant for offering me the opportunity to undertake this work and for his support and suggestions throughout, also for telling me repeatedly that I am not James T. Kirk. I shall boldly go and split my infinitives elsewhere.

My thanks to all those at Sandvik-Osprey Ltd who have supported this project over the last 3 years and especially to Gwyn, Alan, Andrew and Robert for their advice and technical input.

I would also like to thank past and present members of the Oxford spray forming group for all their help and support. In particular, Robin Vincent, Trevor Knibbs, Simon Hogg, Ian Stone, Matt Hedges, Tim Rayment , Jiawei Mi and Keyong-Ho Baik. In the wider Oxford 'metal bashing' community, I thank you all for the many useful discussions, tips and advice over the last 3 years – Ian, Leo, Keyna, Steve..... there are too many to name you all, but you know who you are!

Many thanks to Chris Salter for help and training with EPMA analysis and Simon Hogg for his assistance and expertise with the EBSD analysis and to both for their help and suggestions thereafter. Thanks also Laurie Walton and Bob Lloyd, for help, advice and patience in the workshop, and for the eternal 'can do' attitude that made working with them such a pleasure.

Particular thanks to all those collaborators who have helped me out with time, techniques, equipment and processing: Bodycote HIP, AWE, TWI, LSM, Westmoreland Mechanical Testing & Research and Astrium Satellites.

While the work was, for the most part fascinating, the importance of maintaining a healthy work-play balance should never be underestimated. For their distraction at work and outside I thank my many friends, old and new. To my family, I thank you for your bemused but continuous support of my academic endeavours throughout the last few years.

Finally, a big thank you to my wife, Jo, for her endless support and encouragement of my work, especially when things were looking bleak.

"So I remember every face, of every man who put me here"
Bob Dylan

AI - May-07

Glossary of terms

BSE	**B**ack **S**cattered **E**lectron
CCTV	**C**losed **C**ircuit **T**ele**v**ision
CE	**C**ontrolled **E**xpansion
CE7	**C**ontrolled **E**xpansion alloy (**7** x 10^{-6} °C^{-1})
CE7+B	**C**ontrolled **E**xpansion alloy (**7** x 10^{-6} °C^{-1})+1%**B**
CE7+P	**C**ontrolled **E**xpansion alloy (**7** x 10^{-6} °C^{-1})+0.9%**P**
CE7+P+Ce	**C**ontrolled **E**xpansion alloy (**7** x 10^{-6} °C^{-1})+1%**P** & 5%**Ce**
CE7+Sr	**C**ontrolled **E**xpansion alloy (**7** x 10^{-6} °C^{-1})+0.25%**Sr**
CE9	**C**ontrolled **E**xpansion alloy (**9** x 10^{-6} °C^{-1})
CE11	**C**ontrolled **E**xpansion alloy (**11** x 10^{-6} °C^{-1})
CMSF	**C**lean **M**etal **S**pray **F**orming
COD	**C**rack **O**pening **D**isplacement
CTE	**C**oefficient of **T**hermal **E**xpansion
DIC	**D**ifferential **I**nterference **C**ontrast
DC	**D**irect **C**urrent
EB	**E**lectron **B**eam (welding)
EBSD	**E**lectron **B**ack **S**catter **D**iffraction
EDM	**E**lectro **D**ischarge **M**achining
EDS	**E**nergy **D**ispersive **S**pectroscopy
EMI	**E**lectro-**M**agnetic **I**nterference
EPMA	**E**lectron **P**robe **M**icro **A**nalysis
GASF	**G**as **A**tomised **S**pray **F**orming
GMR	**G**as to **M**etal **R**atio
GSD	**G**rain **S**ize **D**istribution
HIP	**H**ot **I**sostatic **P**ressing
ICP	**I**nductively **C**oupled **P**lasma
IPF	**I**nverse **P**ole **F**igure
MMC	**M**etal **M**atrix **C**omposite
MOR	**M**odulus **O**f **R**upture
ODS	**O**xide **D**ispersion **S**trengthened

OES	**O**ptical **E**mission **S**pectography
OxCE7	**Ox**ford Binary **CE7**
PF	**P**ole **F**igure
RE	**R**are **E**arth
RF	**R**adio **F**requency
ROM	**R**ule **O**f **M**ixtures
RT	**R**oom **T**emperature
SE	**S**econdary **E**lectron
SEM	**S**canning **E**lectron **M**icroscope
S-O	**S**andvik-**O**sprey
TPRE	**T**win **P**lane **R**e-**E**ntrant
WDS	**W**avelength **D**ispersive **S**pectrometry
WDX	**W**avelength **D**ispersive **X**-ray spectography
XRD	**X**-**R**ay **D**iffraction
XRF	**X**-**R**ay **F**luorescence

1.0 Introduction

The principle of all spray forming processes is the atomisation of a liquid metal to form a myriad of variously sized droplets, which are subsequently collected on a substrate, and solidified into a coherent, near fully dense preform (Singer 1983). A variety of sprayed preform shapes can be produced depending on the geometry of the process, including cylindrical billets, tubes and strip (Grant 1995a). The thermal conditions at the preform surface during deposition have been shown to be critical to the final microstructure (Mathur 1989) and much of the research in spray forming has attempted to understand the complex relationships between process parameters, the preform surface temperature and the resulting preform microstructure. Spray forming was originally conceived by A.R.E. Singer in the early 1970s as a spray rolling process (Singer 1983, 1972), and has been developed further and commercialised by Sandvik-Osprey (Neath U.K.) and ~25 other Sandvik-Osprey licensees (Leatham 1999). Commercial spray forming applications include the manufacture of controlled coefficient of thermal expansion (CE) Si-Al alloys for thermal management applications.

The increasing power and density of modern avionic and satellite electronics demands efficient heat dissipation to prevent the premature failure of semiconductor devices. Failure rates increase dramatically as device temperatures increase: typically for every 10°C temperature rise, the lifetime of a GaAs or Si semiconductor device is reduced by a factor of 3 (Jacobson 1997). Device heat dissipation and cooling is usually achieved by the use of heat sinks,

heat spreaders and electronic packaging materials. Ideal thermal management materials have a coefficient of thermal expansion (CTE) of 7 - 9 $x10^{-6}$ $°C^{-1}$ closely matched to GaAs or Al_2O_3, in order to minimise thermally induced interfacial stresses between chip and thermal management material. Other desirable properties include: high thermal conductivity >100 W/mK; A low density < 3g/cm^3 due to the cost premiums associated with added weight in the aerospace industry.

A variety of thermal management materials have been developed (Jacobson 1997), but none can be considered ideal as all compromise on one or more key properties e.g. density, thermal conductivity, CTE, machinability, toxicity or cost. Hypereutectic Al-high Si alloys have a combination of physical properties that make them attractive for thermal management applications as they balance the low density and CTE of Si with the high ductility and thermal conductivity of Al. However Al-high Si presents significant problems, typically cracking and poor integrity in solidification processing. Sandvik-Osprey have developed spray forming as an efficient and cost-effective process for the manufacture of bulk Al-high Si alloys with Si concentrations up to 70 wt%. Spray forming of Al-70Si - (hereafter referred to as CE7 because of its 'controlled expansion' CTE of 7x10^{-6} $°C^{-1}$) - was carried out at Sandvik-Osprey (Neath, UK) and at Oxford University.

The objectives of this thesis are:

1. To investigate the processing-microstructure-property relationships in commercially manufactured CE7 and benchmark this material for comparison of subsequent alloy developments.

2. To investigate and quantify the effect of service environment on commercially manufactured CE7.

3. To investigate methods of improving the mechanical performance of CE7 by primary processing and alloy additions.

The thesis is divided into the following Chapters: Chapter 2 reviews the literature relevant to thermal management and spray forming Si-Al alloys; Chapter 3 describes the procedures for spray forming of Si-Al billet preforms, and the microstructural and mechanical characterisation techniques; Chapter 4 describes the results of Sandvik-Osprey CE7 characterisation; Chapter 5 describes the results of chill cast Al-50Si alloy modification experiments; Chapter 6 describes the results of CE7+X spray forming experiments; Chapter 7 discusses the relationships between processing, microstructure and properties in Sandvik-Osprey CE7; Chapter 8 discusses the mechanisms of refinement observed in chill cast Al-50Si; Chapter 9 discusses the spray forming and subsequent processing of CE7+X alloys, the role of alloy additions, the effect on the microstructure and physical properties; Chapter 10 presents the conclusions and Chapter 11 contains suggestions for further work.

This research has in part been published as
(A. Lambourne, P.S. Grant, S. Hogg, A. Ogilvy, Inzynieria Materialowa 3(140) p.616-619, 2004).

2.0 Literature survey

The literature relevant to thermal management materials will be considered, introducing a variety of commercially used materials and comparing these in terms of key mechanical properties in Section 2.11 – 2.14. Emerging and novel materials such as Sandvik-Osprey CE7 are introduced and compared to commercially used materials in Section 2.15 – 2.16. The microstructure and properties of CE7 forms the basis of this study and the manufacturing process is central to many aspects of microstructure and the resultant properties. The Spray forming process used in the commercial manufacture of CE7 is therefore reviewed in detail in Sections 2.2.1 – 2.2.5.2. The problems and advantages of a spray formed microstructure are introduced in Section 2.2.8. Al-Si alloy microstructure, conventional processing routes, and modification / inoculation are reviewed in Section 2.3 – 2.3.1.1. Bulk manufacturing processes which may offer an alternative to spray forming for the manufacture of Al-high Si alloys are reviewed in Sections 2.3.2 – 2.3.4 and the manufacture of CE7 by spray forming is introduced in Section 2.3.5. The literature relating to the microstructure and properties of spray formed Al-Si, including CE7 is reviewed in Sections 2.4 and 2.5.

2.1 Thermal management materials

As electronic circuitry becomes increasingly dense and powerful, the amount of waste heat produced has also increased. If this were not effectively dissipated, then many electronic devices would overheat and fail prematurely. Thermal management materials exist to support and encase chips and circuit boards but also to act as a heat sink to cool the electronics. Figure 2.1 shows a typical example of high density circuitry supported and encased by a thermal management material (indicated). Figure 2.2 shows a schematic cross section through the same circuit board array, showing thermal and electronic lead-through connections and package assembly. For an overview of the importance and applications of thermal management materials, the reader is directed to Zweben (1998). The desirable thermal management properties are: high thermal conductivity (>100W/mK), high specific stiffness, low density (<3g/cm^3) and, most importantly, a coefficient of thermal expansion (CTE) matched to the chip / circuit board (typically ~7 – 9 x10^{-6} °C^{-1}). This is important as it prevents differential thermal expansion, which causes thermal fatigue and cracking at interfaces and within components. CTE mismatch between Si chips and heat sink materials is reported as being responsible for brittle fracture of the Si chip, p-n junction failures, bowing of layered assemblies and other failures associated with cyclic stresses (Mavoori 1998). Electronic packages operating in space applications e.g. satellites, undergo particularly severe thermal cycling as they move in and out of the earth's shadow, typically with a service temperature range +125 to -125°C

(Rawel 2001), while in aerospace applications the typical range is -30°C to + 60°C (Jacobson 1997).

A range of materials have been developed to fulfil the thermal management role although no single material can be considered ideal. Table 2.1 compares some of the key properties of some commonly used thermal management materials.

Table 2.1 The key property data for materials widely used in thermal management applications. Values shown in bold are those properties appropriate for microwave circuitry power dissipation (Jacobson 1997).

Material	**CTE** @20°C ($x10^{-6}$ °C^{-1})	**Thermal conductivity** W/mK	**Density** g/cm^3
Ideal Value	**7 - 9**	**>100**	**<3**
Aluminium	23.6	**230**	**2.7**
Copper	17.6	**391**	8.9
Cu- 75W	**8.8**	**190**	14.6
Be-30BeO	**8.7**	**210**	**2.1**
Be-51BeO	**7.5**	**220**	**2.3**
BeO	**7.2**	**260**	**2.9**
Cu-85W	**7.2**	**180**	16.1
Al-68SiC	**6.9**	**150**	**3.0**
Cu-85Mo	**6.7**	**160**	10
Alumina	**6.7**	20	**3.9**
Kovar	5.8	17	8.2
Titanium	5.6	15	**4.5**
Molybdenum	5.1	**140**	10.2
Aluminium Nitride	4.5	**180**	**3.3**
*Al-50Si (CE11)	**11.0**	**140**	**2.5**
*Al-70Si (CE7)	**6.8**	**120**	**2.4**

* CE alloys are those produced by Sandvik-Osprey by spray forming, discussed in 2.1.5

Figures 2.3, 2.4 and 2.5 show the density, thermal conductivity and CTE of some of the most widely used thermal management materials, and are described below. CTE data in Figure 2.5 is incomplete, representing the available data in the literature for materials of interest.

2.1.1 Kovar (17Co-53Fe-29Ni +1% trace elements)

Kovar is one of the most widely used packaging materials. However, with a density of 8.2g/cm^3 it is considered too dense for aerospace or satellite applications. Kovar also suffers from relatively poor thermal conductivity of ~17 W/mK compared with >100 W/mK for many of the alternative materials, though exhibits an excellent CTE match of ~6 x10^{-6} ◦C^{-1}.

2.1.2 Be base materials.

Several different thermal management alloys have been developed based on the Be-BeO system. These alloys have a relatively low CTE of 8-9 x10^{-6} ◦C^{-1} at 25◦C, high thermal conductivity of 210W/mK and low density of 2.2g/cm^3. However problems associated with the toxicity of Be makes each manufacturing step complex and costly. Be/BeO materials are consequently limited to high value niche applications in the satellite industry.

2.1.3 Cu-85W & Cu-85Mo.

Cu-85W (Aegis Inc 1992) and Cu-85Mo (Narumi Corp 1987) alloys have a relatively high thermal conductivity of 170 W/mK and low CTE of 7x10^{-6} ◦C^{-1} which has a relatively weak dependency on temperature. However, the density of Cu based materials is the highest of any of the thermal management materials at 16.1 g/cm^3 and 10.0 g/cm^3 for Cu-85W and Cu-85Mo respectively. These alloys are generally inappropriate for use in the aerospace industry owing to the high cost penalties associated with added weight (Mullers 2000, Kocdemir 2000).

2.1.4 Al-68 ±2SiC.

Al-68 ±2SiC (Hivol) is a metal matrix composite (MMC) material developed by AEA Technology based upon a SiC particulate reinforced aluminium alloy, manufactured by pressure assisted melt infiltration of a SiC preform. The relatively high thermal conductivity of 150 W/mK and low density of 3.0 g/cm^3 make Hivol attractive for aerospace and space applications. However, Hivol suffers from a strongly non-linear variation in CTE with temperature, and is comparatively difficult to machine into thermal management packages (Johnson 2003).

2.1.5 CE7 (Al-70Si).

CE7 is a proprietary alloy produced by Sandvik-Osprey and is based on the aluminium-silicon binary system. The problems of coarse, acicular Si and anisotropic properties associated with hypereutectic Al-Si alloys (Si>12.2%, Murray 1984) are overcome by spray forming which gives a co-continuous network of primary Si and Al rich phases. The resulting properties are well-suited to thermal management applications in aerospace, space and other industries, CE7 has a density of 2.4g/cm^3, a stable, linear CTE of ~7x10^{-6}°C^{-1} and a thermal conductivity of 120 W/mK. Sandvik-Osprey produce a range of Al- 27-70wt% Si alloys, where varying the relative proportion of Al and Si it is possible to select a desired CTE within the range 17-7x10^{-6}°C^{-1}, as shown in Figure 2.6 (Jacobson 1997). The processing, microstructure and properties of CE7 are discussed in more detail in sections 2.2, 2.4 and 2.5 of this chapter.

2.1.6 Novel materials

Alumina is a traditional substrate material with a CTE of 6.7 $x10^{-6}°C^{-1}$ and a density of 3.9g/cm^3, however the low thermal conductivity of 20W/mK makes it appropriate only as part of a composite package. Along with the more widely used materials presented, other materials have been investigated for thermal management applications. Cu is of interest and several approaches have been taken to reducing the CTE of Cu without impairing the thermal conductivity. Datta (1999), investigated Cu melt infiltration of a CVD deposited, C fibre network to create an interpenetrating 3-dimensional structure with an isotropic CTE of approximately $6x10^{-6}°C^{-1}$, depending on the volume fraction of carbon fibre. Mavoori (1998) developed a Cu matrix composite using fine fibres of shape memory Ni-44Ti to reduce the CTE to $4x10^{-6}°C^{-1}$.

Ting (1994) reported excellent thermal management properties using CVD deposited, polycrystalline diamond fibres as the reinforcement phase in MMCs with a thermal conductivity of 500-1,700 W/mK and a tailorable CTE in the range 0-$15x10^{-6}°C^{-1}$. However, multiple complex process steps and a low production rate made further development prohibitively expensive.

Olin Corp (1997) developed a technique for manufacturing graphite interpenetrated with 10-40% Cu, Al or Ni by melt infiltration, with a density of 1.9 -3.1gcm^{-3} CTE of 7.7-$8.6x10^{-6}°C^{-1}$ and a thermal conductivity of 130-175 W/mK. Despite this attractive range of physical properties, the multi-step,

multi-layer approach to building a thermal management package again was inevitably costly.

The problem with many of the 'novel' materials is the combination of high production costs and difficulties in producing package shapes, and manufacturing the materials in commercial volumes. The low cost and ease of processing associated with polymers is attractive for thermal management applications and their low thermal conductivity has been increased by the addition of thermally conductive but electrically insulating fillers such as AlN (Rehme 1997, Fandel 2000). However despite some progress, the thermal management properties are not yet competitive with metallic based competitors (Rentsch 2000).

2.2 Spray forming

Singer (1970, 1972) first developed the idea of gas atomised spray forming in the 1970's in which a high pressure gas jet impinges on a stable melt stream to cause atomisation. The resulting droplets are then collected on a target, which can be manipulated within the spray and used to form a near-dense billet of near-net shape. Figure 2.7 shows a schematic of a typical spray forming plant. Spray forming has found applications in specialist industries such as: stainless steel cladding of incinerator tubes; Ni superalloy discs and rings for aero-engine applications; Al/Ti, Al/Nd and Al/Ag sputter targets; Al-Si alloys for cylinder liners; and high speed steels (Grant 1995a).

The gas atomised spray forming (GASF) process typically has a molten alloy flow rate of 1-20kg/min^{-1}, although twin atomizer systems can achieve metal flow rates of up to 80kg/min^{-1} (Shaw 1997). Special steel billets of 1 tonne or more have been produced by spray forming on a commercial basis, together with Ni superalloy ring blanks of up to 500kg and Al alloy extrusion billets of up to 400kg (Grant 1995a).

2.2.1 Advantages of spray forming

Spray forming offers certain advantages over both conventional ingot metallurgy and more specialist techniques such as powder metallurgy. Firstly, it is a flexible process and can be used to manufacture a wide range of materials, some of which are difficult to produce by other methods, e.g. Al-5wt%Li alloys (White 1989a) or Al-SiC, Al-Al_2O_3 MMCs (Harris 1988, Willis 1998). The atomisation of the melt stream into droplets of 10-500μm diameter, some of which, depending on diameter, cool quickly to the solid and semi-solid state provide a large number of nucleants for the residual liquid fraction of the spray formed material on the billet top surface (Grant 1995a). The combination of rapid cooling in the spray and the generation of a large population of solid nucleants in the impacting spray leads to a fine equiaxed microstructure, typically in the range 10 - 100μm, with low levels and short length scales of internal solute partitioning (Strivatsan 1995). These microstructural aspects offer advantages in material strength because of fine grain size, refined distribution of dispersoid and / or secondary precipitate phases, as well as tolerance to impurity ‘tramp’ elements. This fine structure in

the ‘as sprayed’ condition means homogenising heat treatments can often be avoided. Because of the complex solidification path (i.e. the rapid transition from superheated melt to solid, liquid or semi-solid droplet to temperature equilibration at semi-solid billet top and final slow cooling to fully solid) of the spray formed material, extended solubility of alloying elements and the formation of metastable phases has also been reported (Strivatsan 1995).

One of the major attractions of spray forming is the potential economic benefit to be gained from reducing the number of process steps between melt and finished product. Spray forming can be used to produce strip, tube, ring, clad bar / roll and cylindrical extrusion feed stock products, in each case with a relatively fine-scale microstructure even in large cross-sections (Grant 1995a). The benefits of GASF over powder metallurgy accrue from the reduced number of process steps where powder sieving, pressing, de-gassing and handling steps and their attendant safety and contamination issues may be removed.

2.2.2 Disadvantages of spray forming

There are two major disadvantages to the gas atomisation spay forming process. The most significant disadvantage is the relatively low process yield with typical losses of ~30% (Tokizane 1996). Losses occur because of overspray (droplets missing the emerging billet), splashing of material from the billet surface, and material ‘bouncing’ off the semi-solid top surface. Many operators of the spray forming process now use a particle injector system to

re-inject the overspray powder, and thus recycle material that would otherwise be lost (Commandeur 2003), or sell the overspray powder as a product in its own right (Chesney 2003). The second major disadvantage is one of process control. As it is essentially a free-forming process with many interdependent variables, it has proved difficult to predict the shape, porosity or deposition rate for a given alloy. Much of the control is based on operator experience and empirical relationships. It is partly the process complexity and lack of robust process control that has prevented the widespread commercialisation of this process. Some developments using feed-back control have proved successful in improving the variations in billet diameter and improving yield in specific systems but these have yet to find widespread implementation (Mingard 1993).

Porosity resulting from gas entrapment and solidification shrinkage is a significant problem in spray formed materials. A typical spray formed billet will contain 1-2% porosity with a pore size dependent on alloy freezing range and various process parameters (Cai 1998). Hot isostatic pressing (HIPing) or thermo-mechanical processing can heal these pores if they are small (<30μm). Despite these disadvantages, spray forming remains an economic process for the production of difficult to manufacture, niche alloys. Large scale porosity is more difficult to heal effectively and must be minimised by careful process control. In some cases, porosity is controlled by alloy additions which react with dissolved and entrapped gas to form a solid phase e.g. Ti added to Cu billets to form TiN with dissolved and entrapped N_2 (Muller 2003). Porosity

- even after consolidation - can limit the applications of spray formed material, for example rotating gas turbine components must have zero porosity because of the detrimental effect on high cycle fatigue.

2.2.3 Commercialisation

In spite of the problems associated with the spray forming process there has been sustained industrial interest in spray forming over the last ~30 years. Sandvik-Osprey (former Osprey Metals Ltd) of Neath, South Wales holds the patents on the process (Osprey 1971, 1974) and have licensed the technology to a range of industries. There are currently ~25 licensees operating around the world, ranging from small research and development plants to full-scale commercial operations. These include successful commercial ventures such as PEAK (Germany) who currently spray form Al-Si cylinder liners for Mercedes Benz; Danspray (Denmark) producing specialist tool steels; and Sandvik Steel producing stainless steel clad tubes for incinerator applications (DGM 2001, Leatham 1999). Research and development activities include: Pennsylvania State University (USA), investigating high strength Al alloys for defence applications and Oxford University investigating Ni superalloys, Al-Si and Al-Li alloys, and others (Grant 1995a). In all of these applications, research concerns the reconciliation of the cost disadvantages and complexity of spray forming with the demand for high performance alloys in niche applications.

2.2.4 Melting

The earliest spray forming work (Singer 1970) was based on a resistively heated electric holding furnace. The melt then passed through a 3mm diameter Al_2O_3 nozzle. However the low flow rate made a high superheat necessary to prevent solidification in the nozzle. The next generation melting procedures in spray forming applications were bottom pour induction units, which offer many benefits. In this system, the melting crucible is directly above the atomiser head with a ceramic nozzle feeding directly from the furnace to the atomiser (Evans 1995). A stopper rod runs through the melt to the top of the pouring nozzle, the rod is withdrawn when the melt reaches the designated temperature for spraying, typically 50 to150°C above the alloy liquidus. Figure 2.8 shows a schematic of this arrangement. Alternatively a pre-prepared plug of alloy to block the nozzle is used, and at a specified superheat this plug melts allowing the contents of the furnace to drain through the nozzle (Johnson 1993). Another problem associated with bottom pour furnaces is the change in flow rate associated with the reducing metalo-static head in the crucible. In some cases, introducing an inert gas overpressure (White 1989a) during pouring can compensate for this effect (Mingard 1993).

An alternative approach is the tilt-pour furnace whereby an induction furnace is tilted to pour the melt into a conical tundish that in turn delivers the molten metal to the melt delivery nozzle (Lambourne 2004). Figure 2.9 shows a schematic of this arrangement that can be operated under inert gas and allows the metalo-static head to be kept approximately constant by

continuously ‘topping-up’ of the tundish. The tilt pour system provides the advantage that melting is decoupled from the spraying procedure so that melting problems and remedial solutions do not effect or disturb the critical set-up of the melt delivery nozzle.

In the most complex melting arrangement, used only for production of Ni superalloy turbine forging blanks by spray forming, vacuum induction melting, electroslag re-melting and cold hearth crucibles have been combined by GE Corp. to control alloy impurity levels and the presence of refractory inclusions in the molten metal supply (Carter 2002, Butzer 1998). Figure 2.10 shows a schematic of nucleated casting process developed by GE Corp. for the controlled melting of Ni superalloys. Clean metal spray forming (CMSF) combines the electroslag refining process, cold walled induction guide and gas atomised spray forming. This approach has led to a reduction in the number of melt related defects (pores, inclusions, etc.), a finer average grain size, the ability to produce larger ingots and the ability to process a wider range of alloys (Kelkar 1999).

2.2.5 Atomisation

There are many different techniques for atomisation of molten metals, many of which are derived from the powder metallurgy industry and have been extensively reviewed elsewhere (Lawley 1986, 1981). For a review of typical powder morphologies and a review of rapid solidification processes the reader is directed to Savage (1984). There are two major atomisation techniques

used in spray forming: centrifugal atomisation for the manufacture of near net shape rings and gas atomisation for the manufacture of billets, tube and strip (Grant 1995).

2.2.5.1 Centrifugal atomisation.

Centrifugal atomisation involves pouring molten metal at relatively low flow rates (0.1- 2kgmin^{-1}) onto a spinning plate, dish or disc, whereby the rotation speed is sufficient to create high centrifugal forces at the periphery and overcome surface tension and viscous forces so the melt is fragmented into droplets. This process is shown schematically in Figure 2.11. Droplet diameters produced by centrifugal atomisation are dependent primarily on the rotation speed, (up to 20,000rpm) and are typically in the range 20 – 1000 μm with cooling rates of the order 10^4 Ks^{-1} (Singer 1983). Centrifugal atomisation is generally conducted under an inert atmosphere of Ar or N_2 to prevent oxidation of the fine droplets or can be operated under vacuum.

2.2.5.2 Gas atomisation.

The melt stream exits the melt delivery nozzle into the spray chamber. The melt stream is protected from being destabilised by the turbulent gas environment in the spray chamber by primary gas jets operating at intermediate inert gas pressure of 2 to 4 bar, the resulting gas flow is parallel to the melt stream to stabilise the melt stream (Aumund-Kopp 2002). The secondary atomiser uses high velocity (250 to 350ms^{-1}), high-pressure (6 to 10 bar) gas jets to impinge on the melt stream to achieve atomisation. This

type of two stage, close coupled atomiser is shown in Figure 2.12. The atomiser jets are usually arranged as an annulus or as discrete jets positioned symmetrically about the melt delivery nozzle (Lawley 1981), or less commonly, arranged as a linear nozzle (Baker 1993, Chu 1996) for the production of strip products. Typical droplet diameters follow a log-normal distribution with powder diameters up to ~600μm with a mass median diameter of ~150μm.

The atomising gas mass flow rate to molten metal mass flow rate ratio is a key parameter in controlling the droplet diameter and hence the cooling rate, billet temperature and resulting solid particle nucleant density. The gas - metal ratio (GMR) is typically in the range 1.5 to 5.5, with yield decreasing and cooling rates in the spray increasing with increasing GMR. Typically at low (1.5) GMR, yield is 75%, if the GMR is increased to 5.0 with all other parameters remaining constant, the process yield is reduced to 60% (Tokizane 1996).

Scanning atomisers have been developed which allow the production of billets of up to 600mm diameter, approximately twice the diameter possible with a static atomiser. The atomiser head is oscillated mechanically through 5 to 10° at a typical frequency of 25Hz, to deflect the melt stream creating a spray path that is synchronised with the rotation speed of the collector plate in order to deposit a parallel-sided billet (Leatham 1995). This arrangement is shown schematically in Figure 2.13. Aumund-Kopp (2002) investigated the influence of scanning atomiser oscillation and collector plate rotation on spray formed

billet and strip shape control. By using programmable oscillating atomiser drives it was possible to improve the shape and shape reproducibility of spray formed deposits. Aumund-Kopp (2002) demonstrated that parallel sided, flat topped billets could be sprayed in a reproducible manner if the substrate rotation and atomiser oscillation frequency were synchronised and optimised for specific alloys and melt flow rates. Twin atomiser systems combine a static and scanning atomiser, making it possible to spray billets of up to 450mm diameter with economic benefits, (Leatham 1995). A schematic of a typical twin atomiser arrangement is shown in Figure 2.14. A large commercial spray forming produced at PEAK using twin atomiser technology is shown in Figure 2.15.

Atomising gas used in spray forming is generally either N_2 and can be either protective or reactive depending on the alloy system, or Ar which is generally entirely inert but more expensive than N_2 (Lawley 1994). Reactive gasses can be introduced in small quantities to the atomising gas to create dispersion strengthened alloys e.g. 0.5 – 10% O_2 in N_2 used to generate oxide dispersion strengthened (ODS) Al alloys (Dai 1998). Comparisons of N_2 and Ar based spray forming showed that with all other factors remaining constant, the billet top temperature was lower with N_2 than with Ar, because of the differences in thermal diffusivity of the two atomising gases: Ar has a thermal conductivity of 0.0179W/mK which is approximately a third less than N_2 with a thermal conductivity of 0.026W/mK (Tillwick 1999).

The mechanisms of melt break up and atomisation have been extensively researched (Unal 1987, Lawley 1981, See 1978), showing that atomisation typically consists of 3 steps: (1) primary break up of the melt stream; (2) molten droplets and ligaments undergo secondary disintegration; (3) particles cool and solidify (See 1978) . Theoretical analysis of the atomisation process to predict droplet size has yielded models providing only moderate agreement with experimental data (Lawley 1981, Bradley 1973a, 1973b, Lubanska 1970). Investigations show that in all cases gas atomisation of molten metal yields a broad range of droplet diameters, typically in the range 10-600μm diameter, with a mean diameter of ~100μm (Grant 1993, Bewlay 1990). Droplet diameter governs the dynamic behaviour of the droplet in flight which in turn determines the time available for in-flight cooling (Grant 1993) which is critical in controlling the resulting billet microstructure (Mathur 1991a). At a flight distance of 300-400mm, Mathur (1989) predicted droplet velocities of 40-90 ms^{-1} for droplet diameters in the range 20-150μm respectively, compared to measured velocities of ~100ms^{-1}, and at distances of up to 180 mm from the atomiser, droplets were still being accelerated by the gas (Bewlay 1989). Droplets cool in-flight predominantly by convection and radiation, and can experience undercoolings of up to 300°C prior to nucleation (Krauss 2002, Tillwick 1999, Xiang 1993, Mathur 1989). Models and experimental measurements show that small droplets (<50μm) very rapidly become fully solid prior to deposition, 50-200 μm droplets will be typically semi-solid and droplets of diameters >200μm will be liquid at deposition (Hattel 1999, Underhill 1997, 1995, Annavarapu 1993). The range of droplet

dynamic and thermal histories result in a billet top surface of 0.3 to 0.6 solid fraction (Mathur 1989, Grant 1990). Not all material that impacts the surface is incorporated into the billet: some solid droplets will bounce or splash-off the billet top surface or be directed out of the deposition region by turbulent gas movement in the chamber. The proportion of droplets that impact the surface compared to the proportion that are incorporated into the billet has been termed the 'sticking efficiency' (Mathur 1991a):

$$SE = SE_\theta \cdot SE_t$$

Equation 2.1

where SE is the overall sticking efficiency, SE_θ is the geometric sticking efficiency dependent on spray angle relative to substrate and SE_t is the thermal sticking efficiency dependent on spray and billet solid / liquid fraction defined as:

$$SE_t = \left(\eta_s f_s + \eta_l f_l\right)\varepsilon$$

Equation 2.2

where η_s and η_l are sticking coefficients of the solid and liquid from the spray respectively, f_s and f_l are the fractions of solid and liquid in the spray and ε is a parameter that varies between 0 and 1 as a function of the liquid fraction on the billet top surface.

2.2.8 Spray formed microstructure

During spraying it is essential to maintain a constant top surface temperature and hence maintain steady-state conditions if a billet with consistent

microstructure is to be produced. At the billet surface, during spraying an enthalpy balance must be maintained where the rate of enthalpy lost H_{out} from the billet by conduction to the atomising gas and through the substrate, convection and radiation must be balanced with the rate of enthalpy input H_{in} from the droplets in the spray (Cantor 1997). There are a variety of factors that can be adjusted in order to maintain these conditions: spray height, atomiser gas pressure, melt flow rate, melt superheat and atomiser configuration, being those parameters most readily adjusted. Typically equipment such as closed circuit cameras and optical pyrometry can be used to monitor billet size / position and top surface temperature (Mingard 1993). If $H_{out} \approx H_{in}$ then a steady temperature is maintained at the billet top surface. The top surface should be in a mushy condition in order to promote sticking of incoming droplets and partial re-melting of solid particles. The necessary partial re-melting of solid droplets explains the absence of dendritic remnants from pre-solidified droplets in the final microstructure (Manson-Whitton 2002). If H_{in} is insufficient to cause significant re-melting, a 'splat' microstructure of layered droplets will form, typical of thermal spray processes such as vacuum plasma spraying (VPS), arc spraying and high velocity oxy-fuel. Cantor (1997) produced processing maps for plasma spraying and spray forming using a steady-state heat balance in terms of the interlayer time (time between deposition events) against average deposition rate per unit area. These maps show the boundaries between banded un-fused microstructure and an equiaxed homogeneous structure. An example of this type of processing map for VPS processed Al-12Si and typical resultant microstructures are shown in

Figure 2.16 (Cantor 1997). Such a processing map does not at present exist for Al-High Si alloys.

The final phase of solidification occurs once droplets have impacted the mushy billet surface and thermal equilibration has taken place between the droplets and the billet. At this stage residual liquid is present as continuous network delineating polygonal grain boundaries, with a typical liquid fraction of 0.3 – 0.5 (Grant 1995a). The cooling rates during solidification of the billet is several orders of magnitude slower than the cooling rate in the spray, at 1-20°Cs^{-1} (Manson-Whitton 2002).

Although one of the benefits of spray forming is purportedly the ability to produce bulk material with fine scale microsegregation and little or no macrosegregation (Doherty 1997), Mingard (2000) showed that as a consequence of the interconnected liquid in the billet there was significant macrosegregation in large spray formed wrought Al billets. The distribution of Cu, Mg and Li in, for example, Al alloy 8091 showed surprisingly pronounced macrosegregation. Figure 2.17(a) shows the distribution of Cu(wt%) in a spray formed 8091 billet, from ~1.4 at the billet centre to 1.92 a the billet periphery. 2.17(b) shows the corresponding Vickers' hardness variation as a function of radial position in the same billet, with increasing Cu content increasing the local Vickers' hardness. These macrosegregation patterns were explained in terms of inverse segregation in which solute rich liquid from the billet centre is sucked back through the primary Al-rich network to feed

solidification shrinkage at the billet periphery. This effect was suggested to be exacerbated by centrifugal effects from the billet rotation (Mingard 2000).

Billet porosity is typically 1-2% with a region of higher porosity in the splat-quenched region adjacent to the substrate as previously described, and shown in Figure 2.16 (Cantor 1997). The very top of the billet often shows increased porosity because the top is rapidly chilled by the atomising gas which continues to chill the billet for 10-60 s after spraying (Cantor 1997). There has also been little progress in understanding and quantifying the underlying physics that controls as-sprayed porosity. Cai (1998) attempted to explain the development of porosity in spray formed materials as a function of primary processing conditions (melt flow rate, gas pressure, flight distance, the type of atomising gas and the liquid metal properties). However, this approach neglected consideration of the billet condition at deposition and this is well known experimentally to be critical in determining the final porosity.

In most cases, the higher porosity at the billet base and top are scalped and recycled. Ultrasonic inspection is sometimes used to determine the depth of the chill zone regions to prevent unnecessary wastage (Muller 2003). Depending on the alloy system and the final application, the remaining bulk material is usually processed to close porosity and subjected to a range of thermo-mechanical treatments. Spray formed materials are rarely used in the as-sprayed condition. In some cases, the residual atomising gas in pores may react with alloying elements to form allegedly beneficial phases (Bricknell

1986, Muller 2003) e.g. N_2 reacting with Ti in Ni superalloy Rene 80 to form a dispersion of TiN.

2.3 Al-Si alloys

The Al-Si binary system has been extensively studied (Mondolfo 1979) as it forms the basis for a large number of casting alloys used widely in the foundry industry that are usually slightly hypoeutectic (<12.2wt%Si). The Al-Si binary phase diagram is shown in Figure 2.18 (Murray 1984).

Hypereutectic Al-Si alloys are of interest as thermal management materials because of their low density and high thermal conductivity. Conventional ingot metallurgy is generally inappropriate for Si contents of >25 wt% Si because of the formation of large, faceted primary Si particles and needles which readily crack and give little strength, ductility or toughness (Hogg 2001, Osprey 1997).

2.3.1 Al-Si casting alloys

Processing hypoeutectic (<12.2wt% Si) Al-Si alloys is well established and understood and alloys can be wrought, conventionally cast, pressure die cast, etc. Al-Si based alloys are designated 4xxx (wrought alloys), 4xxx0 (cast alloys) and Al-Mg-Si alloys have the designation 6xxx (wrought alloys) and 6xxx0 (cast alloys). These alloys have found a variety of applications in the automotive and other industries where they are used predominantly in high temperature, wear resistant applications, such as pistons and cylinder liners.

Some commercial hypereutectic alloys are produced with Si concentration up to 18%Si. However above 18%Si, machinability and castability becomes prohibitively difficult (Tenekedjiev 1989). Above ~27wt% Si, primary Si forms a continuous 3D network, leading to inhibited flow, segregation, and incomplete die filling, making conventional casting very difficult (Hogg 2001, Deiwwanit 1996). Figure 2.19 shows the as cast microstructure of Al-70Si with Si needles of up to several mm in length (Osprey 1997). The formation of large Si needles and faceted particles must be suppressed to maintain the strength, ductility and hermeticity required for electronic packaging applications. Typical electronic packages have a wall thickness of 1-3 mm and discrete Si grains of high aspect ratio and several millimetres in length make cast Si-Al unsuitable for these applications (Osprey 2001).

2.3.1.1 Al-Si alloy modification

The formation of acicular primary Si can be suppressed by the addition of various inoculants and modifiers which affect both the nucleation of Si and / or Si growth in either primary or eutectic solidification. The objective of these additions is to promote a more spherodised or fibrous primary and eutectic Si morphology. It is well established that additions of P and Na have a refining effect on the Si eutectic phase (Mascare1953). However the efficacy of these additions fades (due to evaporation in the crucible) due to their high vapour pressure which makes them difficult to add in a predictable and repeatable manner (Tenekedjiev 1990). P is typically added as Fe-P or Cu-P, though occasionally as Al-P master alloy (Brooks 1995). It is generally accepted that

the P forms AlP in the melt, and is isomorphous with respect to Si (Ghost 1964), thus AlP is a strong nucleant of Si and significantly refines the primary Si. Alternative alloy additions whose behaviour can be more readily predicted and controlled have been investigated including Mg, Cr, Ti, Sr, Sb, B, Fe, Ce, Bi, as well as less common additions such as Y, Nd, Ge, Ga, Cd, S, Te, Se, and LiC, and have formed the basis of many extensive reviews (Rooey 1972, Lu 1995, Tenekedjiev 1990, Heshmatpour 1997).

Sr has a similar effect to Na at 50-200ppm, yielding significant refinement of the normally coarse acicular primary Si to form a fine fibrous structure (Dahle 2001). Sr and Na both operate by the twin-plane re-entrant edge (TPRE) mechanism, whereby Na or Sr atoms are adsorbed on the TPRE sites of the {111} plane of the Si. They prevent preferential epitaxial growth on this plane and force the Si to grow along branch directions <100> and <110> yielding a fibrous structure (Jenkinson 1975). An alternative mechanism for the flake to fibrous transformation is 'impurity induced twinning' (Lu 1987, 1989) whereby elements of large atomic radius (where $r_{addition} / r_{Si} \geq 1.65$) are collected on the solid-liquid growth front. The accumulation of ad-atoms at the {111} Si growth plane prevents further growth, increasing local undercooling hence and twinning by promoting growth in branch directions rather than the preferred <111> plane. Suitable elements that have atomic radii within these limits include Rb, K, Ba, Sr, Ca and Yb. Deformation processing of Al10Si and Al16Si has demonstrated that Sr modification (0.02%) makes significant hot work (60% reduction) possible (Mulazimoglu 1993).

Sb falls outside this atomic radius range with $r_{Sb} / r_{Si} = 1.55$; however additions of ~0.05% yield an acicular, refined eutectic similar to the uniform 'lacelike' dispersed structures of Na or Sr modified Al-Si. A structural refinement is obtained which is time independent; i.e. there is no evaporation of Sb over time in the crucible (Liu 1998). Sb is not compatible with other modifying elements, and P in particular mitigates the beneficial effects of Sb modification even in trace quantities. Where Sb is present with other modifiers, typically coarse Sb containing intermetallics are formed that preclude the growth of an effectively modified structure. No adsorption of Sb onto Si has been reported (Liu 1998) and the mechanism of Sb refinement remains unclear, although it is thought to alter undercooling conditions. Hansen (2000) and Nogita (2003) claim that Sb promotes impurity induced twinning despite being outside the atomic radius range defined by Lu (1987).

Wang (1999b) reported that additions of up to 600 ppm B can refine eutectic Si and that AlB_2 particles formed from B+Al or transformed from AlB_{12} act as nucleants for Si although this mechanism was disputed by Nogita (2003). B is one of the few elements with any solid solubility in Si and as such is of interest for its potential effect on the solidification of Si.

Owing to detrimental interactions, co-inoculation of Al-Si with P + (Sr, Na, Ca, Sb, etc) is not possible and alternative elements have been sought which enhance or complement the effect of P in order to allow refinement of Al-Si alloys with higher Si levels (Xian 1994). Rare earth (RE) elements have been demonstrated to be effective inoculants at relatively high concentrations of 2-

3%, often added as 'Mischmetal' which is a mixture of Ce, La and Nd, in the proportion ~3.6:1.8:1 respectively (Chang 1998a, 1998b). Chang (1998a) reported refinement of primary Si and a change from flake to fibrous eutectic. Chang (1998a) suggested that the AlCe phases at the periphery of the primary Si alter local undercooling conditions and inhibit growth by poisoning Si attachment sites.

Co-inoculation with 1.2% $RE_{(mischmetal)}$ + P was demonstrated to be effective in an Al-20Si alloy(Xian 1993) . Further study of this system with additions of 2 – 7% $RE_{(mischmetal)}$ + 50ppm P revealed a strong dependence of primary Si size with RE addition (Jirattiticharoean 2004). Primary Si was nucleated by AlP and further refined by competitive growth of Al_2Si_2Ce and the poisoning of Si attachment sites.

It should be noted that cooling rates have a significant effect on primary Si size and morphology as well as the scale of eutectic structure. Cooling rate is rarely quoted in papers on alloy modification making a valid comparison of modifier effects difficult.

2.3.2 Semi-solid processing

The cooling rates in ingot metallurgy are too slow to prevent the formation of acicular Si phases, making it necessary to seek alternative production techniques with faster cooling rates for hypoeutectic Al-Si alloys, or methods that inhibit the growth and coalescence of primary Si. Semi-solid processing of Al-30 and Al-50Si alloys changed the primary Si morphology from plate to

rounded elongated rod, and significantly reduced the primary Si size (Diewwanit 1996). This is achieved by mechanical stirring of the semi-solid alloy which progressively fragments and rounds the primary Si particles resulting in an equiaxed primary Si structure interpenetrated by Al-Si eutectic lamellae.

Re-heating spray formed Al~30Si into the semi-solid state generates a microstructure that exhibits thixotropic properties i.e. the apparent viscosity decreases with increasing shear rate or time at a constant shear rate and on standing the viscosity rises and returns to the original value (Hogg 2001). The mechanical properties, segregation, porosity and die filling of Al-30Si-5Cu and Al-30Si-5Cu-2Mg during thixoforming has been investigated and the Mg containing alloy found to have enhanced thixoformability predominantly due to finer primary Si (Hogg 2001, Ward 1996). For lower Si content alloys (< ~30wt%) thixoforming may offer an attractive alternative to spray forming for the manufacture of thermal management materials.

2.3.3 Powder metallurgy of Al-Si alloys

Powder metallurgy is perhaps one of the most obvious choices for the processing of Al-high Si alloys because control of the feedstock powder diameter may provide control of the size and morphology of the primary Si particles. Al20-50Si has been manufactured by milling of Al and Si powder, followed by hot pressing of the 15μm powder at 550°C and 500MPa. The resultant microstructure demonstrated good Si particle wetting and Si

distribution, while the continuous Al matrix provided enhanced toughness (Yilmaz 1996a, 1996b).

Sumitomo Electric Industries (Japan) patented a process for the production of Al30-60Si alloys for thermal management applications (Sumitomo1989, 1990a, 1990b) involving the atomisation of molten Al-Si alloy into powder followed by sieving and grading of the powder, and then forming to near net shape by hot plastic working. However there is at present limited evidence of commercial applications of this patent. Elkem, (Norway) developed a processing route for Al and Ti alloys containing 2- 40% Si . Typically Si-Al with additions of V,Cr,Mn,Fe,Ni and Co, and Si modifier additions of Sr, B or P was vacuum induction melted and cast into bars, which were then used as feedstock for melt spinning. The melt spun ribbon was then milled to <500μm and consolidated by sintering, pressing and hot isostatic pressing (Elkem 1994). A similar process route was adopted by RSP Technology (Holland). Melt spun Al17-40Si ribbon was chopped then consolidated in a single operation by combined pressing and extrusion (Senden 2004). Both Elkem and RSP Technology report that the resulting microstructure is fine grained and the Si refined, yielding homogeneous, isotropic mechanical properties (values not reported).

2.3.4 Melt infiltration of Al-Si alloys

Melt infiltration of a porous powder billet has been investigated by Chen (1994) to manufacture Al-high Si alloys. A 50vol% Si billet was prepared by

cold pressing of Si with a water / phosphate binder, and was then infiltrated with molten Al-30Si-1Mg at 900°C and a 41MPa Ar pressure. This technique yielded an interpenetrating structure consisting of the Si phase and a Al-rich phase containing 3wt%Si, with an overall composition of 31wt%Al and 69wt% Si. However low infiltration rates and the multi-step production route increased process cost. Furthermore, there were several significant problems with melt infiltration. Han (1997) showed that the wetting characteristics of molten Al alloys were highly temperature dependent, with a superheat of ~500°C usually required to achieve wetting of the Si preform. Infiltration rates were proportional to the diameter of the capillary network in the billet and as a fine microstructure is usually desirable, this led to slow infiltration rates. It was possible to achieve higher infiltration rates by use of an inert gas overpressure or vacuum impregnation processes, though these both damaged the delicate pre-form billet (Han 1997). For lower Si volume fraction, of ~6 vol% it was possible to reduce cycle time by using a mechanically driven die and ram assembly combined with vacuum assistance to infiltrate Si with molten Al (Peng 2000). Despite the problems and costs associated with melt infiltration for Al-high Si alloys, there are some examples of commercial success in other systems. HIVOL is an Al-SiC MMC from AEA Technology for thermal management applications and is manufactured by pressure assisted infiltration in which moulds are filled with SiC powder followed by pressurised molten Al alloy infiltration. This technology is now operated under licence by AMETEK (USA) and is enjoying some commercial success.

2.3.5 Spray forming of Al-Si alloys

Spray forming has been investigated as a process for the manufacture of metal matrix composites (MMCs) with potential thermal management applications. Ibraham (1991) reviewed the development of production routes for MMCs, including spray forming, rheocasting and melt infiltration. Other spraying processes such as: low pressure plasma deposition, high velocity oxyfuel spraying, combined flame / electric arc spraying and modified gas – metal arc welding will not be considered in this review as they are not relevant to the production of bulk alloys for thermal management applications. The reader is directed to Lawley (1994), Ibraham (1991) and Strivatsan (1995) for further details.

In spray forming, a ceramic phase can be introduced to the liquid metal either by direct particle injection during deposition of a ceramic phase or by reaction of the molten alloy with reactive additions to the atomising gas; the latter procedure is termed reactive spray forming (Lawley 1994).

In spray forming with particle injection, a fluidised bed typically is used to feed ceramic or metallic particulate through an injection nozzle into a region close to the point of atomisation. The particulate is forced into the liquid metal either at atomisation, in flight or at deposition to produce a homogeneous distribution. As well as providing possible mechanical benefits or allowing the recycling of overspray powder, the particulate also cools the spray and billet, requiring re-optimisation of the spray forming parameters and possibly further catalysing of the nucleation of solidification.

One of the limiting factors is the size restriction on particles that can be injected because fine powders of <5μm are lost as overspray because they follow the gas flow out of the chamber (Willis 1987). Willis (1987) achieved 30 – 40 Vol% SiC in a range of different spray formed alloys including Al-Li - 8090, and 2xxx series Al alloys.

Particulate injection is inappropriate for the manufacture of Al-high Si as it is difficult to achieve sufficient volume fraction of Si without encountering problems of: inhomogeneous distribution of the injected (Si) phase in the matrix; excessive porosity; high oxide content (associated with the large surface area to volume ratio of the injected powder); and low yield because of loss of particulate in the turbulent atomising gas (Leatham 2004). Sandvik-Osprey Metals have investigated this technique using an Al-15Si master alloy and injecting ~3μm Si particles at flow rates calculated to yield 35, 45 and 55vol% Si in the sprayed billet. Despite use of a concentric atomiser and injector, to reduce the overspray losses described above, these trials deemed it impractical to form Al-high Si alloys by this technique (Osprey 2001) due to the difficulty of injecting in a controlled and reproducible manner.

2.4 Microstructure of gas atomised spray formed Al-Si

Sandvik-Osprey (UK), GMMT (UK), Alcatel Espace (France) and TNO (Holland) investigated Al-Si alloys for thermal management under a BRITE-EURAM research program in 1993 – 97 (Brite-Euram 1997). Considerable difficulties were encountered in manufacturing Al-high Si alloys using powder

metallurgy routes similar to that proposed by Sumitomo Electric Industries (Sumitomo 1989, 1990a, 1990b), and Sandvik-Osprey suggested and then demonstrated the feasibility of producing Al-high Si materials straight from melt using spray forming rather than conventional powder metallurgy routes. Furthermore, billets of up to 60kg were demonstrated, giving much greater scope for scale-up than powder metallurgy based routes. As-sprayed Al-high Si billets were scalped (to remove the porous outer layer), hot isostatic pressed to reduce porosity and finally machined to produce heat sinks, housings or other thermal management packages. This process was patented by Sandvik-Osprey in 1996 (Osprey 1996) with subsequent overseas patents filed (Osprey 1997, 2001).

Because of the protected intellectual property and relatively recent advent of spray formed Al-high Si alloys, literature relating to all aspects of the material including microstructure is scant. The author is fully aware of the current commercial status of Sandvik-Osprey ‘controlled expansion’ (CE) alloy product range based on Al-high Si alloys, but the current state of knowledge in the public domain only can be reviewed here.

The microstructure of spray formed Al-high Si CE hypereutectic alloys consists of a primary Si phase and a minority Al-rich phase, which is last to solidify, and grows through the primary Si open network (Jacobson 1997). Figure 2.20 shows a typical microstructure of spray formed Al-70Si alloy where the dark phase is primary Si, and the pale phase is the Al rich phase.

Hogg (2001) investigated spray formed Al-36Si and observed a 'halo' effect of Al-Si eutectic around the periphery of primary Si grains, whereby the eutectic adjacent to primary Si is devoid of eutectic Si. This effect is common in faceted / non-faceted eutectic alloys, whereby the non-faceted phase (Al) will surround the faceted phase (Si) and not vice versa. The liquid adjacent to the nucleated primary Si is enriched in Al due to solute rejection and the liquid, of eutectic composition, nucleates around the Si phases to form a halo or 'divorced eutectic'.

Fine scale porosity in spray formed Al-Si alloys can be reduced to <0.1 area% by a post spraying hot isostatic pressing (HIPing) at a temperature approaching the Al-Si eutectic liquidus (Jacobson 1997). No pressureless heat-treatment of Al-high Si alloys is possible because of problems of cracking, consequently it is essential to control the as sprayed microstructure as subsequent alteration or modification is impossible (Osprey 2001). The large freezing range of Al-70Si of ~640°C shown in Figure 2.18 makes inverse segregation, as previously described, a significant problem. Solidification shrinkage in the billet centre can be eliminated by controlling the cooling and solidification of the liquid metal which remains in the billet after spraying is complete, using a Sandvik-Osprey patented technique in which the billet is insulated immediately after spray forming is complete and a chill applied to the base (adjacent to the substrate) to drive the solidification front along the length of the billet from base to top (Osprey 2001). In this way porosity and

solidification shrinkage in the bulk material can be concentrated at the billet top and scalping losses are minimised.

Hogg (2000) used transmission electron microscopy (TEM) to investigate spray formed Al-30Si and observed the presence of Al nanoprecipitates of typically 5-10 nm of a spheroidal morphology in the primary Si phase. Although this investigation considered only Al-30Si, again, it may be expected that similar precipitates may exist in Al-high Si alloys produced by spray forming. These features may be of interest when considering electrical and RF screening properties.

2.5 Properties of spray formed Al-Si

The continuity of the Al rich phase in spray forming Al-high Si alloys has several beneficial effects: the electrical conductivity allows plating with Au, Ag, Cu or Sn (Jacobson 1998,1997), which is essential as plating provides the substrate for reaction soldering and improves the hermeticity. Plating of Al-high Si has been demonstrated to remain blister free both in service and during welding and brazing operations (Brite-Euram 1997). Relatively high electrical conductivity of $<10^{-6}$Ohm.cm also makes these alloys appropriate for machining by electro-discharge machining (EDM). As the wt% Si is increased, the resistivity also increases, with a sudden increase occurring when the Si phase fraction becomes so high that the Al phase loses connectivity, at ~85wt% Si (Ogilvy 2003). Electrical conductivity also provides RF (Radio

Frequency) and EMI (Electro-Magnetic Interference) screening (Osprey 2001).

Electronic packages intended for aerospace or satellite applications consist of a box with appropriate RF and DC feed-throughs. This box contains, protects and cools the circuitry. Once the contents are soldered in place, a lid is EB (Electron Beam), laser or resistance welded to seal the package (Jacobson 1998, 1997). This means the package material must not only be weldable but also the weld and the material must have a high degree of hermeticity. Spray formed Al-Si has been proven to be EB weldable and has passed an industry standard He permeability test (Jacobson 1997).

Severe cost premiums are associated with every added kilogram of weight in aerospace and space industries. Typically over the life of a commercial aircraft, each added kilogram will increase the fuel and running costs by around £50,000 (White 1990). In satellite applications cost penalties at launch are ~£30,000/kg (Kunes 1998). At 2.4g/cm^3, Al-70Si is lower density than many common thermal management materials (Jacobson 1997).

Sandvik-Osprey have demonstrated that Al-high Si alloys can be readily machined using conventional cemented carbide or poly-crystalline diamond cutting tools, the latter giving considerably extended tool life. Tool wear is highly dependent on cutting speed: on finishing operations, tool life is approximately halved for each 5 m/min increase in cutting speed above the optimum. Machining trials have demonstrated that it is possible to achieve

wall thickness of as little as 0.6mm, though care must be taken to minimise bending stresses (Osprey 2002). Al-70Si has a high specific stiffness, but low toughness and a commensurate high sensitivity to surface flaws. Typical properties are: UTS of 80MPa, a Young's modulus of ~130GPa and a fracture toughness of ~3.0MPa $m^{1/2}$ (Osprey 2004, 2001).

2.6 Summary

- There are a range of materials which fulfil the needs of the thermal management industry,
- All materials are in some aspect a compromise of properties (e.g. a good CTE match, but high density).
- Spray formed Al-70Si (CE7) has an excellent balance of thermal management properties and is a potentially competitive alloy in this niche market.
- Spray forming has been successfully demonstrated as the only viable means of manufacturing bulk Al-high Si (<50%Si) alloys with sufficient strength to be commercially useful.
- Aspects of CE7 processing are poorly understood and require investigation. (For example it may be possible to further refine the spray formed microstructure and enhance properties by using particle injection or alloy modification).
- Investigation of process parameters may enable optimisation of the desirable thermal management properties of CE7 to the commercial benefit of Sandvik-Osprey.

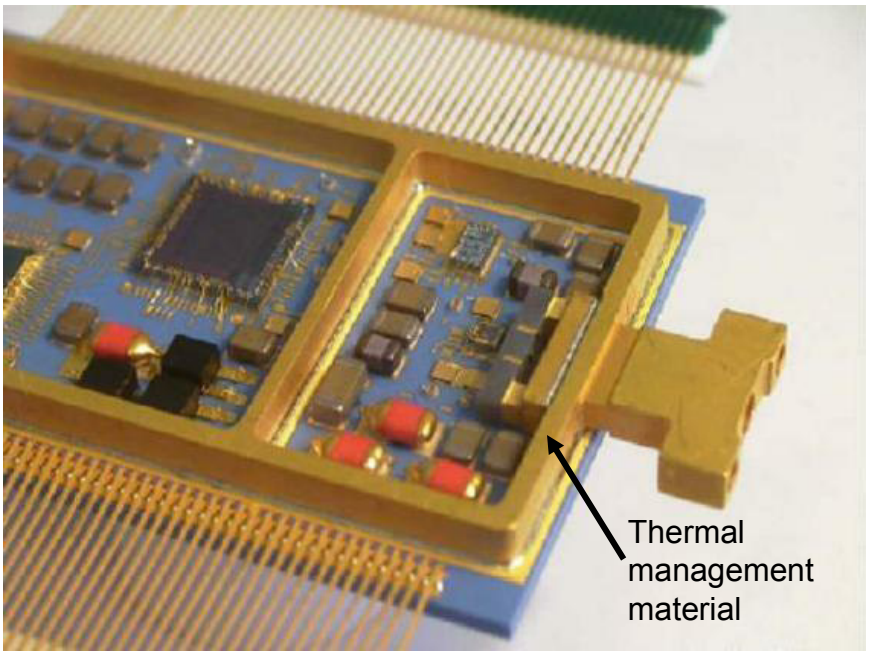

Figure 2.1

Typical optoelectronics package prior to fitting of the lid

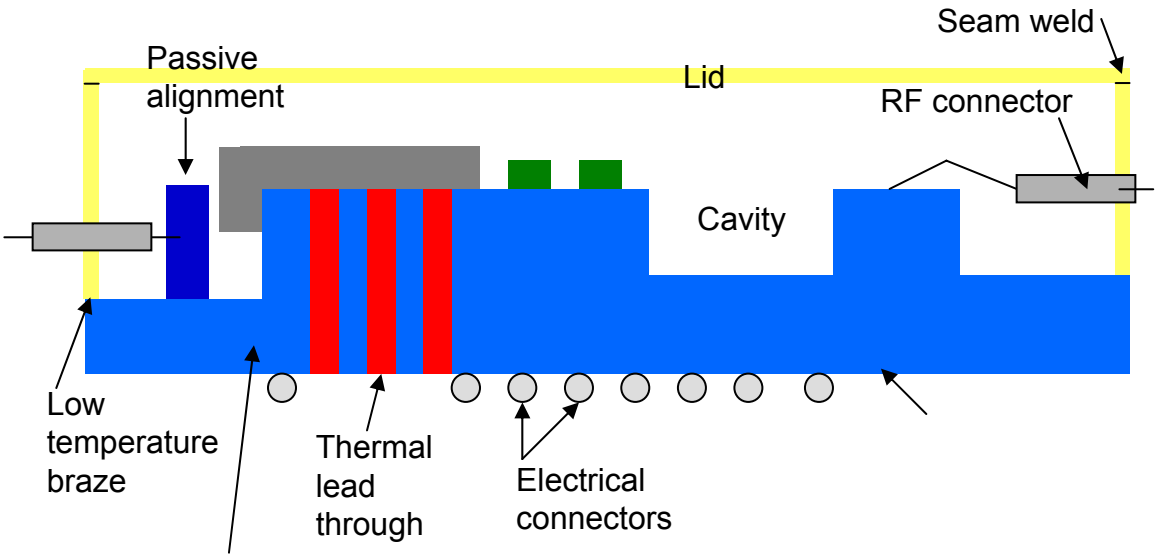

Thermal management material with gold electroplating, and electronic and thermal lead throughs, resistors and other components indicated

Figure 2.2

Schematic cross section through typical opto-electronics package (Figure 2.1)

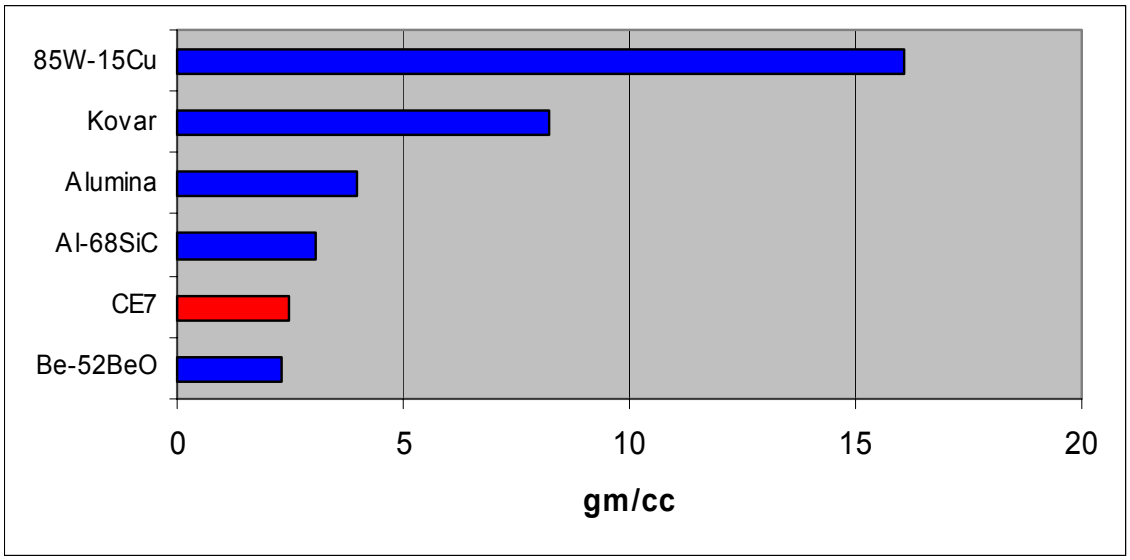

Figure 2.3
The density of common thermal management alloys.

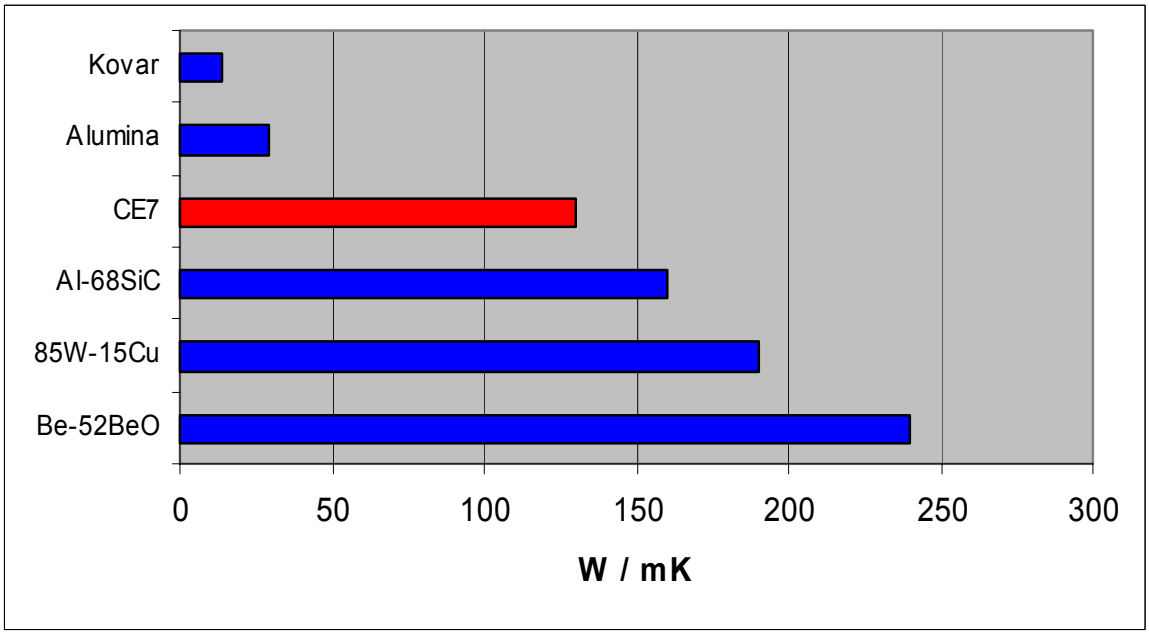

Figure 2.4
The thermal conductivity of common thermal management alloys.

Note: CE7 is spray formed Al-70Si

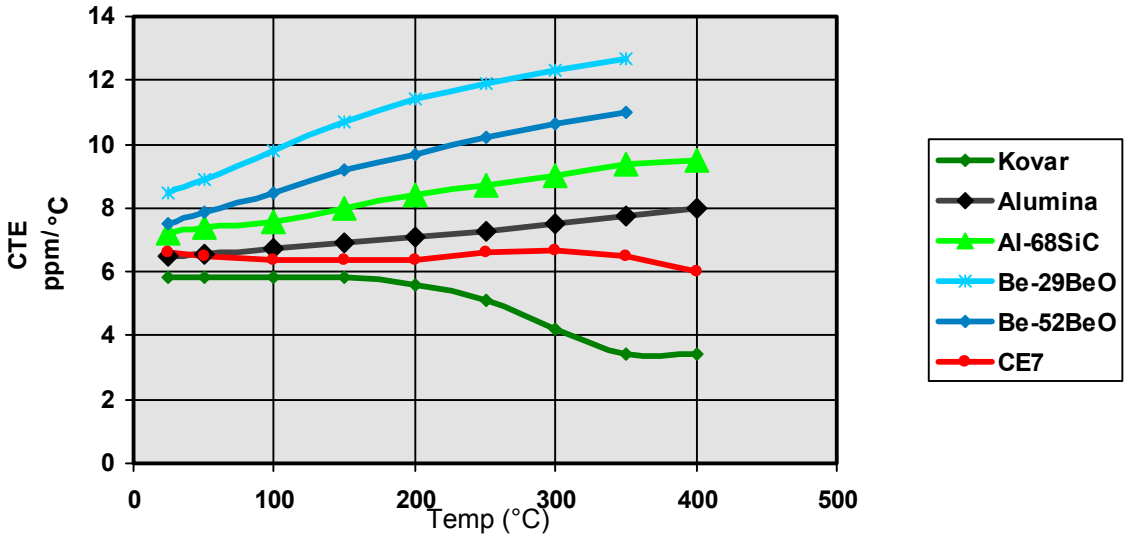

Figure 2.5
The variation of CTE with temperature of some common thermal management alloys
Note: CE7 is Spray formed Al-70Si

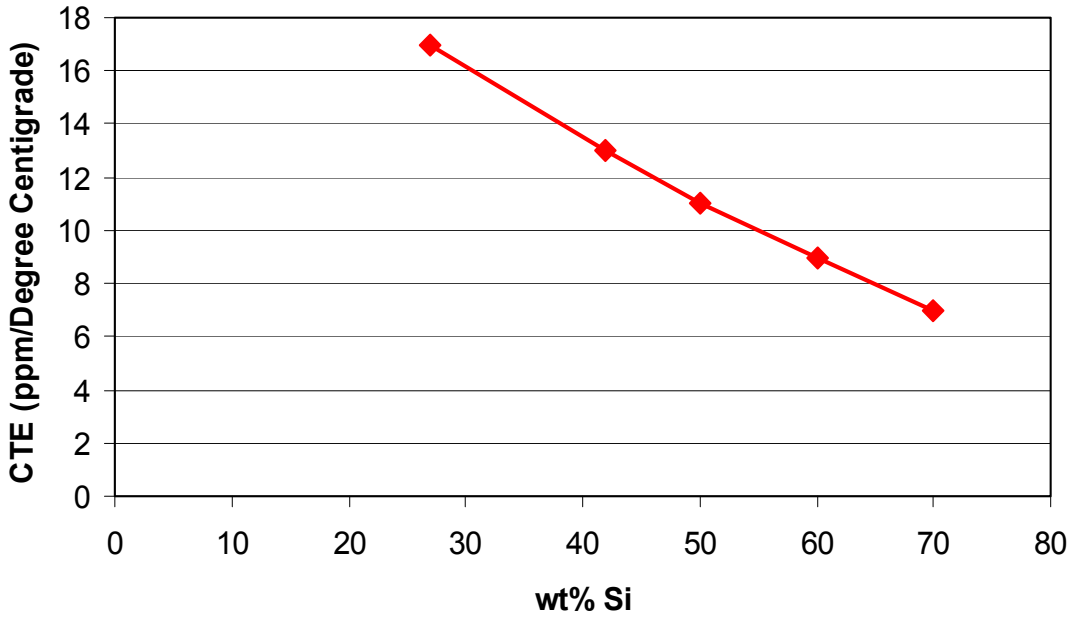

Figure 2.6
The relationship between Si content and CTE in Al-Si alloys manufactured by spray forming

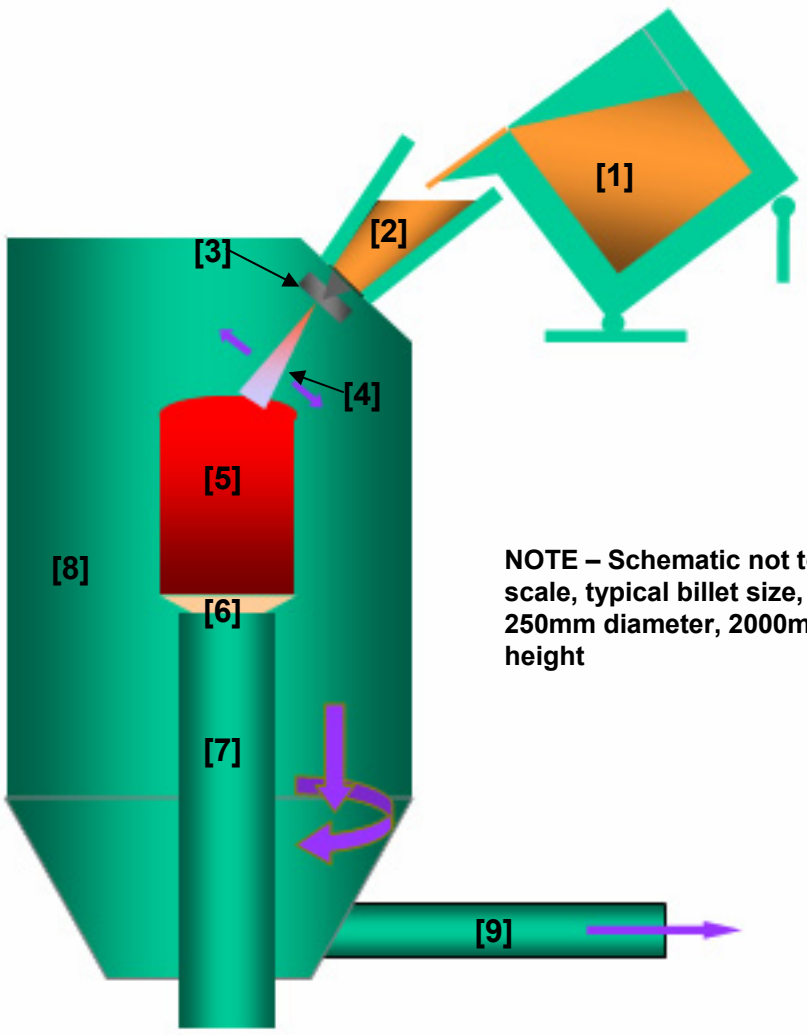

Figure 2.7
Schematic of Sandvik-Osprey spray forming plant; [1] Tilt-pour induction furnace, [2] Tundish, [3] Atomiser, [4] Spray, [5] Billet, [6] Substrate, [7] Ram (rotate and retract), [8] Chamber, [9] Exhaust.

The sequential operations being;

[1] Melting
[2] Atomisation
[3] Droplet flight
[4] Droplet impact
[5] Solidification

NOTE – Schematic not to scale, typical billet size, 250mm diameter, 2000mm height

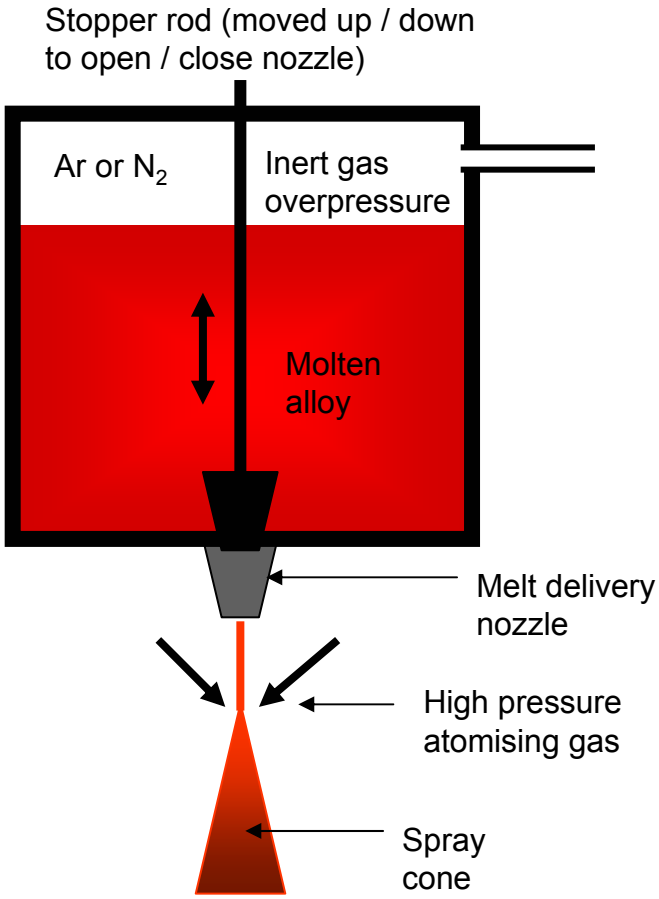

Figure 2.8

Schematic diagram of a bottom pour furnace arrangement for spray forming

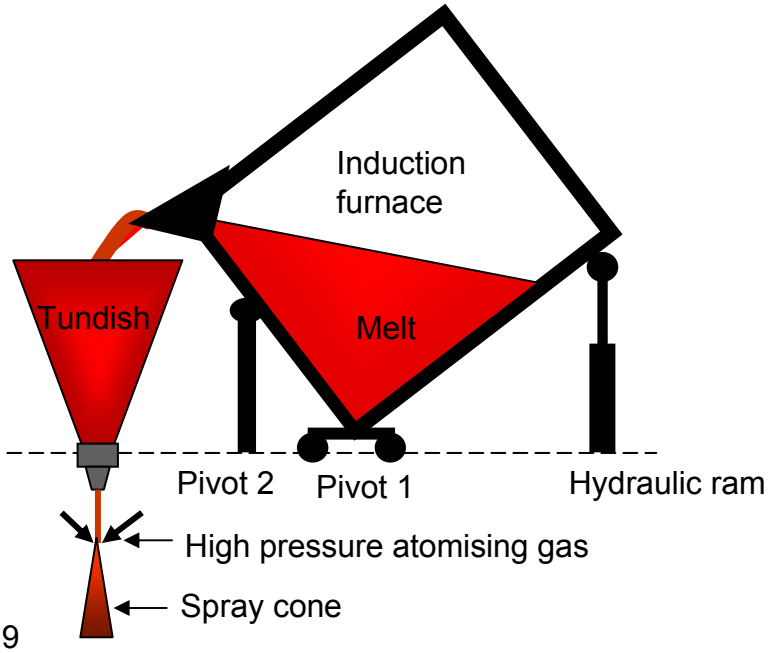

Figure 2.9

Schematic diagram of a tilt-pour furnace arrangement for spray forming

Figure 2.10
Schematic of the GE Corp. 'clean metal spray forming' (CMSF) system, for production of high quality Ni superalloy billets.

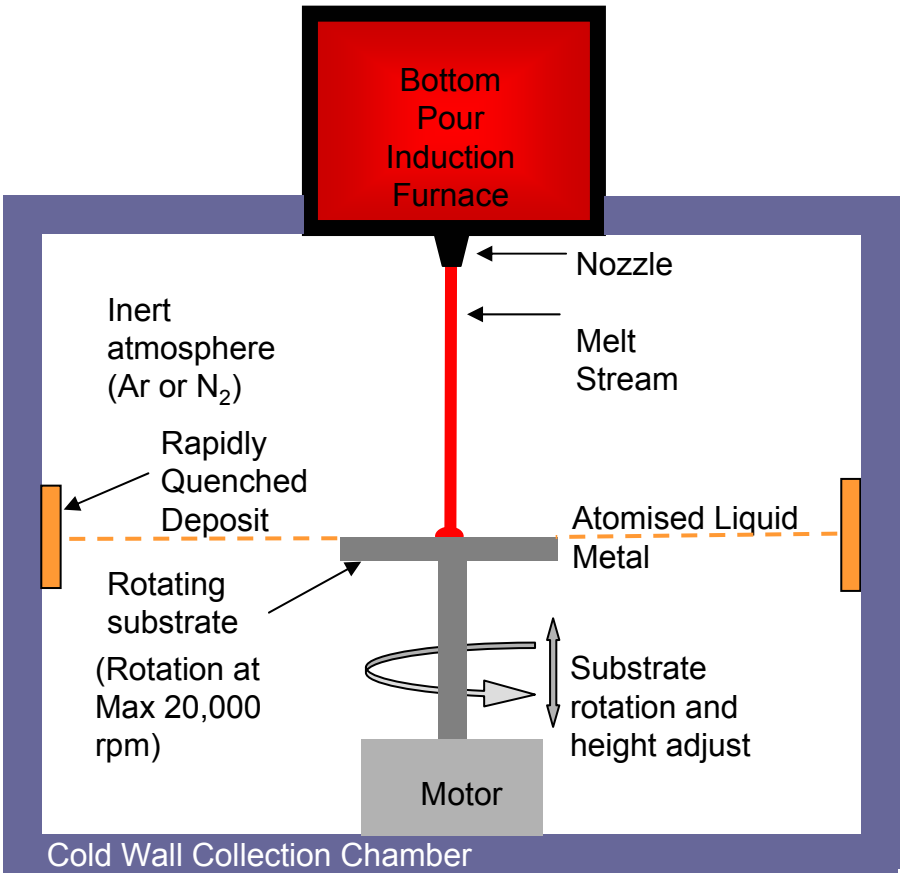

Figure 2.11
Schematic of centrifugal atomisation and spray forming.
[1] The superheated charge pours out of the furnace via the nozzle.
[2] The melt hits the centre of the spinning plate or dish.
[3] Centrifugal force overcomes surface tension effects at the plate periphery
[4] The melt is fragmented into droplets
[5] The atomised droplets collect and coalesce on the chamber wall or substrate

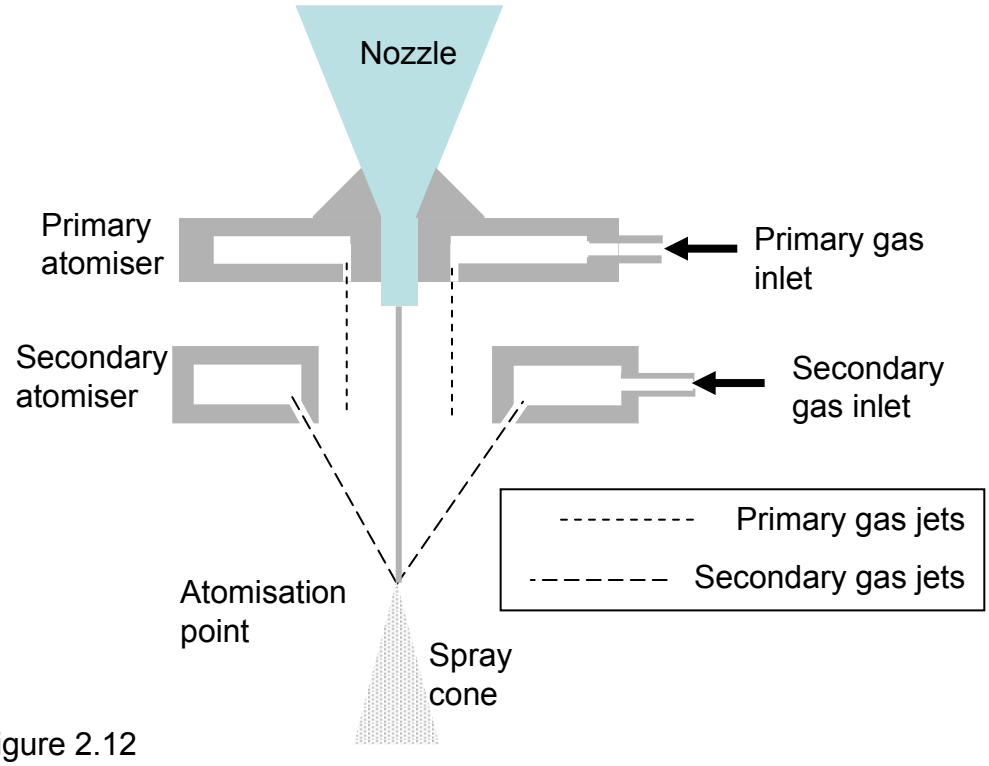

Figure 2.12

Typical 2 stage close couples atomiser using a primary atomiser parallel to the melt to stabilise the melt stream and a secondary atomiser to fragment the melt into droplets

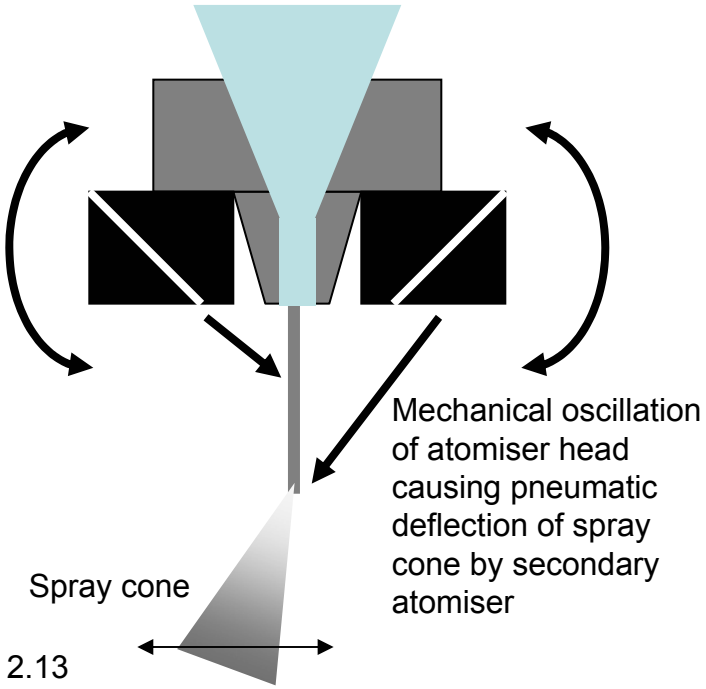

Figure 2.13

Scanning atomiser using mechanically oscillated secondary atomiser assembly to deflect the spray cone

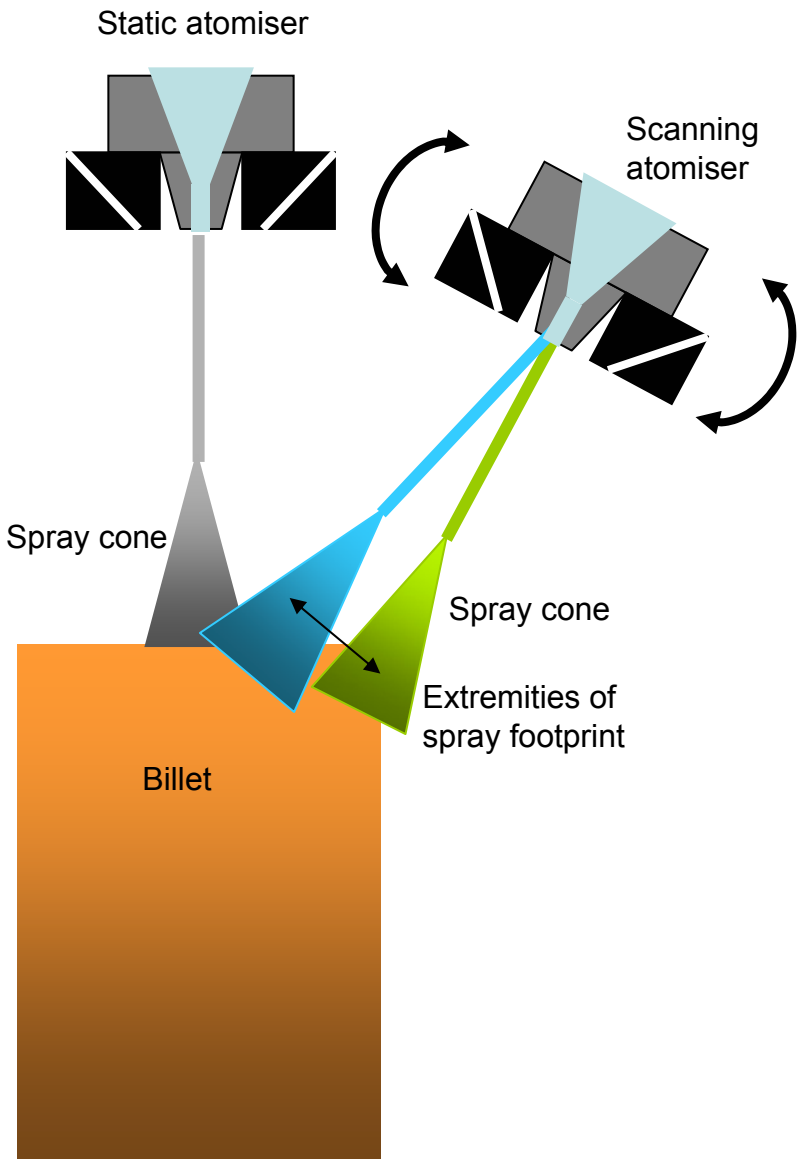

Figure 2.14

Twin atomiser system using a static atomiser and a scanning atomiser to increase deposition rate

Figure 2.15

Spray formed Al-20Si billet produced at PEAK, representing the current state of the art in large scale spray forming

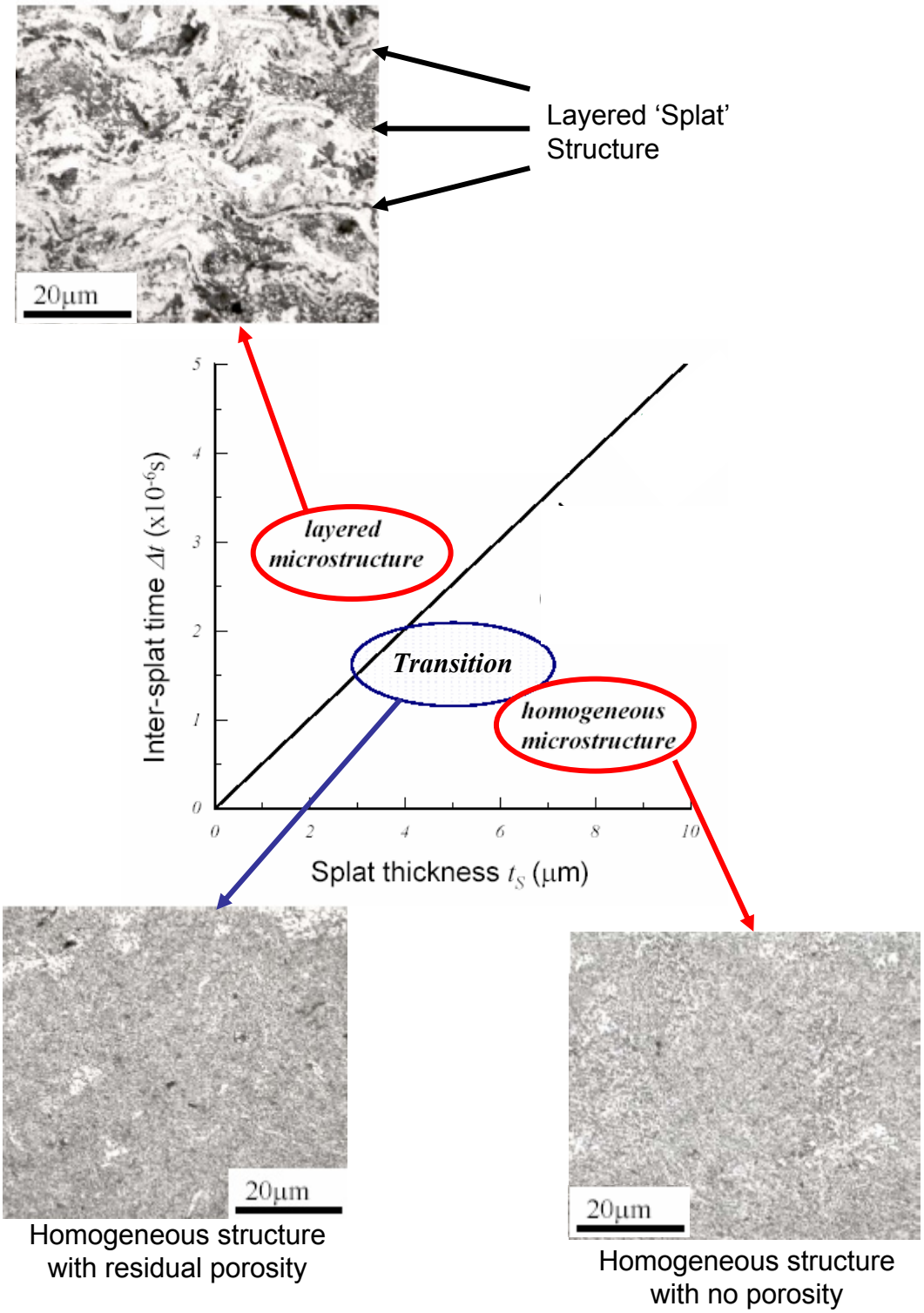

Figure 2.16

Processing diagram showing the influence of splat thickness (determined by droplet size or spray height) and inter-splat time on the microstructure of a Al-12Si alloy manufactured by Vacuum Plasma Spraying (VPS). Cantor, 1997

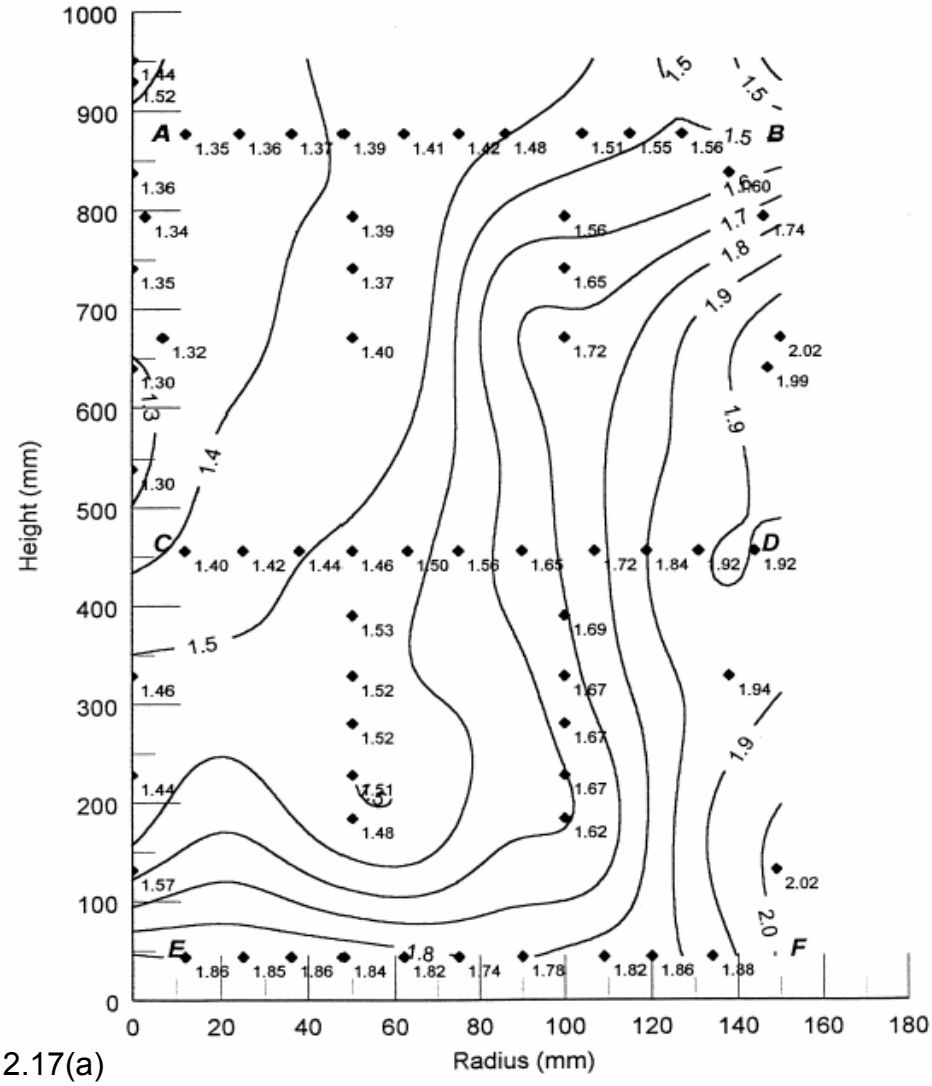

Figure 2.17(a)
Macro segregation map showing the distribution of Cu concentration in spray formed 8091 (Mingard 2000).

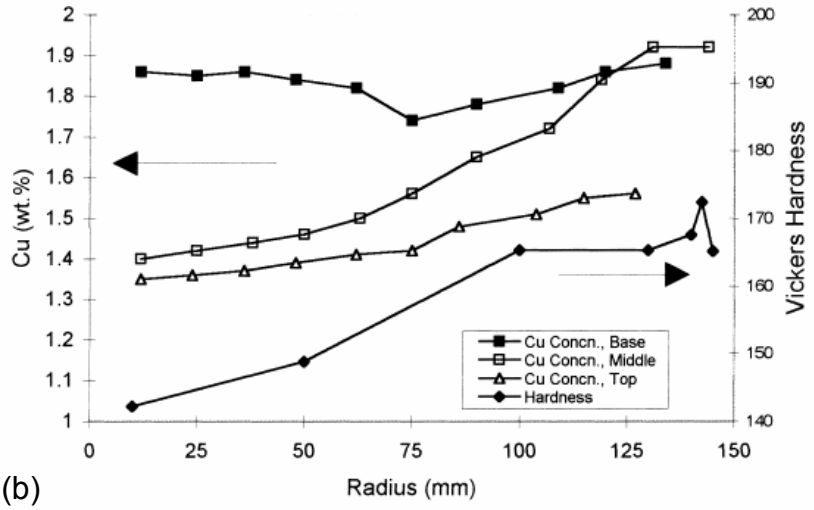

Figure 2.17(b)
Variation of Vickers hardness with Cu concentration across a radial section of spray formed 8091 (Mingard 2000).

Figure 2.18

Binary Al-Si phase diagram (Murray 1984)

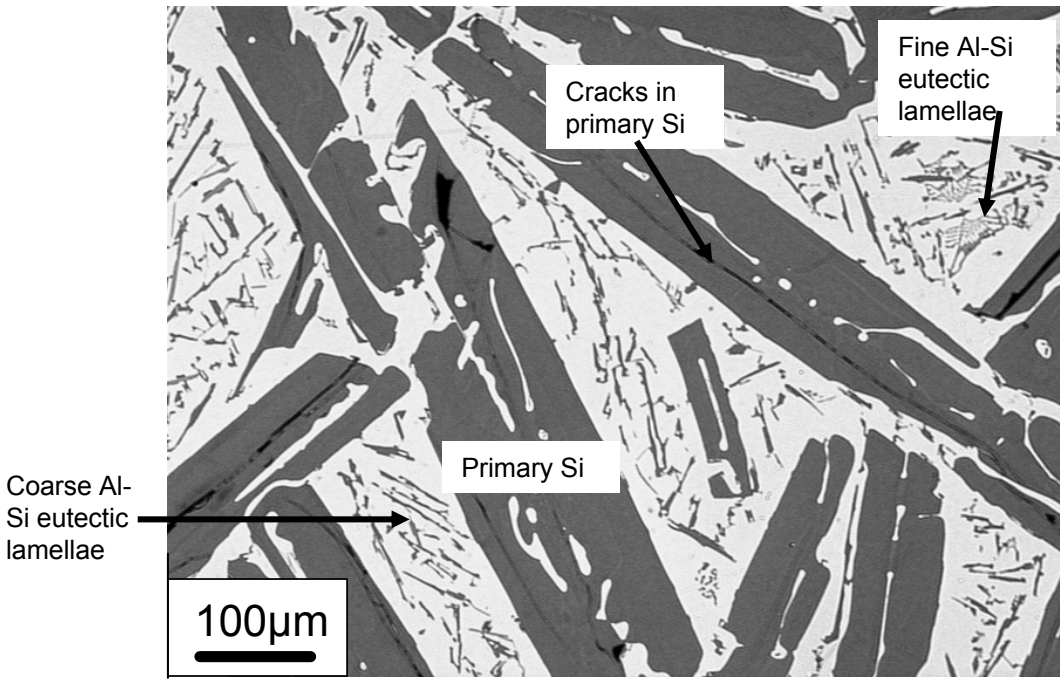

Figure 2.19

Typical micrograph of cast Si-30Al.

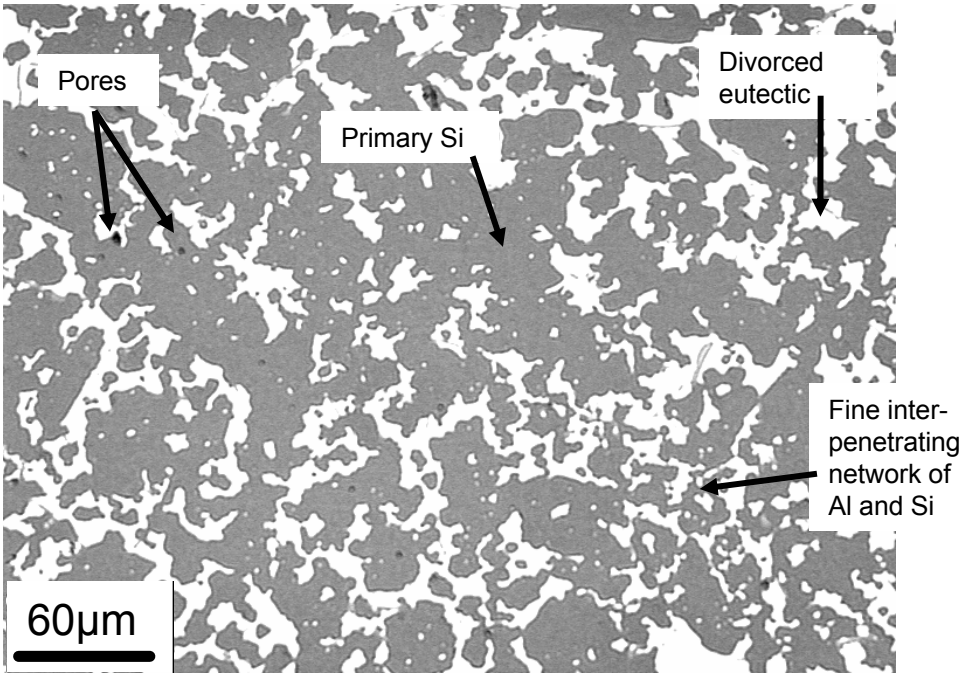

Figure 2.20

Typical micrograph of spray formed Si-30Al (CE7), Note the absence of 'splat' microstructure due to thermal equilibration and partial re-melting of droplets

3.0 Experimental programme

Manufacture of commercial CE7 material for this research was undertaken at Sandvik-Osprey Metals Ltd as detailed in Section 3.1. A wide range of characterisation techniques were used to investigate the structure and properties of CE7. Microstructural characterisation included optical microscopy, image analysis, EPMA and EBSD techniques, as detailed in Section 3.2. The physical characterisation of CE7 presented difficulty in terms of sample preparation and handling as well as selection of suitable techniques for this unusual material. The characterisation techniques and the associated sample preparation is detailed in Section 3.3. Sandvik-Osprey have largely optimised the primary processing of CE7 and it was hoped that further alloy development could be achieved through ternary additions to refine the microstructure. Section 2.3.1.1 reviewed the modification of conventional Al-Si casting alloys, and a range of Si modifiers suggested by the literature were selected and used to modify high Al-50Si chill castings as described in Section 3.4. Four alloy modifiers were then selected and used in spray forming of modified CE7 at Oxford University. The Oxford spray forming plant, differences in the spray forming process at Oxford and the manufacture of these alloys is detailed in Section 3.5.

3.1 Spray Forming at Sandvik-Osprey Ltd

3.1.1 Background

Sandvik-Osprey (formerly Osprey Metals Ltd) has for the last ~8 years focused their spray forming activities on Si-Al alloys. During this time they have developed understanding of the problems of spray forming Si-Al binary alloys. As explained later in this chapter these problems include low toughness, flaw sensitivity, porosity and processing difficulties. CE7 material supplied by Sandvik-Osprey at the beginning of this research programme represented the state-of-the-art in foundry practice, spray forming, post-spray cooling and downstream processing. The Sandvik-Osprey material was used as a best-practice baseline with which subsequent alloy or process development at Oxford was compared.

3.1.2 Alloy Selection

The family of CE alloys produced by Sandvik-Osprey consists of 5 binary alloys of Al and Si. As described in Section 2.1.5, varying the proportion of Si to Al in the range 27 to 70% Si alters the alloy coefficient of thermal expansion (CTE) from 7 to 17 $x10^{-6}$ $°C^{-1}$ respectively, matching the CTE in specific applications to minimise thermal expansion mis-match. CE7 (Si-30Al) has a CTE of 7ppm/°C closely matched to the CTE of GaAs and Al_2O_3 (circuit board substrates), and is of potentially major commercial significance to Sandvik-Osprey. CE7 was selected as the focus for this research because of this commercial importance and because of the lack of fundamental knowledge about the processing-structure-property relationships in this material.

3.1.3 Manufacture of CE7 at Sandvik-Osprey Ltd

A CE7 billet was manufactured by gas atomised spray forming at Sandvik-Osprey as follows: A Al-70Si alloy charge was induction heated to ~150°C superheat and then poured into a ceramic lined, conical tundish. The melt then passed through a ceramic melt delivery nozzle and was then atomised using high pressure N_2 in a two stage atomiser comprising low pressure primary and high pressure secondary atomisers, each using a circular arrangement of discrete gas outlets concentric with the nozzle, as described in Section 2.2.5.2. Al-70Si overspray powder from previous spray forming runs that had previously been sieved and sized was injected throughout the spray forming as a method for recycling some of the overspray powder that is an inherent part of the spray forming process. In addition to the optimised 'best practice' billet, samples of 3 CE7 materials of different particle injection ratios (from 26 to 48%) were also supplied by Sandvik-Osprey in order to investigate the influence of particle injection on the microstructure and properties of CE7. Overspray injection was achieved using a fluidised bed particle injector with N_2 transport gas and delivery into the spray via a modified primary atomiser. The resultant spray cone consisting of atomised and injected particles was intercepted by a circular rotating ceramic substrate placed on an inclined ram which was progressively withdrawn during spray forming in order to keep the melt delivery to the billet surface distance constant, (termed spray distance or spray height). The equipment is shown schematically in Figure 3.1. The exact manufacturing parameters such as melt flow rates, gas flow rates, atomiser geometry, etc are proprietary and can not be disclosed here.

3.1.4 Post spray processing

As soon as the melt was exhausted spray forming was complete, the billet was removed from the chamber and placed into a steel box lined with high temperature refractory insulation and a chill applied to the base of the billet base, for ~12 hours, as shown schematically in Figure 3.2 (Osprey 2001). The billet surface porous layer was removed and an ultrasonic probe was used to confirm the absence of gross porosity in the billet centre. The billet was then sectioned across the diameter using a WC tipped band-saw. Half the billet was supplied to Oxford in the as sprayed condition and half was supplied after hot isostatic pressing (HIPing) conducted by Bodycote-HIP (Chesterfield, UK) at 140MPa for 16 hours at 565°C under a N_2 atmosphere. 'Canning' or encapsulation of the material was conducted as it was thought that porosity may be interconnected.

In some cases CE7 thermal management CE alloys are fabricated into multi-alloy components using a diffusion bonding process. This allows the different CTE properties of different CE alloys to be exploited in different areas of a thermal management component. CE7-CE11 and CE7-CE17 laminates are investigated under thermal cycling conditions as described in Section 3.3.8. In both laminates an Al interlayer is used to minimise interfacial stresses between the two CE alloys. Laminates are diffusion bonded at elevated temperature and pressure under conditions similar to Sandvik-Osprey HIPing conditions. Exact processing conditions are proprietary.

3.2 Microstructural characterisation

3.2.1 Sample preparation

Optical Microscopy Sample Preparation

Samples were prepared for metallographic examination by optical and electron microscopy by mounting them in conductive Durofast epoxy hot mounting resin with mineral filler for edge retention. Mounting was conducted in a Struers Primo press with a cure temperature of 175°C and a mounting pressure of 43kN. Samples were then ground and polished using a semi-automated ATM Saphir 350E polishing unit, and up to 6 samples were prepared simultaneously using a multi-sample, counter-rotating polishing head. Grinding operations used progressively finer SiC paper of 240, 400, 800 and 1200 grit, followed by polishing with 9 and 3μm diamond suspensions and a final polish with an aqueous solution of 0.06μm colloidal SiO_2. Samples were swabbed in methanol to remove polishing residue and dried with a hot air drier. Some variations to this sample preparation for electron microscopy is detailed below.

Electron Backscatter Diffraction (EBSD) Sample Preparation

For EBSD examination the orientation of the sample to the billet was critical. 12mm diameter samples were cut using electro-discharge machining (EDM) from 25mm square 6mm thick samples taken from the billet in known orientations. These samples fitted directly into the microscope sample holder and mitigated the need for conductive resin or silver dag. Polishing was done by hand using the same regime as for optical microscope samples with a final polish using non-crystallising colloidal silica to minimise residual stress.

Electron Probe Micro Analysis (EPMA) Sample Preparation

For EPMA analysis additional polishing using a 0.05μm Al_2O_3 suspension was used to remove traces of SiO_2 contamination from the surface. This would otherwise confuse the investigation of the Si distribution in the EPMA. To prevent charging, samples were coated with C in an Edwards 12E6 vacuum evaporation unit.

3.2.2 Optical microscopy

Optical microscopy was conducted using a Zeiss Axioplan 2 reflected light microscope equipped with differential interference contrast (DIC), black and white digital imaging equipment and Zeiss KS400 image capture and analysis software. Objective lenses of 5x, 10x, 20x, 50x and 100x and an eyepiece magnification of 10x were used to image the sample microstructure and macrostructure. Several techniques were investigated in an attempt to view Si-Si and Al-Al grain boundaries.

For Al-Al grain boundaries, three methods investigated were:

[1] Rapid heating to 600°C (above the eutectic temperature of 577°C) and quenching to provide grain boundary topographic contrast by virtue of grain boundary wetting.

[2] Anodising of the Al phase in Barker's reagent (2-4% HBF_4 acid in H_2O at 20V DC)

[3] Etching in Keller's etch (1ml HF, 2ml HCL, 3ml HNO_3 in 94ml Water).

For Si-Si grain boundaries, all grain etches contained HF and all relied on the formation of oxide and differential dissolution at grain boundaries. Some etches in the literature are optimised to investigate specific orientations such as the Sirtl etch for <111> surfaces (Sirtl 1961) and Seiter etch for <100> surfaces (Seiter 1977). The etches below were suggested to be effective for any grain orientation:

[1] The Dash etch: 1ml HF acid , 1ml HNO_3 acid , 10ml $C_2H_4O_2$ acid, 4-16 hrs (Dash 1956).

[2] The Wright etch: 60ml HF acid , 30ml HNO_3 acid , 60ml $C_2H_4O_2$ acid , 60ml deionised water , 30ml of solution of 1g K_2CrO_4 in 2 ml of water, 2g(Cu NO3)2. 3H2O, 5 - 10 min, (Wright 1977).

[3] The Secco etch: 2ml HF acid ,1ml K_2CrO_4 (0.15 molar in water), 5 - 10 min, (Secco d'Aragona 1972).

However all these etches for both Al and Si were ineffective in both cases, probably because of the interference of the other phase in the reaction chemistry. Samples were viewed therefore in the un-etched condition and grains and their boundaries only clearly imaged using EBSD.

3.2.3 Image analysis

Image analysis was used to measure porosity distributions, phase fractions and the interface length per unit area between Al and Si phases using Zeiss KS400 software and Image J, a free Java application for image analysis and processing. The interface length per unit area between the Al (strictly Al-rich

phase since there is significant solubility of Si in Al, but termed Al phase here for convenience) and Si phases was investigated because it was believed to be related to the toughness of CE7 since the Al phase had been observed to deflect or blunt cracks propagating through the Si phase. Interface length was measured using Image J and a custom macro given in Appendix 3.1(a). Calibration allowed a conversion between pixel size and microns and yielded an interface length measurement per unit area sampled in mm/mm^2. All analyses was performed at x200 magnification under identical lighting conditions. Typical images at each stage of analysis are shown in Appendix 3.1(b). Porosity distributions were measured on-line using Zeiss KS400 software by setting a grey-level threshold to remove the Al and Si phases leaving only porosity. Using the macro given in Appendix 3.2 porosity was expressed as an area percentage of the analysis area.

3.2.4 Scanning Electron Microscopy (SEM)

A JEOL 840a scanning electron microscope fitted with an EDS (energy-dispersive spectroscopy) detector was used to investigate polished and fractured samples. Because the emission lines for Al and Si are very close (Al Kα=1.48keV, Si Kα = 1.73keV) quantitative EDS in CE7 was not possible. The EDS INCA software used correction factors to mitigate these peak interference problems. However, one of the assumptions is that Al and Si are present as a homogeneous phase acting as a point source. Since CE7 is a two phase microstructure this assumption is not valid. Nevertheless, qualitative EDS

mapping of Al and Si, on fracture surfaces provided valuable information on the prevalent fracture mode in CE7.

3.2.5 Electron probe micro analysis (EPMA)

EPMA was performed using a JEOL JXA 880R using an accelerating voltage of 15keV. This equipment was fitted with four WDS (wavelength dispersive spectrometry) detectors. WDS spectrometers are based on Bragg's law and use moveable, shaped monocrystals as monochromators. By using different WDS spectrometers to measure Al and Si phase X-ray emission it was possible to mitigate the problems of peak interference previously described.

EPMA was used to produce elemental maps and to investigate the composition of primary phases and intermetallic phases which resulted from the presence of trace impurity elements. However, interference and interaction volumes effects imply that for microstructural features <5μm accurate quantification of composition is unsafe. Interference occurs where the incident beam excites X-ray emission from the surrounding or underlying material resulting in misleading spectra for the feature of interest.

3.2.6 Electron back scatter diffraction (EBSD)

A JEOL 6500 fitted with a sample holder inclined at 70° and suitable detectors was used in conjunction with TSL software to investigate CE7 grain orientations. EBSD relies on positioning the specimen within the SEM chamber such that a small angle, typically 20°, is made between the incident electron beam and the

specimen i.e. the sample is inclined at 70°, so the proportion of backscattered electrons that are able to undergo diffraction and escape the specimen surface is enhanced. The resulting diffraction pattern is captured and processed to obtain the orientation of the crystallographic planes in the interaction volume. From the interaction volume over the sample surface a 2D representation of grain orientations relative to some external axis is obtained.

EBSD data was combined with EDS data obtained simultaneously and EDS data was used to separate the Al and Si EBSD data sets i.e. Al and Si phase grains could be separated in the EBSD image. This was achieved using the TSL software for un-mounted samples from known billet orientations.

Although prior to this project, little was known about CE7, it was assumed that the primary Si phase was polycrystalline (Osprey 2001). It had been difficult to confirm and quantify this assumption, because of the difficulty in chemically etching Si-Si high angle (<15°) grain boundaries as discussed in Section 3.2.2. This problem was overcome by using EBSD with combined EDS; similarly EBSD orientation maps made it possible to investigate Al grains even if they were inter-penetrated by Si. However grain size measurements were sensitive to the microscope conditions and the grain size resolution was limited by the step size (distance between adjacent analysis sites) used during the scan.

$$\textit{Area of grain} = \textit{Minimum No of analysis points in the grain} \times \textit{step size}^2 \times \sqrt{\frac{3}{2}}$$

Where: the grain is defined as adjacent analysis sites with <5° mis-orientation, the minimum No of analysis points in grain is set at 5 (less analysis points than this can not be called a discrete grain with any confidence), the step size is the

distance between adjacent analysis sites and $\sqrt{3}/_2$ is a correction for a hexagonal analysis grid. Thus the resolution can be calculated for the 2 sets of analysis conditions used in this study:

[1] Step size 1.5μm & 5 points per grain = minimum grain resolution of 3.5μm

[2] Step size 0.3μm & 5 points per grain = minimum grain resolution of 0.7μm

EDSD data was also used to investigate texture both in Si and Al phases using pole figures (PF) to show how the specified crystallographic direction of grains are distributed in the sample reference frame, and inverse pole figures (IPF) where the orientation distribution of a sample axis is shown on a stereogram plotted with respect to crystallographic orientation.

3.3 Physical characterisation

3.3.1 Fracture toughness

Fracture toughness expresses a material's resistance to brittle fracture when a pre-existing a crack or defect is present. If a material has high fracture toughness it will tend to undergo ductile fracture. Brittle fracture is characteristic of materials with low fracture toughness, as the stress intensity factor around a crack tip or defect reaches a critical value K_c, unstable fracture occurs and K_c is termed the fracture toughness. The plane strain fracture toughness, K_{Ic} is dependent upon specimen geometry and metallurgical factors (ASTM 1997).

However it is often difficult to perform a valid test for K_{Ic}. In particular sample preparation of complex geometry test specimens from brittle, defect sensitive

materials can be problematical. For this reason, alternative procedures to obtain K_{1c} in these materials have been developed. These procedures generally use small indentations to introduce and extend micro-cracks that are then measured; K_{1c} can then be estimated.

3.3.2 Vickers fracture toughness technique

A standard Vickers hardness testing machine with low loads (typically in the range 0.5 – 20.0Kg, Tancret 2000) was used to indent and crack a brittle material and the ratio of load to (crack length)$^{3/2}$ can be related to fracture toughness. The critical load for crack propagation depends upon the material and type of indenter, but typically for a Vickers (diamond) indenter and Al_2O_3 with $K_{1C} < 4$ MPa m$^{1/2}$, the critical load at which cracks will nucleate and propagate from the corners of the indent is <1kg. The length of a crack, 2*c,* at the indent corner is related to the fracture toughness by (Anstis 1981, and reported by Ponton 1989a):

$$K_{1c} = 0.016\left(\frac{E}{H}\right)^{1/2}\left(\frac{P}{c^{3/2}}\right)$$

Equation 3.1

where: *E* is Young's modulus (GPa), *H* is the mean contact or indentation pressure exerted by the Vickers indenter, *H* is given by H=P/2a^2 where a is the indentation half-diagonal length (m), (Ponton 1989a), and *P* is the load (N). The crack length c (μm) must be measured from the centre line of the indent to the crack tip on the surface of a well polished sample. This method, though widely used is not yet standardized and the numerical constant (0.016) can differ in

various formulas and other exponent values have been proposed (Lawn 1980, Lankford 1982, Tanaka 1987). The advantage of the technique lies in its simplicity and low volume of material necessary for the test.

When using the indentation technique for fracture toughness measurement, ideally one of two forms of cracking should result [i] radial-median 'halfpenny' cracks, or [ii] radial Palmqvist cracks (Ponton 1989a). It is important to establish the development of radial-median 'halfpenny' cracks under the indenter, shown schematically in Figure 3.3. If radial Palmqvist cracks develop, the formula for fracture toughness must be adjusted accordingly. For most ceramics of low and moderate fracture toughness, the radial-median 'halfpenny' crack develops during indentation and Equation 3.1 is valid. In some interpenetrating phase composites and multi-phase ceramics containing a ductile re-enforcement phase, the fracture behaviour does not conform to either the Palmqvist or halfpenny models (Lube 2001, Wegner 2001). In these cases the re-enforcement phase alters the crack path and the conditions of Equation 3.1 are not satisfied, yielding a varying measure of fracture toughness.

3.3.3 Hertzian indentation

In Hertzian indentation, a hard, spherical indenter, in this case Si_3N_4, is pressed into the flat surface of a brittle sample. The substrate is prepared by standard metallographic polishing techniques as described in Section 3.2.1, except the preparation procedure finishes with polishing in 9μm diamond suspension, and leaves a high density of surface flaws. As the indenter is pressed into the

surface, a tensile, radial stress field is generated around the contact zone, as shown in Figure 3.4. At a critical load, the crack tip stress intensity factor in one of the surface flaws will be sufficient to propagate the flaw into a ring crack which encircles the indenter. The initiation of the ring crack is detected by an acoustic emission probe on the back of the indenter. The load at which the ring crack forms is measured by an integral load cell and used to calculate K_{1c}. The calculation procedure followed was taken from Warren (1995a, 1995b) and is given in Appendix 3.3. Hertzian indentation testing was conducted on flat parallel sided specimens, using a CK10 one tonne micro indenter manufactured by Engineering Systems Ltd. Sample preparation, machine set up and calibration was conducted in accordance with the operational guidelines and closely followed the test procedure described by Warren 1995a. Data was recorded manually.

3.3.4 Modulus measurements

Young's modulus E is usually measured from the elastic portion of a stress σ – strain ε curve using $E = \sigma/\varepsilon$. However because of the difficulty in manufacturing defect free tensile test specimens and the small range of elastic behaviour in these materials Young's modulus was measured by impulse excitation. Impulse excitation is a non-destructive technique that is suited to brittle ceramic and glass materials and relies on the fundamental measurement of the resonant frequency of test specimens following excitation with single elastic strike by an impulse tool. A transducer (such as a non-contacting microphone) senses the resultant vibrations and resonant frequency and the signal is then analysed as a

function of the known geometry and density of the sample. Figure 3.5 shows a schematic of the test apparatus used in this study with the impulse point and resultant standing wave and flexure nodes indicated. The test pieces require an aspect ratio of 5 – 20 and the technique is only appropriate for elastic, homogeneous, isotropic materials and porosity free materials, consequently only HIPed CE alloys were investigated with this technique. Modulus measurements were obtained for the entire range of standard CE alloys in order to determine the variation of modulus with Si content. Samples were prepared in accordance with ASTM E1876-01 (ASTM 2002) using mechanical grinding and lapping to nominal dimensions of 60mm x 8mm x 4mm $\pm$ 0.10mm. Exact measurements for each specimen were measured with Vernier callipers. Ten samples were prepared and measured and each sample was measured 10 times.

Measurements at Oxford were compared with those obtained by impulse excitation specimens of a different geometry (120mm x 20mm x 10mm) tested at CERAM, a NAMAS certified research laboratory. The Oxford Results were in good agreement with those obtained at CERAM. A copy of the CERAM test report is given in appendix 3.4.

3.3.5 Optical emission spectroscopy (OES)

Macrosegregation effects in CE7 were investigated using optical emission spectroscopy (OES) with a Spectro, Spectrolab LAVFAO 5A. A longitudinal section of as sprayed CE7 was cut from the billet diameter, milled flat and then

finished with a surface grinder (Al_2O_3 wheel at 2300rpm) to ensure a flat surface free from contamination and a gas seal around the sample area. A grid of OES measurements was made over the prepared section with a spacing of 10mm. Although Si concentrations exceeded the calibrated measurement tolerance limits, Al concentrations were within tolerance as were trace elements concentrations, so that Si concentrations were calculated by difference. Al, Fe and Cu concentrations at each grid point were then presented as a contour plot using Tecplot software.

3.3.6 Coefficient of thermal expansion (CTE) measurements

The coefficient of thermal expansion of HIPed CE7 was measured using a Netzsch DIL-402PC at Sandvik-Osprey Ltd on test bars cut using a diamond saw, lapped to a 3μm finish with a diamond suspension and of dimensions, 5.5 x 5.5 x 45.0mm. The sample table and sample holder material were fused silica, tempered prior to use and a W reference sample was cycled prior to each measurement to provide baseline behaviour. The heating profile was RT to 525°C (just below the alloy liquidus of 577°C), at 4°C/min.

3.3.7 Bend strength

Three and four point flexural bend testing has been developed to measure the bend strength of brittle materials, eliminating problems associated with the gripping of samples and ensuring that failure occurs in the centre of the specimen.

The bend strength was investigated using a Lloyd Instruments 200R configured for 4-point bend testing, with a crosshead speed of 0.5 mm/min and automated data logging. The outer supports were 38.1mm apart and the inner supports were 19.05mm apart. Alignment of the support and loading anvils is critical with brittle materials, and self-aligning anvils were employed. The 4 point bending jig used is shown in Figure 3.6(a). Bend test samples of 60.0mm x 8.0mm x 4.0mm were produced by grinding, lapping and finishing with a 9μm diamond paste. A schematic of the test jig used is shown in Figure 3.6(b), and with reference to the dimensions L,S,W and T shown, the modulus of rupture (MOR) was obtained from:

$$MOR = 1.5F\left(\frac{L-S}{WT^2}\right)$$

Equation 3.2

where F is the applied force.

Due to the limited volume under tensile load during 4 point bending, the MOR is an over estimate of the real strength of brittle material, and will be discussed further in Section 4.2.6. Since samples of ceramic-like brittle materials fail at a range of stresses because of the variations in the Si flaw distribution and orientation from sample to sample, statistical methods of expressing the resulting strength distributions are required; the most used is the Weibull modulus. A Weibull modulus plot is obtained from a plot of $\ln\{\ln[1/P_s]\}$ against $\ln\sigma_f$, where P_s is the probability of survival from a ranked order list of failure stresses σ_f (ASTM 1995). If the data on the Weibull plot lie on a straight line

(there is no bimodal or higher orders of failure), then the gradient of a best fit straight line to the data is termed the Weibull modulus, m.

m = 2-5 indicates a very large scatter and is typical of traditional refractories and ceramics; m = 5-10 is a typical value for most ceramics; m = 10-20 is typical for advanced engineering ceramics; and m = >30 typical of metals.

Weibull plots were used to investigate the 4-point bend test data of different CE alloys, and for materials after thermal cycling.

3.3.8 Thermal cycling

Thermal cycling is critical for CE alloys because in satellite and avionic thermal management applications a typical operational temperature range is from –50°C to +150°C (Jacobson 1997). Thermal cycling of CE7 was performed using a ACT EOS 330TCS environmental chamber shown in Figure 3.7(a); the chamber size was 70mm x 80mm x 80mm. The thermal cycling profile employed is shown in Figure 3.7(b) consisting of 90min ramp from -50 to +150°C, a 5min dwell and a 90min ramp from +150 to -50°C and a further 5min dwell. This was the fastest ramp time available. Samples were subjected to 106 thermal cycles and vacuum dye penetrant crack inspection was performed after 53 and 106 cycles. Thermally cycled samples were then investigated by four point bend testing and microstructural inspection.

3.3.9 Vacuum dye penetrant inspection

Samples were prepared by milling all surfaces and polishing with 1200 SiC paper. Samples were placed in a Petri dish in a vacuum chamber, the chamber

evacuated and a manipulator used to tip the dye over the sample and the Petri dish filled sufficiently to cover the sample. The vacuum pump was then switched off and the chamber allowed to leak back up to atmospheric pressure over ~1 hour. The increasing pressure in the chamber 'pushes' the low viscosity dye into the surface defects of the sample. The apparatus for this procedure is shown in Figure 3.8. The sample was then removed from the chamber and any excess dye was removed by swabbing the surface with acetone. The remaining dye was drawn to the surface by capillary action. The sample was then inspected either by eye or using a Wild Photomakroskop M400 with a Wild PhotoAutomat MPS light metering and photographic system. The conventional illumination system was replaced with side lighting from 2 Cheng Ming SME-26 UVa light sources with an emission wave length of ~300 – 370nm while the dye fluoresced at 365nm . A 35mm camera was used to capture images of the fluorescing defects and were quantified using image analysis.

3.4 Chill casting and alloy selection trials

As previously described in Section 3.2.3, the interface length between the Al and Si phases was considered important in determining alloy toughness. One of the objectives of the research was to identify strategies to increase alloy toughness. A significant effort was therefore dedicated to investigate how the primary Si crystal size could be reduced or the globular Si morphology modified by ternary alloying additions.

3.4.1 Alloy modification

Over 90% of all Al casting alloys contain between 6 and 22% Si (ASTM 1988) and there is therefore a large amount of literature concerning the modification of Si in Al alloys. However, no literature could be found concerning modification of Si-Al alloys with Si concentrations >40%Si (Elkem 1994). It was therefore difficult to gain any guidance from the literature which elements may modify the primary Si in spray formed Al-70Si. Following a review of the literature and especially (Rooey 1972, Lu 1995, Tenekedjiev 1990, Heshmatpour 1997) a list candidate elements was drawn up, based on their reported ability to nucleate primary Si, inhibit Si growth or otherwise refine the primary Si network;

P [Phosphorus]

Refines primary Si network by the formation of AlP which nucleates Si, AlP is diamond cubic structure isomorphous to Si, (Ghost 1964). Widely used in hypoeutectic Si-Al alloys, with typical additions in the range 0.05 – 0.3wt%.

Na [Sodium]

Widely used in hypoeutectic Si-Al alloys where it affects the growth kinetics of Si and promotes a fine, fibrous eutectic, suppressing the formation of acicular needles. Na has a stronger refining effect than Sr but is more difficult to handle and the modification effect more transient owing to the high vapour pressure of Na, (Dahle 2001).

Sr [Strontium]

Widely used as a replacement for Na as it is easier to add and does not 'fade' (evaporate) in the crucible. Sr affects the growth kinetics of the twin plane re-

entrant edge growth mechanism by poisoning attachment sites (Jenkinson, 1975) and is widely used in hypoeutectic alloys in concentrations of 0.01 - 0.05wt% typical addition, (Dahle 2001).

Bi [Bismuth]

Lowers the solid-liquid interface energy in Al. Bi is used as a Si refiner in some commercial alloys such as AA4104 (Al-0.2Bi-10Si) in order to improve machinability, (ASTM 1998).

Sb [Antimony]

Promotes an acicular, fine scale, lamellar structure Si in hypoeutectic alloys at concentrations of 0.1 – 0.5wt%, (Hansen 2000, Liu 1998). Sb is not compatible with other modifiers because Sb based intermetallics form.

Mg [Magnesium]

Refines Si in Al-30Si-5Cu thixo-forming type alloys in concentrations of 0.5 – 1.0wt%, (Hogg 2001, Ward 1996). The underlying mechanism is not fully understood, but is thought to be based on modification of interfacial energy.

Ti [Titanium]

Ti reacts to form TiN and this could be exploited to form TiN in situ with the atomising gas during spray forming i.e. reactive spray forming (Lawley 1994). TiN may then pin Si grain growth in the mushy zone.

B [Boron]

Boron is one of the few elements with any solid solubility in Si, a property exploited in Si semiconductor doping. B also forms Al-B intermetallics which may nucleate primary Si or inhibit Si growth, (Nogita 2003).

Ce [Cerium]

Ce along with some other rare earth elements has been demonstrated to be effective in inhibiting Si growth and coarsening. When used in combination with P inoculation, two mechanisms refine the primary Si; AlP nucleation of Si and Ce inhibition of Si growth (Chang 1998a &1998b). Typically the mean primary Si size being reduced from 60 to 46μm with 6.5% RE (Mischmetal: Ce, La, Nd in the ratio 3.6:1.8:1) addition in conjunction with 50ppm P, (Jirattitcharoean 2004).

3.4.2 Chill Casting

The time and cost of spray forming all the Si-Al-X alloys from the list above was prohibitive, thus a method of assessing the efficacy of the short-listed elements was required. Small scale chill casting was selected for screening alloy additions. To maintain a relatively high cooling rate during solidification, a water cooled mild steel mould was selected, shown in Figure 3.9a. The cooling rate of subsequent castings was measured as ~8°C/s from 1000°C to 577°C, the alloy freezing range. The mould had a 15° taper to allow easy removal of the small, ~120g castings. The water flow through the cooled mould is shown in Figure 3.9b. Although it was recognised that the chill cast approach would not replicate the nucleation and cooling conditions experienced during spray forming, it was envisaged that it would allow the efficacy of the elements to be ranked.

Al-50Si LSM master alloy waffle was used as the primary feedstock with a liquidus temperature of ~1040°C. The alloy was inductively heated in a clay-graphite crucible and the temperature monitored using a K-type thermocouple in

a re-crystallised Al_2O_3 sheath. At a temperature of 1100°C (60°C superheat), the melt was poured manually into the water cooled mould. The chill casting apparatus used is shown in the annotated photograph in Figure 3.10. The wt% of each element, the method of addition and the form and composition of each master alloy investigated is summarised in Table 3.1. It was not possible to source a small quantity of Na master alloy for modification trials and Sr was used as a substitute.

Table 3.1 Chill casting alloy additions: The wt% of each alloy addition, the method of addition and the form and composition of each master alloy used is summarised

Wt % of addition		**Method of addition**		**Form**	
0.5% P		Add to melt at T_{pour}, cast after 5min		Cu-15P 20mm Shot	
1.0% P		Add to melt at T_{pour}, cast after 5min		Cu-15P 20mm Shot	
0.4% Sb		Add to melt, raise temp to T_{pour}		Al-1.1Sb	
1.0% Bi		In crucible from beginning		Al-8Bi Waffle	
0.5%B		In crucible from beginning		Al-8B Bar	
0.5% Ti		Add to melt at T_{pour}, cast after 5min		Al-10Ti Bar	
2.0% Mg		Plunge under melt, cast after 3min		100% Mg Ingot	
0.05% Sr		Add to melt at T_{pour}, cast after 3min		Al-10Sr Waffle	
5.0% Ce		In crucible from beginning		Al-20Ce Plate fragments	
5.0% Ce,	1.0% P	In crucible from beginning	Add to melt at T_{pour}, cast after 5min	Al-20Ce Plate fragment	Cu-15P Shot

3.4.3 Alloy selection

Five Si-Al-X billets were spray formed at Oxford, with the nominal compositions shown in the Table 3.2.

Table 3.2 The nominal composition of the five CE alloy billets spray formed at Oxford.

Experiment number	Nominal alloy composition	Designation
011	Al-70Si	OxCE7
017	Al-69Si-**1B**	CE7 + B
018	Al-66Si-5.3Cu-**0.9P**	CE7 + P
019	Al-61.8Si-5.6Cu-**1.0P- 5.0%Ce**	CE7 + P + Ce
020	Al-69.5Si- **0.5Sr**	CE7 + Sr

OxCE7 provided a comparison with the Si-30Al baseline billet supplied by Sandvik-Osprey. The four Si-Al-X alloys were chosen based on the results of the chill casting trials (detailed in Chapter 5.0). The selection of modification elements was supported by Elkem (1994), where Si modification was achieved with additions of B, P or Sr added to powder metallurgy processed Al<35Si. Owing to the unusual compositions of the Oxford spray formed alloys, it was necessary to source the raw materials for these experiments from a variety of different suppliers and purchase feed stock in a variety of different forms and these are summarised in Table 3.3.

Table 3.3 Composition, master alloy form and suppliers of alloy additions used in spray forming experiments at Oxford University

Master	Form	Supplier
Al-20Si	10kg Ingot	Avon Metals Ltd
Si Chip	Electrical scrap (20-90mm diameter blocks)	Osprey Metals Ltd
Al-8B	Waffle	London & Scandinavian Metals
Cu-15P	1 - 3mm shot	W. M. Rowland Ltd
Al-55Ce	Vacuum induction melted master alloy. 20mm plate	Less Common Metals Ltd
Al-90Sr	25g Sr modifier packs sealed in Al tubes.	Timminco Metals (USA)

Owing to the different melting points, vapour pressures and dissolution times, the ternary alloy additions were added in a different ways to the Si-Al, based upon foundry 'best practice' as recommended by suppliers and other experts.

Boron: There was no difficulty adding B and there was no significant evaporation. The Al-8B master alloy was placed in the crucible with the primary charge of Si chip and Al-20Si ingot. This approach maximised time for AlB_{12} dissolution and distribution in the melt.

Phosphorus: P was added as Cu-15P shot. In order to make the handling easier, the shot was packaged in Al foil parcels which were added by plunging under the liquid Si-Al alloy surface with tongs, the foil melted rapidly and the small size of the Cu-P shot aided rapid dissolution. The Cu-P master alloy was added once the pour temperature had been reached (1450°C) and de-gassing was complete. This approach sought to minimise the time for P evaporation.

Cerium: Al-55Ce dissolves at ~1220°C, and was added to the melt once the primary Si-Al charge was molten at around 1230°C. The charge was then heated further to the pour temperature and the P added as previously described.

Strontium: Sr was added to the melt once the charge had reached the pour temperature of 1470°C and de-gassing was complete. The dross was skimmed from the surface and the modifier packs of Al wrapped Sr were added by plunging them under the surface of the melt using tongs.

3.5 Spray forming at Oxford University

3.5.1 Spray forming plant

Spray forming was conducted at the Begbroke Science Park, using an Al spray forming unit designed and commissioned by Sandvik-Osprey. The plant configuration was similar to the spray forming plant used at Sandvik-Osprey: a tilt-pour induction furnace; a 2 stage scanning atomiser using N_2 and manually controlled ram / substrate withdrawal. However, the geometry of the Oxford spray forming plant differed from the Osprey plant in several key ways that are relevant to the approach and results obtained:

[1] The Oxford plant has a vertical ram with the tundish – nozzle – atomiser arrangement inclined at 30° to the vertical axis of billet rotation. The Sandvik-Osprey plant uses an inclined ram and vertical pour arrangement.

[2] The Oxford plant uses a re-usable stainless steel substrate rather than the disposable Cordrite ceramic plates used by Osprey.

[3] The spray height in the Oxford plant is 700mm, compared with 890mm at Sandvik-Osprey.

[4] The induction furnace capacity at Oxford is ~60kg compared with ~150kg at Sandvik-Osprey with correspondingly lower furnace power.

[5] The spray chamber at Oxford has a larger volume than that at Sandvik-Osprey and overspray / gas extraction fans are scaled correspondingly with respect to chamber volume. The Oxford plant allows higher spraying pressures to be used without rupturing the explosion relief panel.

[6] The Oxford spray forming system did not have a particle injection system, while Sandvik-Osprey routinely use overspray re-injection in commercially produced CE alloys.

Overall the melting, spraying and post spray cooling conditions at Oxford were consequently different to those at Sandvik-Osprey although specific processing conditions at Oxford were chosen to mimic as closely as possible the Sandvik-Osprey conditions within these constraints. The spray conditions used for the Oxford spray forming experiments are summarised in Table 3.4 and detailed experimental record sheets are given in Appendices 3.5(a-e).

Table 3.4 Summary of spray conditions used in the Oxford spray forming experiments.

Experiment Number	T_{pour} (°C)*	Melt delivery nozzle ID (mm)	Charge weight (kg)	Primary atomising pressure (Bar)	Secondary atomising pressure (Bar)†	Spray height (mm)
011	1415	5.5	50	2.0	9.0	700
017	1450	5.5	50	2.0	8.0	700
018	1450	5.5	50	2.0	8.0	700
019	1450	5.5	50	2.0	7.0	700
020	1470	5.5	50	2.0	7.0	700

* Progressively increased to improve fluidity and yield
† Progressively decreased to reduce porosity and improve process yield

Experiment 011 sought to mimic the Sandvik-Osprey process conditions, however post-experiment analysis of the data log indicated significant cooling of the melt in the tundish, which caused solidification of the melt in the melt delivery nozzle ('freeze-off'), prematurely ending the experiment. Billet 011 also exhibited significant porosity (up to 30 area%), and under advice from Sandvik-Osprey the secondary gas pressure was reduced for subsequent experiments. This had the effect of increasing the mean droplet size thus increasing the mean spray temperature and hence the liquid fraction at the billet surface. It was envisaged that these measures would yield a reduction in porosity and a greater process yield. Experiments 017 and 018 were conducted under identical conditions with a secondary atomiser pressure of 8Bar and a pour temperature (T_{pour}) of 1450°C compared with 9Bar and 1415°C in experiment 011, this was sufficient to prevent 'freeze-off' of the melt in the nozzle. The reduction in secondary gas pressure reduced the as-sprayed porosity of billets 017 and 018 to ~1.6 area% and 6.7 area% respectively. Examination of billets 017 and 018 revealed areas of gross porosity in the billet centre, again indicating the

secondary gas pressure was too high. Subsequent experiments sought to remedy this by further decreasing the secondary atomiser pressure to 7Bar for experiment 019. Experiment 020 also used an atomiser pressure of 7Bar and a further increased T_{pour} of 1470°C, these combined measures successfully reduced the as-sprayed porosity to <1 area%. These differences in process parameters were under advice from Sandvik-Osprey and resulted in a progressively improving billet quality, with reduced porosity and increased process yield as shown in Table 6.1.

3.5.2 Melting

Melting of charge material was carried out in a rammed refractory crucible induction heated by an Inductotherm power-trak VIP 75R rated to 75kW. BN refractory furnace wash was used to coat the inside of the crucible, spout, thermocouples and foundry tools. Typically, a charge of 50kg consisting of Al-20Si master alloy ingots and elemental Si chip was melted in an open furnace. This arrangement is shown in Figure 3.11. The melt was typically heated to 1450°C, representing a superheat of ~220°C. Melting was monitored initially by a K-type mineral insulated, stainless sheath thermocouple. At 1250°C the K-type thermocouple was at the upper limit of its capability so was removed and replaced by an R-type, Al_2O_3 insulated thermocouple encased in a Sialon tube. De-gassing was carried out using Ar, bubbled through the melt via a graphite lance with a porous graphite head. Ar was passed through the melt at the rate of 6l/min for 20 minutes beginning when the melt reached ~1350°C. Despite bubbling cold gas through the melt, the melt temperature continued to rise since

the graphite de-gassing lance coupled with the applied induction. The temperature during melting was logged manually every 5 mins and recorded on the experimental record sheet. Key operations such as de-gassing or addition of master alloys were also recorded with corresponding time and temperature.

The molten alloy was transferred into a conical tundish by means of a manually operated tilt-pour mechanism, remotely monitored by CCTV and controlled from a separate control room. The tundish arrangement is shown in Figure 3.12. To prevent the melt from excessive cooling in the tundish which may result in 'freeze-off' (solidification) in the tundish or subsequently in the nozzle, it is common practice to manually pre-heat the tundish using a propane torch. The melt delivery spout and then the tundish were pre-heated for 5 minutes each. After this was complete and the melt was at the pouring temperature, the mezzanine, all other areas of the equipment and the entire laboratory were evacuated and sealed so that pouring and spray forming was controlled entirely remotely. Once all safety procedures had been completed and atomising gas conditions had been established (see Section 3.5.4) the melt furnace was tilted and the molten alloy delivered to the tundish. The tundish provided an immediate reservoir of molten alloy, while the nozzle at the base of the tundish delivered the melt stream to the atomiser. The melt level in the tundish was kept at a constant height by monitoring and topping-up as appropriate to give a metallostatic head of ± 8mm throughout. Once the furnace was empty and the alloy level in the tundish began to reduce, the secondary gas pressure was

ramped down progressively in an attempt to maintain a reasonably constant gas-to-metal mass flow rate ratio.

3.5.3 Spray chamber

The spray chamber provided a sealed environment preventing any egress of metallic powder or N_2 or ingress of O_2. The chamber and all associated components were constructed of non-spark austenitic stainless steel to exclude sources of ignition. Prior to the start of spraying the spray chamber was sealed manually and all the various ports and doors and purged with N_2 to reduce the chamber O_2 concentration progressively. The chamber was kept airtight by an Al foil gasket over the melt delivery nozzle. The first molten metal to pass through the nozzle broke the seal and the molten metal flowing through the nozzle maintained the seal to the tundish.

The O_2 concentration in the chamber was monitored during purging prior to spraying. The software controlling the O_2 sensor was calibrated before purging using a calibration gas source and the calibration had a lifetime of 1 hour after which it must be repeated. The software controlling the equipment was interlocked to prevent any molten metal being introduced to the chamber while the O_2 concentration was above 100ppm. During spray forming, O_2 concentration was monitored and if the concentration reached 150ppm, the control software intervened and instigated an automatic shutdown procedure in order to render the equipment safe. In the event of an explosion caused by sudden reaction of powder with O_2 and in the presence of an ignition source, an explosion relief panel at the back of the chamber vented through an external wall into a secure compound. No such events occurred. The chamber door was

closed by a safety interlocked pneumatically secured locking bar and 8 toggle clamps. In combination these provide explosion resistance and sufficient clamping force to compress the rubber door seal. The spray chamber is shown in Figure 3.13.

3.5.4 Atomisation

The melt passed through an Al_2O_3 filter in the tundish shown Figure 3.14 and into a ZrO_2 melt delivery nozzle with an internal diameter of 5.5mm. The nozzle was located concentrically with respect to the primary and secondary atomisers, shown schematically in Figure 3.15(a). The primary atomiser consisted of 12 jets of 1.4mm diameter exiting parallel to the melt stream shown in Figure 3.15(b), and was used to stabilise the melt stream (prevent break up) and to protect the melt stream from the turbulent gas flow in the chamber caused by secondary gas flow. The secondary atomiser consisted of 18 jets of 4.0mm diameter, angled at 7° to the spray axis, focussed to a point on melt stream, as shown in Figure 3.15(a). While this arrangement was inefficient in terms of small diameter powder manufacture, this two-stage arrangement reduced the instances of melt freeze-off at the nozzle tip (Mathur 1989, Lawley 1986) and it has been further shown to be a robust, reliable and reproducible arrangement for all alloy types. Further, it is not obvious that small powder diameters (<80μm) are beneficial for spray forming. The gas supply to the primary and secondary atomisers was independently controlled, and atomisation was monitored by CCTV allowing operators to make adjustments as necessary during the spray forming process. For example, the primary gas pressure could

be increased if the melt stream became unstable, as often occurred towards the end of the experiment as the melt flow rate began to decrease.

The primary atomiser was static, whereas the secondary atomiser was mechanically scanned to deflect the spray cone from the centre to the edge of the substrate. The stroke of the scanner arm and the angle of the scan was set-up by temporarily replacing the secondary atomiser with a low power laser. The laser acted as a spray-axis pointer and allowed the scan profile relative to the collector plate to be assessed. The scan profile was set with turning points of 25mm from the substrate centre and 5mm from the substrate edge. The eccentric cam on the mechanical scanner arm was designed to give a brief dwell at the extremes of the scan. The precise details are proprietary.

3.5.5 Collection

The spray, consisting of a myriad of solid, semi-solid and liquid droplets, was intercepted by a rotating stainless steel substrate. The substrate was prepared by grit blasting (80psi, 36 grit, Gyson grit blaster) in order to create a rough surface to maximise adhesion. The substrate rotation was selected to be out-of-phase with the atomiser scan speed in order to form a cylindrical billet. A CCTV camera was mounted outside the chamber, and the video image of the billet formation relayed in real-time to the control room where an operator adjusted the ram retraction rate to maintain a constant height between the billet top surface and the end of the melt delivery nozzle. In general, this meant slowly increasing the retraction rate until pseudo steady-state deposition conditions were achieved, then as the tundish emptied and the melt flow rate decreased,

decreasing the ram retraction rate. The temperature of the semi-solid top surface of the billet was monitored during spraying by two LAND pyrometers (U2 300/1100 one colour pyrometer and a V1 600/1600 two colour pyrometer). The output from these cameras was logged by the control PC and gave an indication of the temperature trend at the billet surface during deposition.

Particles that did not impact the substrate and become incorporated into the billet were carried out of the chamber as overspray by the extraction fan. The powder was carried by the N_2 through a wet scrubber system which collected all the particulate matter in a water filled holding tank where it slowly oxidised. The major components of the scrubber system and their function are shown in Figure 3.16.

3.5.6 Control system

As previously described, once melting was complete, control of the entire spray forming process was conducted from the control room. The user control interface was divided into two distinct tasks, requiring different operators. Control of the substrate manipulation and atomisation was via a touch-screen PC interface using National Instruments Lookout™ software. The software communicated with the electronic, pneumatic and hydraulic actuators of the spray forming plant through a series of National Instruments Field Point modules. Safety interlocks in the software made it impossible for spraying to proceed until specific criteria were fulfilled (for example melt could not be

poured into the tundish until a chamber O_2 reading of <100 ppm had been obtained).

The second aspect of the control system was the manual tilt-pour mechanism described in section 3.5.2. The furnace was hydraulically tilted on a two-stage pivot, and melt dispensed into the tundish. The level in the tundish was monitored by a video camera with a real time display in the control office. The operator dispensed melt into the tundish using a variable speed joy-stick, and maintained an approximately constant melt level in the tundish.
The images from all of the monitoring cameras were video recorded to allow experiments to be re-examined. Key processing parameters (listed fully in 3.5.8) were logged automatically via the control software. An overview of the control room is shown in Figure 3.17.

3.5.7 Post spray cooling

The Osprey processing conditions required that the semi-solid billet was removed from the ram and placed into an insulated box, with a chill applied to the billet base, as previously described. (Osprey 2001)

The vertical ram configuration of the Oxford spray forming plant made a rapid removal of the billet from the chamber difficult. Typically, a fully solid, cool billet is removed with a grab-arm as shown in Figure 3.18, but this takes time and careful operation, and, owing to the localised pressure in the jaws, is not suitable for a semi-solid billet. There were also health and safety concerns

regarding the handling of a semi-solid billet at ~750°C. Therefore in order to mimic the Osprey processing conditions, it was necessary to adapt the plant and operating procedure to allow the slow, directional cooling of the billet in the chamber while *in-situ* on the ram.

Directional cooling from the base was achieved by using a refractory lined 'top-hat' placed over the billet and the application of compressed air through a Cu heat-sink below the substrate. The surface temperature of the billet was measured by a K-type thermocouple passing through the top of the 'top-hat' to press on the top of the billet. A second thermocouple was inserted into a purpose made hole in the Cu heat sink to monitor the heat sink temperature. A schematic of this arrangement is shown in Figure 3.19.

3.5.8 Post experiment

Following spray forming, the billet, the solid skull in the furnace / tundish and the dross, were weighed. This total was taken from the original charge and the remainder was assumed to have been lost as overspray. This allowed an approximate 'mass through nozzle' value to be obtained, and from the experiment duration, an average melt mass flow rate was calculated.

The computer control system was set to log various process parameters during spray forming, typically: the primary, secondary gas pressures, ram withdrawal rate and rotation speed, atomiser scanner speed, chamber pressure, extraction fan speed, chamber temperature and exhaust temperature. After spraying was complete the control system was used to log the controlled cooling of the billet

via the two thermocouple inputs previously described. These data combined with the video footage from the monitoring cameras provided valuable information about each experiment and allowed detailed comparison of different spray forming experiments.

3.5.9 Hot isostatic pressing (HIPing)

The 4 modified CE7 alloys spray formed at Oxford all exhibited porosity inherent to the spray forming process. Prior to any mechanical testing HIPing was conducted externally by Bodycote HIP, Chesterfield, UK. The optimum process conditions for modified alloys were not known therefore 2 sets of process conditions were tried:

[1] The Densal® Cycle comprises a set of proprietary process conditions used for porosity removal in conventional Al alloys; it is an accredited process recognised by aerospace end users such as Airbus and Boeing.

[2] A sample of each material was also HIPed at 500°C at 140MPa for 240min, in order to investigate the effect of different HIPing parameters on the resultant microstructure.

Both cycles were conducted under a nitrogen atmosphere at a temperature <520°C owing to the presence of an Al_2Cu phase in the CE7+P and CE7+P+Ce alloys. This occurred due to the addition of P as a Cu-P master alloy. Al_2Cu has a has a comparatively low melting temperature of 524°C making processing at

or above this temperature impossible. These conditions therefore differed from the conditions used by Osprey for the processing of CE7 which were typically 16 hours at 140 MPa and 565°C. In all cases 'canning' or encapsulation of the material was conducted as it was thought that porosity may be interconnected.

3.5.10 MTDATA simulation

MTDATA is proprietary thermodynamic software developed by the National Physical Laboratory. It was used to assess the phase equilibria and solidification of the modified CE7 alloys used in the spray forming trials at Oxford. The database of elements for MT DATA is not exhaustive and did not include Ce or P, therefore only additions of Cu, B and Sr could be simulated using this software package. Solidification conditions for both equilibrium and Scheil solidification conditions were considered. Under equilibrium conditions complete diffusion in the liquid and complete diffusion in the solid phase is assumed, implying solute redistribution between the solid and liquid phases in accordance with the phase diagram. Under Scheil conditions 4 assumptions are made [1] the phases are in equilibrium, [2] there is no diffusion in the solid state, [3] there is complete composition uniformity through the liquid phase, [4] densities are equal for solid and liquid phases. Cooling curves obtained during post spray cooling were compared to the MT DATA simulation and used to assess the phases which formed during the final stages of solidification.

3.6 Summary

- CE7 was manufactured under 'best practice' conditions by Sandvik-Osprey and supplied to Oxford in the HIPed and as-sprayed condition.
- Controlled post-spray cooling and HIPing were used to minimise porosity in Sandvik-Osprey CE7.
- Sample preparation techniques were established appropriate to optical and electron microscopy.
- EPMA was used to investigate the Si and Al phases and to analyse intermetallic particles.
- EPMA was used to investigate grain size and texture in both the Al and Si phases.
- Two indentation techniques were investigated as methods of generating fracture toughness data.
- Impulse excitation was used to measure Young's modulus.
- Macrosegregation was investigated using optical emission spectroscopy.
- The effect of thermal cycling on bend strength and Weibull modulus of Sandvik-Osprey CE7 was investigated.
- Chill casting was used to investigate the effect of alloy additions on Al-50Si.
- One binary and four modified CE7 alloys were spray formed at Oxford University.
- The suite of characterisation techniques defined previously for the Sandvik-Osprey CE7 material were applied to Oxford CE7 alloys.

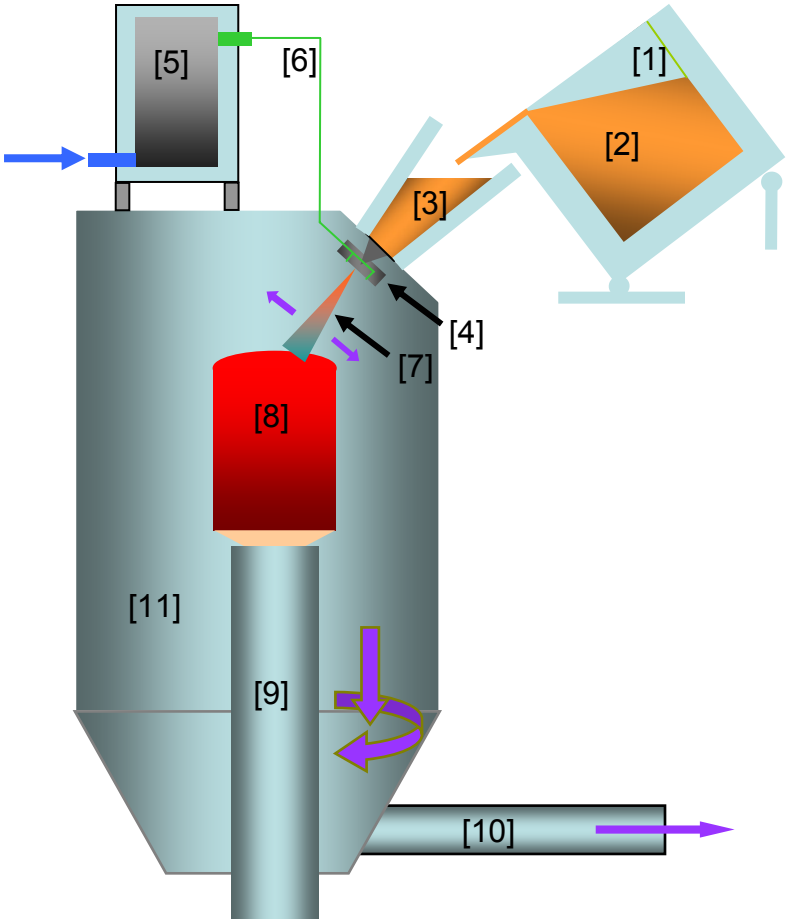

Figure 3.1: Schematic of the Sandvik-Osprey spray forming plant: [1] tilt pour furnace, [2] superheated melt, [3] tundish, [4] scanning atomiser, [5] fluidised bed particle injector, [6] particle delivery + transport gas, [7] spray cone, [8] billet, [9] ram [10] exhaust chamber, [11] spray chamber

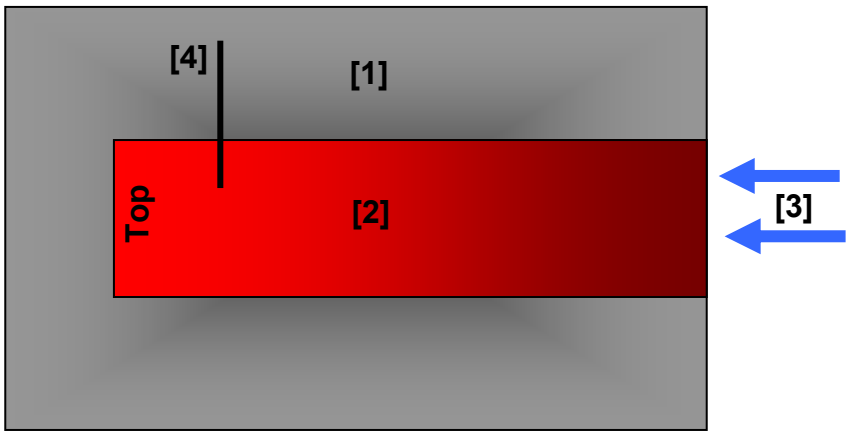

Figure 3.2: Schematic of post spray cooling arrangement at Sandvik-Osprey: [1] insulated 'coffin', [2] semi-solid billet, [3] forced air cooling applied to base of billet, [4] monitoring thermocouple (not logged)

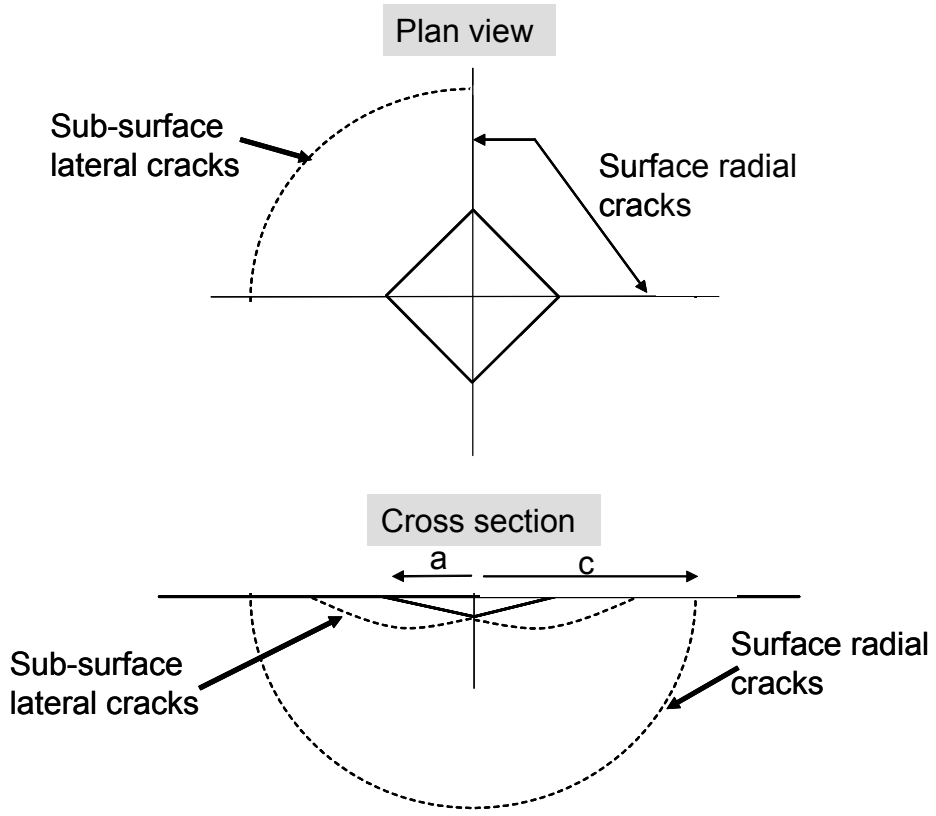

Figure 3.3: Vickers indentation 'half-penny' cracks as used to determine fracture toughness, (after Ponton & Rawlings Mat Sci Tech, 1989, Vol 5, pp 866)

C = Crack length

a = Contact area

P= Load

r_c= Radius of maximum tensile radial stress

E = Young's modulus

V = Poisson's ratio

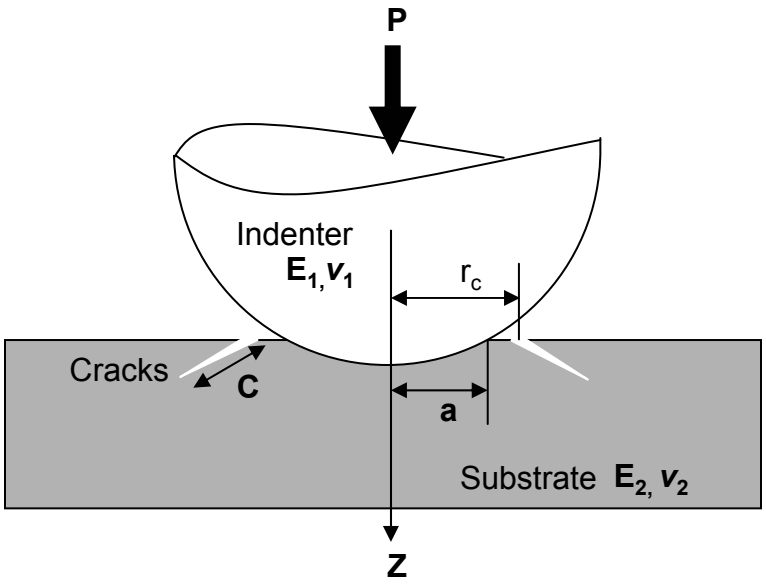

Figure 3.4: The geometry of Hertzian contact in the CK10 Hertzian indenter.

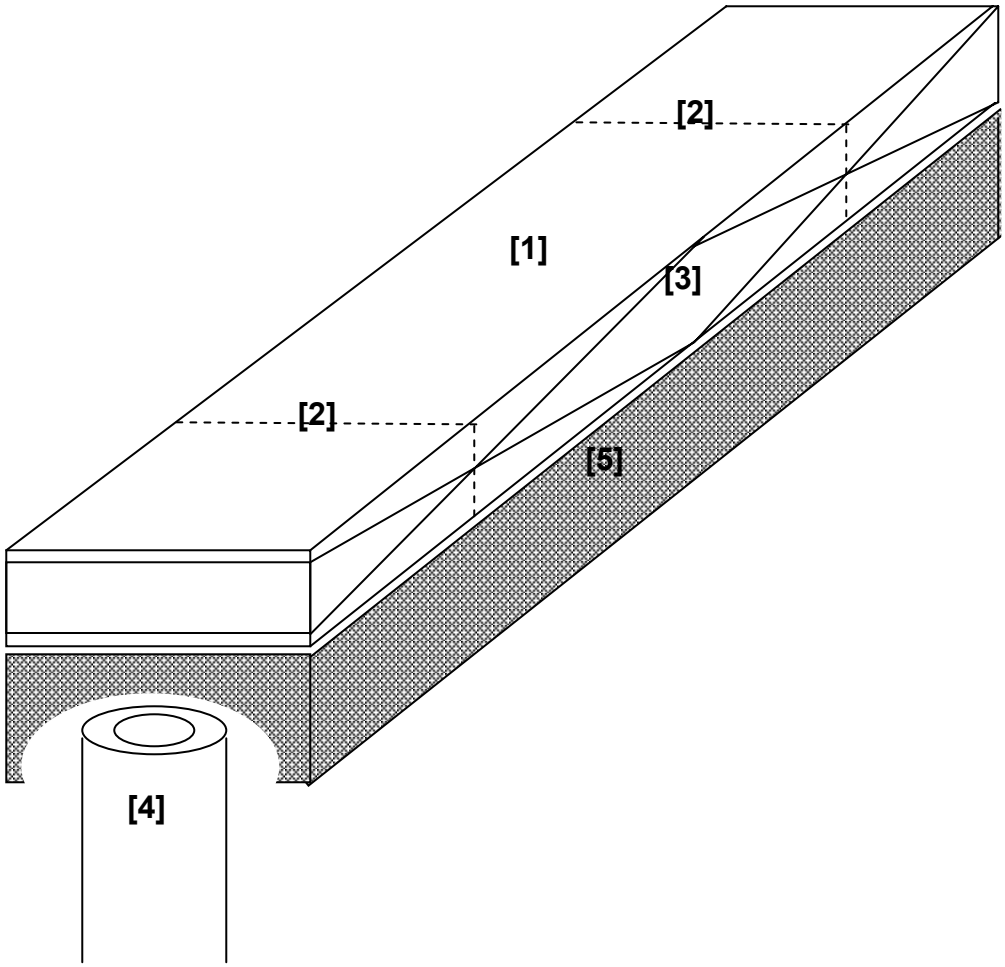

Figure 3.5: Impulse excitation determination of Young's modulus (E). [1] excitation point, [2] flexure nodes, [3] standing wave at resonant frequency, [4] non-contacting microphone, [5] foam support. ASTM 2002

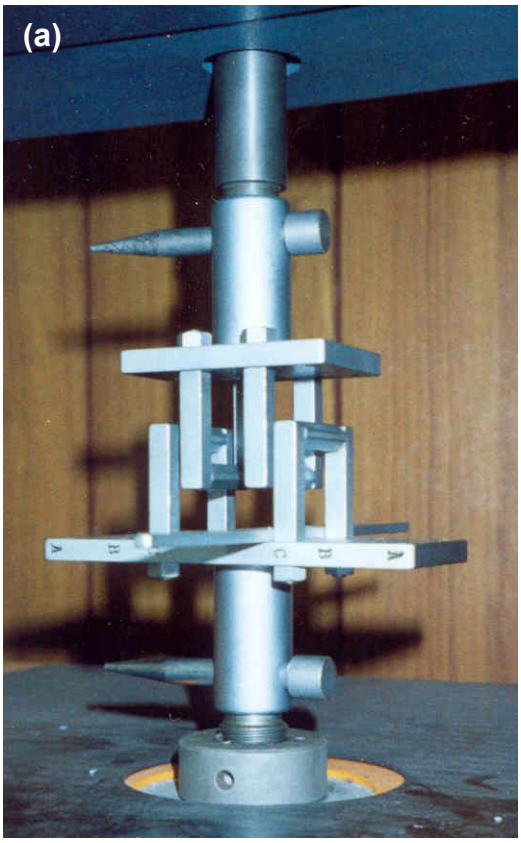

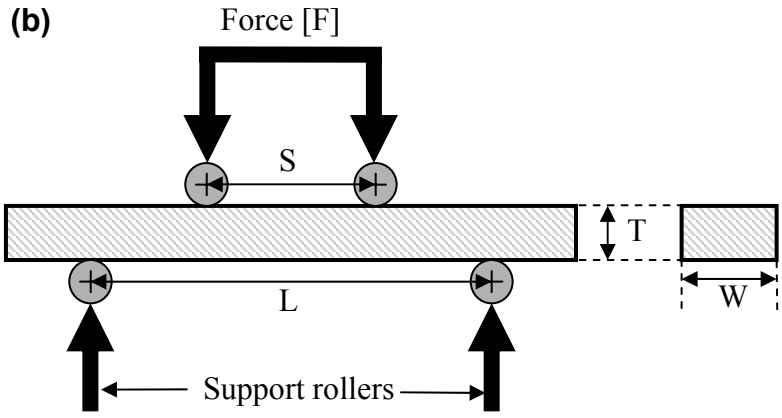

$$\sigma_{max} = 1.5F.(L-S) / W.T^2$$

Figure 3.6: (a) The 4 point bend test jig at Sandvik-Osprey; and (b) 4 point bend test arrangement

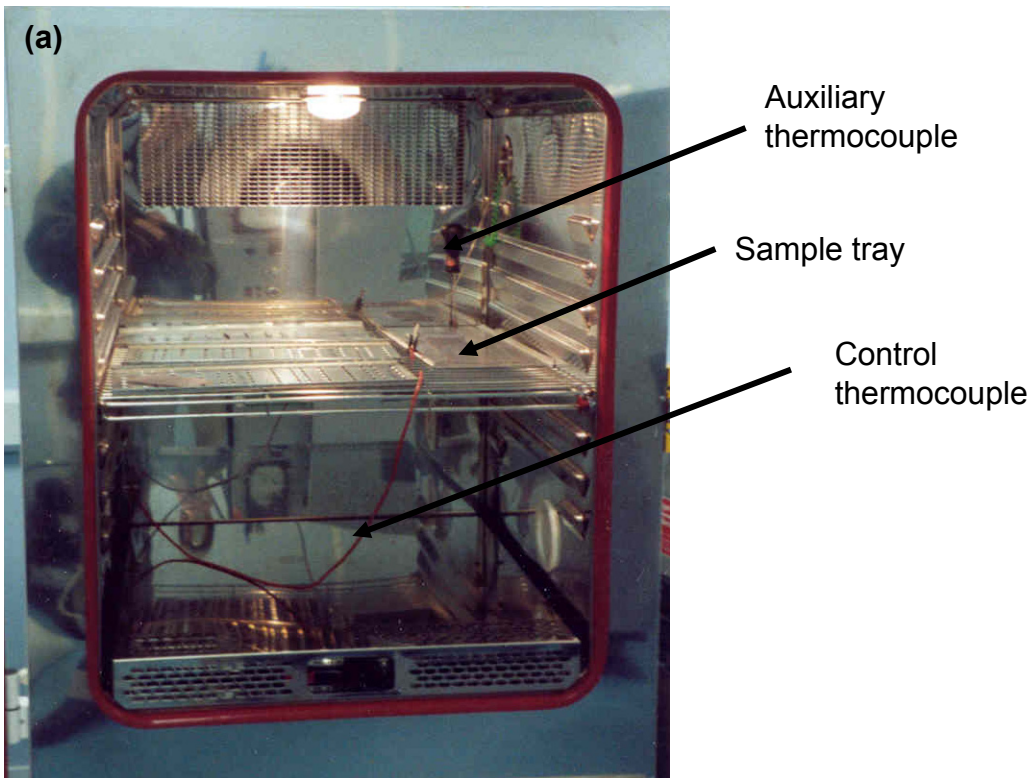

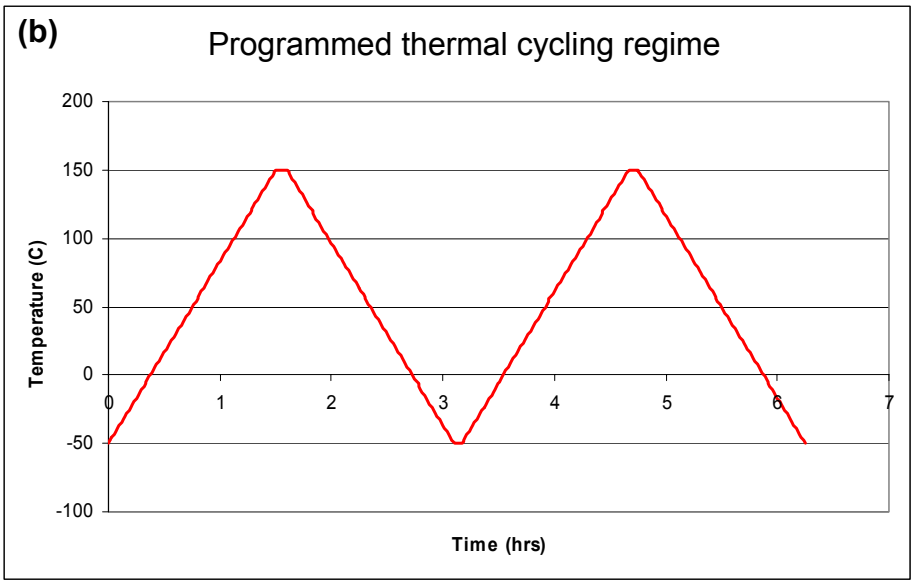

Figure 3.7: (a) The EOS 330TCS environmental chamber at TWI used for thermal cycling experiments; and (b) A schematic of the programmed thermal cycling regime

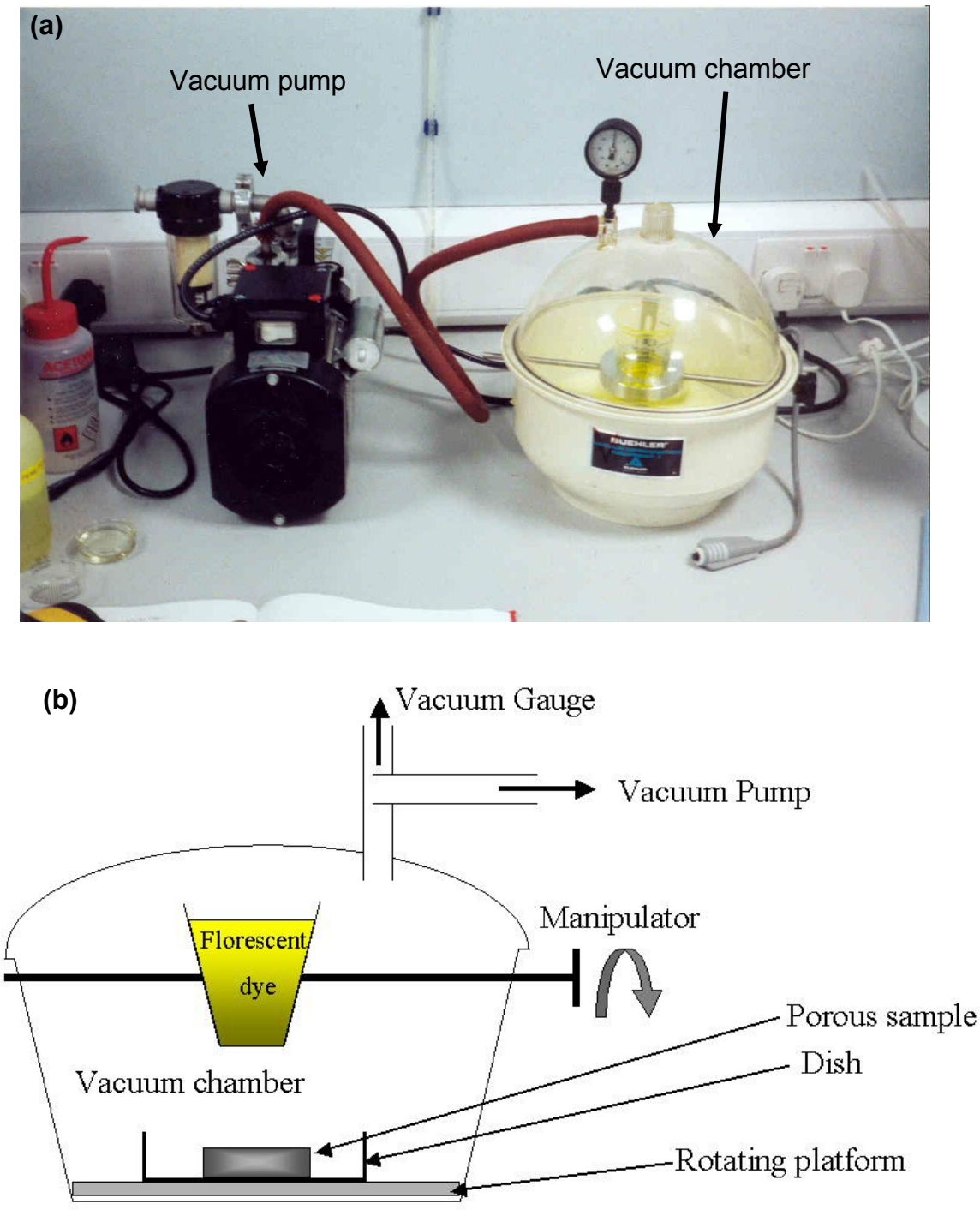

Figure 3.8: (a) Vacuum dye penetrant impregnation equipment at Oxford, (b) schematic of chamber arrangement.

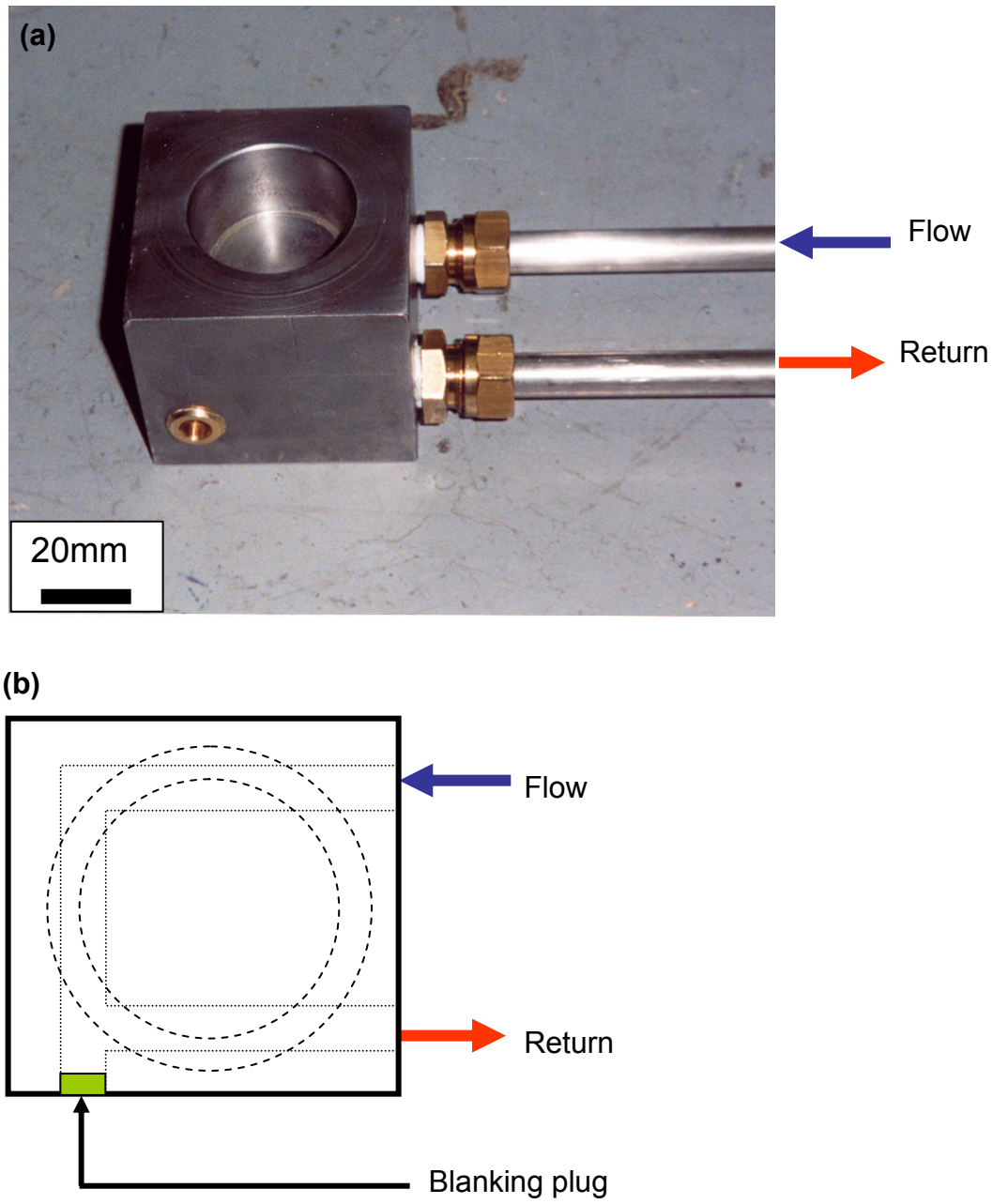

Figure 3.9: (a) Water cooled mould used in chill casting experiments (b) schematic of water channels through mould base

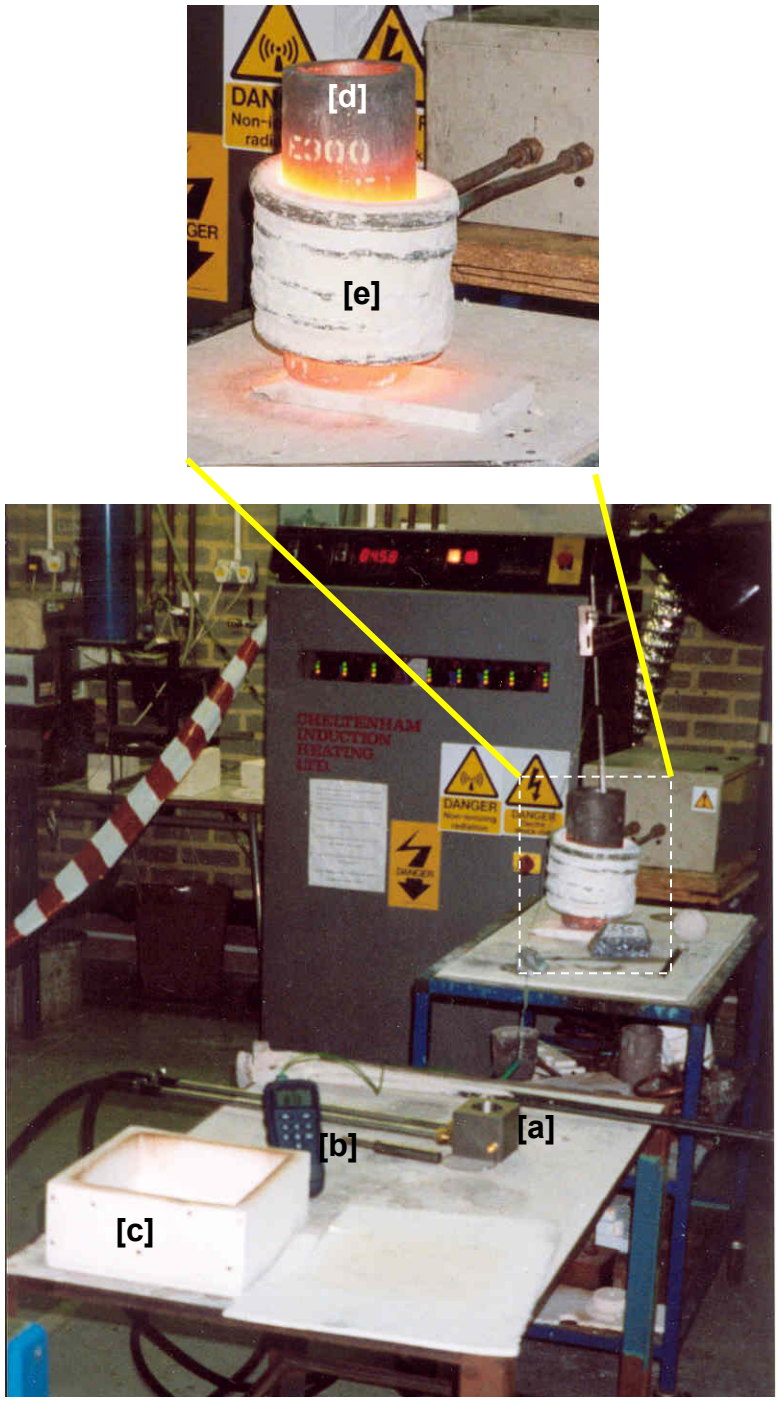

Figure 3.10: Chill casting apparatus used in alloy modification experiments: [a] Water cooled mould, [b] thermocouple reader, [c] sand lined dross box, [d] E300 Morganite stand-alone, clay-graphite crucible, [e] induction coil

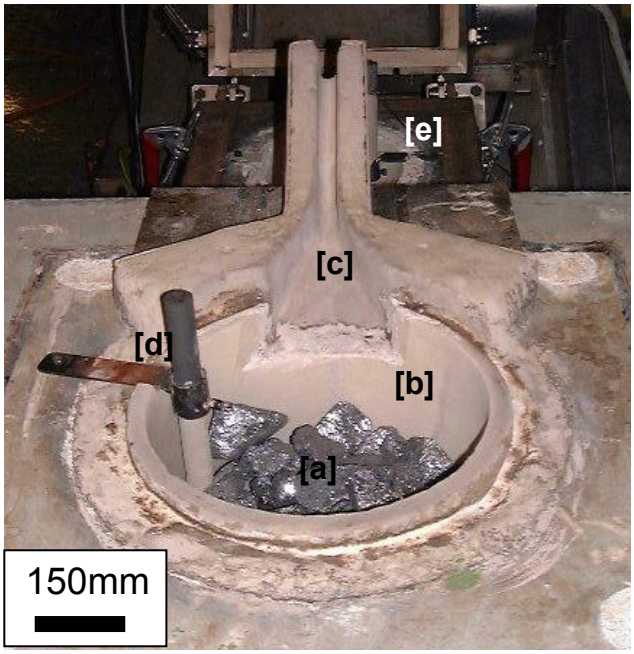

Figure 3.11: The melt crucible: [a] charge, [b] BN coated crucible, [c] spout, [d] thermocouple sheath, [e] tundish.

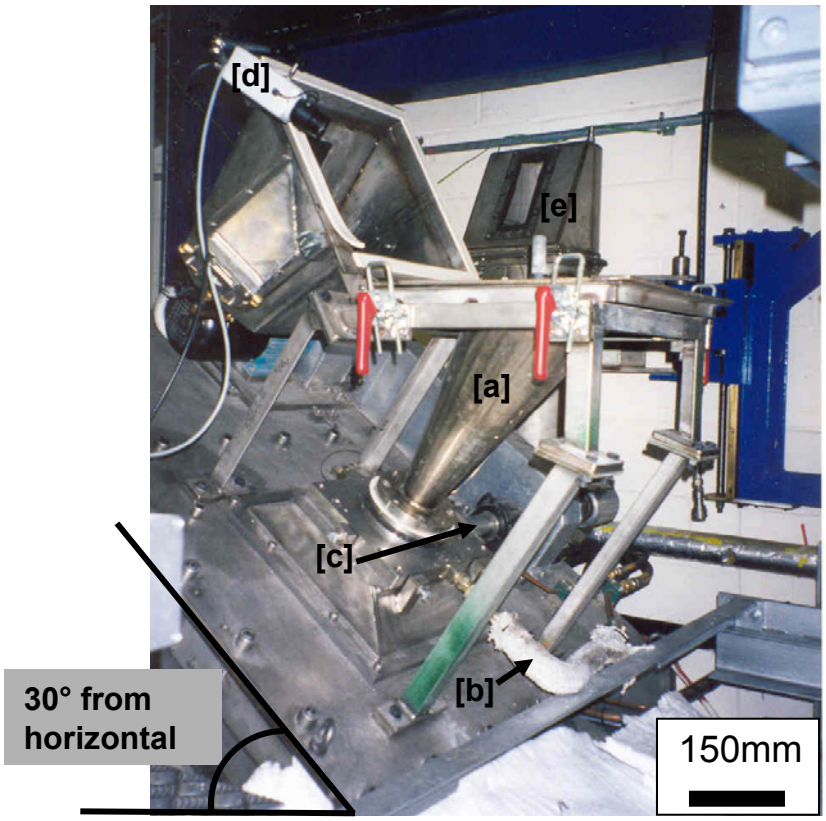

Figure 3.12: Osprey Tundish: [a] ceramic lined stainless steel tundish, [b] gas supply to primary atomiser, [c] scanner arm and gas supply to secondary atomiser, [d] tundish monitoring CCTV camera, [e] emergency melt dump system.

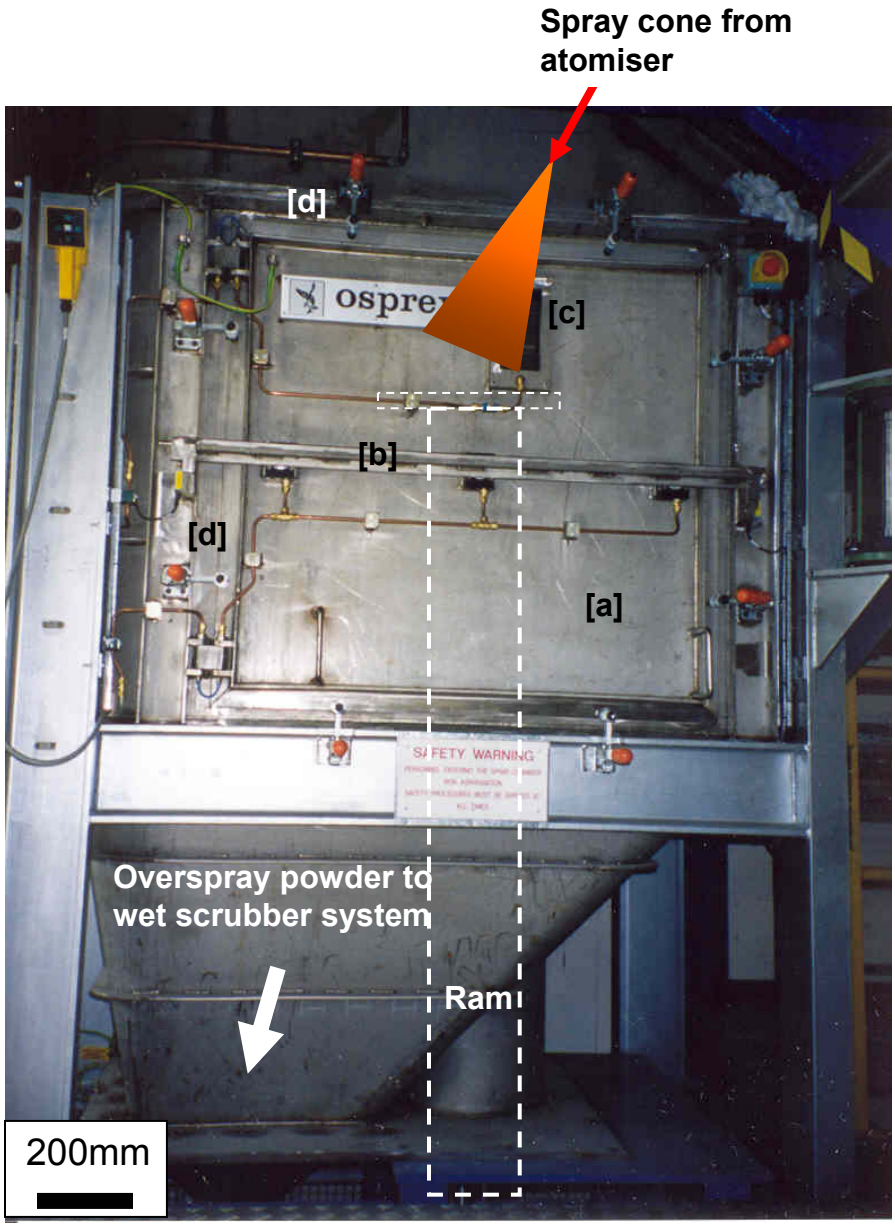

Figure 3.13: The Oxford spray chamber: [a] chamber door, [b] locking bar secured with pneumatically fired pins, [c] observation window, [d] 8 door clamps. The approximate ram position overlaid in white, and the spray cone is indicated in orange

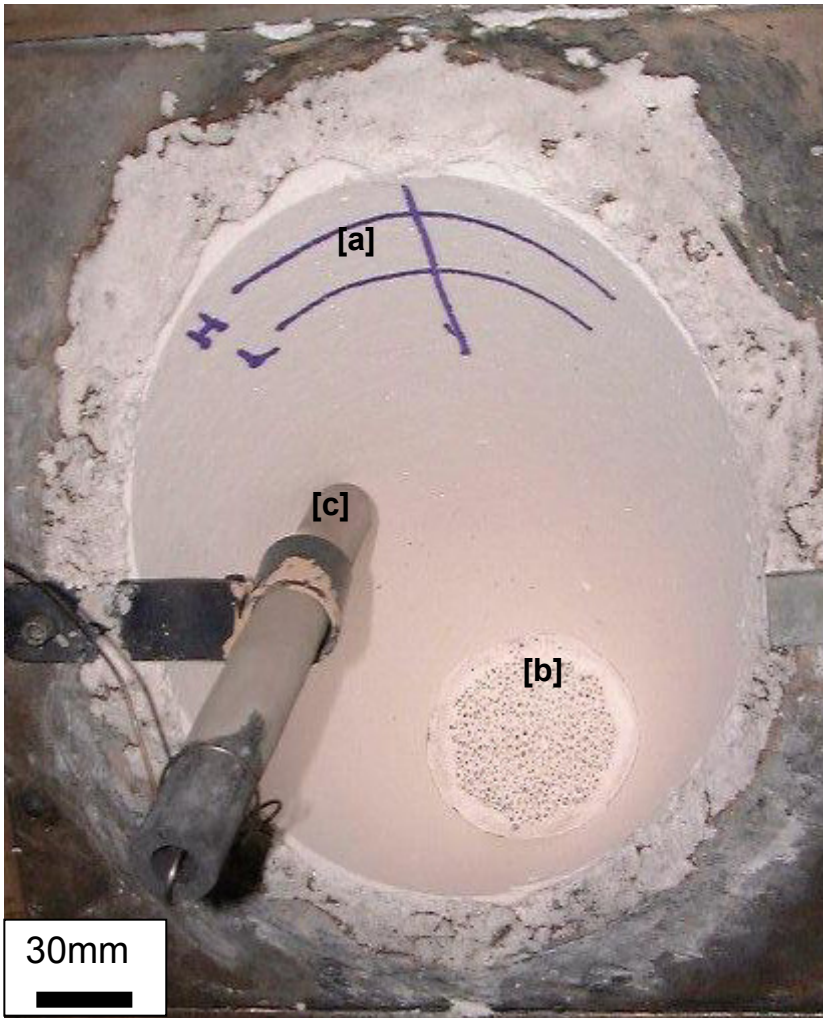

Figure 3.14: Tundish and filter on Oxford spray forming plant: [a] High & low markers for pour operator (~14mm separation), [b] Alumina filter to remove dross scale and oxide, [c] Thermocouple sheath.

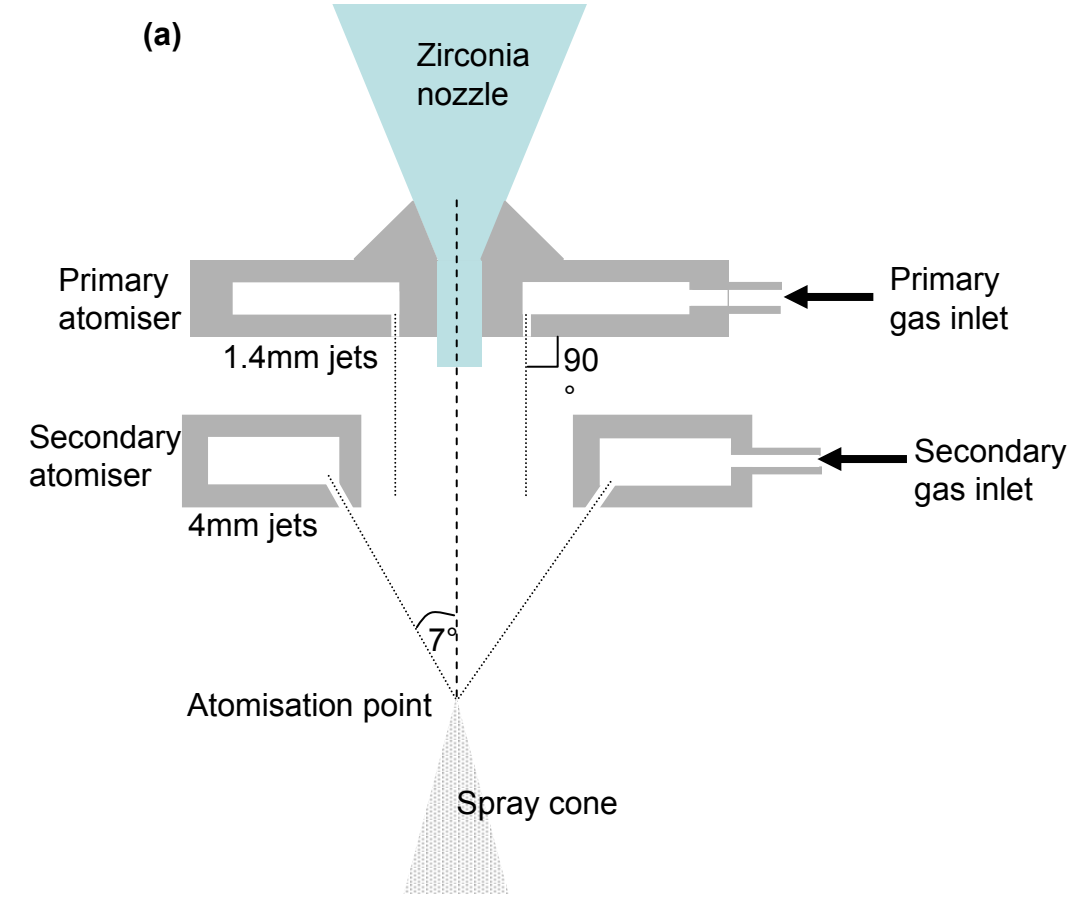

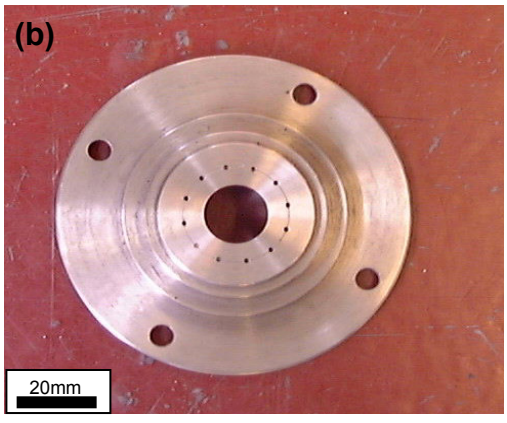

Primary atomiser

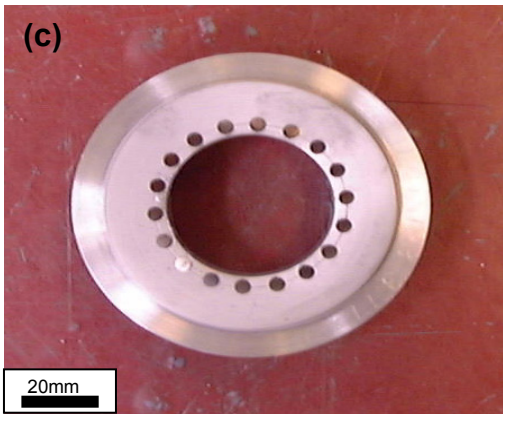

Secondary atomiser

Figure 3.15: (a) schematic of the arrangement of the melt delivery nozzle, primary and secondary atomisers; (b) photograph showing the primary atomiser; (c) photograph showing the secondary atomiser

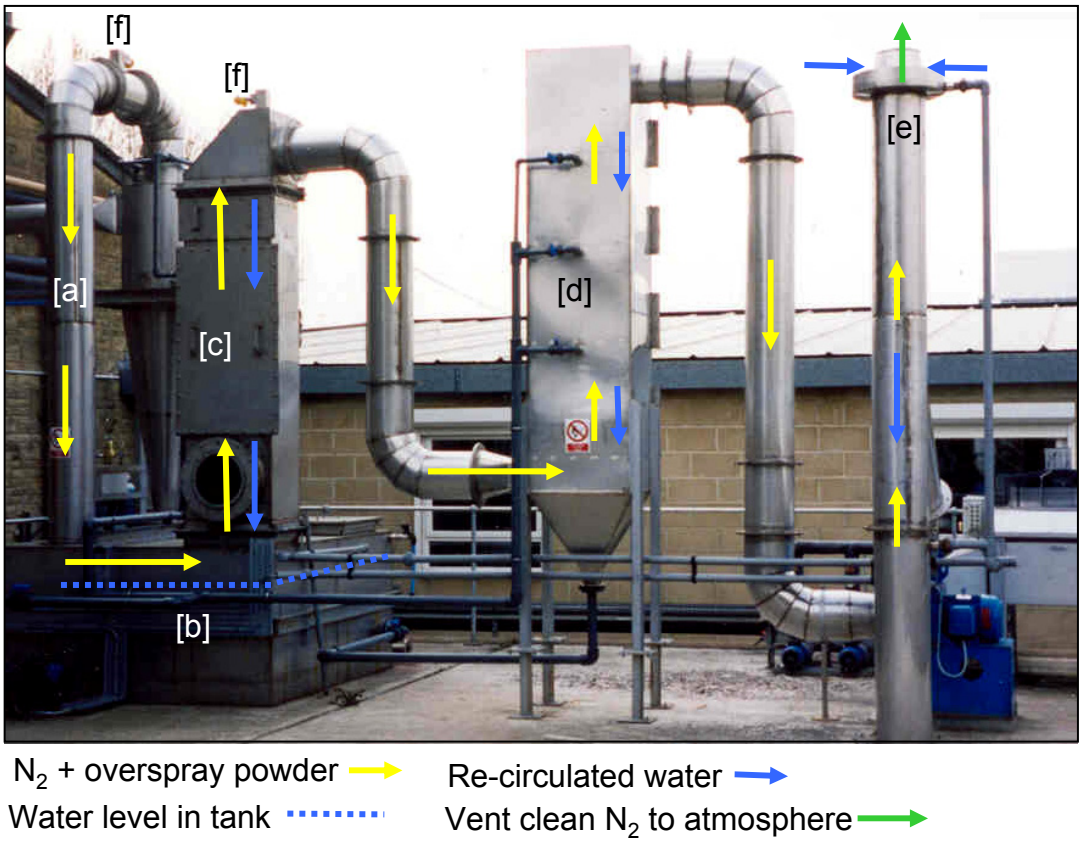

Figure 3.16: The wet scrubber system: [a] overspray powder from spray chamber, [b] settling tank, [c] counter flowing water filter No1, [d] counter flowing water filter No2, [e] annular water spray, [f] hydrogen vents.

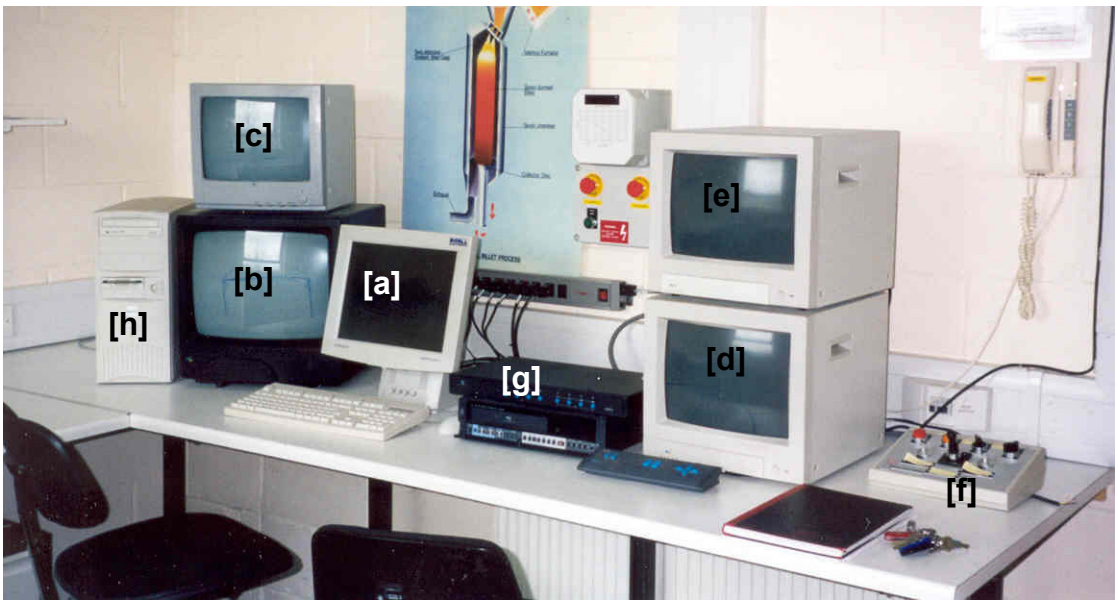

Figure 3.17: Osprey control room: [a] touch-screen operator interface, [b] substrate / billet growth, [c] atomiser/ melt steam, [d], melt level in tundish, [e] 4 way screen split of a, b, c plus plant overview [f] tilt-pout joystick and speed controls, [g] image control and logging, [h] control PC.

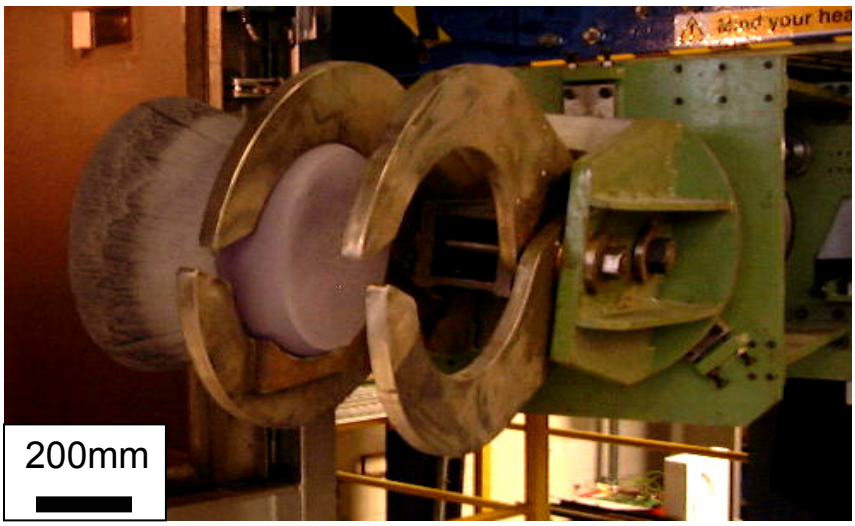

Figure 3.18: Billet removal arm extracting billet from chamber.

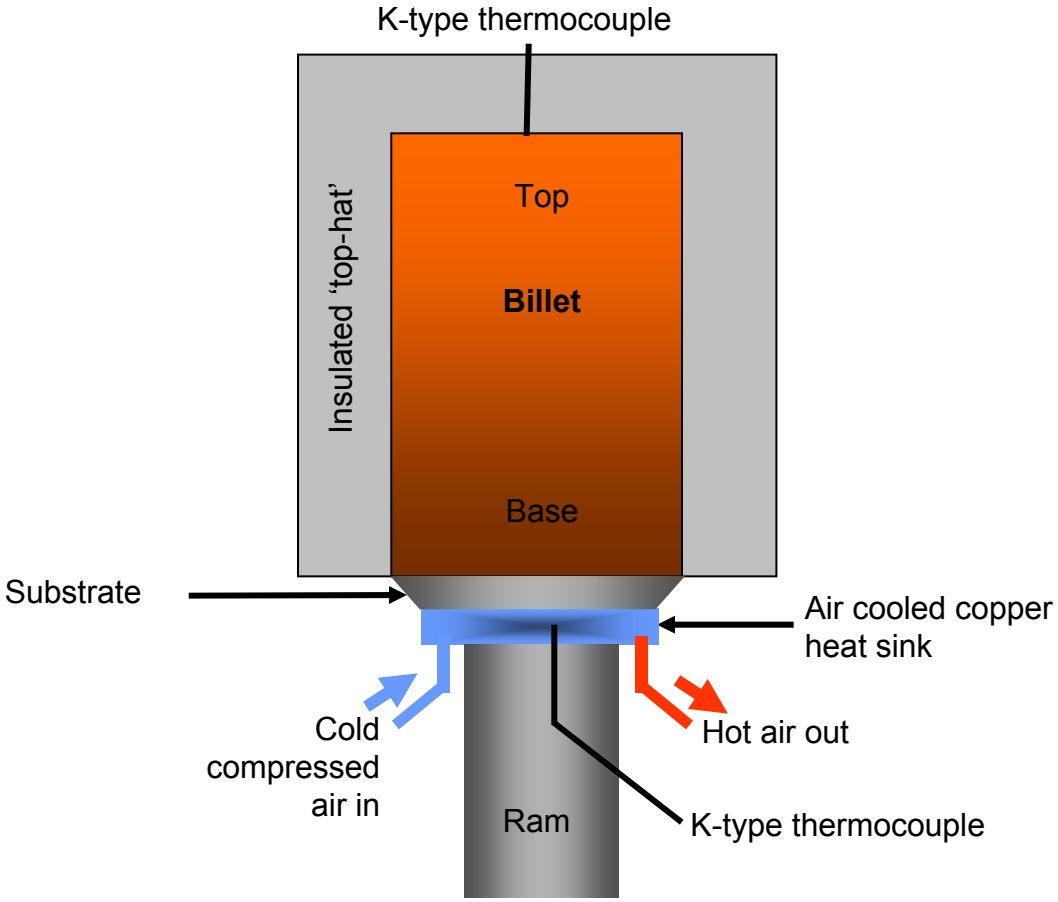

Figure 3.19: Schematic of *In situ*, controlled post spray cooling.

Chapter 3:

Experimental appendices

Experimental Appendices

3.1(a,b)	Image J macro used for interface length analysis
3.2	Zeiss KS400 macro used for phase fraction and porosity mapping
3.3	Procedure for determining K1c- from Hertzian indentation
3.4	Results of CERAM impulse excitation testing of CE7
3.5(a-e)	Run sheet for experiment 011, 017, 018, 019, 020

(a) **Load pre-set calibration**

```
run("Set Scale...", "distance=1.875 known=1 pixel=1 unit=micron
global");
```

Threshold greyscale image to binary image

```
run("Threshold");
```

Invert image

```
run("Invert");
```

Spatial convolution for smoothing and edge detection

```
run("Convolve...", "text1='-1 -1 -1 -1 -1 -1 -1 -1 -1 -1 -1 -1 24 -1 -1 -1
-1 -1 -1 -1 -1 -1 -1 -1 -1 ' normalize");
```

Invert image

```
run("Invert");
```

Remove all except interface pixels

```
run("Skeletonize");
```

Count pixels and measure connectivity, show result

```
run("Analyze Particles...", "minimum=1 maximum=999999 bins=200
show=Nothing display size clear record summarize");
```

Close image

```
run("Close");
```

(b)

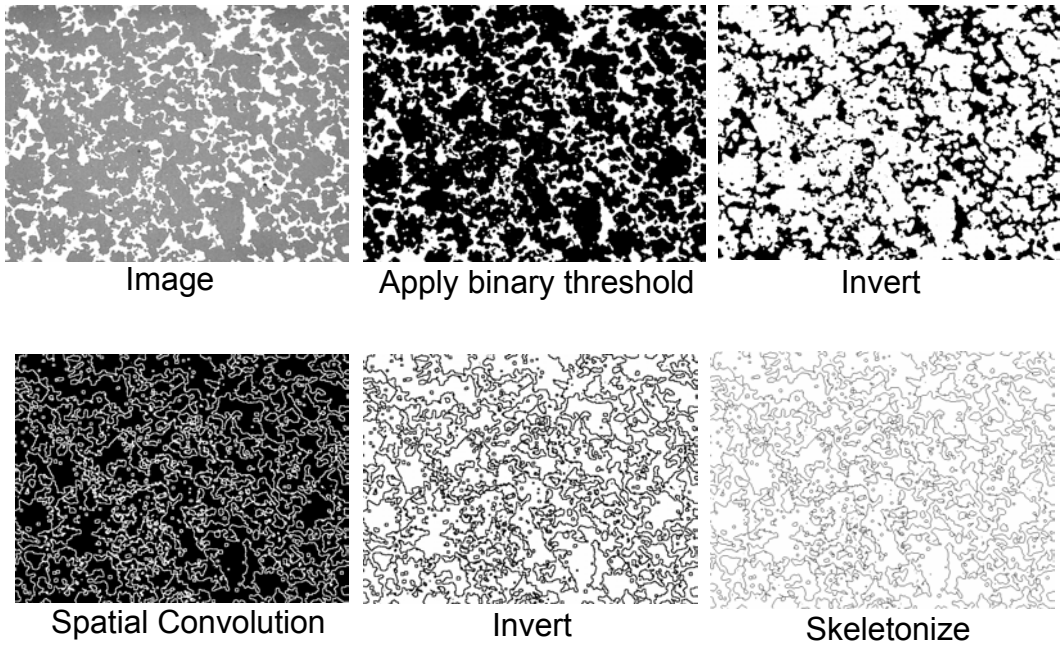

Appendix 3.1

(a) Image J macro used for interface length analysis of optical micrographs. Lines in bold describe the subsequent command line

(b) Sequential micrographs showing image analysis

```
Clear images and Graphics from System
Gclear 0
imgdelete "*"
showwindow "display",1
Input file database name
DBnew "ALEXIS_Al",1
DBnew "ALEXIS_Si",1
DBnew "ALEXIS_pores",1
Acquire image from microscope camera
MSsetprop "FIELDFEAT","FLDAREAP[%]=SUM(100*AREA/FRAMEAREA)"
Start of while / endwhile loop
while
tvlive
tvinput 1
 imgdisplay 1
Set grey scale to threshold phases
 ! greydisc 1,2,64,225,225,225,255
 dislev 2,3,0,70,1
 dislev 2,4,80,148,1
 dislev 2,5,218,255,1
 Measurement
 MSmeasmask 5,1,"ALEXIS_Al",1,2,10
 MSmeasmask 4,1,"ALEXIS_Si",1,2,10
 MSmeasmask 3,1,"ALEXIS_pores",1,2,10
Repeat measurement command box
MByesno "Another frame?"
   if _STATUS==0 : break
If Yes, continue to endwhile, if No break to after endwhile
Endwhile
Show individual data files
datalist "ALEXIS_Al",0,0
wait 5000
datalist "ALEXIS_Si",0,0
wait 5000
datalist "ALEXIS_pores",0,0
```

Appendix 3.2

Zeiss KS400 macro used for phase fraction and porosity mapping of optical micrographs which converts grey scale image into area fraction of Al, Si and porosity. Lines in bold describe the subsequent command line

A grid array of indents was produced, each site being ~1mm from any other site, the load to initiate a ring crack noted for each indent. The recorded loads were then placed in ascending order and assigned a corresponding rank (n) (lowest load = rank 1). The failure probability F(p) was then calculated by:

$$K_{1c} = \sqrt{\frac{E * P_{\min}}{CR}}$$

F(p) = n/n+1
F(p) (ordinate) was then plotted against load (abscissa) in a pseudo-Weibull plot, an extrapolation through the vertical portion of the curve is then required to obtain a value of P_{min}. K_{1c} is then calculated from:

$$E^* = \frac{1}{\frac{1-\upsilon_1^2}{E_1} + \frac{1-\upsilon_2^2}{E_2}}$$

Where:
P_{min} is the minimal load for fracture determined from the graph described
C is constant determined from the poisons ration of the material
R is the radius of the indenter
E* is calculated from the Poisson's ratio and the Young's modulus of the indenter and the substrate calculated from:
Where:
V_1 = Poisson's ratio of the indenter
V_2 = Poisson's ratio of the substrate
E_1 =Young's modulus of the indenter
E_2 =Young's modulus of the Substrate

Appendix 3.3
Procedure for Calculation of K1c from Hertzian indentation data

(Warren, 1995a, 1995b).

0013

YOUR PARTNER IN MATERIALS AND TECHNOLOGY CERAM

Queens Road Penkhull
Stoke-on-Trent ST4 7LQ
Tel: +44 (0) 1782 764444
Fax: +44 (0) 1782 412331
E-mail: info@ceram.com
http://www.ceram.com

TEST REPORT

Client's Name and Address:
Mr R Ross
Osprey Metals Ltd
Red Jacket Works
Miland Road
Neath
West Glamorgan
SA11 1NJ

Date Issued	:	12 March 2003
Laboratory N°	:	P030514KTT/R178/
Our Reference	:	KT/LMP/P030514KTT/R178/
Date(s) Tested	:	12 March 2003
Date Received	:	12 March 2003
Client's Mark	:	See below
Client's Reference	:	Mr R Ross

MEASUREMENT OF MODULUS OF ELASTICITY (YOUNG'S MODULUS, E) MODULUS OF RIGIDITY AND POISSONS RATIO AT ROOM TEMPERATURE

1 SAMPLES RECEIVED

Three metal test bars marked 03M000151 CE7, 03M000152 CE11 and 03M000153 CE17, of nominal dimensions 120 mm x 20 mm x 10 mm, were received for testing.

2 TEST METHOD

It should be noted that this is not as yet, either a British or International Standard. The test method, CERAM R117: 2002 is described in:

W R Davies "Measurement of the Elastic Constants of Ceramics by Resonant Frequency Methods" Trans.Brit.Ceram.Soc.67, (11) 515, 1968.

The Modulus of Elasticity (Young's Modulus, E) and the Modulus of Rigidity (G) were measured by determining the fundamental longitudinal and fundamental torsional resonance's using direct drive and detection.

Poissons Ratio was calculated using the formula:

$$P.R = \frac{E}{2G} - 1$$

3 RESULTS

Sample No	Modulus of Elasticity (GPa)	Modulus of Rigidity (GPa)	Poissons Ratio
03M000151 CE7	129.2	51.2	0.26
03M000152 CE11	121.4	48.6	0.25
03M000153 CE17	91.8	35.8	0.28

NOTE: The results given in this report apply only to the samples that have been tested.

END OF TEST REPORT

Appendix 3.4

Results of CERAM impulse excitation testing of CE7.

AL

BEGBROKE SPRAY FORMING PLANT
PROCESSING PARAMETERS

DATE	26/2/03	RUN NUMBER	011
MATERIALS	CE7 [Al-70Si] 18kg master alloy + 32kg Si chips		
OBJECTIVES	Benchmark Oxford material / conditions against Osprey		
Team Leader	A. Lambourne		
Operators	TK pouring, SH Co-ordination, RV melting, AL Software		

MELTING

Melt Temperature	1415°C	Crucible Liner Type	Fibre liner
Max. Induction Power	kW	Tundish Type	Ceramic fibre
Degassing	Y / ~~N~~	Nozzle Type and Size	5.5 / ZrO_2
Degassing time	20 min	Charge Weight	50.0kg
Degassing flow rate	6 l/min	Filter Type	Al_2O_3
Inert Gas System	~~Y~~ / N	Inert Cover Gas Type	~~Ar / N_2~~

ATOMISING

Gas Type	N_2	Chamber Purge Time	12 min
Primary Type	P030	Primary Gas Pressure	~~3.00~~ 2
Secondary Type	3.77	Second. Gas Pressure	~~7.20~~ 9
Scanning Angle	—	Scanning Frequency	16·6 Hz
Max Chamber Pressure	See Data log	Max Extraction Fan Speed	See Data log

DEPOSITION

Collector Type	Stainless Steel	Collector Size	250 mm
Spray Height	700 mm	Ram Position	235
Rotation Speed	2.25 Hz	Edge Position	5 mm
Withdrawal Speed	0.5 mm/min	Centre Position	25 mm
Pre-form Weight	~ 11 Kg	Pre-form Height	120 mm
Chamber O2 Level	< 150ppm	Pre-form Diameter	~ 250 mm
Total Run time	min sec	Billet Weight	9.75 Kg
Tundish Weight	lots	Metal Flow Rate	Kg/min
Skull Weight	lots	Yield	%

Not calculated

Freeze off in Nozzel
- Blocked or melt superheat too low?

Appendix 3.5(a)

Run sheet for experiment 011, Oxford CE7

BEGBROKE SPRAY FORMING PLANT
PROCESSING PARAMETERS

DATE	**10/02/2004**	RUN NUMBER	**017**
MATERIALS	**Al-70Si Plus 1% B**		
OBJECTIVES	Modify CE7 using Boron		
Team Leader	A. Lambourne		
Operators	**TK** Melting / pouring, **SH** Co-ordination / safety, **RV** melting, **AL** Control / De-gassing, **IP** Observation / safety		

MELTING

Melt Temperature	1450°C	Crucible Liner Type	None
Max. Induction Power	kW	Tundish Type	Ceramic fibre
Degassing	Y / ~~N~~	Nozzle Type and Size	5.5 / ZrO
Degassing time	20 min	Charge Weight	50.0kg
Degassing flow rate	~6 l/min	Filter Type	Al_2O_3
Inert Gas System	~~Y~~ / N	Inert Cover Gas Type	~~Ar / N_2~~

ATOMISING

Gas Type	N_2	Chamber Purge Time	
Primary Type	P030	Primary Gas Pressure	2.00
Secondary Type	3.77	Second. Gas Pressure	8.0
Scanning Angle	—	Scanning Frequency	16 Hz
Max Chamber Pressure	See Data log	Max Extraction Fan Speed	See Data log

DEPOSITION

Collector Type	Stainless Steel	Collector Size	250 mm
Spray Height	700 mm	Ram Position	245
Rotation Speed	2.25 Hz	Edge Position	5 mm
Withdrawal Speed	~0.5 mm/min	Centre Position	25 mm
Pre-form Weight		Pre-form Height	
Chamber O2 Level	< 150ppm	Pre-form Diameter	~ 250 Ø
Total Run time	5 min 03 sec	Billet Weight	15.56
Tundish Weight	11 kg	Metal Flow Rate	Kg/min
Skull Weight	9.3 3kg	Yield	~31 %

skull / dross

15.6 billet
9.3 skull (+ spill)
11.0 Tundish
3.0 dross → = 38.9

overspray = 11.1 kg.

Appendix 3.5(b)

Run sheet for experiment 017, CE7+B

BEGBROKE SPRAY FORMING PLANT
PROCESSING PARAMETERS

DATE	**18/02/2004**	RUN NUMBER	**018**
MATERIALS	**Al-70Si Plus 1% P**		
OBJECTIVES	Modify CE7 using Phosphorous		
Team Leader	A. Lambourne		
Operators	**TK** Melting / pouring, **SH** Co-ordination / safety, **RV** melting, **AL** Control / De-gassing, **IP** Observation / safety		

MELTING

Melt Temperature	1450°C	Crucible Liner Type	None
Max. Induction Power	75 kW	Tundish Type	Ceramic fibre
Degassing	Y / ~~N~~	Nozzle Type and Size	5.5 / ZrO
Degassing time	20 min	Charge Weight	50.0kg
Degassing flow rate	~6 l/min	Filter Type	Al_2O_3
Inert Gas System	~~Y~~ / N	Inert Cover Gas Type	~~Ar / N_2~~

ATOMISING

Gas Type	N_2	Chamber Purge Time	~ 12 min
Primary Type	P030	Primary Gas Pressure	2.00
Secondary Type	3.77	Second. Gas Pressure	8.0
Scanning Angle	–	Scanning Frequency	16·6 Hz
Max Chamber Pressure	See Data log	Max Extraction Fan Speed	See Data log

DEPOSITION

Collector Type	Stainless Steel	Collector Size	250 mm
Spray Height	700 mm	Ram Position	245
Rotation Speed	2.25 Hz	Edge Position	5 mm
Withdrawal Speed	~0.5 mm/min	Centre Position	25 mm
Pre-form Weight	22·04	Pre-form Height	190 mm
Chamber O2 Level	< 150ppm	Pre-form Diameter	250 → 230 Taper
Total Run time	5 min 52 sec	Billet Weight	22·04 kg
Tundish Weight	10·44 kg	Metal Flow Rate	Kg/min 6·8
~~Skull~~ Weight	1·58 kg	Yield	44 %

Dross

Furace & Tundish

Skirt = 1.90 kg

Billet = 22·04
Skirt = 1·90
OSP = 14·04
= 37·98 Through nozzle

Dross = 1·58
Furnace/Tundish Skull = 10·44
WASTE.

Appendix 3.5(c)

Run sheet for experiment 018, CE7+P

BEGBROKE SPRAY FORMING PLANT
PROCESSING PARAMETERS

DATE	**16/03/04**	RUN NUMBER	**019**
MATERIALS	**Al-70Si (Plus 1% P + 5% Ce)**		
OBJECTIVES	Modify CE7 using Phosphorous & Cerium		
Team Leader	A. Lambourne		
Operators	**TK** Melting / pouring, **SH** Co-ordination / safety, **RV** melting, **AL** Control / De-gassing, **IP** Observation / safety		

MELTING

Melt Temperature	1450°C	Crucible Liner Type	None
Max. Induction Power	75 kW	Tundish Type	Ceramic fibre
Degassing	Y / ~~N~~	Nozzle Type and Size	5.5 / ZrO
Degassing time	20 min	Charge Weight	50.0kg
Degassing flow rate	~6 l/min	Filter Type	Al_2O_3
Inert Gas System	~~Y~~ / N	Inert Cover Gas Type	~~Ar / N_2~~

ATOMISING

Gas Type	N_2	Chamber Purge Time	13 min 30 sec
Primary Type	P030	Primary Gas Pressure	2.00
Secondary Type	3.77	Second. Gas Pressure	7.0
Scanning Angle	–	Scanning Frequency	16.6 Hz
Max Chamber Pressure	See Data log	Max Extraction Fan Speed	See data log

DEPOSITION

Collector Type	Stainless Steel	Collector Size	250 mm
Spray Height	700 mm	Ram Position	245 mm
Rotation Speed	2.25 Hz	Edge Position	5 mm
Withdrawal Speed	~0.5 mm/min	Centre Position	23 mm
Pre-form Weight	23 Kg	Pre-form Height	190 mm
Chamber O2 Level	< 150ppm	Pre-form Diameter	Tapered 210@ Top.
Total Run time	min sec	Billet Weight	~~Tapered~~ 23.08
Tundish Weight	4.82	Metal Flow Rate	Kg/min
Skull Weight	5.68	Yield	46 %

Furnace skull — 5.68 Kg
Tundish skull — 4.82 Kg
Dross — 1.46 Kg
Skirt — 1.32 Kg

Appendix 3.5(d)

Run sheet for experiment 019, CE7+P+Ce

BEGBROKE SPRAY FORMING PLANT
PROCESSING PARAMETERS

DATE	24/03/04	RUN NUMBER	020
MATERIALS	Al-70Si (Plus 0.25% Sr)		
OBJECTIVES	Modify CE7 using Strontium		
Team Leader	A. Lambourne		
Operators	**TK** Melting / pouring, **SH** Co-ordination / safety, **RV** melting, **AL** Control / De-gassing, **IP** Observation / safety		

MELTING

Melt Temperature	1470°C	Crucible Liner Type	None
Max. Induction Power	75 kW	Tundish Type	Ceramic fibre
Degassing	Y / ~~N~~	Nozzle Type and Size	5.5 / ZrO
Degassing time	20 min	Charge Weight	50.0kg
Degassing flow rate	~6 l/min	Filter Type	Al_2O_3
Inert Gas System	~~Y~~ / N	Inert Cover Gas Type	~~Ar / N_2~~

ATOMISING

Gas Type	N_2	Chamber Purge Time	14 min
Primary Type	P030	Primary Gas Pressure	2.00
Secondary Type	3.77	Second. Gas Pressure	7.0
Scanning Angle	–	Scanning Frequency	16·6 Hz
Max Chamber Pressure	See Data log	Max Extraction Fan Speed	See Data log

DEPOSITION

Collector Type	Stainless Steel	Collector Size	250 mm
Spray Height	700 mm	Ram Position	245
Rotation Speed	2.25 Hz	Edge Position	5 mm
Withdrawal Speed	~0.5 mm/min	Centre Position	23 mm
Pre-form Weight	19·44	Pre-form Height	190 mm
Chamber O2 Level	< 150ppm	Pre-form Diameter	230 mm
Total Run time	5 min 30 sec	Billet Weight	19·44
Tundish Weight	7·90	Metal Flow Rate	6·2 Kg/min
Skull Weight (furnace).	4·08	Yield	38·8%

Furnace 4·08
Tundish 7·90
Dross 4·90
Skirt −2·44

50 − 38·76 = 11.24

Appendix 3.5(e)

Run sheet for experiment 020, CE7+Sr

4.0 Results - CE7 manufactured at Sandvik-Osprey Metals Ltd.

Section 4.1.1 and 4.1.2 describe the primary processing and post spray forming cooling and HIPing operations, and the compositional analysis of the Sandvik-Osprey billet is given in Section 4.1.3. The physical characterisation techniques previously described in Section 3.3 were used to investigate Sandvik-Osprey CE7 and the results are given in Section 4.2. The microstructural characterisation techniques previously described in Section 3.2 including optical microscopy, EPMA and EBSD were used to investigate Sandvik-Osprey CE7 and the results are given in Section 4.3.

4.1 Manufacture

4.1.1 Spray forming

Spray forming conditions at Sandvik-Osprey are proprietary. The material examined in this thesis represented the state-of-the-art for CE7 (Si-30Al) and was both typical and reproducible. Detailed process conditions were disclosed to the author in order to develop the Oxford process conditions and where direct comparisons could be made, for example in the post spray thermal history of the billet, there was good agreement.

4.1.2 Hot isostatic pressing (HIPing)

Hot isostatic pressing of the Sandvik-Osprey CE7 billet was conducted by Bodycote HIP, Chesterfield, UK. The processing conditions defined by Sandvik-Osprey were 565°C for 16 hours at 140MPa. Image analysis before

and after HIPing showed that porosity was typically reduced from around 2.0-4.0 area% in the as-sprayed condition to <0.1% after HIPing.

4.1.3 Bulk compositional analysis

The composition of Osprey CE7 was analysed using inductively coupled plasma (ICP) analysis combined with wet chemical gravimetric analysis, optical emission spectroscopy (OES) and fused bead X-ray fluorescence (XRF). Samples were taken from the middle-centre position in each billet i.e. 50% of the billet height on the axis of rotation. Gravimetric / ICP analysis was conducted by the analytical laboratory at London Scandinavian Metals Ltd, using calibrated equipment and reference standards whereas OES and XRF analysis were conducted in Oxford. The measured compositions are compared to the nominal composition of the alloy in Table 4.1 below:

Table 4.1: The nominal composition and measured composition of CE7 manufactured at Sandvik-Osprey.

Analysis	**Sample Mass**			**Impurities**			
		Al	**Si**	**Cu**	**Fe**	**Zr**	**Ti**
Nominal	--	30	70	--	0.32‡	0.0006‡	--
Gravimetric / ICP (Solid)	20g / 10g	33.29	65.83	0.02	0.37	0.03	0.02
Gravimetric / ICP (Powder)	20g / 10g	16.55	82.8	0.003	0.58	0.041	0.026
OES	Bulk	31.83	67.76*	0.004	0.30	0.046	0.056
XRF†	Bulk	22.19	77.49	--	0.26	0.04	0.04

*calculated by difference
‡calculated from feedstock certification analysis
†One point calibration for high Si content

The measured elemental concentrations varied significantly with the different analysis techniques, demonstrating the difficulty in accurately measuring the composition of this material. The fine-scale interpenetrating networks of Al and Si based phases made dissolution of Al for ICP and gravimetric analysis problematic. Al and Si peak overlaps in XRF analysis made quantitative analysis difficult outside the calibrated range. A one point calibration at relatively high Si concentrations compensated to some extent for peak overlap, but did not yield sensible results. Overall, Table 4.1 suggested that OES analysis for the Al and impurity concentrations, followed by calculation of the Si concentration by difference provided the most sensible analysis for alloy composition. This approach was then adopted and all subsequent concentrations are presented on this basis.

4.2 Physical characterisation

4.2.1 Vickers indentation

As described in Section 3.3.2, this approach for fracture toughness measurement relied upon establishing whether the induced cracking mechanism was radial-median 'halfpenny' cracks' (shown in Figure 3.3). A series of Vickers indentations were made at loads of 1, 2.5, 5 and 10Kg, and the corresponding crack lengths measured. With reference to Ponton (1989a, 1989b) and Lube (2001) these data were plotted in Figure 4.1(a) as $P/c^{3/2}$ against indentation load P, in order to test Equation 3.1. Ponton (1989a) has shown that for Vickers indents with fully developed cracks, c is proportional to $P^{3/2}$ i.e. $P/c^{3/2}$ is a constant at different indentation loads. Therefore for Equation

3.1 to be satisfied, the data in Figure 4.1(a) should show a horizontal line with $P/c^{3/2}$ independent load P. Data for CE7 presented in Figure 4.1(a) shows $P/c^{3/2}$ was not constant, and indicated that the point force model was not an appropriate description of the behaviour of CE7 under Vickers indentation (Lube 2001). The fracture behaviour in 4.1(a) could be explained by R-curve behaviour, whereby toughness apparently increases with crack propagation. Plotting crack length c against K_{1c}, R-curve behaviour can clearly be seen from this material, as shown in Figure 4.1(b). The reasons for this will be considered in more depth in Section 7.4.3. Because of R-curve behaviour, it is understood that where a Vickers derived K_{1c} is calculated by this technique it is not a true measure of fracture toughness, and when used at a fixed load (5kg) for all subsequent testing, it is used only to rank and compare fracture behaviour of Sandvik-Osprey CE alloys and Oxford modified CE7. Using this approach, HIPed CE7 had a nominal 2.55MPam$^{1/2}$.

4.2.2 Hertzian indentation

Following the method of Warren (1995a, 1995b) Hertzian indentation of Sandvik-Osprey CE7 in the as-sprayed and HIPed condition was presented in a pseudo-Weibull plot of probability of failure (P_f) versus load to failure and is shown in Figure 4.2. Extrapolation of the data to a vertical asymptote gave an estimation of the minimum load for failure P_{min} which was then used to calculate K_{1c} as described in Appendix 3.3 and as shown in Table 4.2.

Table 4.2: K_{1c} and P_{min} calculated from Hertzian indentation.

Alloy (condition)	P_{min} (N)	K_{1c} (MPa $m^{1/2}$)
CE7 (As sprayed)	53	0.82
CE7 (HIPed)	205	1.68
CE9 (HIPed)	166	1.41

Table 4.2 shows that HIPing of CE7 increased the minimum load to fracture and the toughness from 53 to 205N and 0.82 to 1.61MPa $m^{1/2}$ respectively. CE9 had a slightly reduced minimum load to failure of 166N and a toughness of 1.41MPa $m^{1/2}$.

4.2.3 Impulse excitation modulus measurements

Modulus testing was performed only after HIPing because of resonant frequency attenuation caused by the presence of porosity. For each commercial CE alloy 10 test pieces were prepared, excitation being repeated 10 times on each sample. The resulting Young's modulus for Sandvik-Osprey CE alloys are presented in Figure 4.3. There was a steady reduction in modulus with increasing Al fraction from 129GPa for Si-30Al (CE7) to 92GPa for Al-27Si (CE17). Poisson's ratio for Sandvik-Osprey CE7, determined by impulse excitation was 0.36. Data were compared to a 'rule of mixtures' calculation based on literature modulus data for pure Si (E= 168GPa, Ericson 1988) and pure Al (E= 70GPa, Askeland 1993). Figure 4.3 shows there is a systematic off-set from ROM behaviour, with the CE alloys showing slightly lower measured moduli, and with the off-set increasing with increasing Si content. This will be discussed further in Section 7.4.1.

4.2.4 Optical emission spectroscopy (OES) macrosegregation mapping

OES was used to assess the distribution of Al and impurity inclusions of Fe within the Sandvik-Osprey CE7 billet manufactured under best-practice processing conditions, and concentration data expressed as a series of contour maps. Figure 4.4(a) and 4.4(b) show the distribution of Al and Fe concentration respectively, with the location of individual data points indicated in black. The missing data in the upper left resulted from a taper in the billet because of progressively decreasing melt flow rate towards the end of billet manufacture. Figure 4.4(a) shows that the Al concentration varied from 30 to 35% at the mid height from centre to edge, and from 25 to 30% from the top to the base at the centre of the billet. Figure 4.4(b) shows that the Fe concentration varied from 0.29 to 0.33% at the mid height from centre to edge, and 0.25 to 0.77 from the top to the base along the centre line of the billet. The radial distribution of Al and Fe was broadly associated with inverse segregation whereby the near surface regions are relatively concentrated and the central regions relatively denuded in solute. Classically this is a shrinkage driven phenomenon and relies upon significant interconnected liquid (Campbell 1993). This segregation pattern has been reported previously in conventional spray formed Al alloy (Mingard 2000, Kahveci 1995). The vertical distribution showed the uppermost regions were strongly denuded in Al, presumably as liquid was drawn back into the billet by the directional solidification of the residual liquid by the base chill. This is discussed in Section 7.2.2 in terms of the partition coefficient, solidification path, heat flow and latent heat of fusion.

4.2.5 CTE measurements

Figure 4.5 shows the thermal expansion coefficient of CE7 in the Y-axis (axial) and X (radial) planes as a function of temperature from 25 to 500°C. In both cases the room temperature CTE progressively increased from ~5x10^{-6} °C^{-1} to ~9x10^{-6} °C^{-1} at 200°C and remained approximately constant until ~400°C when there was a steady decrease to ~8x10^{-6} °C^{-1} at 500°C. At all temperatures the CTE in the Y plane was ~1x10^{-6} °C^{-1} greater than the X plane and both X and Y samples had average CTE higher than nominal CTE for CE7 quoted by Sandvik-Osprey of 7.0x10^{-6} °C^{-1}. This can be explained by the effect of macrosegregation (and hence composition) on CTE in different parts of the billet as discussed in Section 7.4.2 and shown in Figure 7.3.

4.2.6 Four-point bend testing

When a sample is subjected to bending as shown in Figure 3.6(b) a compressive stress is generated in the upper surface and a tensile stress in the lower surface. As the tensile strength of brittle materials is much less than the compressive strength, fracture commences at the tensile surface. The modulus of rupture (MOR) from Equation 3.2 is higher than the true tensile strength because only one face of the sample is under tension and due to the limited volume of material under tensile load. Integration of the stress distribution inside the component results in expressions for strength as a function of the Weibull modulus *M* for components under different loading conditions, e.g. 3-point or 4-point bending. If the strength in uniform tension i.e. uniform stress in the total volume of the sample is determined to be $\sigma_{MOR} = \sigma_t$, then for 4-point bending:

$$\frac{\sigma_{MOR}}{\sigma_t} = \left[\frac{\left[4(M+1)^2\right]}{(M+2)}\right]^{\frac{1}{M}}$$

Equation 4.1

For example, from Equation 4.1 above, σ_{MOR} / σ_t = 1.245 for a value of *M*=20. Therefore the estimated UTS (σ_t) of a material in uniaxial tension with M=20 and σ_{MOR} from four-point bend tests can be calculated from; $\sigma_t = \sigma_{MOR} / 1.245$. The four-point bend test data used to calculate the Weibull modulus, *M,* and to estimate the UTS, and the data are presented in Table 4.4. Further discussion of these bend test results can be found in section 7.4.4.

Table 4.4: Results summary for 4-point bend testing of HIPed Osprey CE7.

Sample No	**Breaking force (N)**	**Modulus of rupture (MOR) (MPa)**
1	795.0	168
2	858.3	184
3	740.8	159
4	734.9	162
5	765.6	169
6	795.6	166
7	796.3	168
8	726.7	157
9	808.0	171
10	810.0	171
Average	**783**	**167**
Standard deviation	**40.9**	**7.7**
Weibull Modulus	**M=21**	
UTS in Uniaxial tension*	**135.2MPa**	

*Calculated from Equation 4.1.

4.2.7 Fracture surfaces

Scanning electron microscopy (SEM) and energy dispersive X-ray spectroscopy (EDS) was used to image and investigate the composition of fractured surfaces of bend test specimens. A secondary electron image of HIPed Sandvik-Osprey

CE7 with the corresponding EDS elemental maps for Si, Fe and Al are shown in Figures 4.6 (a)-(d), respectively. Comparison of 4.6(a) and 4.6(b) suggested that relatively smooth faceted areas in 4.6(a) were the primary Si phase, whereas regions showing surface more characteristic of ductile behaviour were reduced in Si and were shown in 4.6(c) to correspond with Al-rich regions and were attributed to the Al-rich secondary phase / eutectic. Figure 4.6(d) shows little evidence of Fe except a slight clustering associated with the inset feature shown in 4.6(a). Closer examination shows a crack in the Si phase in this region, and suggested the presence of Fe-rich intermetallics and their possible involvement in Si cracking. Figures 4.7(a) and 4.7(b) show secondary electron images of as-sprayed Sandvik-Osprey CE7 fracture surfaces, 2 failure mechanisms are apparent; brittle transgranular (failure through grains following certain crystallographic planes) failure of the Si phase indicated in 4.7(a) and discussed in section 7.4.4, and the ductile ‘cup and cone’ intergranular (following the grain boundaries) failure in the Al-rich phase, as indicated in 4.7(b). In the as-sprayed condition there were small, irregular pores of 20-30μm as indicated in Figure 4.7(b), these pores were typically completely eliminated during HIPing as shown in Figure 4.6(a).

4.2.8 Thermal cycling and vacuum dye penetrant inspection

Thermal cycling was conducted on HIPed and as-sprayed Sandvik-Osprey CE7 material, Figures 4.8 and 4.9 show a diffusion bonded CE7-CE11 laminate and a CE7-CE17 laminate respectively.

Laminated CE alloys were of interest since thermal management packages often require a different CTE in different parts of the same package. The CTE of these materials were nominally 7, 11 and 17 x 10^{-6} $°C^{-1}$ for CE7, CE11 and CE17 respectively. It should be noted that the microstructure of these three CE alloys differs due to the different Si content in each. All are spray formed binary Al-Si alloys; CE7 being Al-70Si, CE11 being Al-50Si, and CE17 being Al-27Si. The reduced Si content in CE11 and CE17 result in a more fragmented Si structure with fine, apparently rounded Si particles embedded in the Al network. The rounding of Si particles in CE11 and CE17 results from the abundance of nuclei for the growth of primary Si, consistent with the primary Si growth model proposed by Wang 1999, this is discussed in more depth in Section 8.2.1. Unusually the primary Si in CE7 material also appears rather rounded as shown in Figure 4.8(a). This may be accounted for by coarsening during multi-stage thermal treatments; Spray forming with slow cool, HIPing to remove porosity and HIP (diffusion) bonding. The coarsening behaviour of Si in CE7 is discussed further in Section 7.3. The primary Si and secondary Al phases in Figure 4.8 and 4.9 described more fully in section 4.3.

The laminate samples used an Al foil interlayer to improve diffusion bonding and reduce CTE mis-match stresses at the interface. Intermetallic phases in the interlayer were not investigated in detail but were assumed to be Al-Fe phases attributed to the typical addition of ~0.5%Fe in commercially available Al foil Conditions for diffusion bonding of laminated CE alloys are proprietary, and constitutes encapsulation at an elevated temperature and pressure, similar to

the HIPing procedure used for these alloys. The CE7 and laminated CE alloy samples were inspected for cracking at intervals through the thermal cycling regime. Vacuum impregnation with a UV fluorescent dye and inspection by eye under a UV lamp revealed no evidence of cracking after 31 and 106 thermal cycles between -50 and +150°C. HIPed and as-sprayed CE7 material was subsequently evaluated by 4-point bend test as described in section 4.2.9 and 4.2.10.

Figures 4.8(a) and 4.8(b) show optical micrographs of the CE7-foil and CE11-foil interfaces respectively in the CE7-CE11 laminate after thermal cycling, indicating no interfacial cracking or delamination. Figures 4.9(a) and 4.9(b) show optical micrographs of the CE7-CE17 laminate after thermal cycling, with a 25μm and 60μm Al foil interlayer respectively and again no interfacial cracking or delamination.

4.2.9 Thermal cycling and 4-point bend testing

Bend testing of Sandvik-Osprey CE7 in the HIPed and as-sprayed condition was conducted on samples after thermal cycling and compared with non-thermally cycled material as shown in Tables 4.5(a) and 4.5(b) and in the Weibull plots in Figures 4.10 and 4.11. These results were used to calculate the modulus of rupture (MOR) and the tensile strength of the material in uniaxial tension. The results are summarised in Tables 4.5(a) and 4.5(b):

Table 4.5(a): Bend test data for as-sprayed CE7 material before and after thermal cycling.

	As-sprayed		*As-sprayed + thermally cycled*	
Sample No	**Breaking force (N)**	**MOR (MPa)**	**Breaking force (N)**	**MOR (MPa)**
1	622.9	129.6	538.1	115.7
2	610.4	131.4	616.8	132.5
3	592.6	127.5	593.6	126.7
4	606	128.3	569.7	121.5
5	669.7	143.2	592.4	128.5
6	581	121.0	604.2	127.0
7	530.4	113.4	622.7	132.5
8	--	--	606.7	126.9
Average	**601.9**	**127.8**	**593.0**	**126.4**
Standard deviation	**42.35**	**9.19**	**27.57**	**5.60**
Weubull Modulus	**M=12.6**		**M=20.8**	
UTS in uniaxial tension*	**93.6 MPa**		**102.2 MPa**	

*Calculated from Equation 4.1

Table 4.5(b): Summary of bend test data for HIPed CE7 material before and after thermal cycling.

	HIPed		*HIPed + thermally cycled*	
Sample No	**Breaking force (N)**	**MOR (MPa)**	**Breaking force (N)**	**MOR (MPa)**
1	795.0	168	724.2	154
2	858.3	184	755.3	160
3	740.8	159	715.3	151
4	734.9	162	712.4	150
5	765.6	169	725.9	154
6	795.6	166	692.2	146
7	796.3	168	758.7	164
8	726.7	157	670.1	146
9	808.0	171	668.1	143
10	810.0	171	--	--
Average	**783**	**167**	**713.6**	**152.0**
Standard deviation	**40.9**	**7.7**	**32.5**	**6.9**
Weubull Modulus	**M=20.6**		**M=21.1**	
UTS in uniaxial tension*	**134.7MPa**		**123.2MPa**	

*Calculated from Equation 4.1

Table 4.5(a) shows that the mean breaking force, modulus of rupture and tensile strength of ~600N, 127MPa and 93.6MPa respectively for as-sprayed CE7 were largely unaffected by thermal cycling. The difference in the Weibull

modulus between the thermally cycled and non-thermally cycled material as shown in Figure 4.10 indicated considerable material variability in the as-sprayed condition. This suggested that prior to HIPing there is little merit in conducting bulk property mechanical tests as the fracture behaviour was dominated by the presence of porosity.

Table 4.5b shows similar data for HIPed Sandvik-Osprey CE7 material. HIPing led to an increase in breaking force, modulus and tensile strength to a mean of 783N, 167MPa and 135MPa respectively, and in each case with a slight reduction in the standard deviation as the material became ‘less variable’. In contrast to the as-sprayed material, thermal cycling led to an undermining of mean properties to 713N, 152MPa and 123MPa respectively, although mean properties remained superior to as-sprayed material. Figure 4.11 shows the corresponding Weibull plot and best-fit lines to the data yielded a modulus for HIPed and HIPed / thermally cycled material of 20 and 21 respectively. In other words, all samples’ properties were undermined by a similar amount by thermal cycling but variability within the data sets remained similar.

4.2.10 Thermal cycling and defect density

Optical microscopy was used to examine the bend test specimens after fracture by 4-point bend testing. The areas examined were those furthest away from the fracture surface and had thus experienced lower stresses. The thermally cycled material contained considerable numbers of micro cracks in the Si phase. The number of cracks per unit area was determined by counting by eye for both

thermally cycled and non-thermally cycled samples and are summarised in Table 4.6. The total crack length was estimated from the average length of 8μm for 50 cracks, in a 24mm^2 analysis area.

Table 4.6: Estimated micro-crack density in thermally cycled and non-thermally cycled HIPed Sandvik-Osprey CE7

HIPed CE7 material condition	**Average no of cracks / 24mm^2**	***Total crack length (μm / 24mm^2)**	***Average crack length (μm / mm^2)**
Thermally cycled	174	1394	58.1
Non-thermally cycled	42	332	13.8

* From a measured average crack length of 8μm

Some examples of typical micro-cracks in thermally cycled material are shown in Figure 4.12. Cracks were often associated with isolated or near-isolated volumes of Si surrounded by the Al-rich phase as indicated in 4.12(a), contained wholly within the Si phase as shown in 4.12(b), or emanating from the Al-Si interface into the Si phase as shown in 4.12(c).

4.3 Microstructural characterisation

The microstructure of Sandvik-Osprey HIPed CE7 is shown in Figure 4.13(a) and consisted of a co-continuous network structure of primary Si and Al-rich phase. The Al phase contained no evidence of the expected Al-rich/Si, non-faceted/faceted eutectic characteristic of hypo or hypereutectic Al based Si alloys and implied a fully divorced eutectic reaction. Interspersed through the Al-rich phase were a variety of intermetallic phases, many of which were investigated by subsequent EPMA analysis as being predominantly Al-Fe-Si and Si-Ti-Zr containing phases as indicated in Figures 4.13(b) and 4.13(c)

respectively. There was some cracking in the primary Si phase and this was often associated with isolated areas of Si surrounded by Al-rich phase as shown in Figure 4.13(c). Cracking occasionally initiated from intermetallics in the Al network and then propagated into the Si network. The Al-rich phase often contained micro-pores as shown in Figure 4.13(b), which usually occurred at the Al-Si phase interface.

4.3.1 Image analysis of interface length

Table 4.7 shows the interface length per unit area for Sandvik-Osprey HIPed CE7 and CE9, as well as the number of discrete Al sites and an Al phase shape factor, where 1 represented a perfect circle and 0 represented a line, calculated from:

$$ShapeFactor = 4\pi \frac{Area}{Perimeter^2}$$

Equation 4.2

Where *A* is the area of an individual Al site and *P* is the corresponding perimeter of that site.

CE7 had approximately twice as many discrete Al sites as CE9 and the interface length per unit area increased correspondingly from 8 to 15mm/mm^2. The Al in CE7 had an average circularity of 0.55 compared to 0.48 for CE9, suggesting equiaxed Al resulting from a slightly less faceted Si structure in CE7.

Table 4.7 Summary of image analysis for CE7 and CE9

Alloy	Si concentration wt%	Average number of discrete Si sites / image*	Interface length (mm/mm^2)	Average circularity
CE7	70	258	14.6	0.55 ±0.02
CE9	60	122	8.3	0.48 ±0.02

* Each image =1.53mm^2

As described in Section 3.1.3, three HIPed CE7 materials manufactured with simultaneous CE7 overspray particle injection mass flow rate ratios were supplied by Sandvik-Osprey and the effect of varying the [overspray re-injection mass flow rate] : [melt mass flow rate] ratio on interface length investigated.

Figure 4.14 shows the variation in interface length with injection ratio x100, indicating that there was an approximately linear relationship between injection ratio and interface length, with an increase in injection ratio from 26 to 48% leading to an increase in interface length from ~8 to 14mm/mm^2. In comparison, CE7 manufactured at Oxford with no co-injection of overspray had an interface length of 8.3mm/mm^2.

4.3.2 Porosity

Figure 4.15 shows the variation in porosity as a function of distance from the base of the as-sprayed CE7 billet measured along axis of billet rotation at the mid-radius. The porosity was at a maximum of ~4.0area% at the billet base, reduced to ~2 area% near the billet top and the error in measured porosity estimated as ±0.4area%. There was a concentrated region of very high porosity at the upper extremity of the billet, as intended resulting from the directional

cooling applied in the final stages of solidification. High porosity of ~30area% was concentrated in a band extending ~25mm downward from the top surface. In production billets at Sandvik-Osprey, the thickness of the high porosity band at the top of the billet would typically be measured by ultrasonic NDT and this zone scalped and re-cycled. Porosity in the HIPed material was <0.1% in all parts of the billet.

4.3.3 Electron probe micro analysis (EPMA)

Electron probe micro analysis (EPMA) was used to investigate both Al and Si phases and intermetallic phases. The Al-rich phase was single phase with generally no evidence of any Si phase within the expected eutectic, or fine scale precipitates. Typically the Al-rich phase contained only approximately 0.27wt% Si in solid solution compared with a maximum solid solubility of 0.05wt% at 300°C (Murray 1984). Assuming all the Si was in solid-solution, then the relatively high concentration may be attributed to the non-equilibrium solidification conditions and possible Si interaction volume effects whereby the incident electron beam stimulates emission from adjacent or underlying regions of Si phase. The primary Si network contained only trace amounts of other elements such as Al, Zr and Cu, either within solid-solution in the Si phase or as surface contamination. A variety of intermetallic phases, presumably resulting from impurity elements, were interspersed through the Al-rich network, with no intermetallic phases in the primary Si network. Bulk elemental analysis showed the most common impurity elements to be Zr at~0.04wt% and Fe at ~0.3wt%, as shown in Table 4.1. Figures 4.16(a) and 4.16(b) show two examples of Si-Ti-

Zr intermetallic particles and 4.13(c) shows a corner of a schematic Si-Ti-Zr ternary plot showing the measured composition of particles of this type. As shown in 4.16(a) and 4.16(b), the morphology of these phases was typically blocky rods or plates of 10 – 15μm length. Superimposed yellow arrows show the direction of crack propagation associated with these particles, with cracks typically deflected by or terminating in the more ductile Al phase. Figure 4.16(c) shows the approximate composition was $Si_{13}Zr_4Ti_3$ and no reference to particles of this composition were found in the published literature. However Si_2Zr (Zatorska 2002) and Si_2Ti (Tanaka 2001) have been previously reported, and it is probable that the $Si_{13}Zr_4Ti_3$ intermetallic was a transition metal silicide with Ti substituting for Zr.

Al-Fe-Si intermetallics were observed in a variety of stoichiometries and morphologies, examples of which are shown in Figures 4.17(a) and 4.17(b). The most numerous Fe-containing intermetallic particles were acicular needles, typically ~10μm long and ~1μm wide as shown in 4.17(a). Their stoichiometry varied considerably and the small cross section made quantitative analysis difficult. EPMA point analysis suggested an average stoichiometry of $Al_7Fe_2Si_3$, possibly indicating $Al_{2.7}FeSi_{2.3}$ or a variant thereof (Gueneau 1995) or the cubic form of α (Al_8Fe_2Si) in script or rod morphology typical of 1xxx and 6xxx series alloys (Allen 1998). A plate morphology Al-Fe-Si particle is shown in Figure 4.17(b), typically ~5-10μm in diameter and distributed throughout the Al network. Analysis suggested a stoichiometry of Al_5FeSi possibly indicating $Al_{4.5}FeSi$

(Hansen 1998) or faceted plate morphology β-phase Al_5FeSi observed in 6xxx series Al alloys (Allen 1998).

It was noticed that in many cases intermetallics would agglomerate together forming complex shapes and morphologies as shown in Figures 4.18(a) and 4.18(b). Typically plates of Al_2Cu were associated with acicular rods of $Si_{13}Zr_4Ti_3$ as shown in Figure 4.18(a). Small, rounded Cu containing particles of ~1μm diameter and of approximate stoichiometry Al_7FeCu_2 (Brown 1956) are shown in Figure 4.18(b), associated with acicular rods of measured composition close to Al_3FeSi and possibly suggesting Al_2FeSi (German 1989).

The small size of many of the intermetallic particles made quantitative analysis difficult because of beam interaction volume effects. Stoichiometries measured by EPMA were therefore only approximate and further work is required to gain a fuller understanding of the intermetallic particles in CE7. X-ray diffraction (XRD) investigations of intermetallic particles was explored but the low volume fraction made it impossible to discern intermetallic peaks within the background scatter. Wet chemical methods for intermetallic phase extraction for subsequent XRD were also investigated but reagents for the dissolution of primary Si without dissolution of the intermetallics were not discovered.

4.3.4 Energy dispersive spectroscopy (EPMA / WDS) mapping

EPMA based elemental mapping of Sandvik-Osprey CE7 microstructure gave an indication of elements associated with specific phase morphologies. Figure

4.19(a) shows a typical backscattered electron image of Sandvik-Osprey HIPed CE7 microstructure with corresponding elemental concentration maps for Al, Si, Zr, Ti and Fe shown in 4.19(b-f) respectively showing the presence of phases described in section 4.3.3. Figure 4.19(b) shows the Al elemental intensity map showing the Al network, co-continuous with respect to the primary Si phase shown in 4.19(c). Figure 4.19(d) and (e) shows the elemental concentration map for Zr and Ti respectively showing two plate morphology $Si_{13}Zr_4Ti_3$ phases. Figure 4.19(e) shows the Fe concentration map showing acicular $Al_7Fe_2Si_3$ and Al_3FeSi phases.

4.3.5 Electron backscatter diffraction (EBSD)

EBSD was used to examine Osprey manufactured binary CE7 in known billet orientations. Samples cut perpendicular to the axis of rotation of the billet were designated Y and samples parallel to the axis of rotation were designated X, as shown schematically in Figures 4.20(a) and 4.20(b). A typical Y-axis EBSD orientation map is shown in Figure 4.20(c), showing an apparently randomly orientated polygonal grain structure consisting predominantly of equiaxed grains of ~30μm, with some larger grains and twinning in many grains. The orientation key corresponding to Figure 4.20(c) is shown in Figure 4.20(d).

Grain boundaries were superimposed on Figure 4.20(c) with grain misorientations designated as, high (5-15°) and high (>15°) angle boundaries delineated in black and dark blue respectively and grain sub-structure (<5°) delineated in pale blue. High angle grain boundaries were the most numerous,

with some substructure indicated in <111> oriented (blue) grains as shown in Figure 4.20(c). The many Si twin boundaries (59-61°) were indicated in red. Figure 4.20(e) shows the inverse pole figure (IPF) corresponding to 4.20(c), suggesting a predominantly random grain orientation with some clustering around the <111> pole.

Concurrently collected EDS data was used to partition the orientation map in Figure 4.20(c) into Al-rich and Si rich components. Figure 4.21(a) shows the same orientation map for Si as 4.20(c) but with the Al-rich phase removed. The random orientation of the Si grains was more evident as shown by the IPF in Figure 4.21(b) and there was a range of grain sizes from <3 to ~60μm and number average grain size of 4.0μm (including twin boundaries as high angle boundaries). Figure 4.21(c) shows the same orientation map but for the Al phase with the primary Si phase removed. Only two large Al grains (one shown in blue and one yellow) were revealed, delineated by high angle grain boundaries and continuously inter-penetrated by the Si matrix. Figure 4.21(d) is the corresponding IPF indicating that these grains were in different orientations, approximating to <111> and <001> and that there were no other significant Al phase orientations. Further EBSD investigation of the Al phase showed that typically the Al-rich phase consisted of large >300μm grains inter-penetrated by the Si matrix.

Examination of a different Y-axis sample showed that in some cases the analysis area consisted of ostensibly of single Al grains >300μm as shown in Figure 4.22(a). Figures 4.22(b) and 4.22(c) show the orientation key and IPF

corresponding to 4.22(a) and is consistent with 4.21(d) confirming a dominant Al orientation in the <111> direction. However as shown in Figure 4.22(a) and in many cases these large, predominantly single grains of Al were interspersed with relatively small regions of fine, equiaxed Al an example of which is shown in Figure 4.22(d) with the corresponding orientation key shown in 4.22(b). These regions showed a much more random arrangement of Al grains and were suggested to have experienced different nucleation and growth conditions associated with a loss of connectivity to the inter-penetrating residual Al-rich liquid in the final stages of solidification this is further discussed in section 7.2.4.

The data set shown in Figure 4.22(a) was further investigated for texture by highlighting regions of Al phase mis-orientation of >7° in a unique colour as shown in Figure 4.23(a). The large, apparently single grain of Al shown in Figure 4.22(a) was revealed to comprise five sub-grains delineated by low (>7°) grain boundaries. The corresponding 001 pole shown in 4.22(b) shows the scatter orientation around the apparent single Al grain. Using a mis-orientation threshold (a software feature allowing areas of low angle sub-structure to be highlighted and delineated) Figure 4.23(c), shows the five sub-grains more clearly where these with low angle grain boundaries are superimposed in white and where, a schematic representation of each cubic crystal orientation is shown around the periphery of 4.23(c). Figure 4.23(d) shows the corresponding pole figure with the colours of each data point consistent with the false colouring of the five sub-grains. Overall, the EBSD investigation of the Al-rich phase suggested that it grows primarily as large, columnar grains in the Y-axis of the

billet and inter-penetrate the pre-existing primary Si network and as illustrated schematically in Figure 4.23(e).

4.3.6 Si grain size

It was possible only to obtain Si grain size measurements by EBSD since chemical etches for Si-Si grain boundaries proved unsuccessful as described in Section 3.2.2.

Initial analysis at a small probe step size of 0.3μm, enabled a minimum grain diameter resolution of 0.7μm as described in Section 3.2.6 and indicated in Figure 4.24(a). Grain size measurements were made both including and excluding twin boundaries as high angle grain boundaries, with the grain size distribution plotted in Figure 4.24(a). Excluding twin boundaries the analysis site contained 435 grains with a mean grain size of 5.5μm, if twins are included as high angle grain boundaries the dataset consisted of 833 grains with a mean grain size of 4.0μm. This showed that on average almost all grains contain one twin plane, although in practice some grains were twinned multiple times as indicated in Figure 4.21(a). Analysis of the data showed a modal distribution with a large population of fine equiaxed grains, with around 48% of grains being <3.5μm diameter. Repeating the grain size measurement on a larger analysis site, using a 1.5μm step size encompassed a larger number of grains and with twin boundaries included as high angle boundaries yielded a similar mean Si grain size of 4.1μm. These data are summarised in Figure 4.24(b). The curves in Figure 4.24(a) for the 0.3μ and 1.5μm step sizes differ due to the different bin sizes used when collating and plotting the data. These trials demonstrated that

if twin boundaries were included as high angle grain boundaries the process was robust, showing that analysing more grains with a coarse step size gave the same mean Si grain size as a smaller analysis area with fewer grains. For all subsequent EBSD grain size analysis a step size of 1.5μm was used. This was done because the data produced at a coarse, 1.5μm step size had been validated by the 0.3μm step size experiment and it enabled the analysis area to be maximised in order to encompass as many large Al grains as possible. In all subsequent analysis twins were included as high angle grain boundaries in the data interpretation.

4.3.7 Al grain size

It was not possible to obtain an Al grain size from EBSD measurements as the grain size actually exceeded the analysis area that was limited by the inclined geometry of the sample holder. As previously described, large Al grains of >300μm were typical, often with some substructure and low angle boundaries as shown in Figure 4.23(c). The larger Al grains were always inter-penetrated by the primary Si phase.

4.4 Summary

- Spray Formed Al-70Si has an interpenetrating network microstructure consisting of primary Si and divorced eutectic (essentially just Al).
- The Si phase consists of fine equiaxed grains of ~4.0μm.
- Al grains were interpenetrated by Si and were >300μm and columnar, orientated in the billet growth direction.
- The Al-rich phase contained a dispersion of intermetallic phases resulting from feedstock impurity.
- Acicular intermetallics were associated with crack initiation.
- HIPing reduced the porosity of the as sprayed billet from 2 - 4% to <0.1%.
- HIPed CE7 has a Weibull modulus of 21, a MOR of 167MPa and estimated UTS of 84MPa, these values represent an improvement over as-sprayed properties.
- Macrosegregation of Al occurs during the final stages of solidification.
- The CTE is ~$7x10^{-6}$ $°C^{-1}$for Al-30 Si and is affected by composition variations resulting from macrosegregation.
- Fracture toughness is low (<3MPa $m^{1/2}$), typical of ceramic materials.
- Thermal cycling initiates and / or propagates cracks in the Si phase resulting in an undermined Weibull modulus and MOR.

Figure 4.1(a)

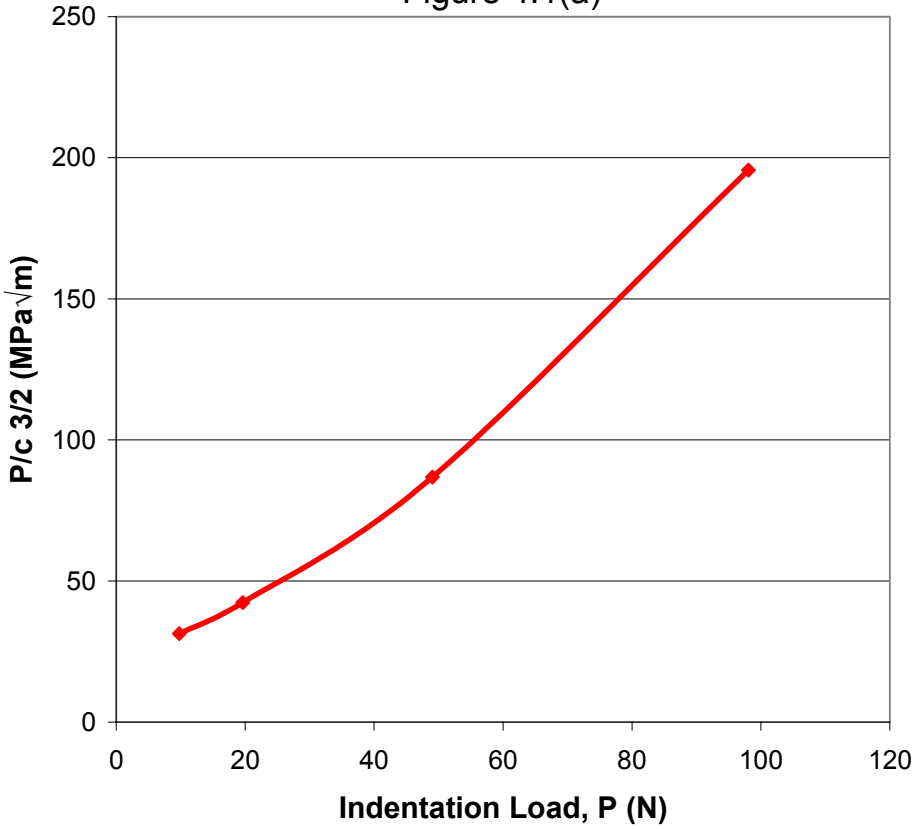

Figure 4.1(b)

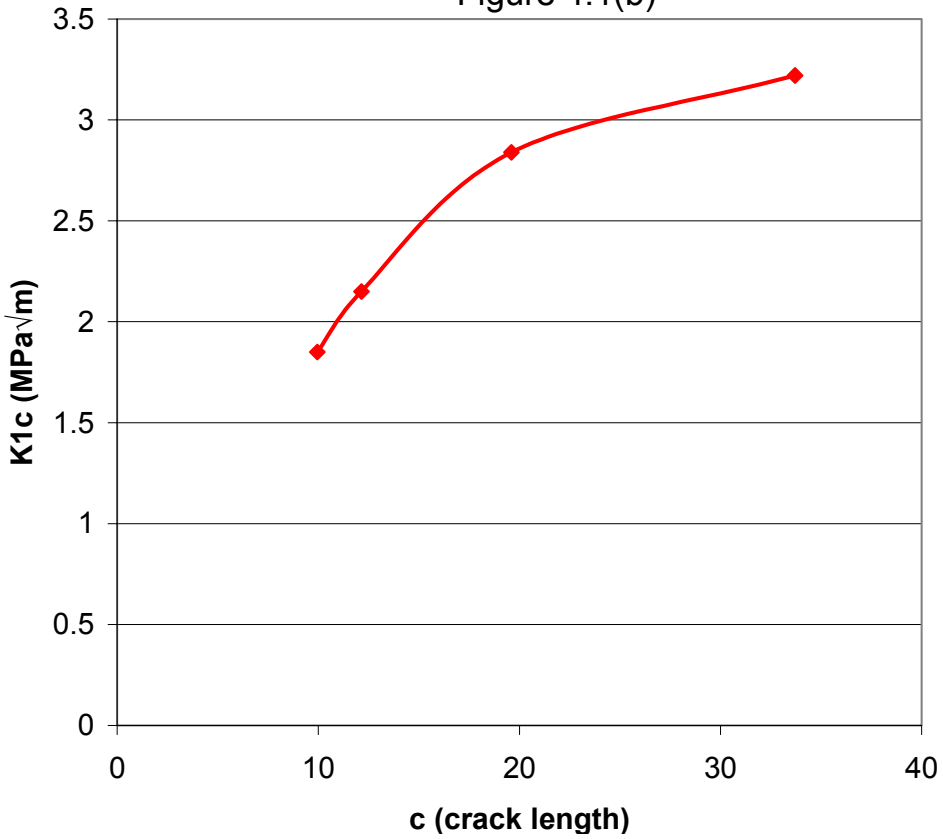

Figure 4.1(a) and 4.1(b)

Plot of (a) $P/c^{3/2}$ at various indentation loads P for Sandvik-Osprey HIPed CE7 showing $P/c^{3/2}$ is not constant with P and (b) plot of K_{1c} against crack length c for Sandvik-Osprey HIPed CE7, showing R-curve behaviour.

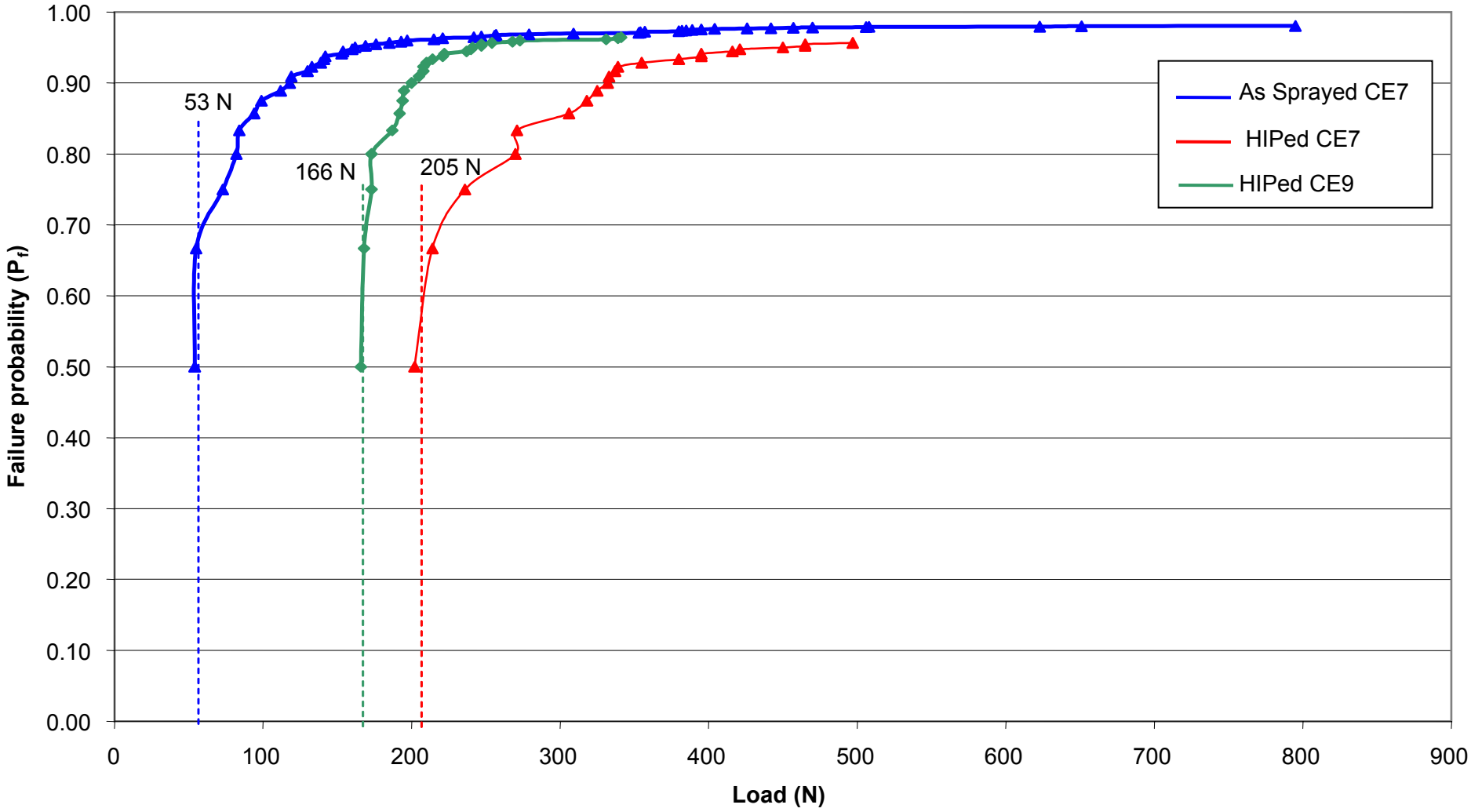

Figure 4.2

Hertzian indentation of Sandvik-Osprey CE7 in the as-sprayed and HIPed condition and HIPed CE9 . Pseudo-Weibull plot of probability of failure (P_f) versus load to failure (N), with extrapolation to determine P_{min}

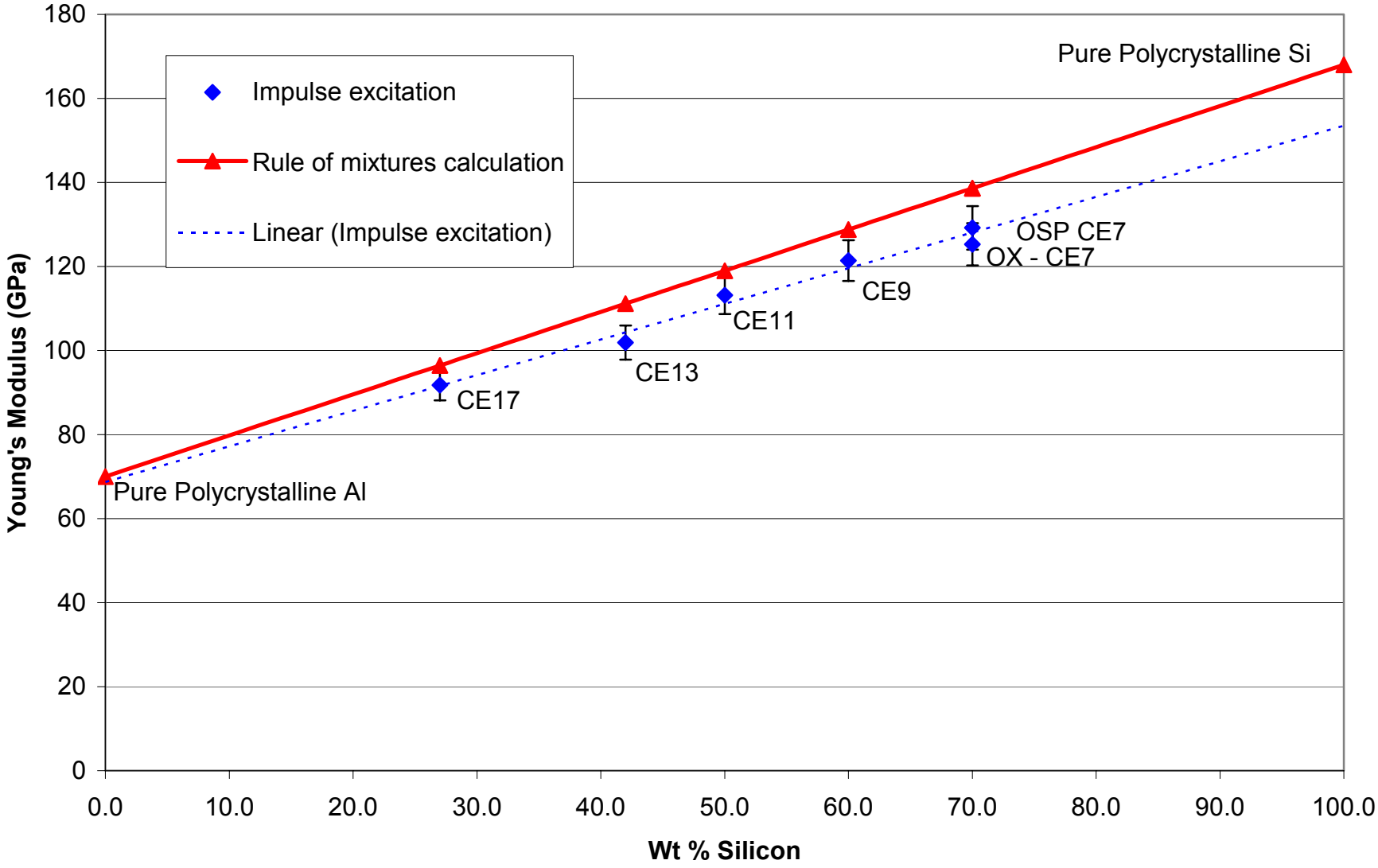

Figure 4.3(a)

Linear fit to Young's modulus determined by impulse excitation as a function of Si content in Sandvik-Osprey CE alloys. Data are compared to a 'rule of mixtures' approach based on literature data for pure, polycrystalline Al and Si.

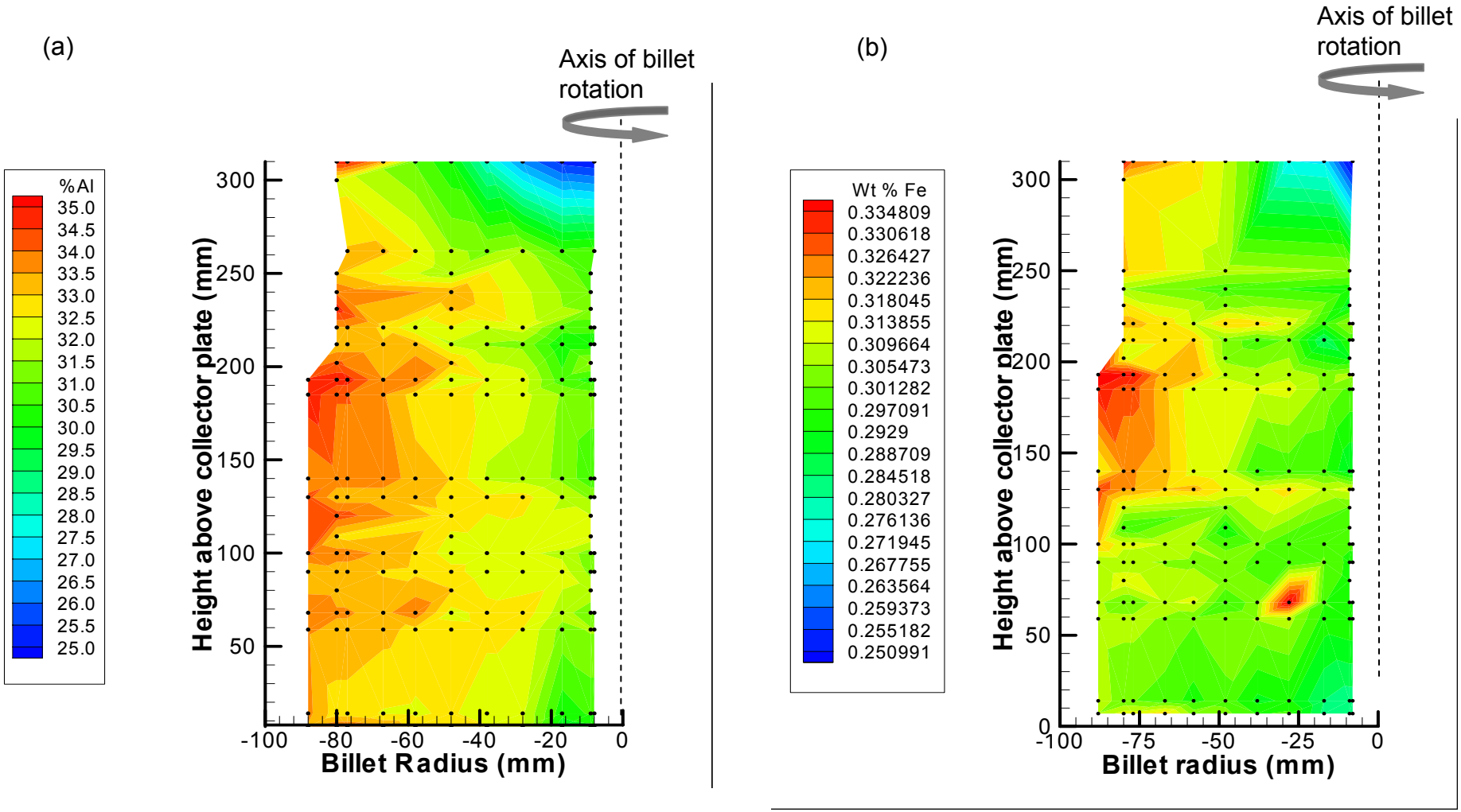

Figure 4.4(a) and 4.4(b)

Optical emission spectroscopy (OES) contour map of (a) Al and (b) Fe concentration in spray formed and HIPed Sandvik-Osprey CE7.

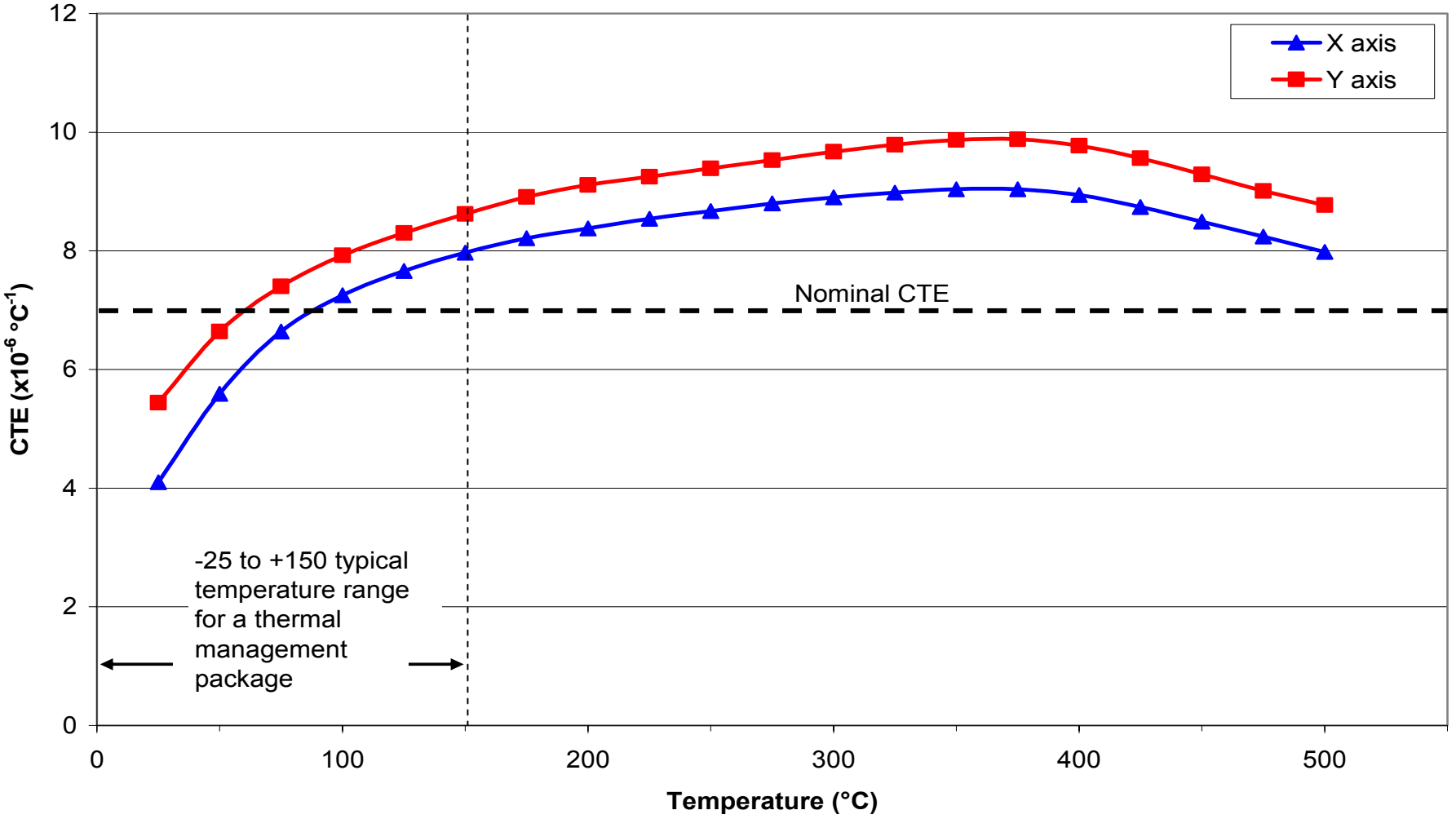

Figure 4.5

Coefficient of thermal expansion (CTE) for Sandvik-Osprey CE7 from samples cut in the billet radial (X) and axial (Y) directions.

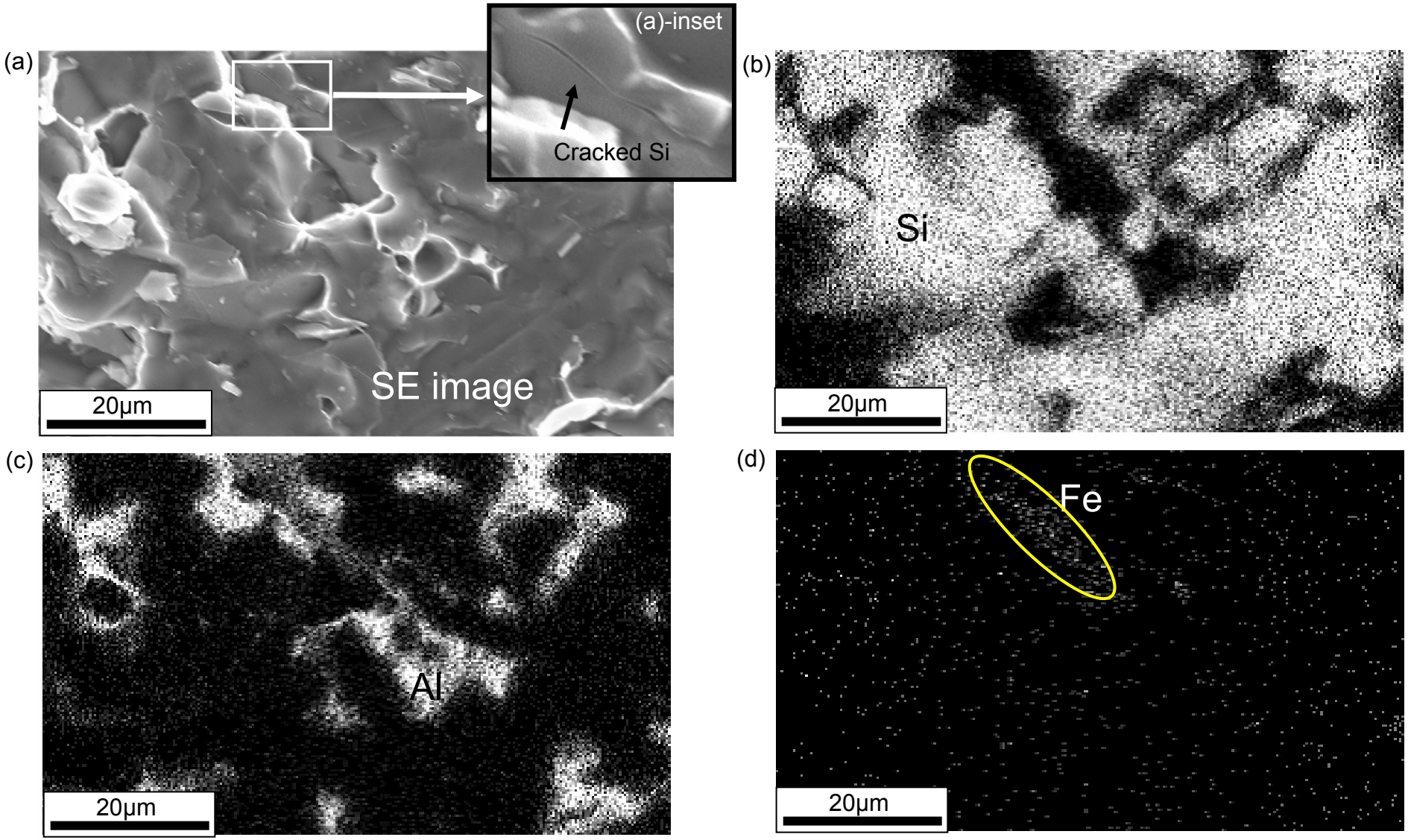

Figure 4.6(a) – 4.6(d)

(a) SEM secondary electron image of Sandvik-Osprey HIPed CE7 bend test specimen fracture surface. (a)-inset, SE image showing cracked Al-Fe-Si intermetallic phase, with corresponding EDS maps for (b) Si, (c) Al and (d) Fe.

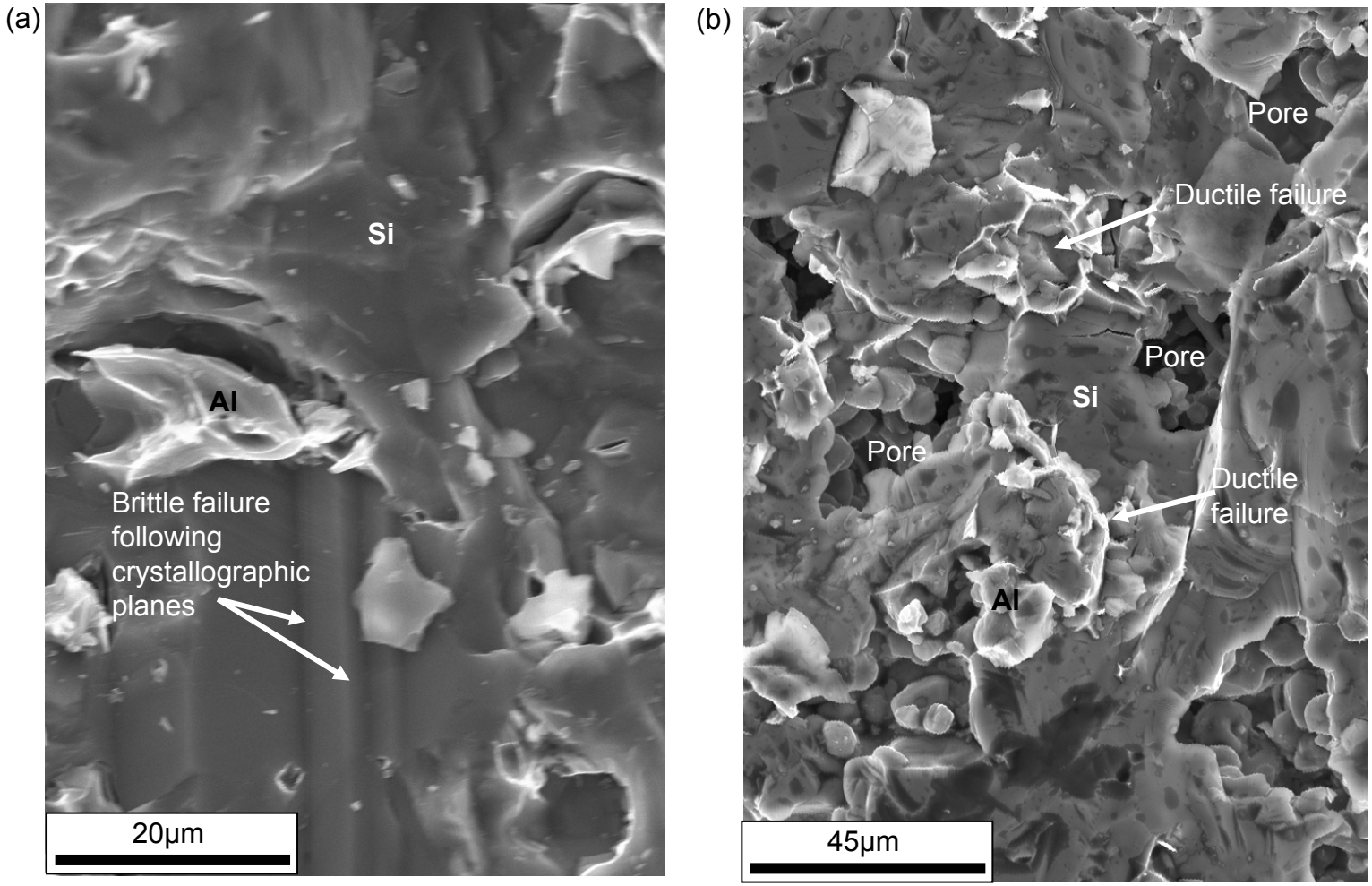

Figure 4.7(a) and 4.7(b)

Sandvik-Osprey as-sprayed CE7 bend test specimen fracture surface SEM secondary electron images (a) with brittle fracture following crystallographic planes and (b) pores in the as-sprayed material and ductile failure of Al grains

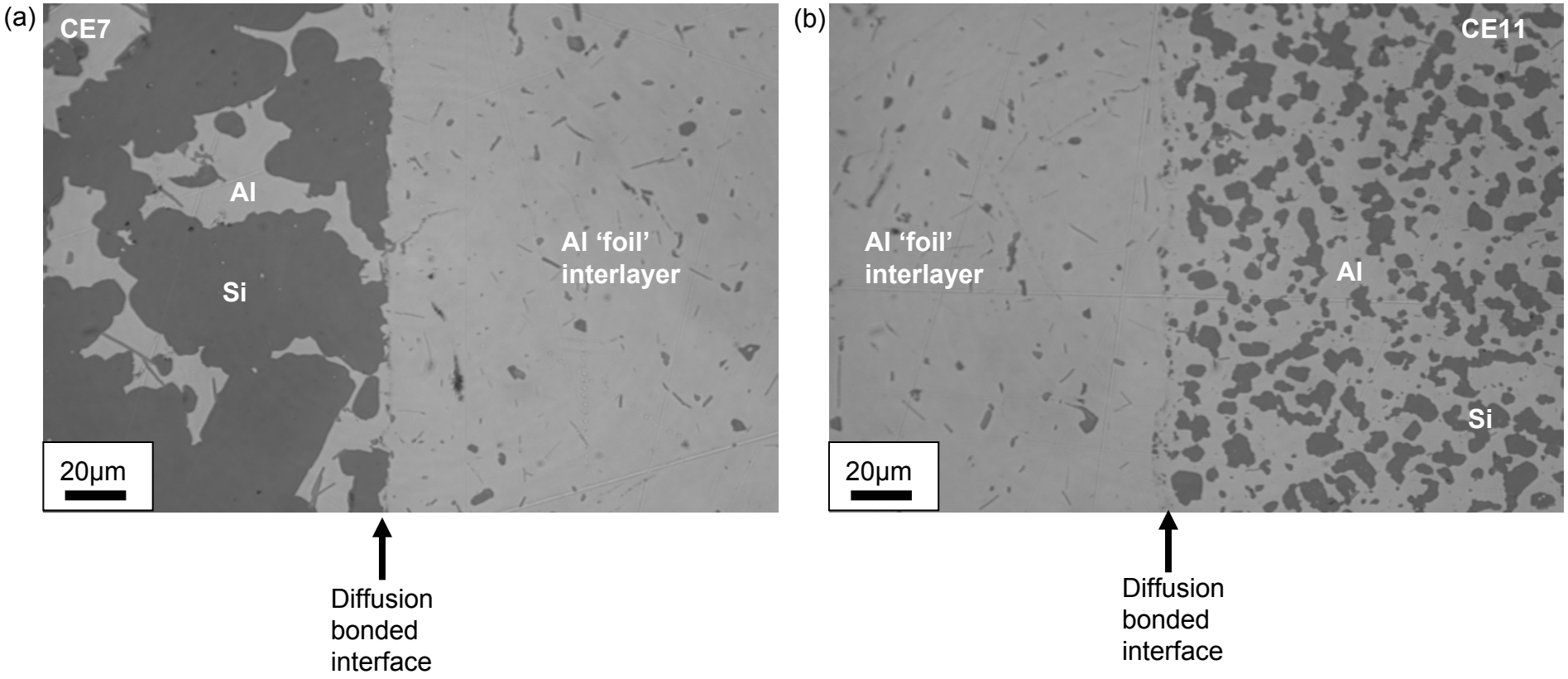

Figure 4.8(a) and 4.8(b)

Sandvik-Osprey CE7-CE11 diffusion bonded laminate with Al 'foil' interlayer. (a) CE7-foil interface, (b) CE11-foil interface. Note no evidence of cracking at the interface of either material.

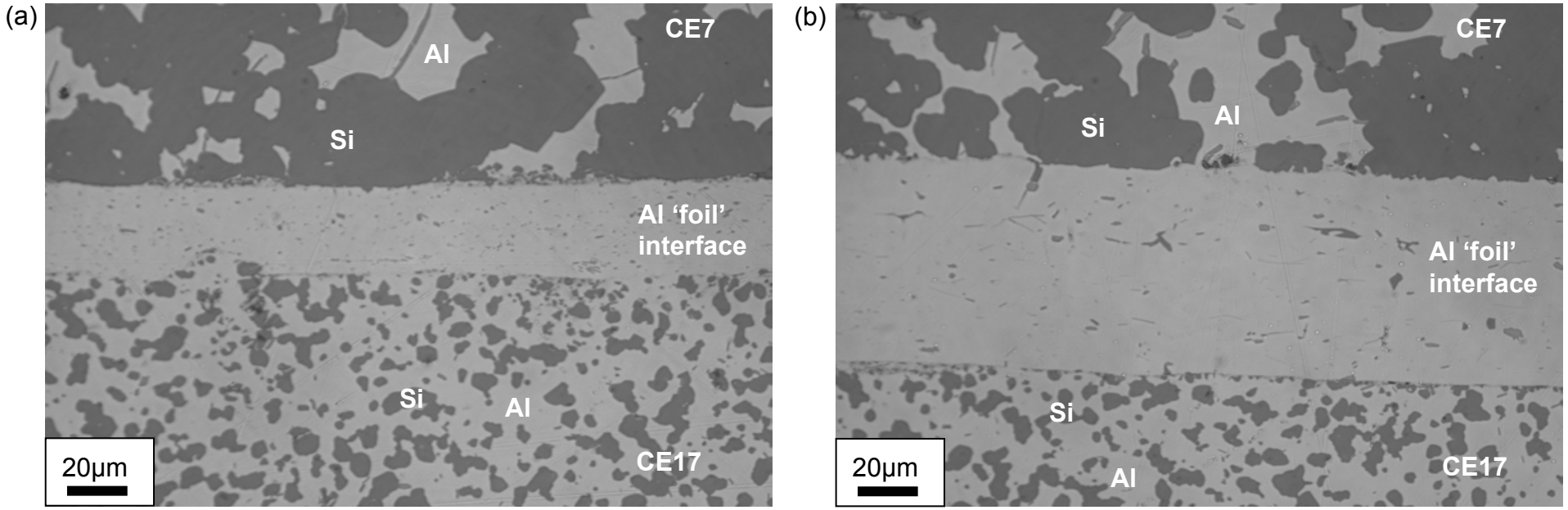

Figure 4.9(a) and 4.9(b)

Sandvik-Osprey CE7-CE17 diffusion bonded laminate with Al 'foil' interlayer. (a) CE7-CE17 interface (25μm interlayer), (b) CE17-CE17 interface (60μm interlayer). Note no evidence of cracking at the interface of either material.

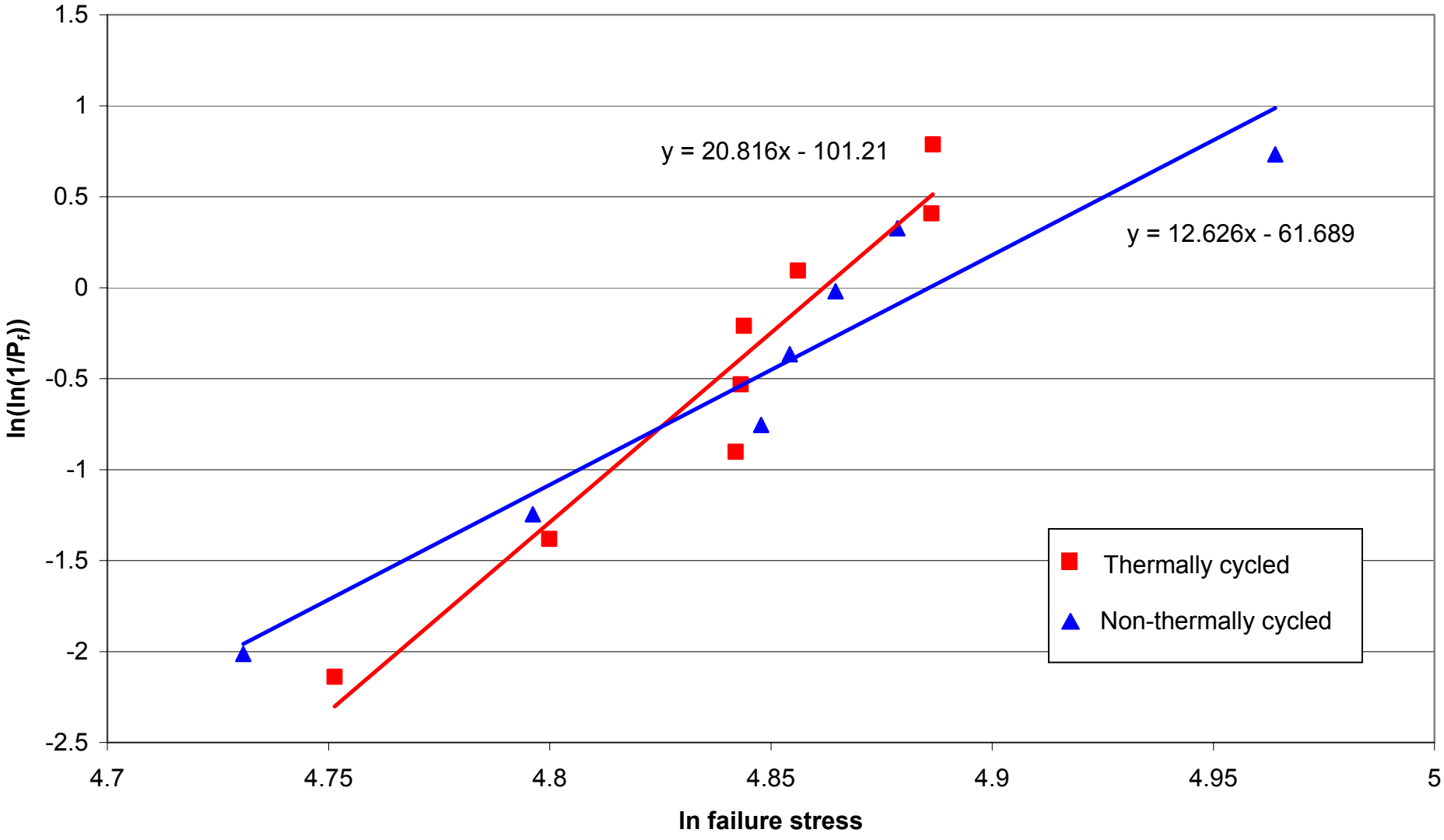

Figure 4.10

Weibull modulus plot of bend test data for as-sprayed Sandvik-Osprey CE7 before and after thermal cycling

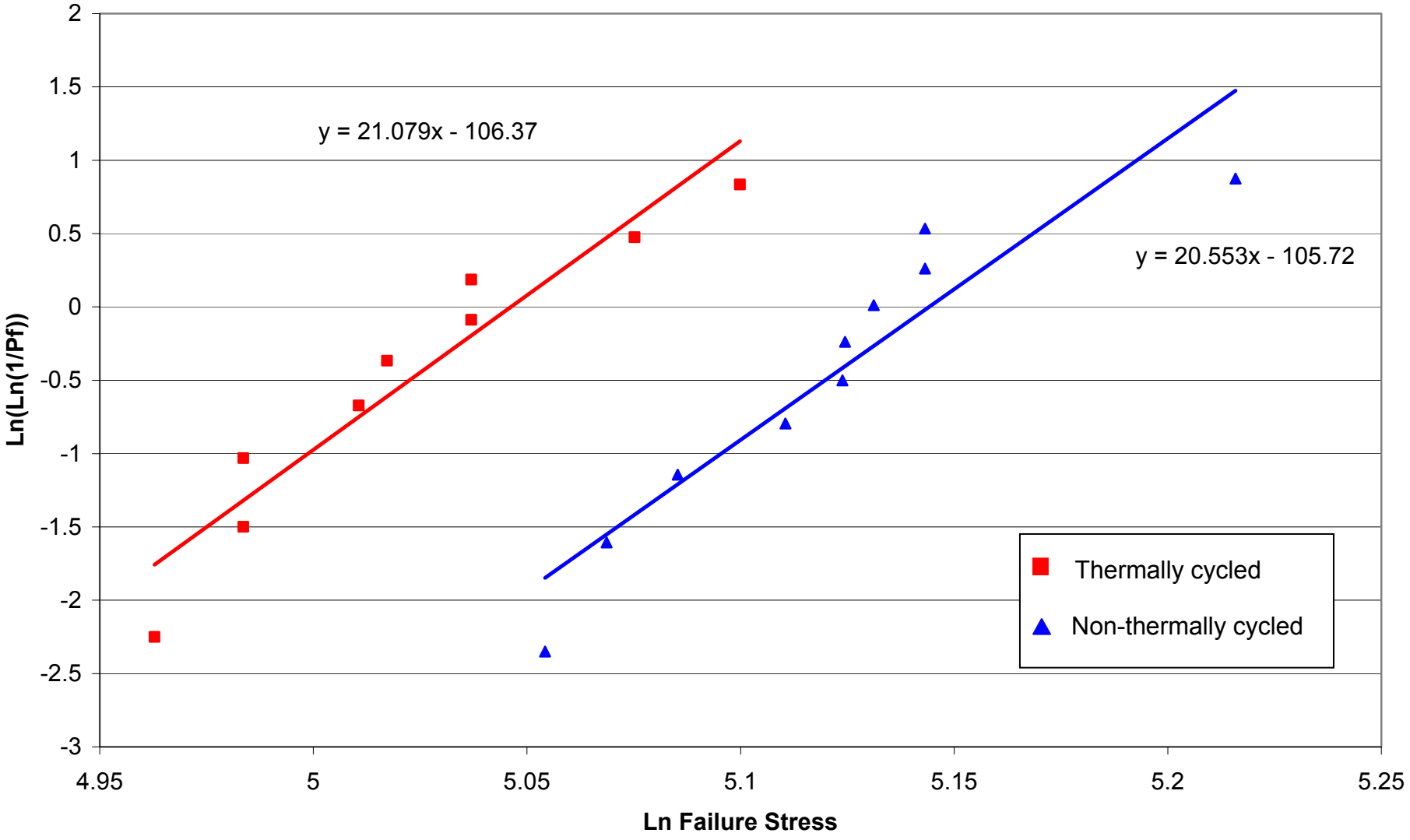

Figure 4.11

Weibull modulus plot of bend test data for HIPed Sandvik-Osprey CE7 before and after thermal cycling

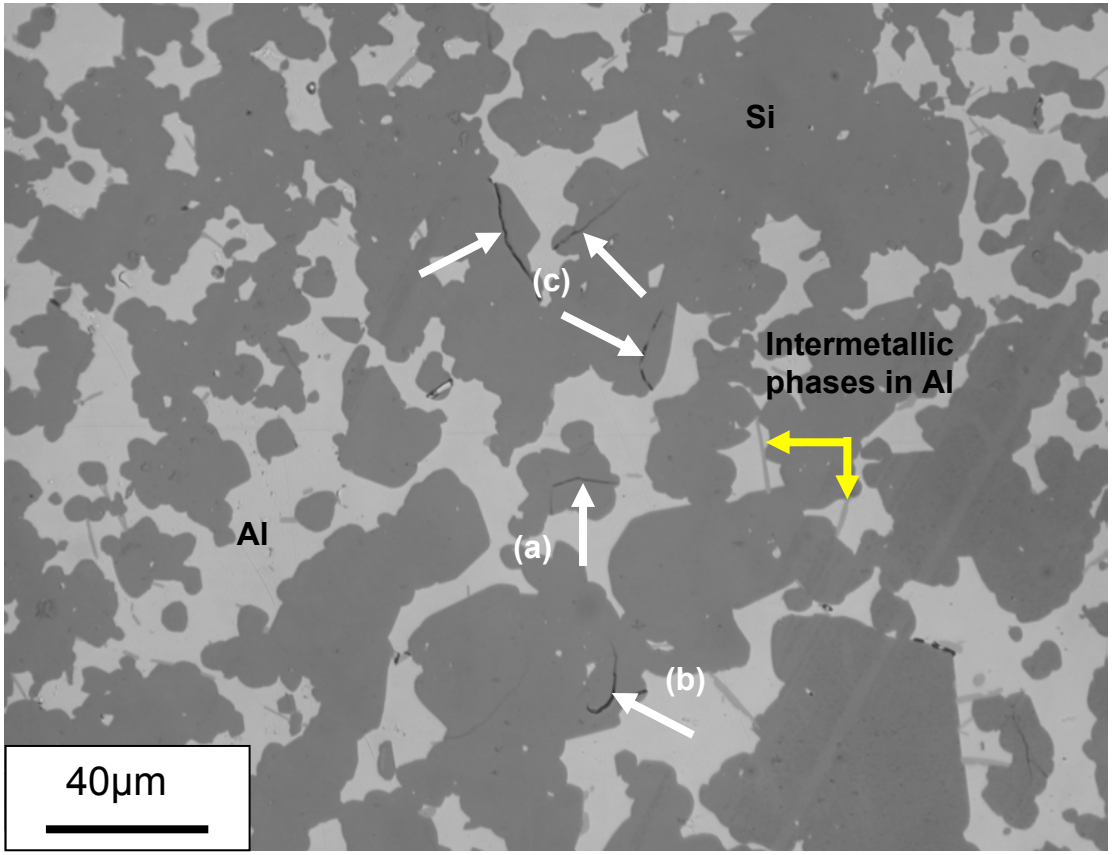

Figure 4.12

Cracks in the Si phase of Sandvik-Osprey CE7 induced by thermal cycling. Cracks are highlighted by white arrows perpendicular to the crack direction, Si and Al phases are as indicated. (a) cracks in isolated volumes of Si surrounded by Al, (b) cracks wholly within the Si phase, (c) cracks emanating from the Al-Si interface into the Si phase

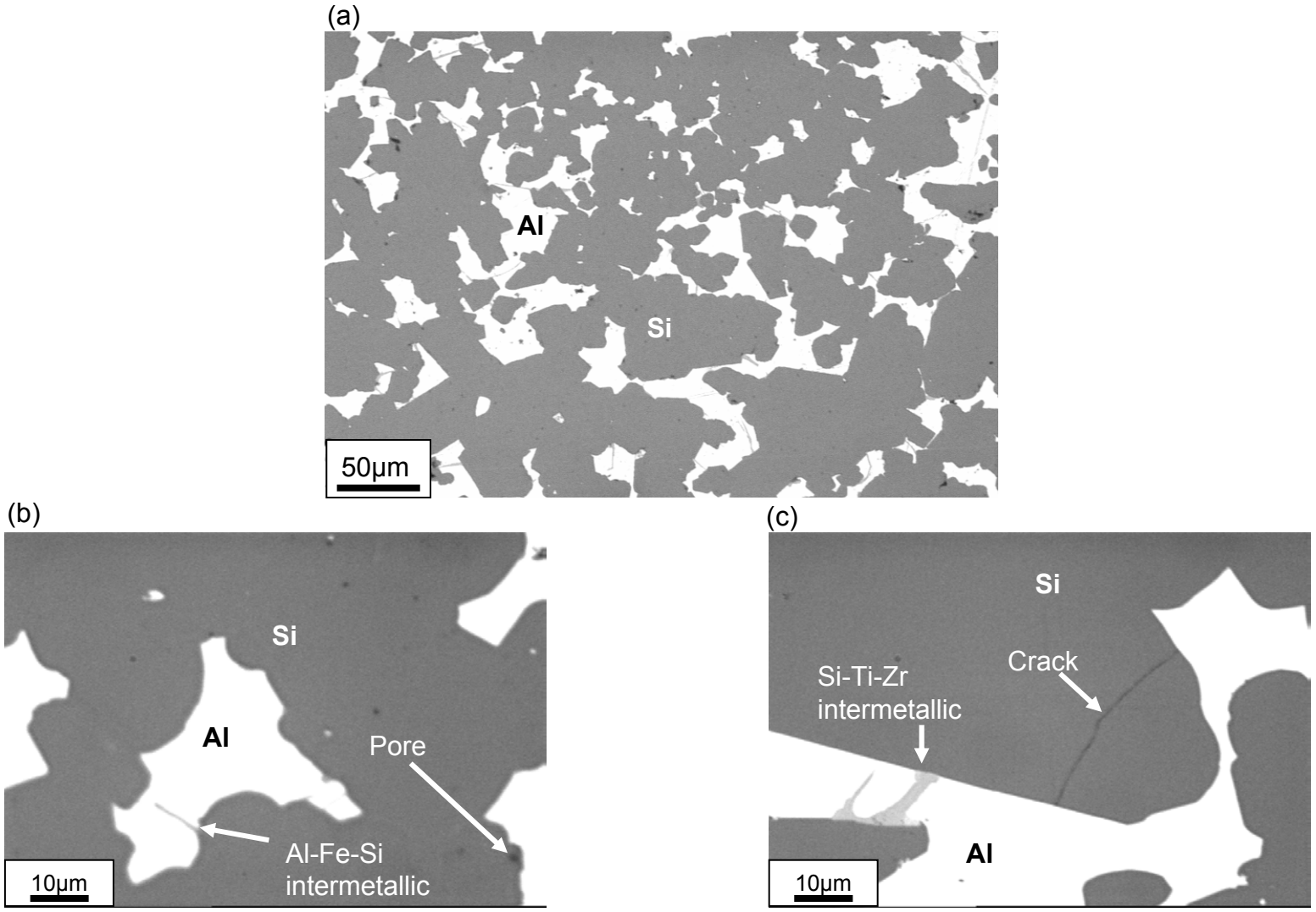

Figure 4.13(a) – 4.13(c)
Optical micrograph of Sandvik-Osprey CE7 showing (a) the co-continuous network structure of Si and Al-rich divorced eutectic, (b) Al-Fe-Si intermetallic particles and micro-pores at the Al-Si interface, and (c) Si-Ti-Zr intermetallic particles, and the cracks in a partially isolated region of Si.

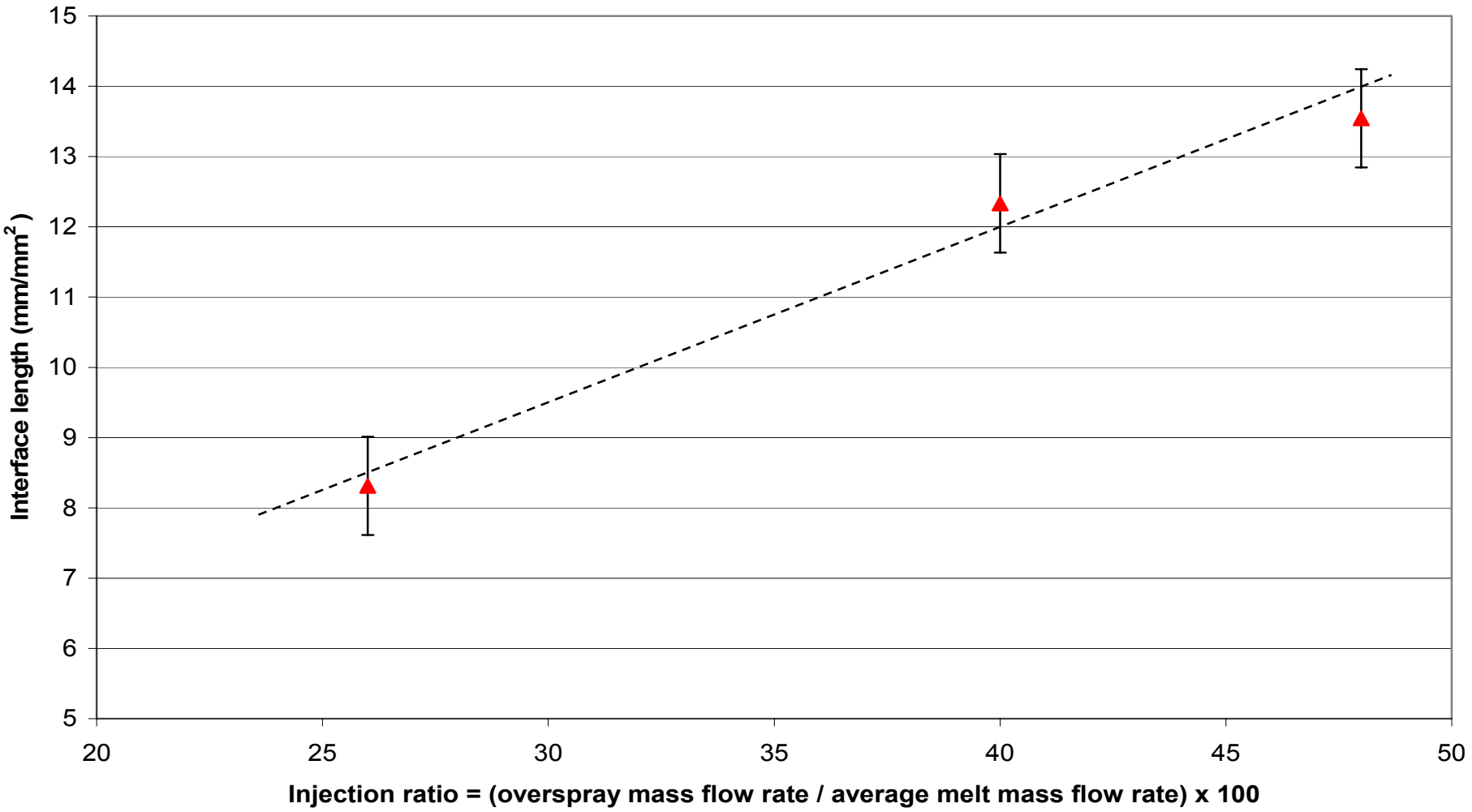

Figure 4.14

Variation in Al-Si phase interface length in HIPed Osprey CE7 as a function of particle injection ratio

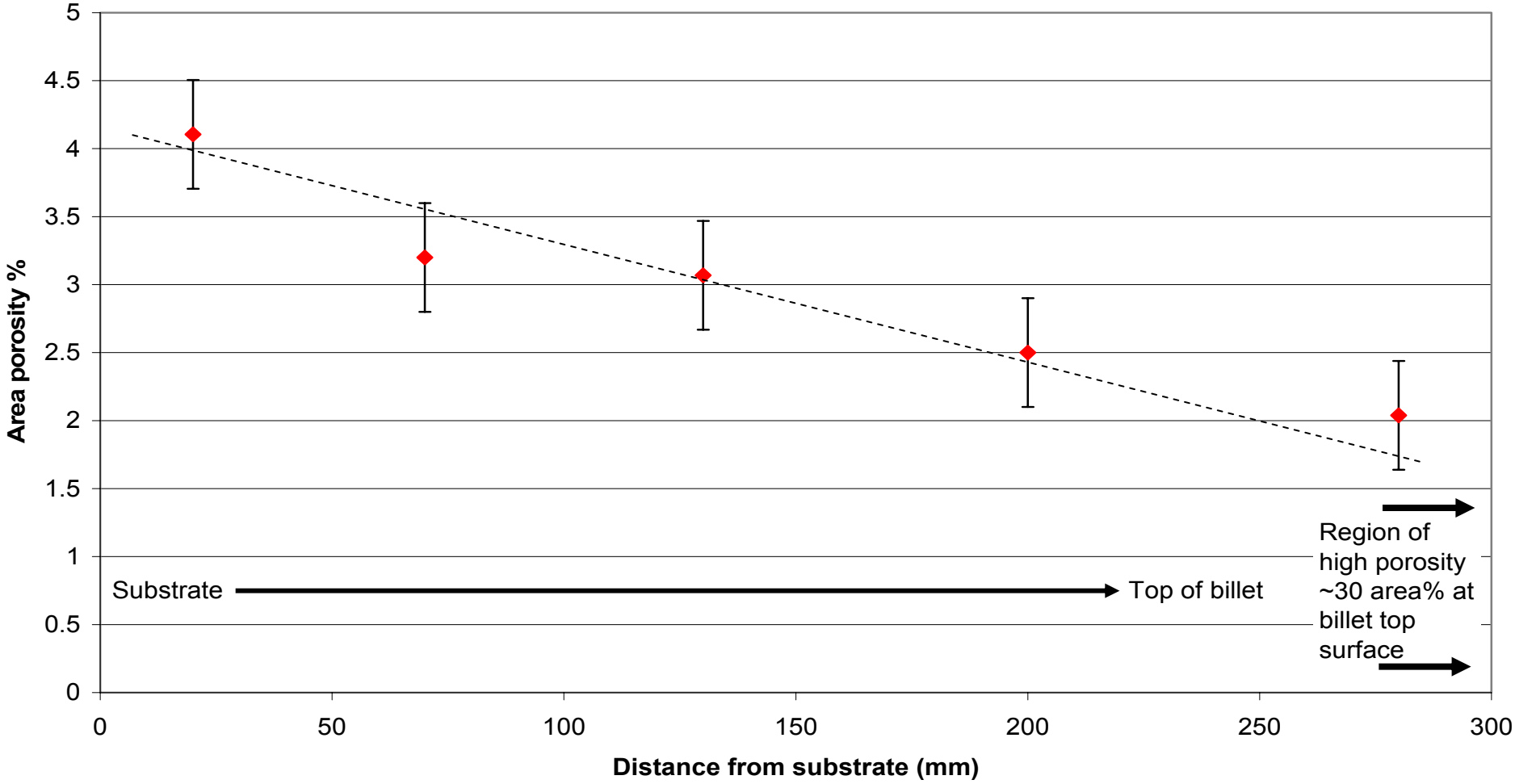

Figure 4.15

The variation in porosity along the billet length in as-sprayed Sandvik-Osprey manufactured CE7

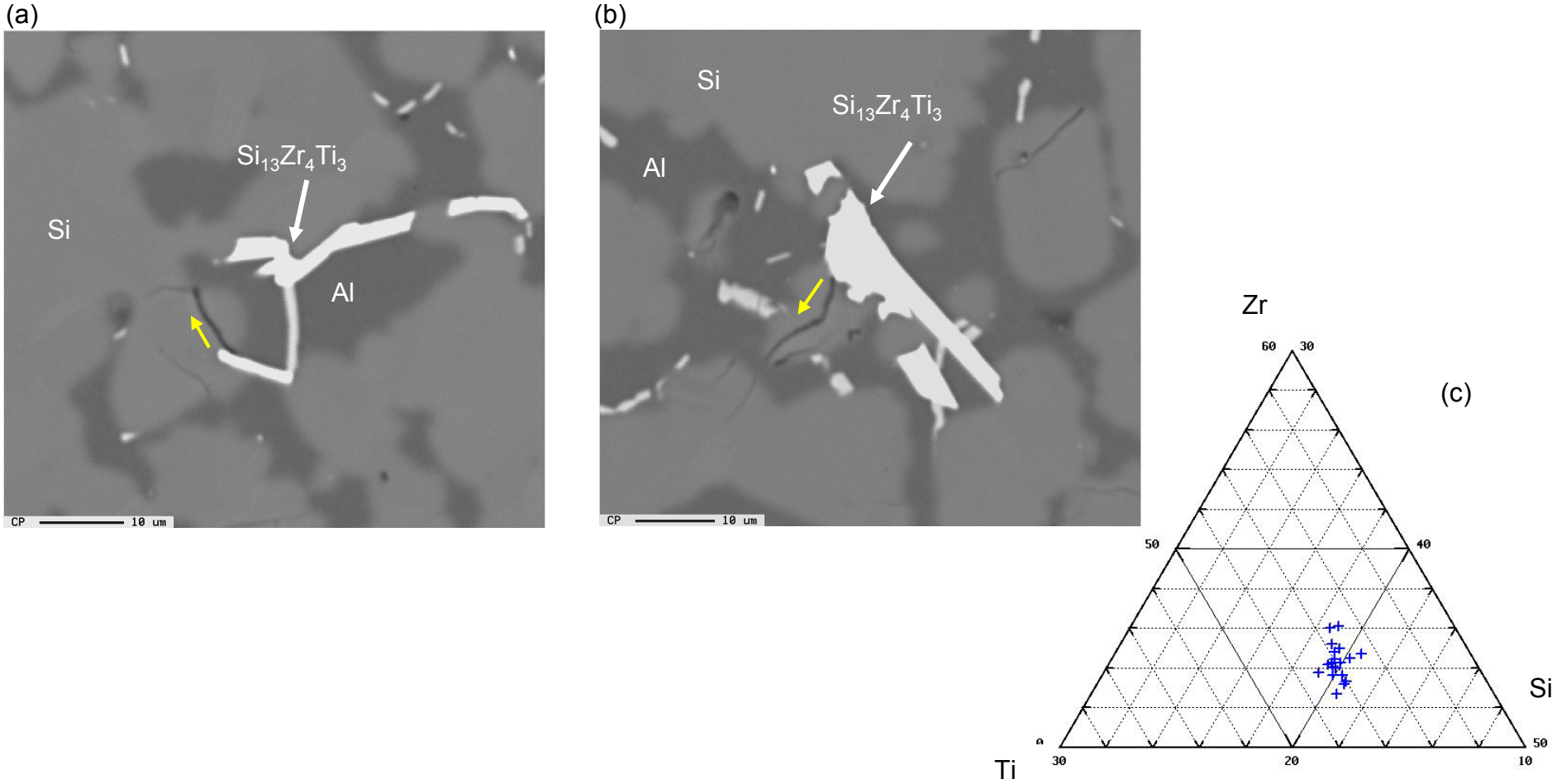

Figure 4.16(a) – 4.16(c)

(a) and (b) typical Si-Ti-Zr rich particles and (c) schematic ternary plot of wt% Si-Ti-Zr indicating particles of approximate composition $Si_{13}Zr_4Ti_3$

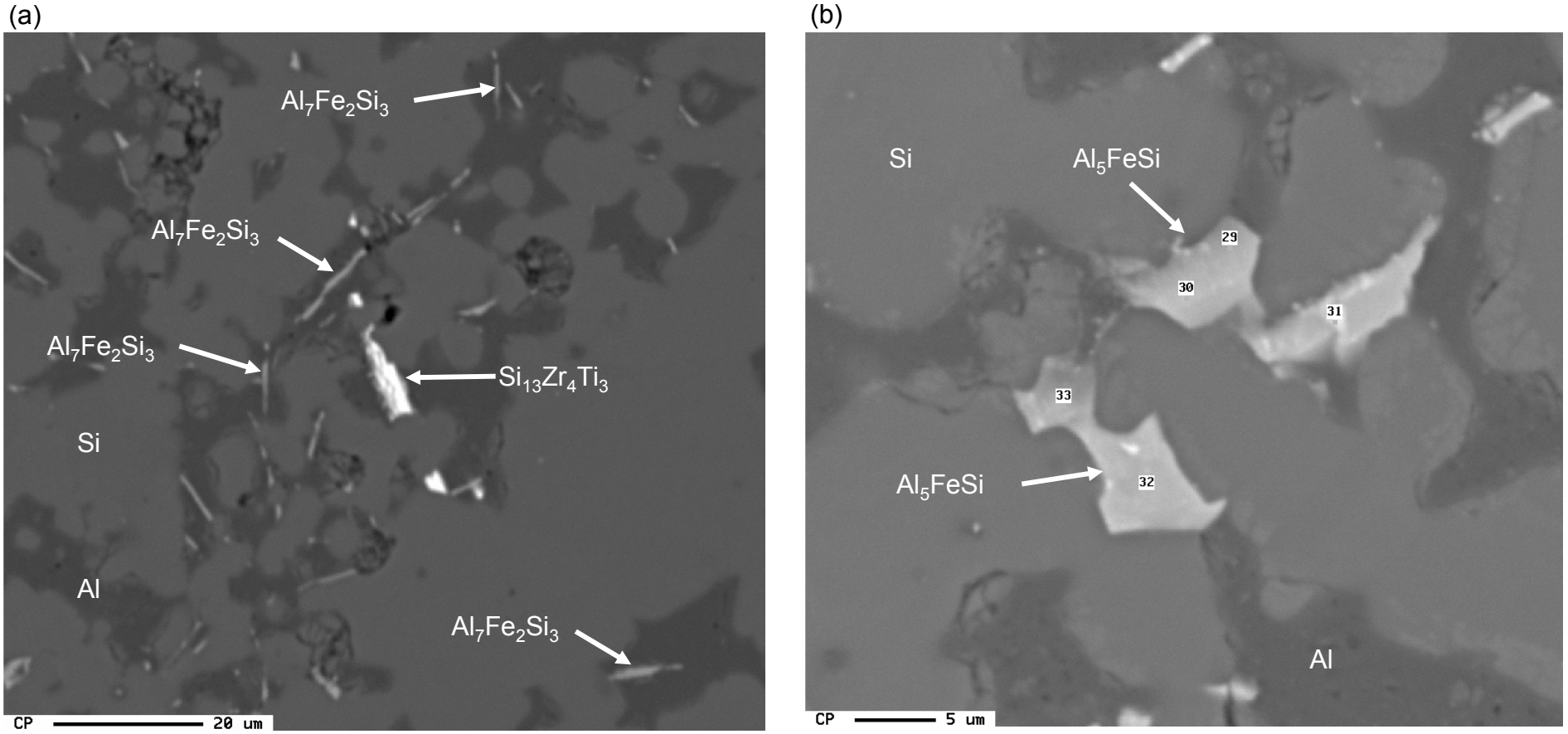

Figure 4.17(a) and 4.17(b)

Backscattered electron image of Osprey CE7 showing (a) $Al_7Fe_2Si_3$ and Al_3FeSi acicular intermetallics in the Al network, (b) Al_5FeSi plates in the Al network

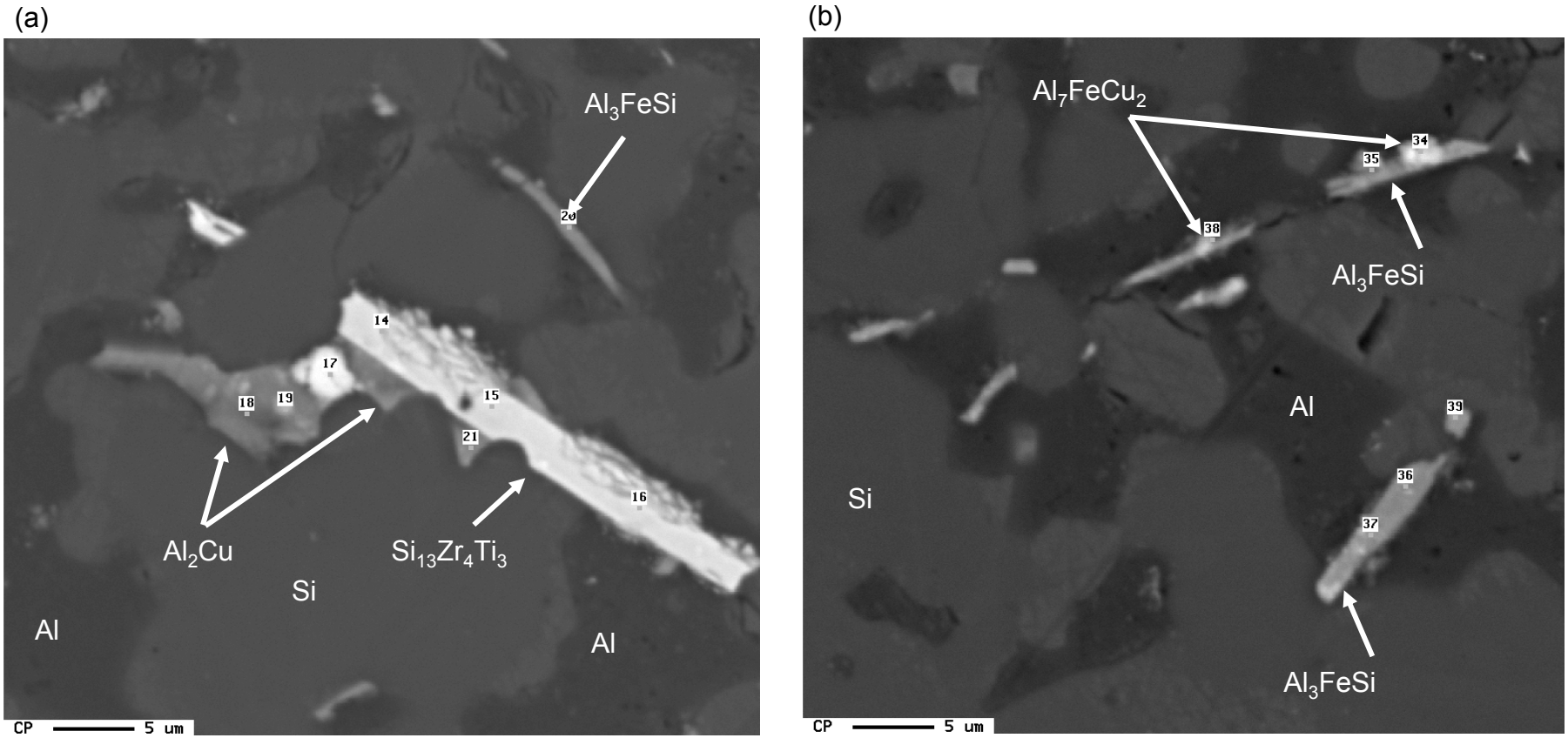

Figure 4.18(a) and 4.18(b)
Backscattered electron image of Osprey CE7 showing (a) Al_2Cu associated with $Si_{13}Zr_4Ti_3$ particles, (b) $Al_{70}Cu_8Fe$ particles associated with Al_3FeSi needles.

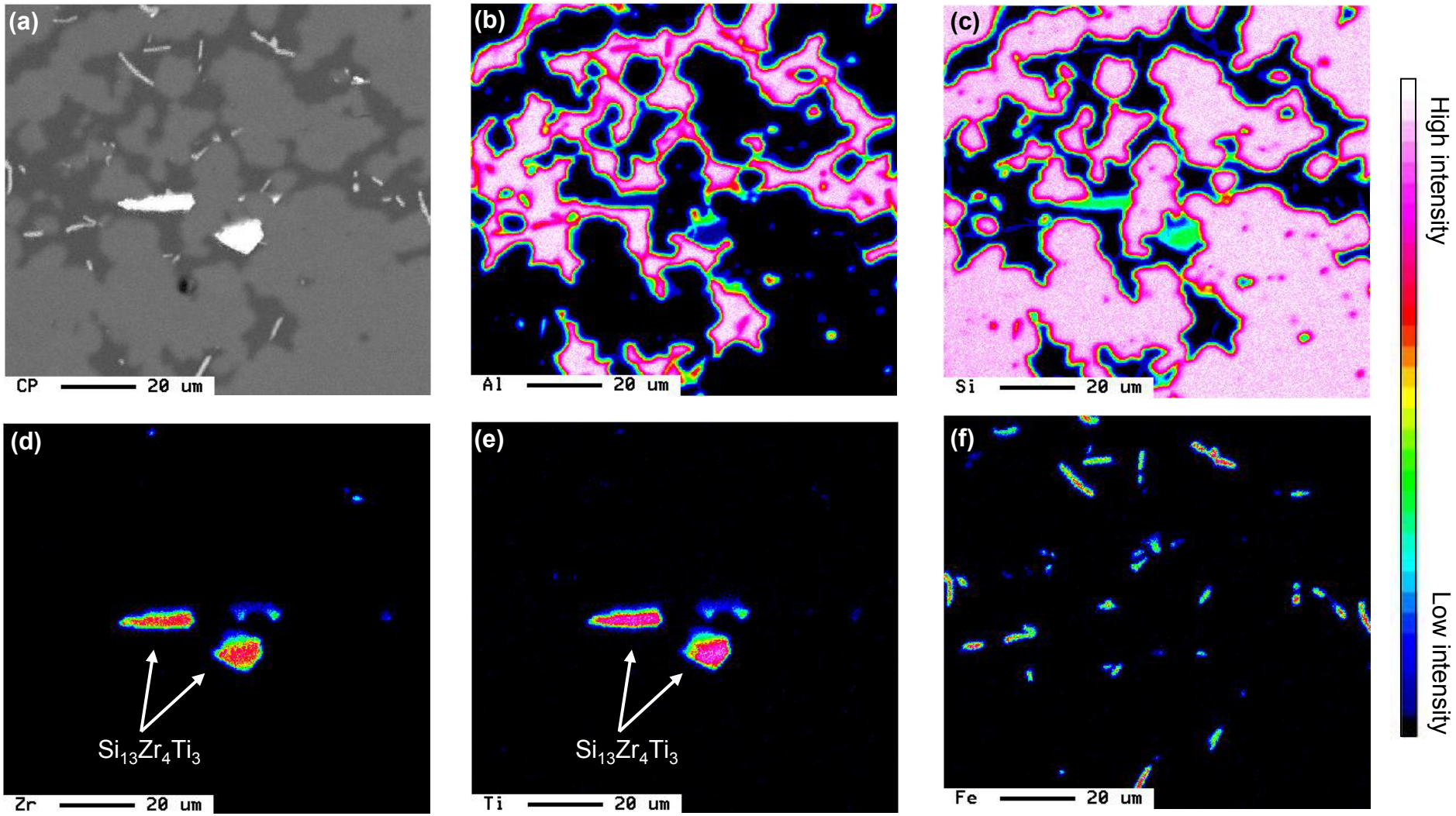

Figure 4.19(a) – 4.15(f)

EPMA elemental maps of Sandvik-Osprey HIPed CE7. (a) backscattered electron image of mapped area, (b) Al intensity map, (c) Si intensity map, (d) Zr intensity map, showing $Si_{13}Zr_4Ti_3$ phase, (e) Ti intensity map, showing $Si_{13}Zr_4Ti_3$ phase, (f) Fe intensity map note showing $Al_7Fe_2Si_3$ and Al_3FeSi phases.

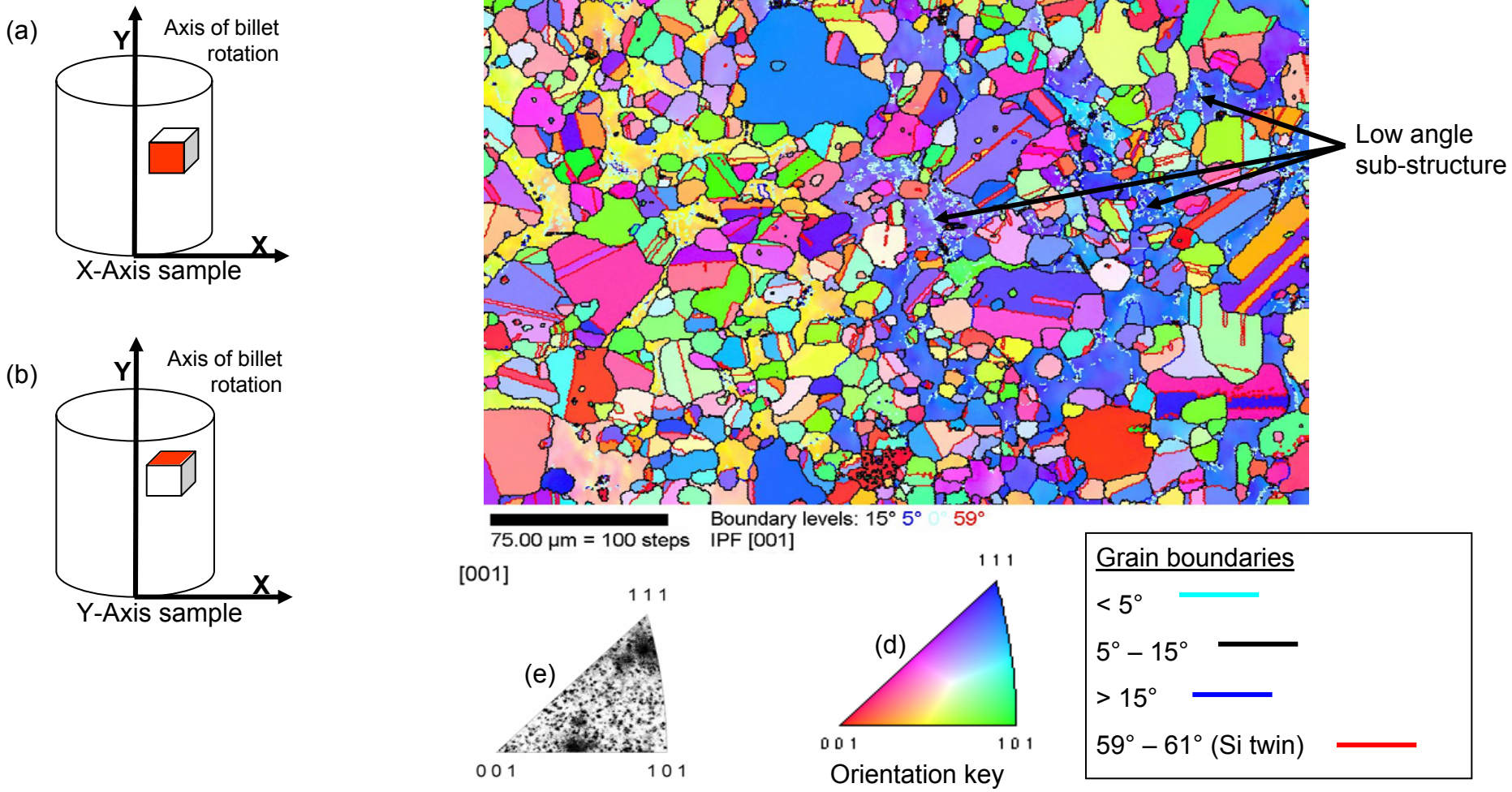

Figure 4.20(a) – 4.20(e)

Designation of (a) X-axis and (b) Y-axis sample orientation relative to macroscopic billet axis, (c) typical Y-axis EBSD orientation map for Sandvik-Osprey CE7 showing orientation of grains with high and low angle grain boundaries and twin boundaries marked, (d) orientation key corresponding to (c), (e) inverse pole figure corresponding to (c)

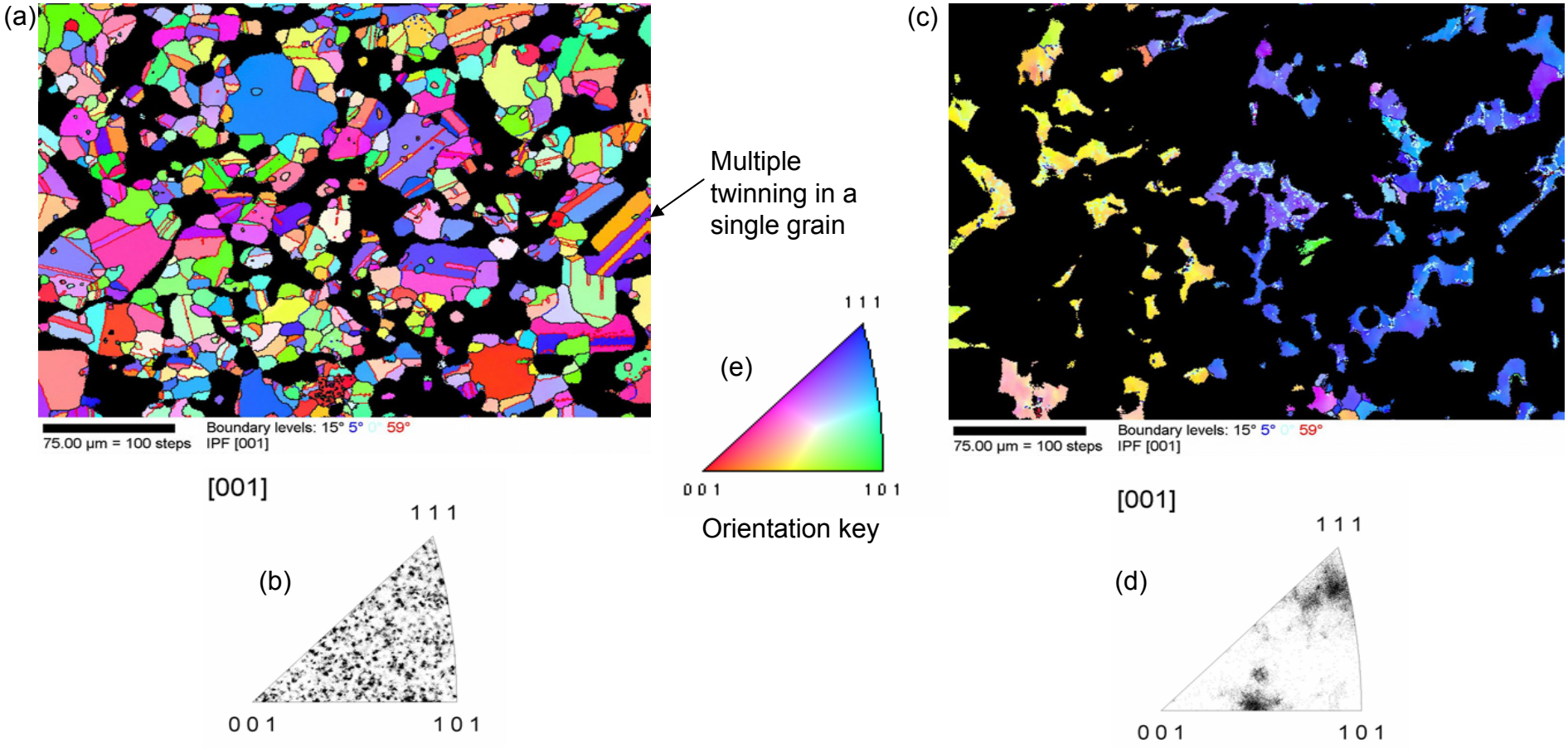

Figure 4.21(a) – 4.21(e)

Sandvik-Osprey CE7 EBSD Y-axis orientation maps. (a) Si dataset with Al removed, (b) inverse pole figure corresponding to (a), (c) Al dataset with Si removed, (d) inverse pole figure corresponding to (c), (e) orientation key corresponding to (a) and (c). **NB** Both 21(a) and 21(c) are derived from the unfiltered dataset shown in 20(c).

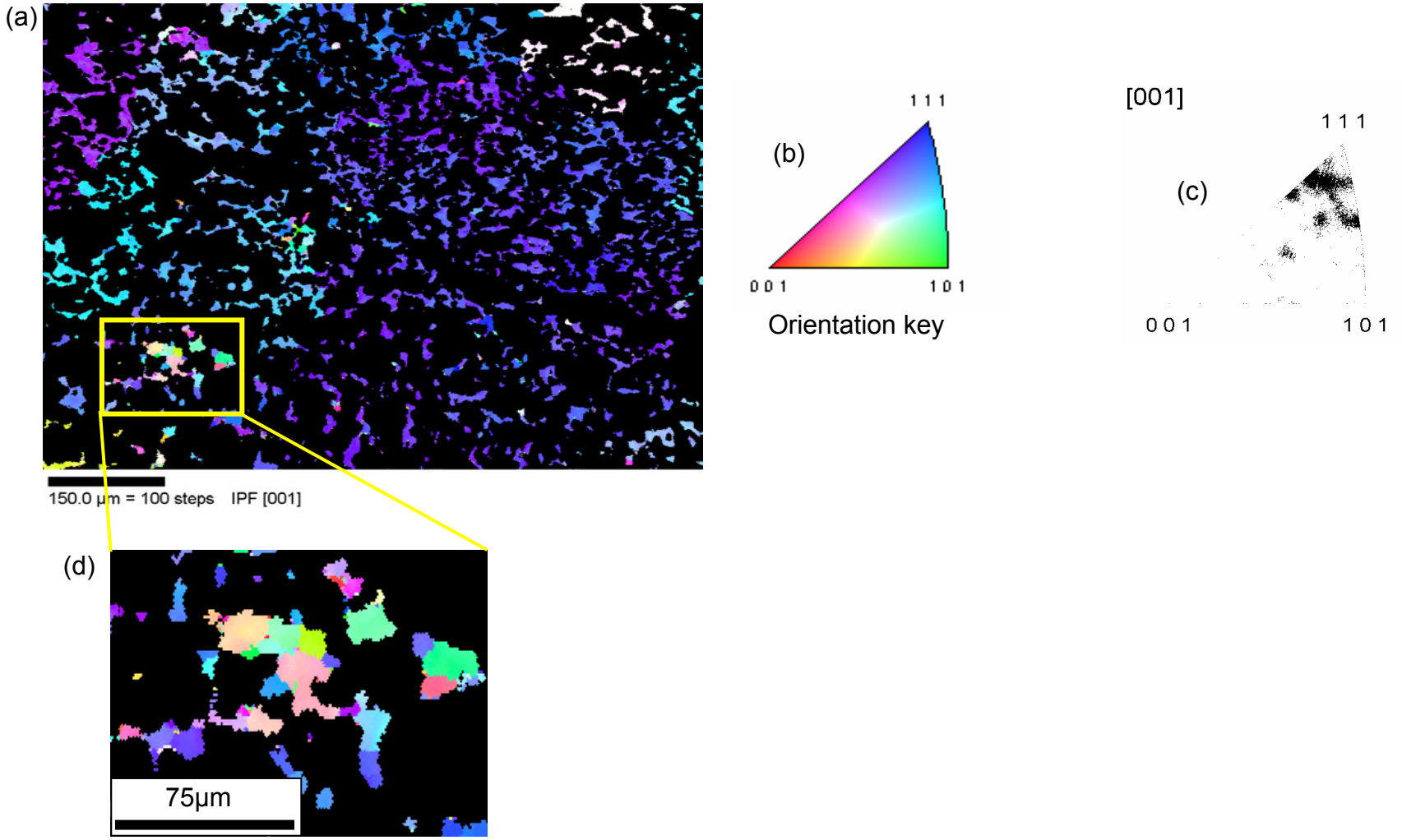

Figure 4.22(a) – 4.22(d)
Sandvik-Osprey CE7 EBSD Y-axis orientation map (a) typical CE7 Y-axis EBSD Al orientation map with Si removed, (b) orientation key, (c) inverse pole figure corresponding to (a), (d) small region of equiaxed, randomly oriented Al grains.

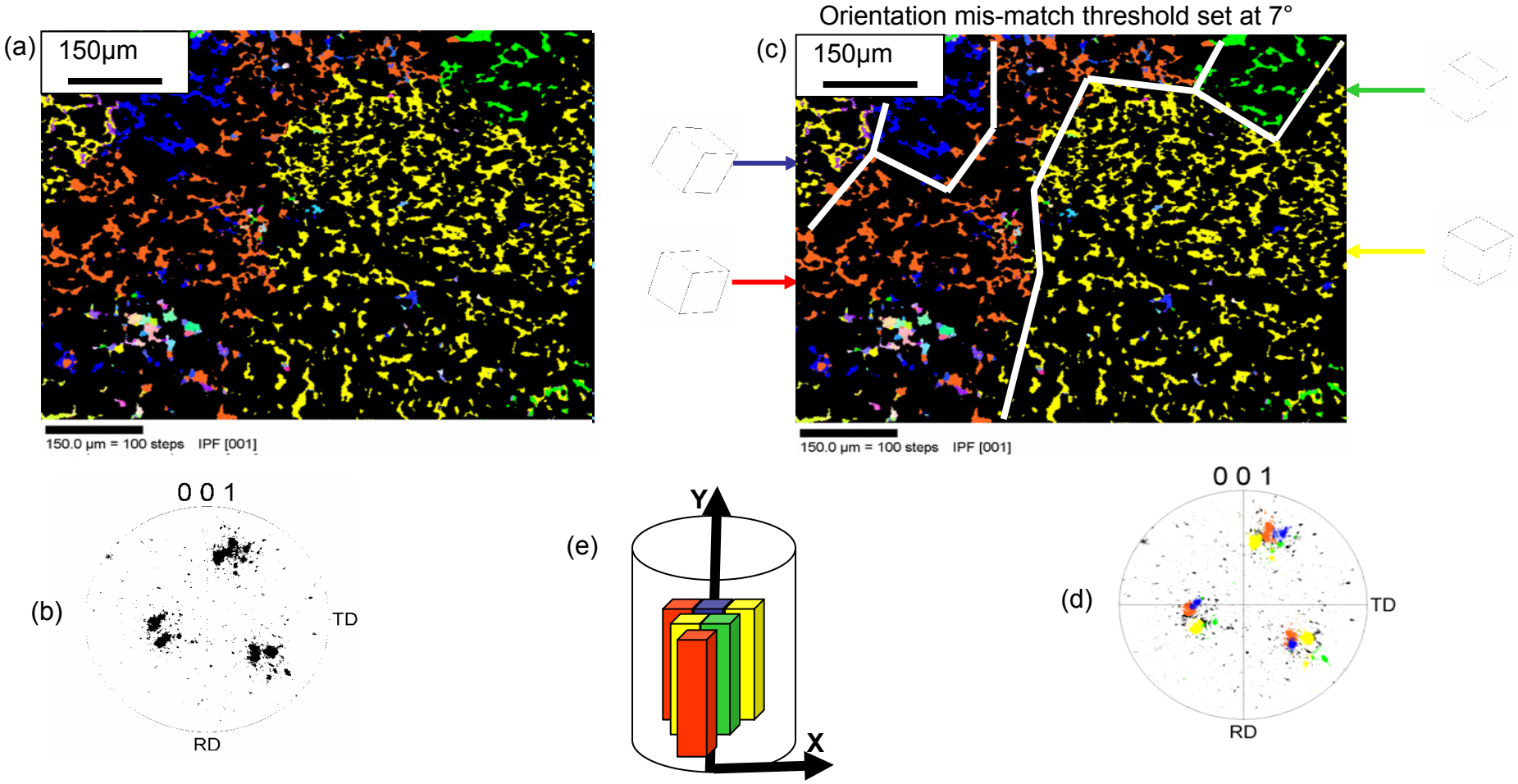

Figure 4.23(a) – 4.23(e)

(a) Sandvik-Osprey CE7 Y-axis EBSD Al orientation map with Si removed, (b) pole figure corresponding to (a), (c) 7° mis-orientation threshold applied to (a) revealing 5 sub-grains, (low angle pseudo grain boundaries superimposed over the image in white) with cubic grain orientation schematic shown for each grain, (d) pole figure coloured to correspond with sub-grains in (c), (e) schematic of columnar Al grain orientation in a sprayformed CE7 billet.

(a)

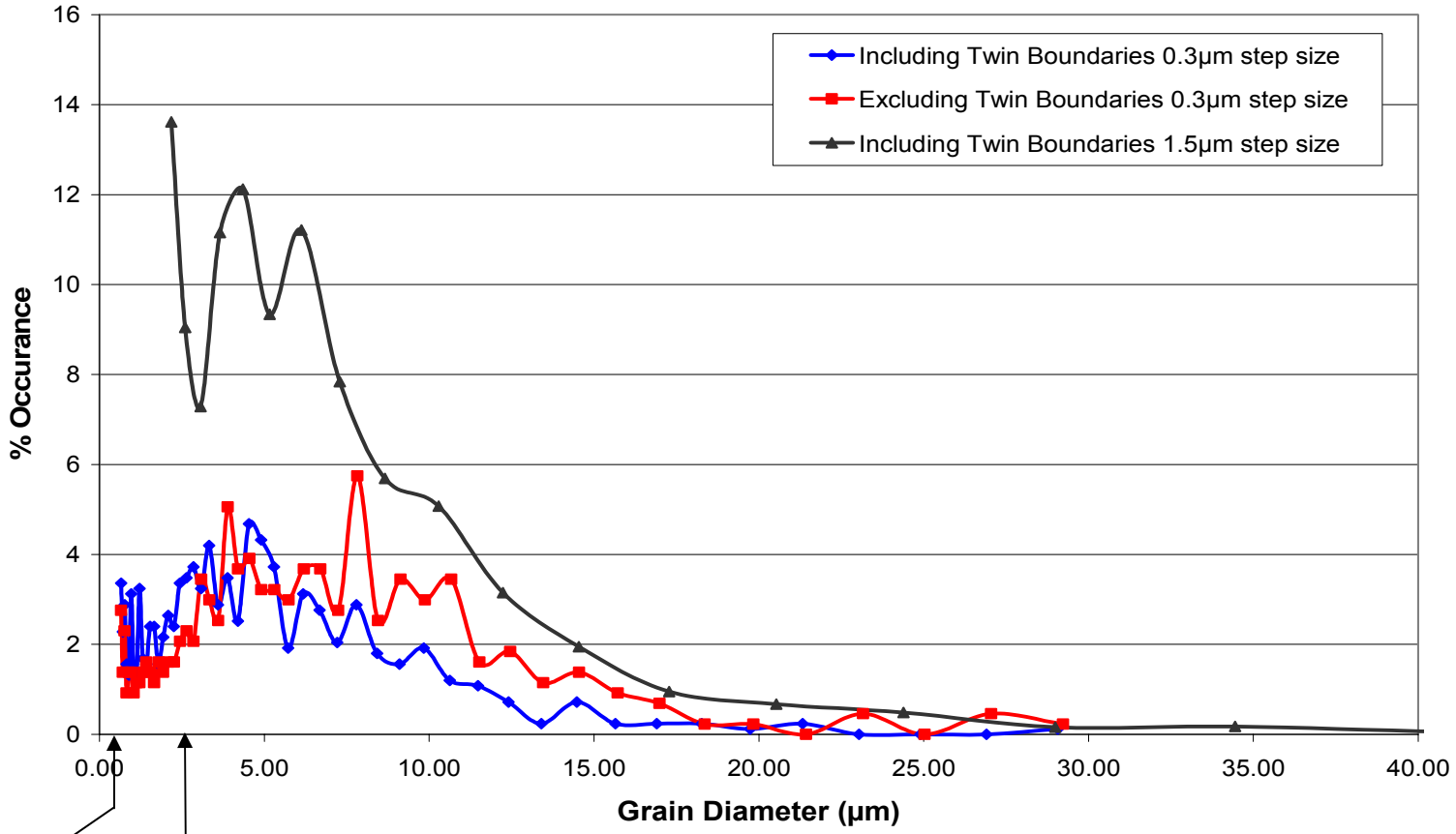

Minimum grain size resolution at 0.3µm step size = 0.7µm diameter

Minimum grain size resolution at 1.5µm step size = 2.3µm diameter

(b)

	Grain size (No of grains)	Step Size
Excluding twin boundaries =	5.5µm (435 grains)	0.3µm
Including twin boundaries =	4.0µm (833 grains)	0.3µm
Including Twin Boundaries =	4.1µm (~2000 grains)	1.5µm

Figure 4.24(a) and 4.24(b)

(a) Si grain size distribution determined by EBSD including and excluding twin boundaries, (b) summary of data including and excluding twins

5.0 Results - Al-50Si Chill casting and alloy selection trials

A chill casting arrangement was used to investigate the effect of various alloy additions on the microstructure of cast Al-50Si. The casting conditions are detailed in Section 5.1. Microstructural characterisation of each of the modified Al-50Si ingots was carried out as described in Section 5.2. The microstructure of each modified alloy is described and compared with a binary Al-50Si ingot cast under the same conditions. Microstructures are described in Sections 5.2.1 to 5.2.11, and summarised in Section 5.3

5.1 Al-50Si Chill casting and alloy selection trials

Melting of ~1.6kg Al-50Si with a liquidus temperature of ~1040°C (Murray 1984) was monitored using a K-type thermocouple, and took typically ~1 hour in a clay-graphite crucible using induction heating where the power was adjusted to minimize melting time without thermal shock induced cracking of the crucible. Figure 5.1 shows a typical thermal history of the feedstock material where the power applied was increased from 4 to 8kW during a 53min heat from RT to 1150°C, a superheat of ~110°C.

Alloy cooling conditions on removal of the applied heat in the water cooled mould were measured using a 0.5mm K-type thermocouple secured to the mould by magnets so that the tip of the thermocouple was in free space in the mould centre. Molten Al-50Si-X alloy was poured into the mould at 1150°C and the temperature recorded using a TC08 Pico-log PC interface. A typical resulting cooling curve is shown in Figure 5.2, demonstrating that between 1150°C and the nominal solidus at 577°C (Murray 1984) an average cooling

rate of ~8°C/s was achieved. Figure 5.2 shows that there was no clear indication of a liquidus arrest, which probably arose because the latent heat evolution is distributed over a very wide freezing range of ~463°C. There was a very small eutectic arrest at ~577°C, despite a liquid fraction of ~57% at the eutectic temperature under equilibrium conditions.

5.2 Microstructural characterisation

All chill cast alloys were examined by optical microscopy at a range of magnifications and the microstructure compared with the Al-50Si binary control alloy. Where comparisons are drawn in the following text, it is always with the control alloy unless stated otherwise. Intermetallic phases are not described in detail since the primary aim of this study was to investigate the effect of alloying additions on the primary Si and Al-Si eutectic structure. No attempt was made to quantify microstructures accurately using image analysis or EBSD techniques as they were intended only to assess and rank the efficacy of possible alloy additions prior to spray forming experiments. Figures 5.3 – 5.14 show reflected light optical micrographs of the chill cast alloys with particular features of interest labelled.

5.2.1 Al-50Si – Control

Figures 5.3(a) – 5.3(c) shows the microstructure of the control Al-50Si chill casting and was typical of an Al-high Si alloy (Osprey 2001). Figure 5.3(a) shows coarse, faceted primary Si rods often of several millimetres in length and width of ~70μm and the inter-primary Si regions comprising a coarse irregular

flake Si/α-Al eutectic. Figure 5.3(b) and 5.3(c) shows the primary Si at higher magnification surrounded by an adjacent halo of eutectic Al, denuded of Si phases. Further away from the primary Si rods, the eutectic structure was re-established with the classic Al-Si faceted / non-faceted morphology (Gigliotti 1970). The primary Si rods were often longitudinally cracked and in places Si rods were interpenetrated by globular Al as shown in Figure 5.3(b) suggesting growth of hollow Si 'hopper' crystals (Wang 1997). The large primary Si grain size was in contrast to the fine (~5μm) Si grain size previously described in Section 4.3.6 in spray formed Al-70Si. Spray formed Al-70Si also exhibited a divorced eutectic, with an absence of eutectic Si in the inter primary Si regions, in contrast to the coarse Si/α-Al eutectic structure observed in chill cast material.

5.2.2 Al-50Si + 0.5%P

Figures 5.4(a) and 5.4(b) shows that P was effective in refining the primary Si phase, changing its morphology and refining the eutectic Si. This was entirely consistent with effects observed by Kyffin 2001 and Arnold 1961. The Si particles had an aspect ratio much closer to unity than that in the absence of P with typical diameters of 50 – 100μm. In some cases short Si rods were formed, typically ~30 x 200μm as shown in Figures 5.4(a) and 5.4(b). At low magnification it is apparent that the large primary Si grains are often fractured resulting in areas of 'pull out' during polishing as indicated in Figure 5.4(a). Figure 5.4(b) shows at higher magnification cracking typical in some of the rod shaped Si particles. The eutectic structure was also refined in comparison to the control alloy, consisting of fine lamellae of Al and Si shown at higher

magnification in Figure 5.4(c) with an approximate inter lamellae spacing of ~2μm compared with ~12μm in the control alloy. A ~5μm halo of Al devoid of eutectic Si was again evident around the primary Si as shown in Figure 5.4(c), exhibiting a reduction in thickness when compared with the Al halo in the control alloy of ~15μm. This reduction results from abundance of nucleation sites which reduces the driving force for epitaxial growth of Si.

The halo effect was not always a consistent band adjacent to the Si but often had a dendritic morphology as shown in Figure 5. 4(c). This dendritic morphology also appeared within the Al-Si eutectic regions as shown in Figure 5.4(c). Samples were cut to avoid the gross porosity and solidification shrinkage which occurred in the centre of each chill casting, however Figure 5.4(c) shows fine distributed shrinkage porosity in the eutectic material.

5.2.3 Al-50Si + 1.0%P

Increasing the P concentration from 0.5% to 1% had a further significant effect on the Si particle size and morphology as shown in Figures 5.5(a) – 5.5(c). The typical primary Si particle size was reduced further to 30-50μm and the Si particle morphology had a more distinct hexagonal impression, as shown in Figure 5.5(b). At higher magnifications in Figure 5.5(c) the usually faceted morphology of the Si/Al was altered to a more curved, less angular morphology on many Si particles. The inter primary Si spacing was small, typically ~20μm, and in many cases the Al halo effect around primary Si particles overlapped and as shown in Figure 5.5(b) a distinct eutectic microstructure was observed only in isolated areas where the inter primary Si spacing was increased locally to

>30μm. An isolated area of very fine scale eutectic is shown in Figure 5.5(c) consisting of a fine lamellae of Si / αAl with a typical inter Si lamellae spacing of 0.5μm.

5.2.4 Al-50Si + 5.0%Ce

Cerium and other rare earth elements were suggested to refine Al-Si microstructures by poisoning Si attachment sites, inhibiting primary Si growth (Xian 1994, Jirattiticharoean 2004). Figures 5.6(a) - 5.6(c) show that for relatively small chill castings with much higher Si concentrations, the addition of 5wt% Ce gave rise to primary Si phase consisting of faceted rods typically of several millimetres in length and often cracked longitudinally. The primary Si rods differed from the control alloy in that the rods were significantly interpenetrated by globular Al, as shown in Figures 5.6(a) and 5.6(b), and suggesting that growth of Si hollow 'hopper' crystals was promoted. Figure 5.6(b) shows the curved and castellated surfaces at the Al-Si interface of many primary Si particles. Figure 5.6(b) and 5.6(c) shows that the eutectic structure was significantly refined with a inter-lamellae Si spacing of ~7μm and consisted of a fine script morphology. Figures 5.6(b) and 5.6(c) show occasional evidence of an Al halo around primary Si particles, however this effect was not as pronounced as previously observed in the P modified alloys.

5.2.5 Al-50Si + 1.0%P + 5.0%Ce

Additions of P and Ce were intended to nucleate Si and inhibit Si growth respectively; it was hoped the resultant microstructure would resemble a more

refined version of the 1%P addition microstructure seen in Figure 5.5. However, primary Si solidified as elongated rods of ~500μm length as shown in Figure 5.7(a), in some cases the rods suggested star morphologies. Figure 5.7(b) shows that many of these rods were longitudinally cracked and / or penetrated by globular Al suggesting the hollow 'hopper' morphology Si as seen for the Ce modified alloy in Figure 5.6. There was again a halo of Al devoid of eutectic Si at the periphery of primary Si phases as shown in Figure 5.7(c). The eutectic structure was a refined script morphology present in the inter-halo regions with an inter-lamellar Si spacing of ~5μm shown in Figure 5.7(b) and 5.7(c).

5.2.6 Al-50Si + 0.5%B

Additions of 0.5%B reduced the size of the primary Si particles from ~3000 x 70μm to ~200 x 20μm although the primary Si particle morphology remained acicular as shown in Figure 5.8(a) and 5.8(b). Many primary Si rods were penetrated by the Al phase. Occasionally (Figures 5.8(a) and 5.8(b)) there was some agglomeration of primary Si particles into rounded Si colonies reminiscent of the globular primary Si in spray formed Al-Si material. The eutectic structure shown in Figure 5.8(c), consisted of a coarse flake morphology and showed no convincing evidence of refinement. Al halo formation was again evident around primary Si as shown in Figure 5.8(c), although it was less distinct than in some alloys because the eutectic structure was relatively coarse.

5.2.7 Al-50Si + 0.05%Sr

On the addition of 0.05wt% Sr, Figure 5.9(a) shows that the primary Si phase consisted of large acicular rods typically 300μm – 1000μm in length and ~90μm width, and were often longitudinally cracked, as shown in Figures 5.9(b). Figure 5.9(c) shows that at the ends of rods were often slightly more rounded smooth curves rather than the sharper faceted end typical of the primary Si described in 5.2.1 and 5.2.4. Sr had a very strong refining effect on the Al-Si eutectic structure, yielding the fine script morphology shown in Figure 5.9(c). An Al halo around the primary Si particles was again evident in Figure 5.9(c) and there were dendritic Al regions within the inter-primary Si regions. There were also long occasionally curved linear features in the inter-Si regions that were first considered to be oxide stringers but were ascribed tentatively as acicular Al-Fe-Si based intermetallic phases. Figure 5.9(b) shows that these particles occasionally disrupted the growth of Al phase during terminal eutectic solidification. The presence of these intermetallics in large fractions was ascribed to an increase in Fe concentration through the Al-Sr hardener used or another accidental mechanism. More complex interaction of Sr-Si-Al and impurities could not be discounted, but was not pursued further since the strong effect of Sr on the Al-Si eutectic was established.

5.2.8 Al-50Si + 1.0%Bi

Figures 5.10(a) shows that the addition of Bi had a small refining effect on the length scale of primary Si particles by reducing length to 500-800μm. Figure 5.10(a) shows the Al phase penetrating the primary Si phase through the

growth of hollow Si 'hopper' crystals, although hopper crystals were not as prevalent as in the Ce (5.2.4) or B (5.2.6) modified alloys. The eutectic structure consisted of fine scale fibrous 'wheat sheaf' lamellar with inter-lamellae spacing of 2.5 – 3.5μm, as shown in Figure 5.10(b) and 5.10(c). Figure 5.10(b) and 5.10(c) also show a well-defined Al halo ~10μm thick devoid of eutectic Si at the periphery of primary Si phases. The halo has a more distinct dendritic morphology, rather than the usually relatively planar interface described previously.

5.2.9 Al-50Si + 2.0%Mg

The Mg modified alloy shown in Figure 5.11(a), exhibited no evidence of refinement of the primary Si phase, with coarse acicular Si rods of >1mm in length that were often cracked longitudinally, as shown in Figure 5.11(b). Interpenetration by Al suggested hollow 'hopper' morphology in some primary Si rods. Figure 5.11(b) also shows a fine script morphology Al-Si eutectic, interspersed with a 'feather-like' phase typically 40-50μm in length, ascribed to Mg_2Si. Mg_2Si is the only stable compound to form in the Mg-Si system often, as a 'Chinese script' or 'feather-like' phase (Dargusch 2004). The Al phase in eutectic regions had a dendritic morphology that was often but not exclusively associated with the Al halo around primary Si particles, as indicated in Figures 5.11(b) and 5.11(c).

5.2.10 Al-50Si + 0.5%Ti

Titanium additions had little refining effect on the primary Si phase. The primary Si particle morphology was a mixture of large 500µm – 1000µm rods, shown in Figure 5.12(a) and a 'star' morphology composed of similar sized 200 - 500µm length rods. The eutectic phase length scale varied with position ranging from a highly refined script phase in Figure 5.12(b) to a comparatively coarse flake morphology. Figure 5.12(a) and 5.12(b) show the eutectic interspersed with regions of dendritic Al. These phases were often, but not exclusively, associated with the Al halo around primary Si particles as shown in Figure 5.12(c).

5.2.11 Al-50Si + 0.4%Sb

The addition of Sb refined the primary Si particles slightly to 200 – 400µm acicular rods, often in a star morphology as shown in Figure 5.13(a). An Al halo surrounded primary Si particles, and a relatively fine-scale fibrous / flake eutectic was interspersed with hexagonal Al-Sb intermetallics typically around 1.5 – 3.0µm diameter and shown in Figure 5.13(b) and 5.13(c). Many of the primary Si rods exhibited longitudinal cracks as shown in Figure 5.13(c).

5.3 Characterisation

5.3.1 Al-50Si+P

Figure 5.14 shows that in P inoculated alloys, the microstructure was significantly refined compared with binary Al-50Si. While most of the chill cast alloys retained a structure that resembled a conventional cast Al-Si alloy, albeit

with different levels of microstructural refinement, the addition of P had the strongest effect on the length scale and morphology of the primary Si phase as shown in Figure 5.14. Three variants of the P modified alloy were investigated subsequently: [1] 0.5%P cast in an un-cooled mould; [2] 0.5%P chill cast with a water cooled mould, and [3] 1.0%P chill cast with a water cooled mould.
The microstructures had progressively more refined primary Si and Al-Si eutectic phases together with Al halo effect as shown in Figure 5.14(a), (b) and (c) corresponding to the conditions [1] to [3] above. Figure 5.14(c) exhibits significant refinement with the same cooling rate as 5.14(b) but an increased AlP nucleant density. The interface length between the primary Si and eutectic Al-Si of each microstructure was measured by image analysis and K_{1c} measured by Vickers indentation as shown in Table 5.1.

Table 5.1 K_{1c} measured by Vickers indentation and interface length for chill cast CE7+P

Alloy (preparation)	**Interface length mm/mm²**	**K_{1c} (MPa $m^{1/2}$)**
Al-50Si+0.5% P (Cast in un-cooled mould)	3.3	1.42
Al-50Si+0.5% P (Chill cast with water cooled mould)	3.5	1.63
Al-50Si+1.0% P (Chill cast with water cooled mould)	4.6	2.03

As the primary Si size decreased, the interface length increased and produced a corresponding increase in fracture toughness as shown in Figure 5.15, suggesting that interface length is important in controlling toughness. The degree of microstructural refinement remains small compared to spray formed

material, Sandvik-Osprey CE7 had an interface length an order of magnitude greater of ~14mm/mm^2 with a corresponding K_{1c} measured by Vickers indentation of 3.14MPa m$^{1/2}$.

5.4 Summary

The key microstructural features of chill cast Al-50Si-X alloys are summarised in Table 5.2 below. Refer to the corresponding Section and Figure for a more detailed description, and micrographs.

Table 5.2. Summary of key Microstructural features in modified Al-50Si chill castings

Alloy (wt%) Section / Figure	**Primary Si** Key Features	**Eutectic** Key Features
Al-50Si 5.1.2 / Fig 5.3	Si rods >1mm x 70µm Hopper crystals	Coarse irregular flake Indistinct Al halo ~15µm wide
Al-50Si+0.5%P 5.2.2 / Fig 5.4	Fine, equiaxed, & short rods, ~50 – 100µm	Fine lamellae ~2µm spacing Weak Al halo, dendritic Al
Al-50Si+1.0%P 5.2.3 / Fig 5.5	Fine, equiaxed ~30 – 50µm Hexagonal, curved faces	Fine lamellae, 0.5µm spacing Strong, interacting Al halos
Al-50Si+5.0%Ce 5.2.4 / Fig 5.6	Si rods >1mm length Hopper crystals Curved, castellated surfaces	Script morphology ~7µm lamellae spacing Intermittent Al halo
Al-50Si+ 1.0%P+5.0%Ce 5.2.5 / Fig 5.7	Si rods >500µm length Star morphology Hopper crystals	Script morphology ~5 µm lamellae spacing Indistinct Al halo
Al-50Si+0.5%B 5.2.6 / Fig 5.8	Rods (200x20µm) and Si clusters / colonies Interpenetrated by Al	Coarse flake morphology Intermittent Al halo
Al-50Si+0.05%Sr 5.2.7 / Fig 5.9	Si rods 300 – 1000µm x 90µm. Rounded rod ends	V. fine script morphology Dendritic Al. Narrow Al halo
Al-50Si+1.0%Bi 5.2.8 / Fig 5.10	Si rods 500 - 800µm length Hopper crystals Angular rods	Fibrous 'wheat sheaf' ~3µm lamellae spacing Defined 10µm Al halo
Al-50Si+2.0%Mg 5.2.9 / Fig 5.11	Cracked Si rods >1mm Hopper crystals	Feather morphology Mg_2Si Fine eutectic Dendritic Al, strong Al halo
Al-50Si+0.5%Ti 5.2.10 / Fig 5.12	Cracked Si rods 500 – 1000µm x 100µm Star morphology	Varied lamellae spacing Al Halo, dendritic Al
Al-50Si+0.4%Sb 5.2.11 / Fig 5.13	Si rods 200 - 400µm length Star morphology	Fibrous flake morphology Al-Sb hexagonal intermetallics

These experiments were effective in screening the efficacy of alloy additions in refining the structure of the primary Si. Four alloy modifiers were selected for subsequent spray forming experiments: P and B were selected for the strong refinement of primary Si and Al-Si eutectic; P+Ce for its effect at promoting unusual Si morphologies; Sr for the rounding of Si rods and strong effect on eutectic. It must be remembered that the solidification path in spray forming is very different from chill casting, and different effects and microstructures were anticipated.

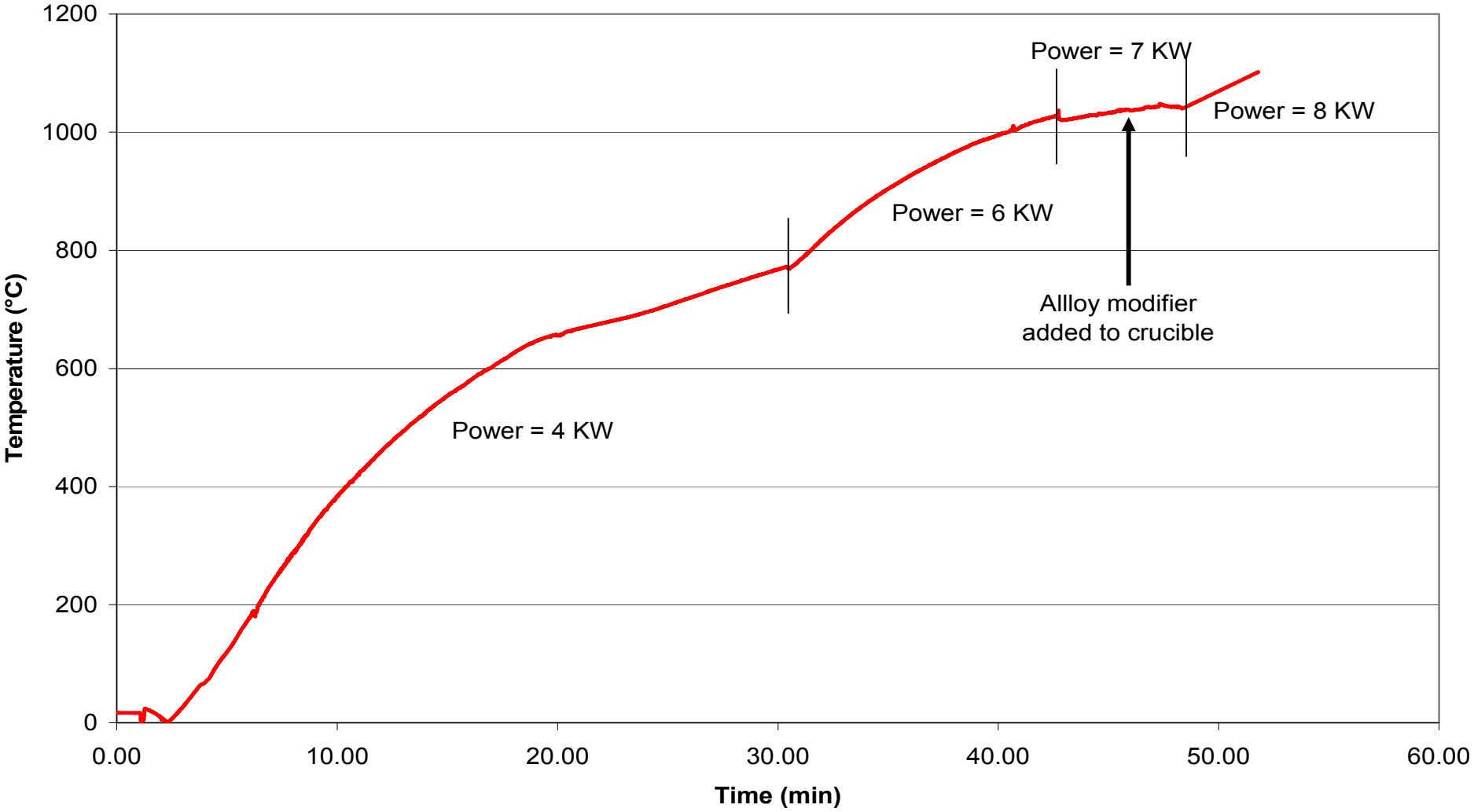

Figure 5.1

Typical heating profile of Al-50Si, inductively heated in a clay-graphite crucible

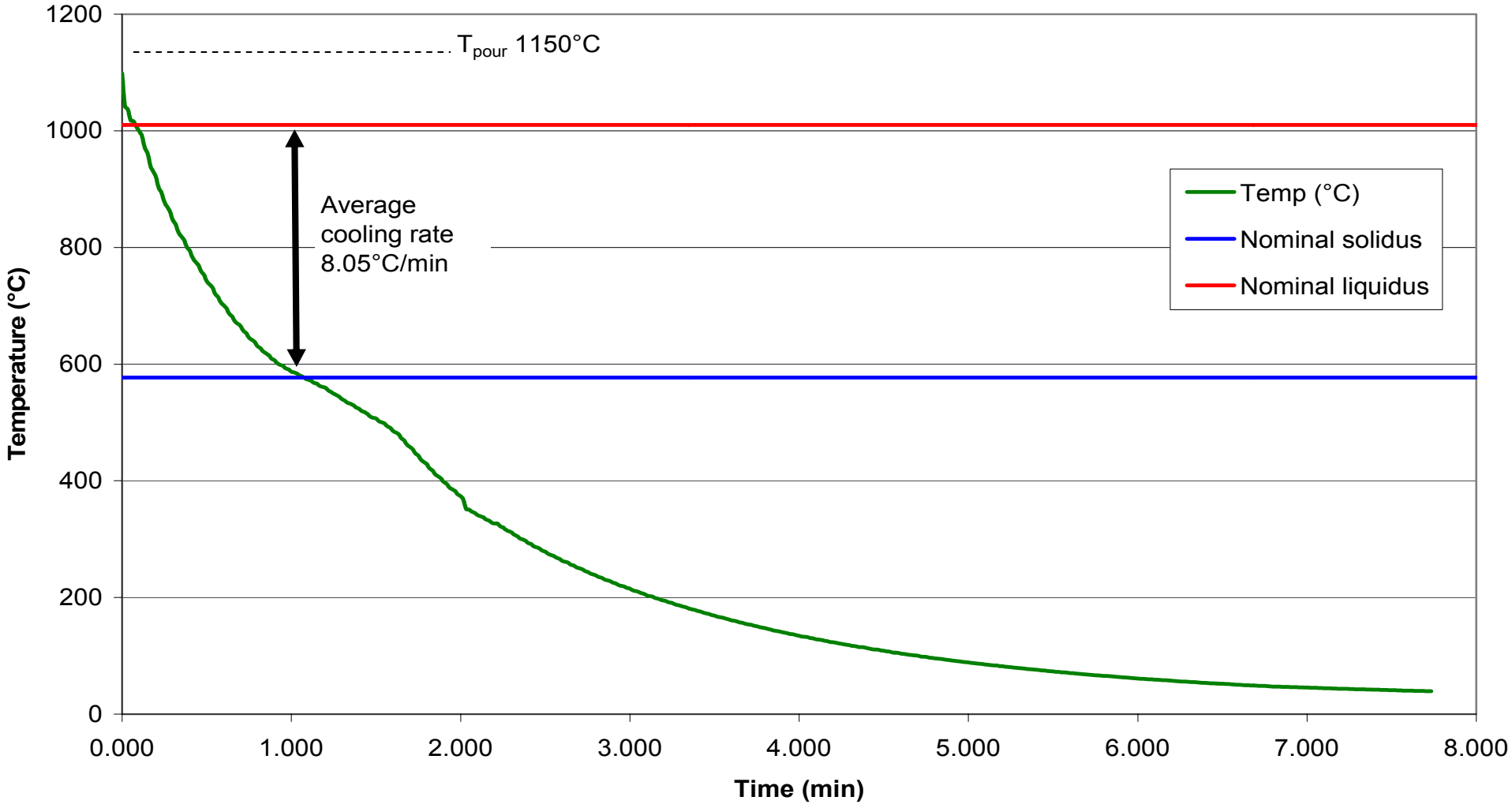

Figure 5.2

Cooling and solidification of Al-50Si in water cooled chill casting mould

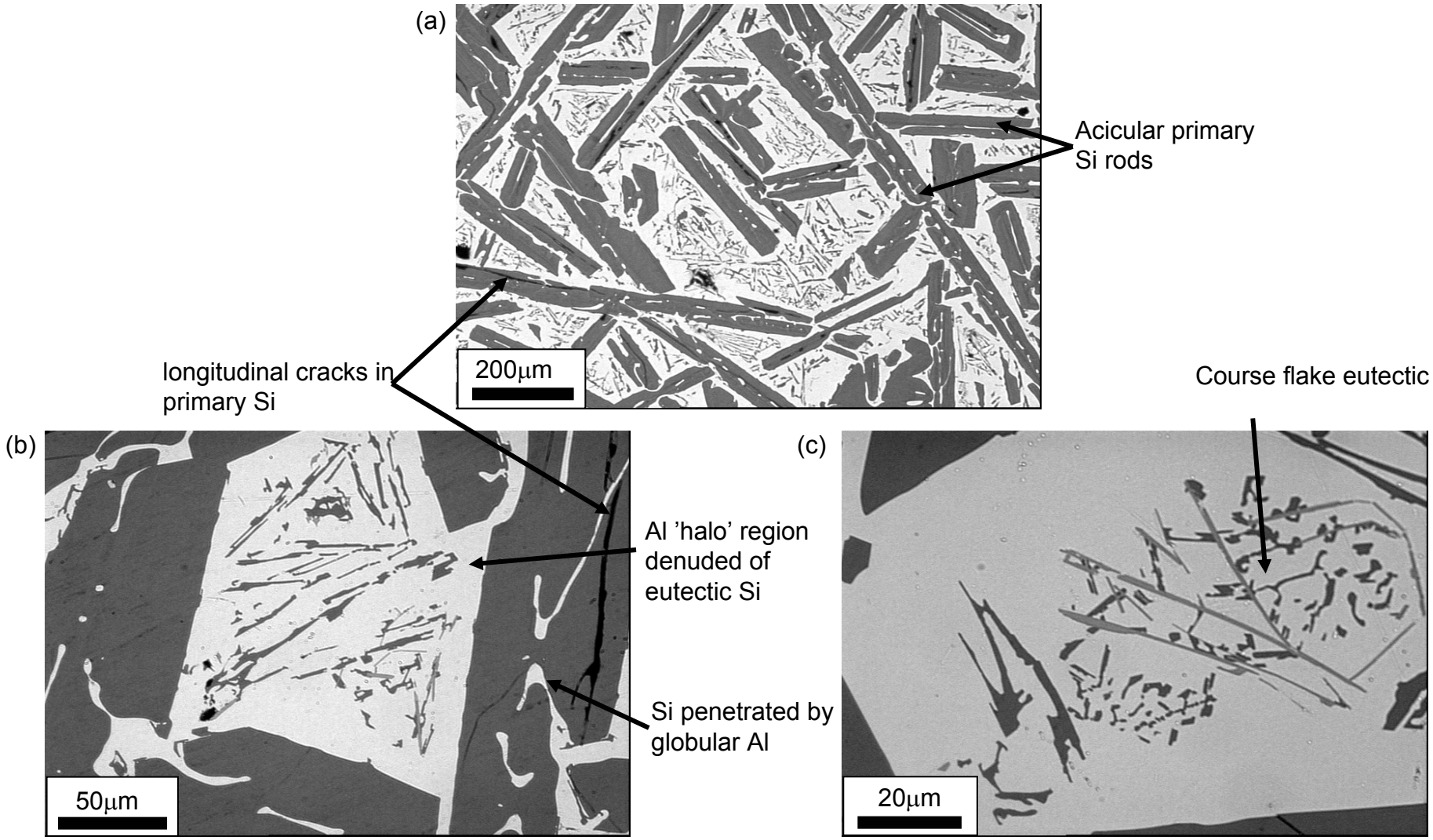

Figure 5.3(a) – (c)

Optical micrographs of chill cast Al-50Si binary control alloy Si penetrated by globular Al

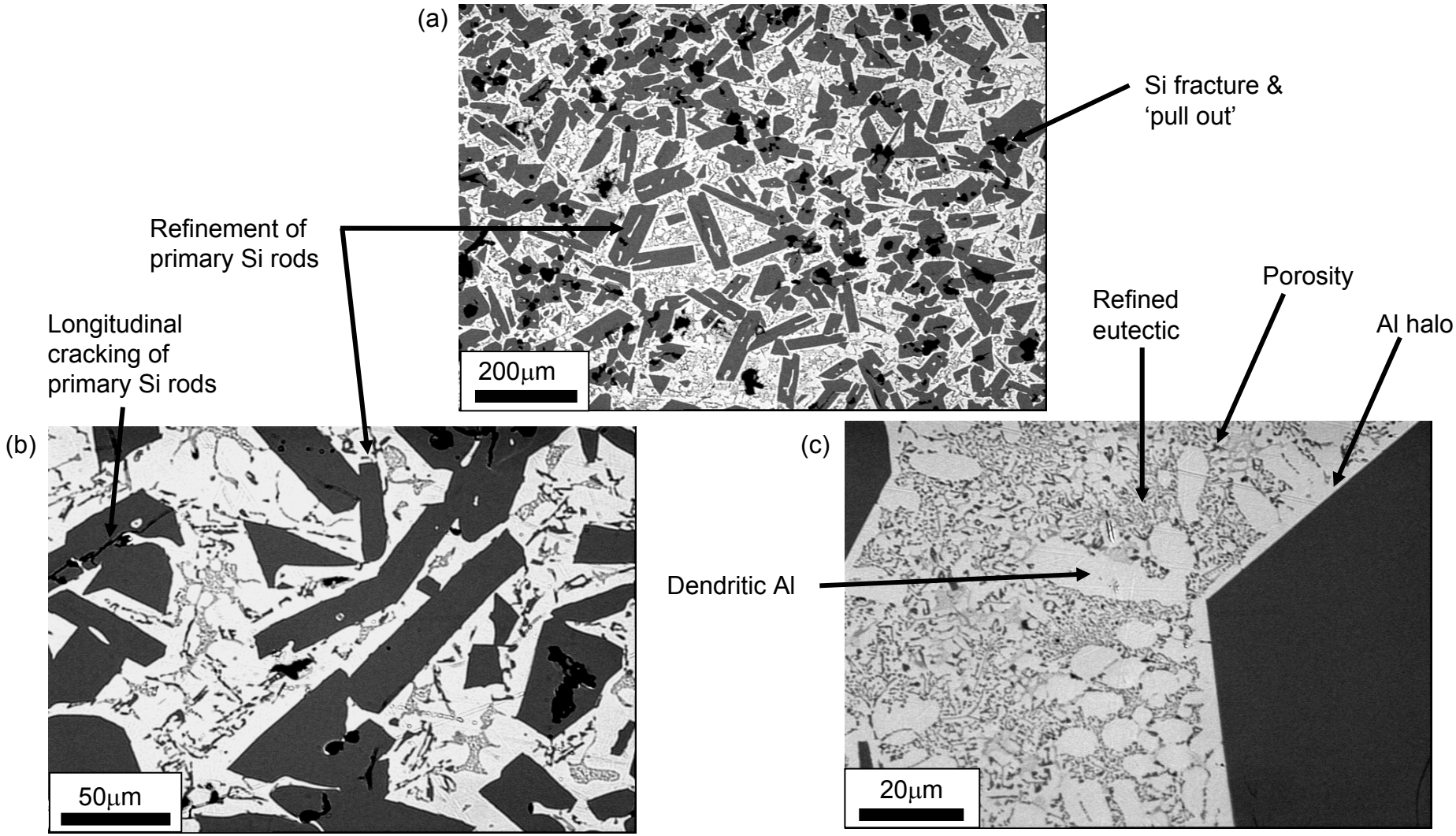

Figure 5.4 (a) – (c)

Optical micrographs of chill cast Al-50Si + 0.5%P.

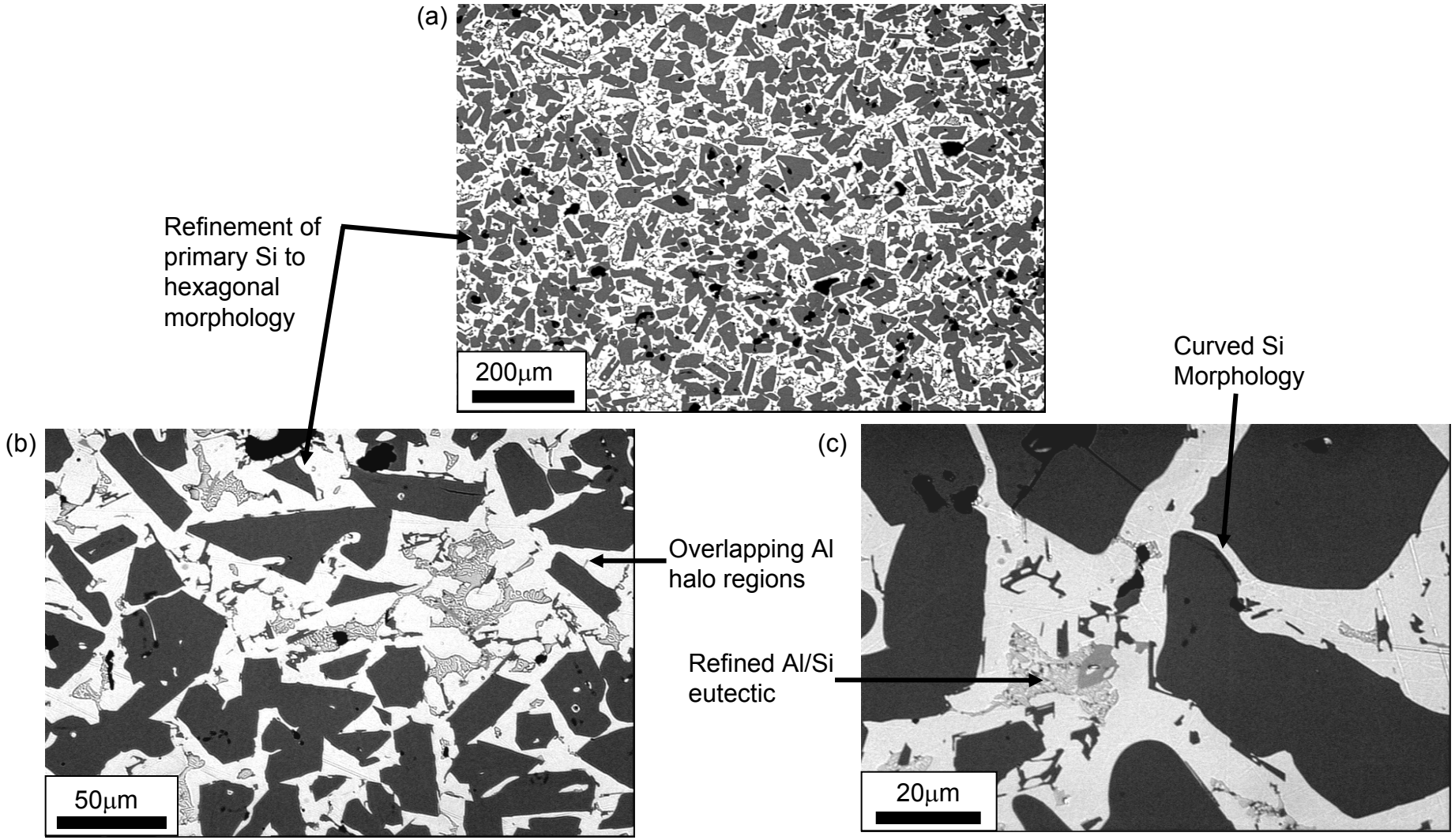

Figure 5.5(a) – (c)

Optical micrographs of chill cast Al-50Si + 1.0%P.

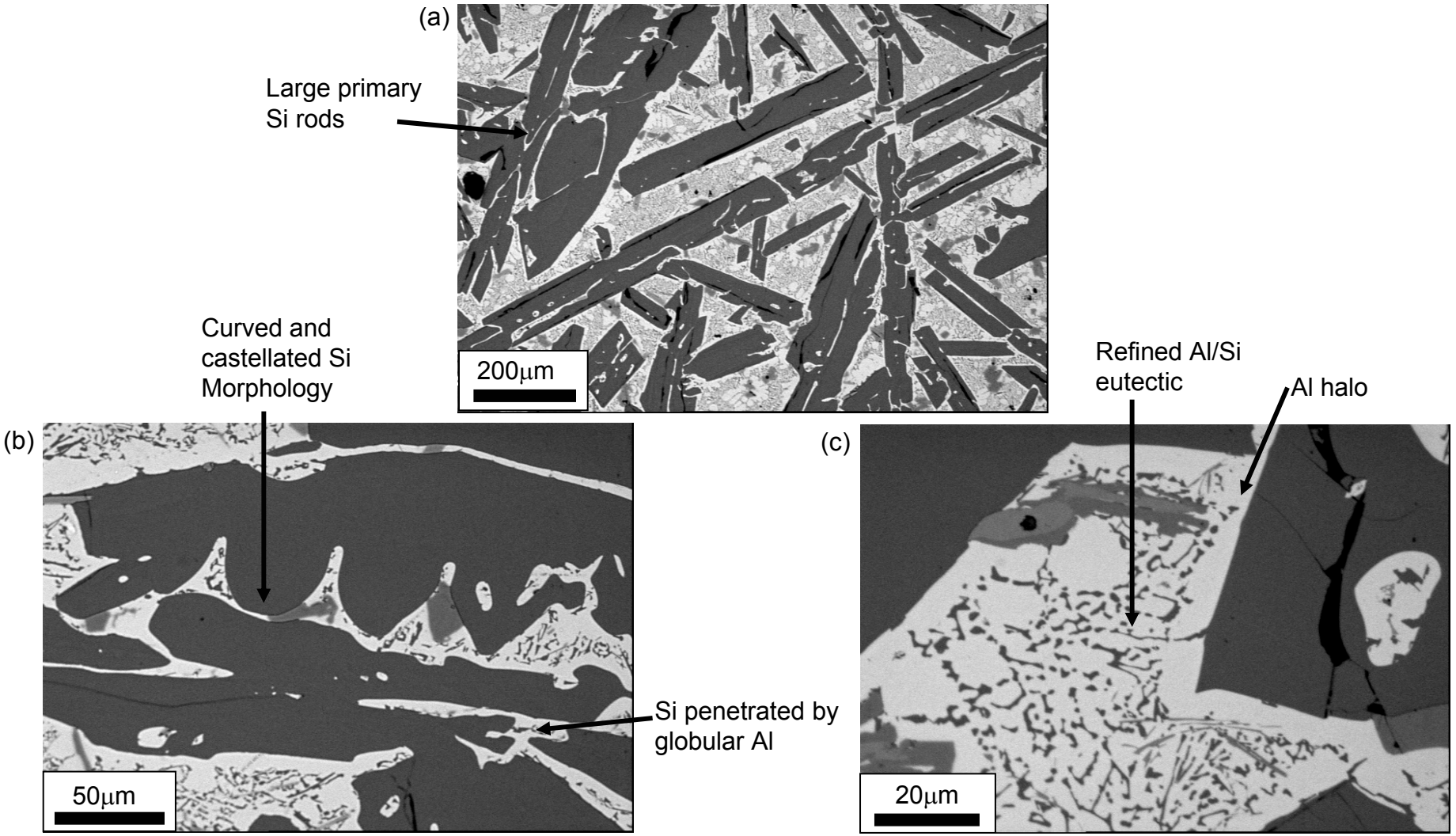

Figure 5.6(a) – (c)

Optical micrographs of chill cast Al-50Si + 5.0%Ce.

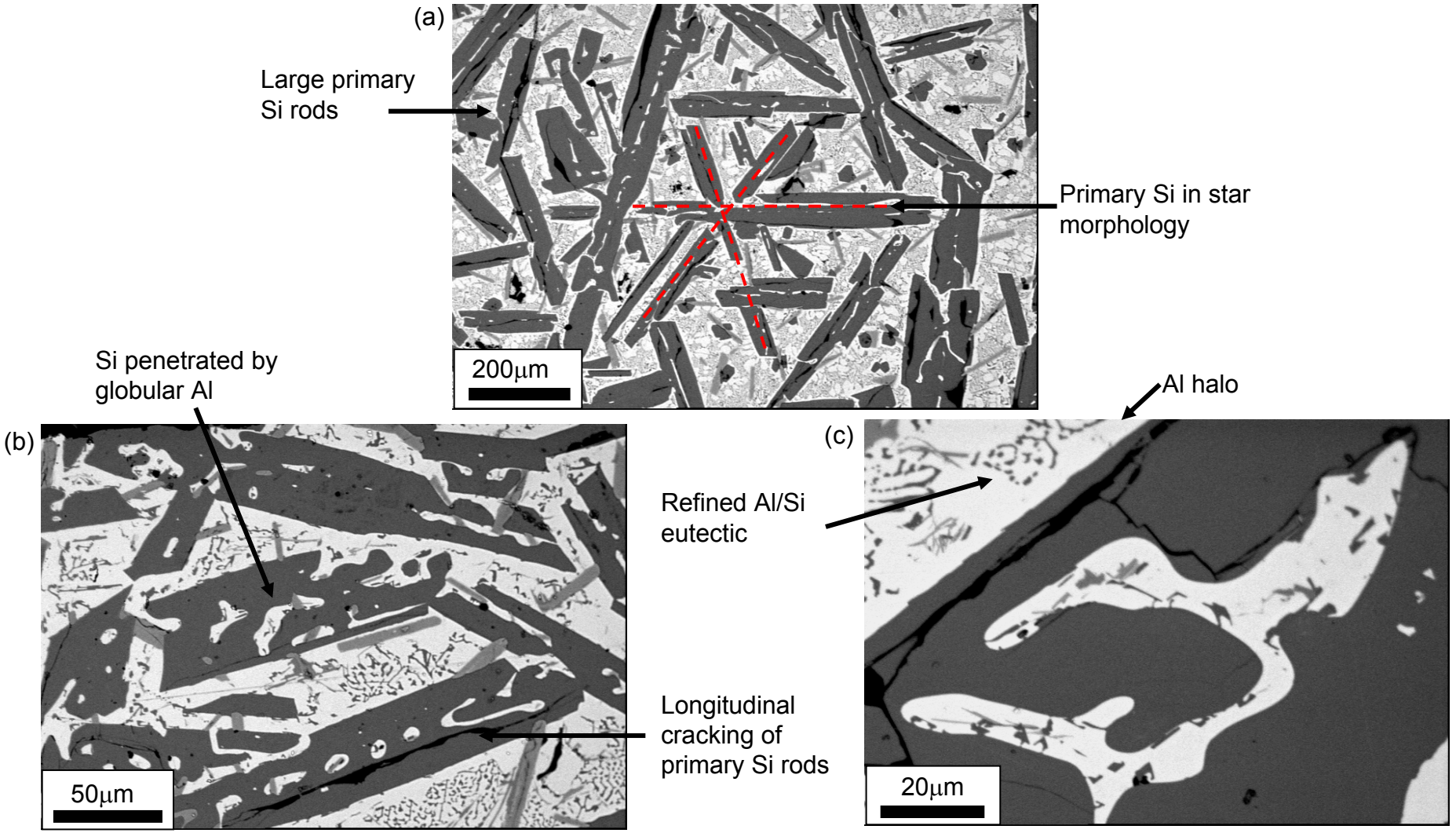

Figure 5.7(a) – (c)

Optical micrographs of chill cast Al-50Si+1%P+5.0%Ce.

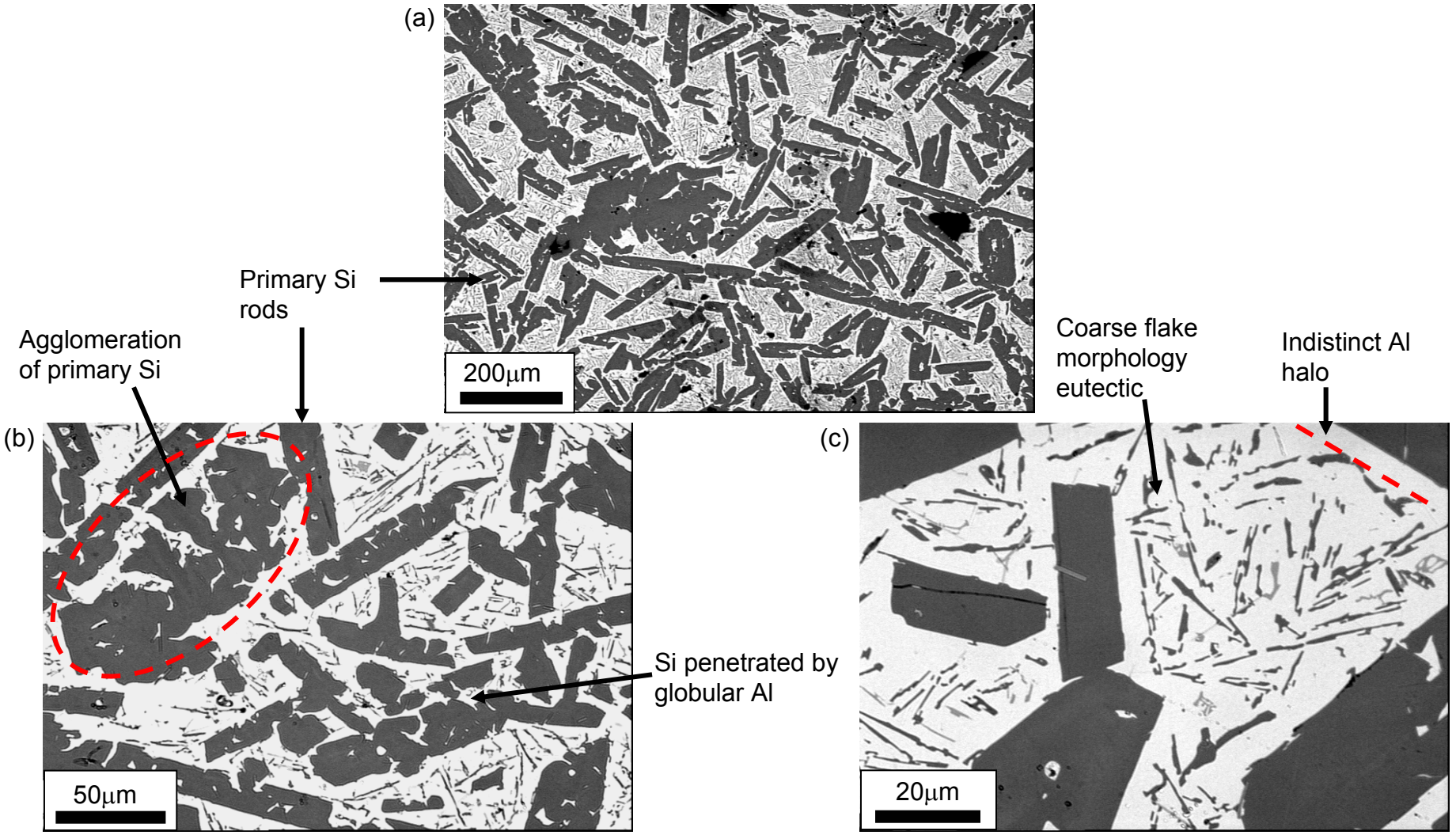

Figure 5.8(a) – (c)

Optical micrographs of chill cast Al-50Si + 0.5%B.

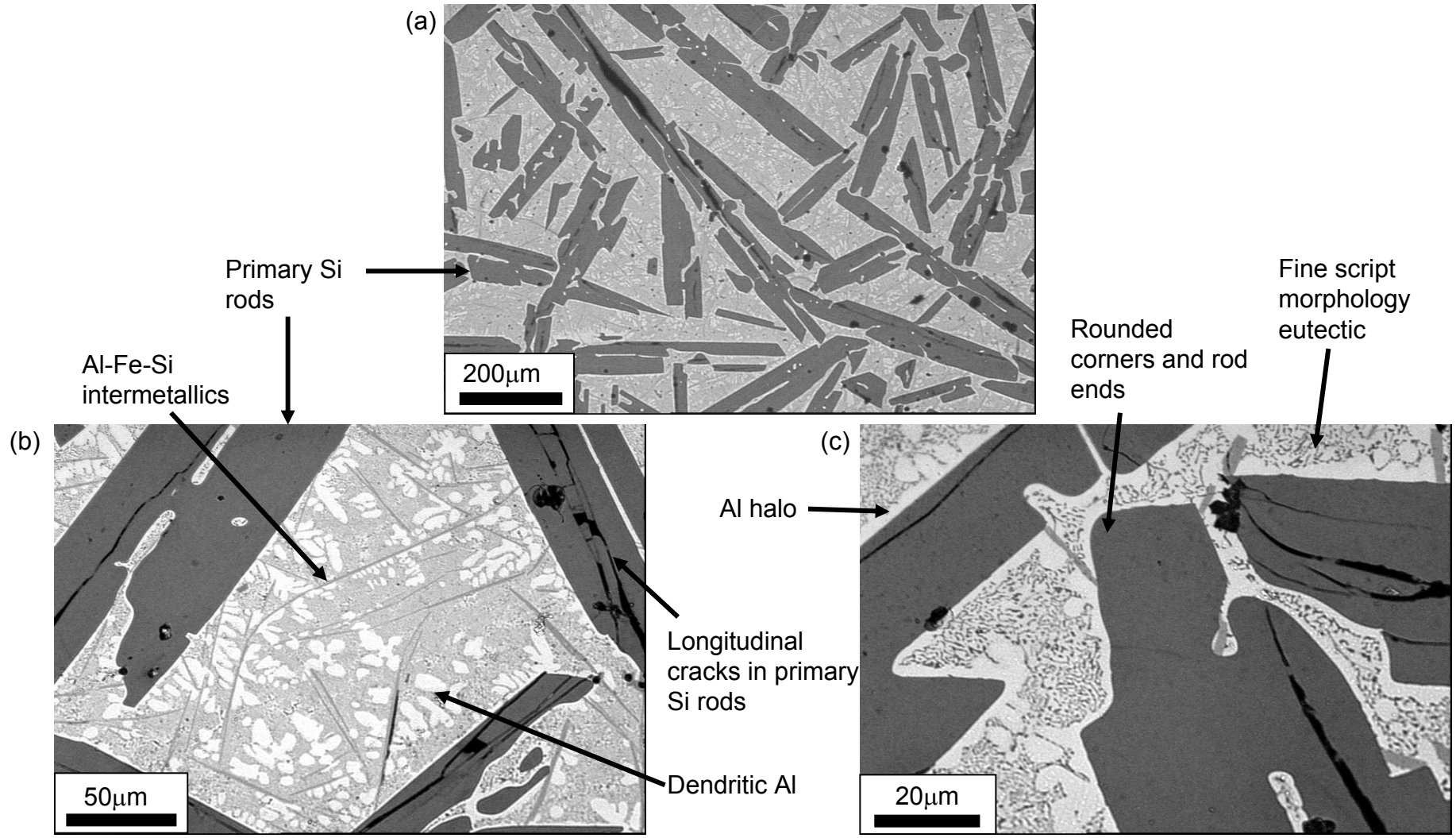

Figure 5.9(a) – (c)

Optical micrographs of chill cast Al-50Si + 0.05%Sr.

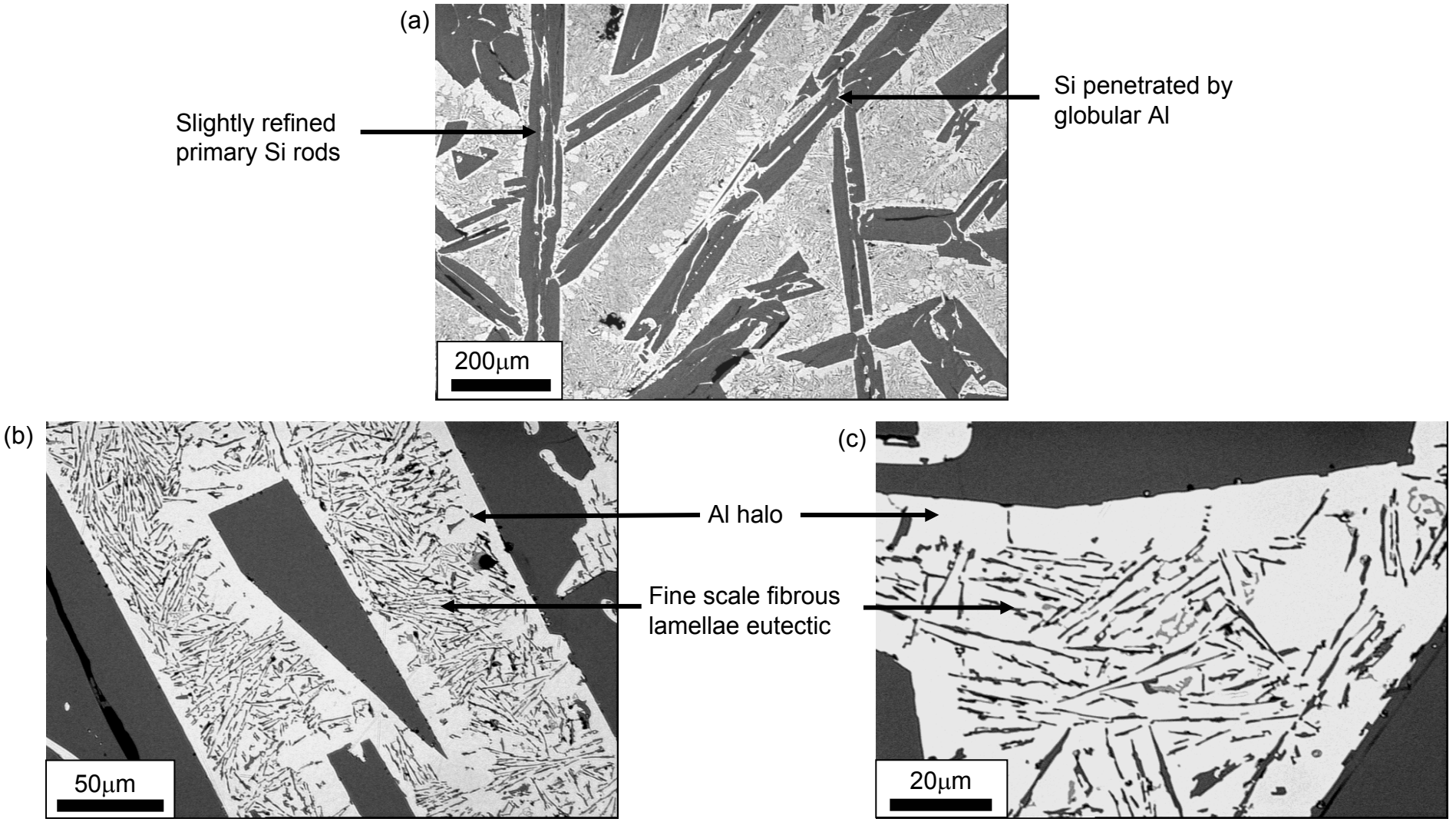

Figure 5.10(a) – (c)

Optical micrographs of chill cast Al-50Si + 1.0%Bi.

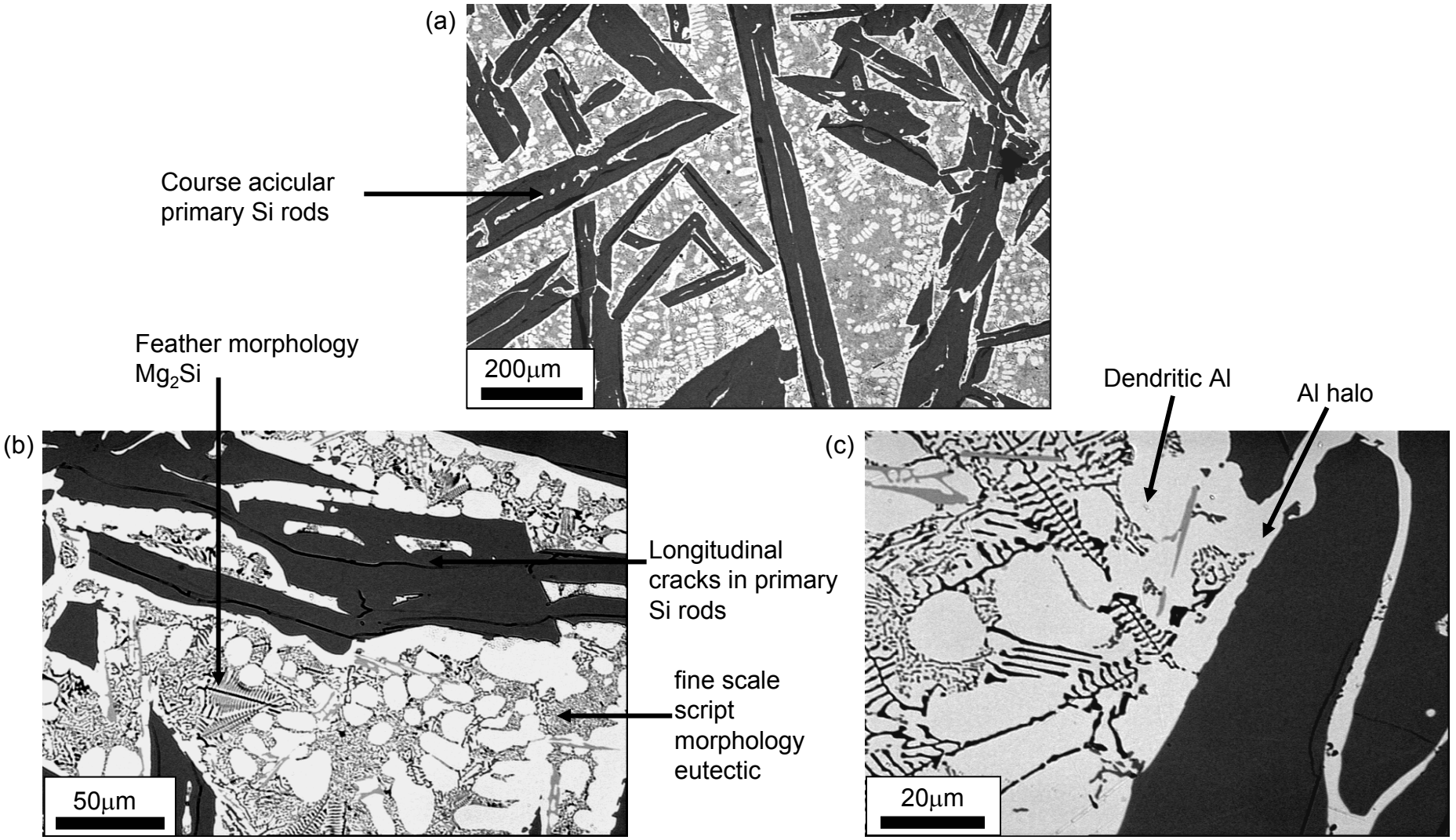

Figure 5.11(a) – (c)

Optical micrographs of chill cast Al-50Si + 2.0%Mg.

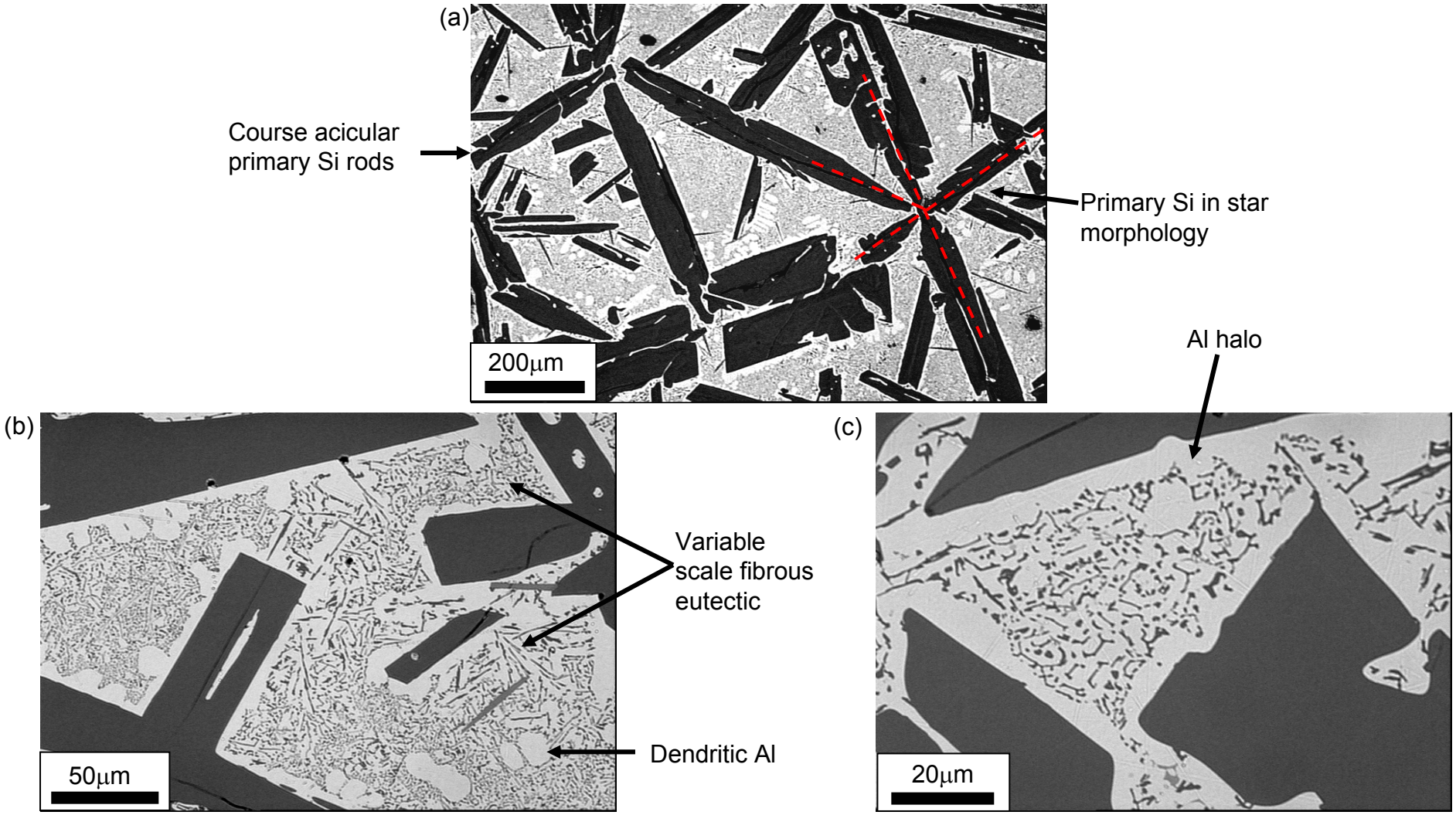

Figure 5.12(a) – (c)

Optical micrographs of chill cast Al-50Si + 0.5%Ti.

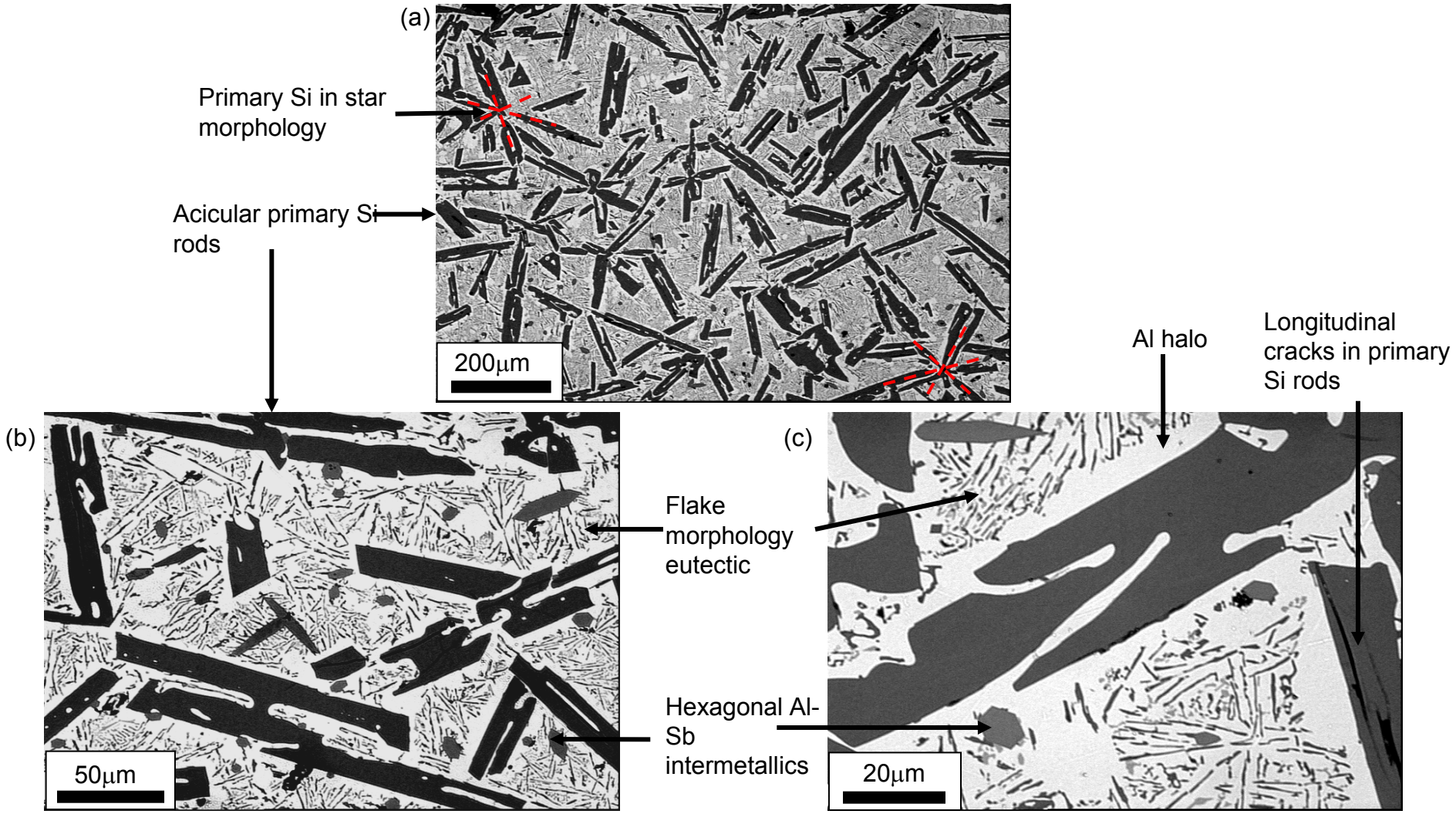

Figure 5.13(a) – (c)

Optical micrographs of chill cast Al-50Si + 0.4%Sb.

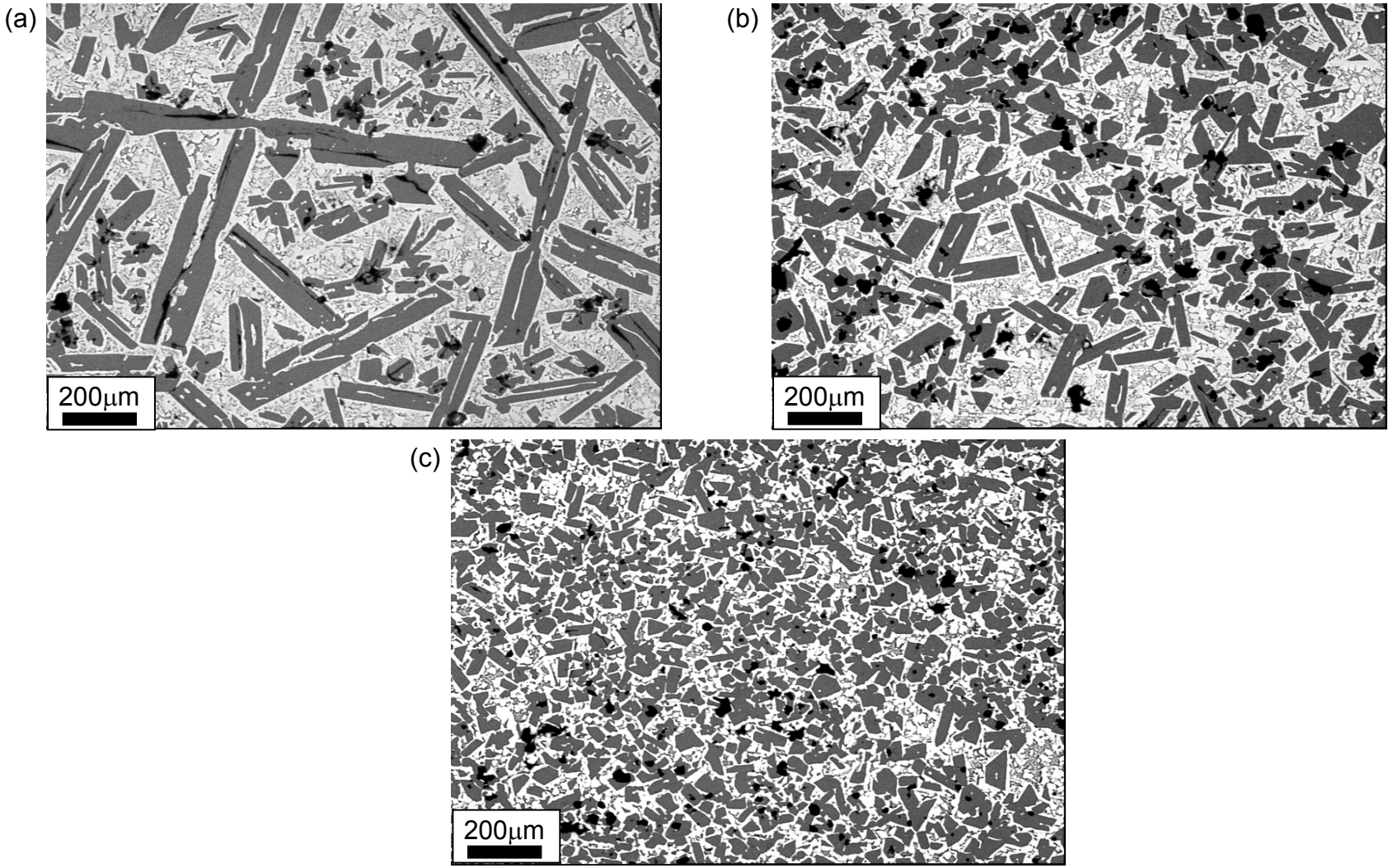

Figure 5.14 (a) – (c)

Optical micrographs at the same magnification showing progressively refined primary Si in chill cast Al-50Si with (a) 0.5%P and slow cooling, (b) 0.5%P and water cooling, and (c)1.0%P and water cooling.

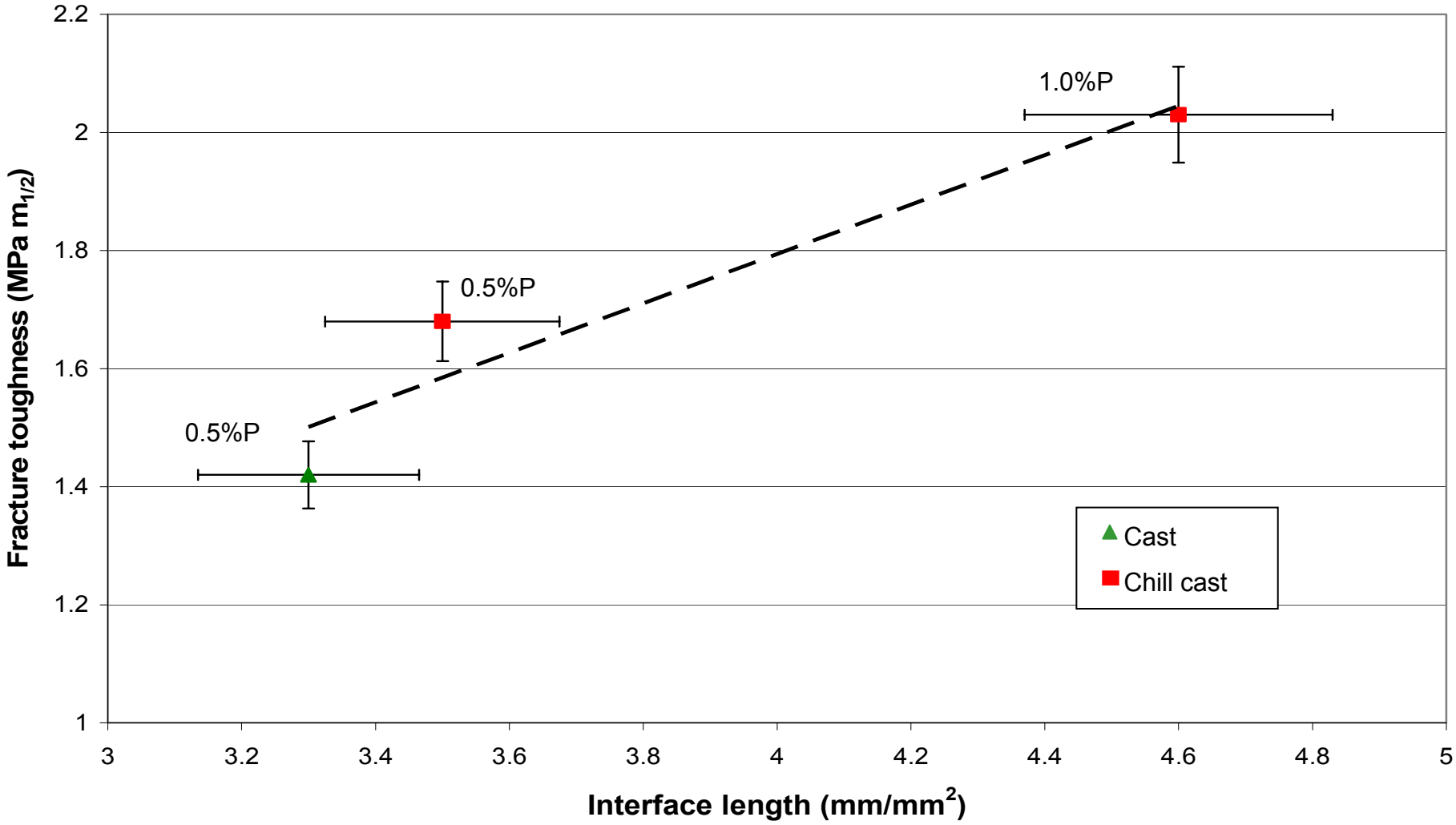

Figure 5.15

Fracture toughness of CE7+P measured by Vickers indentation as a function of interface length.

6.0 Results - Modified CE7 alloys manufactured at Oxford University.

The spray forming including post-spray cooling conditions and the HIPing of spray formed billets are described in Sections 6.1 and 6.2 respectively. Solidification profiles and phase formation was compared with predictions from MTDATA in Section 6.3. The physical characterisation procedures used in Section 4.2 were used again, to investigate the properties of Oxford modified CE7 alloys, results are given in Section 6.4. Microstructural results are presented in Section 6.5. Microstructural characterisation of Oxford modified CE7 alloys was conducted using optical microscopy, image analysis, EPMA and EBSD, revealing intermetallic phases and the effect of modification on Al and Si grain sizes.

6.1 Processing

6.1.1 Melting

The charge temperature and furnace power during melting was recorded manually by the furnace operator and a typical heating profile is shown in Figure 6.1. Events such as the addition of Si, de-gassing and skimming of dross are indicated, with de-gassing typically beginning once the charge reached 1250°C and volatile (P & Sr) alloy additions being added after de-gassing was complete. Typically melting took ~180 min with a progressively increasing induction power from 30 to 75 KW. Temperature was increased progressively by steadily increasing furnace power. Small differences in the melting time, temperature and power requirements occurred due to the differences in induction coupling characteristics of the different furnace loads. At a temperature approaching the

required spray forming temperature, typically ~1450°C, furnace power was adjusted to maintain a constant melt superheat.

6.1.2 Processing

During spray forming, process parameters were logged at 1Hz by the Osprey control PC. The processing parameters comprised two sets: those which were manually controlled; and those which comprised feedback information only.
Manually controlled parameters: secondary atomiser gas pressure, primary atomiser gas pressure, ram retraction rate and extraction fan speed.
Process feedback: chamber pressure, gas supply pressure, ram position, scanner speed, ram rotation speed, scanner / ram synchronicity, exhaust gas temperature and chamber temperature.
Figure 6.2 shows the typical billet growth rate (calculated from the ram withdrawal rate and ram position assuming that the billet top surface was at a fixed point in space), primary atomiser pressure and secondary atomiser pressure as a function of time. During the initial ~1min of spraying, a low secondary atomiser pressure of ~4bar was used until steady-state deposition began. Figure 6.2 shows a step increase in the secondary atomiser pressure from 4 to 7bar after ~1min, which coincided with the beginning of ram withdrawal. It was often necessary to adjust the pressure of the primary atomiser towards the end of spraying in order to stabilise the melt stream and compensate for reducing metallostatic head, with the pressure typically increasing from 2 to 2.8bar. The gas pressure tended to overshoot the set points by ~0.3 bar, and take 10 - 20s to stabilise. This was unavoidable but to

some extent was mitigated by ramping from one set point to another in a series of smaller steps.

6.1.3 Pyrometry

Two pyrometers were used to give an indication of the temperature trend on the billet top surface during spraying. The data could not be considered as absolute temperatures because of problems of calibration of the one-colour pyrometer for the non-linear emissivity of Si with respect to temperature (Jain 1971) and significant problems caused by obscuration by re-circulating powder transported by the turbulent N_2 flow in the chamber. Temperature data was filtered manually to remove obscuration 'noise' in an attempt to improve the relevance and scatter of the data. Figure 6.3 shows the temperature data split into 4 regions: (i) initial deposition where the atomiser pressure was low (~4bar) and the billet temperature was correspondingly high (~1200°C); (ii) steady-state deposition where the billet top surface temperature was approximately constant at ~1100°C; (iii) final deposition where the gas flow rate was constant but the metal flow rate decreased with decreasing metallostatic head in the tundish, causing a reduction in billet surface temperature from ~1100 to ~800°C; and (iv) post spray once spraying was complete and the billet top temperature apparently increased because of the removal of powder from the chamber and stopping of the atomising gas that chilled the billet top. Temperature data for all spray forming experiments followed the same general thermal trend and suggested good process repeatability.

6.1.4 Post spray cooling

The efficacy of the air cooled substrate to drive the solidification of billet liquid from the billet base to the top was tested using a ceramic heater to heat the air cooled substrate and boss to ~100°C. A 3mm thermocouple was inserted into a 3.1mm hole in the air cooled substrate. The temperature from 100°C to room temperature was logged at 1Hz, with and without compressed air flowing through the assembly. Figure 6.4 shows that with no compressed air, cooling was ~0.5°C/min, while with compressed air flowing, the cooling rate was increased by approximately a factor of four to ~2.0°C/min. During spray forming, the air cooled substrate was connected to a compressed airline as soon as deposition was complete and the N_2 was purged from the chamber (typically ~3min). The insulated 'top hat' was also then placed over the billet with a thermocouple placed in contact with the billet top surface. The top surface temperature was recorded for ~2 hours and a typical thermal history is shown in Figure 6.5, together with similar data for Sandvik-Osprey CE7 supplied by Sandvik-Osprey. Recorded temperatures for all Oxford billets started at ~710°C except for CE7+P that started at ~740°C. The Sandvik-Osprey billet temperature was first recorded at ~665°C and then cooled relatively slowly because of its larger mass. The temperatures in Figure 6.5 did not correspond accurately to billet temperature because of the imperfect thermal contact of the thermocouple, and the expected temperature gradients between the billet core and periphery. CE7+B and CE7+Sr showed temperature arrests at ~565°C, presumably corresponding to the Al-Si eutectic solidification at 577°C. CE7+P exhibited two temperature arrests at 534 and 510°C that were ascribed to Al-Si

eutectic reaction suppressed by the presence of Cu and the formation of Al_2Cu respectively, CE7+P+Ce exhibited temperature arrests at 620, 553 and 508°C with the first two ascribed to the formation of Al-Ce-Cu-Si phases of different stoichiometries identified during subsequent electron microscopy, and the latter attributed to the formation of Al_2Cu. Solidification profiles are considered further in Section 6.3. Figure 6.5 shows that at the end of spray forming, billet top surface temperature was ~700 – 740°C corresponding to a liquid fraction of ~30% (calculated from the Al-Si phase diagram, Figure 2.18). Relatively slow, directional solidification then occurred in CE7+B, CE7+Sr, CE7+P+Ce, CE7+P materials taking ~60, ~75, ~95 and ~105 minutes to reach completion respectively.

4.1.5 Process yield

Table 6.1 summarises the process yield data for Oxford billets together with Sandvik-Osprey data. Oxford spray forming experiments had a typical process yield in the range 31 - 46% and much lower than ~78% at Sandvik-Osprey because Sandvik-Osprey re-injected overspray powder and recycled the 'skull' and other 'waste'. Overspray collection and re-injection was not possible using the current Oxford equipment. The average melt flow rate at Oxford was 0.09-0.12kg/s similar to the Sandvik-Osprey melt flow rate of 0.11kg/s.

Table 6.1. Process yield data for spray forming experiments at Oxford and Sandvik-Osprey.

Alloy	CE7+B	CE7+P	CE7+P+Ce	CE7+Sr	S-O* CE7	S-O* Comment
Run time (s)	303	352	318	318	1232	
Melt flow rate (kg/s)	0.09	0.11	0.12	0.10	0.11	
Charge wt (kg)	50	50	50	50	188	Powder + charge
Billet wt (kg)	15.56	22.04	23.08	19.44	26.40	
Skirt wt (kg)	1.54	1.90	1.32	2.44	--	Not measured
Overspray wt (kg)	11.10	14.04	13.64	11.24	107.9	Recycled
Dross wt (kg)	3.00	1.58	1.46	4.90	5.0	Waste
Tundish wt (kg)	11.00	6.80	4.82	7.90	2.20	Waste
Skull wt (kg)	7.80	3.64	5.68	4.08	49.4	Recycled
Total waste (kg)	34.44	27.96	26.92	30.96	7.2	Dross + skull
Total yield (%)	31.12	44.08	46.16	38.88	78.6	= Billet wt / (billet wt + waste) x100

*S-O, Sandvik-Osprey

6.2 Hot isostatic pressing (HIPing)

Encapsulation and HIPing of Oxford modified CE7 alloys was conducted by Bodycote HIP (Chesterfield, UK) using the parameters previously described in Section 3.5.9 Table 6.2 compares the post-HIP porosity under the three different HIPing conditions with as sprayed porosity.

Table 6.2: Area percent porosity in the HIPed and as-sprayed condition.

	Porosity (area%) determined by image analysis			
Alloy	**As sprayed**	**Densal®** Proprietary conditions	**Specified HIP** 500°C/140MPa 4h	**Sandvik-Osprey HIP** 565°C/140MPa 16h
Osprey CE7	2.0 – 4.0 [note 3] *±0.24 – ±0.62*	See note [1]	See note [1]	0.1 *±0.03*
Ox CE7 (binary)	1.62 [note 4] *±0.16*	See note [1]	See note [1]	0.07 *±0.02*
CE7+B	1.94 *±0.14*	0.88 *±0.09*	0.37 *±0.01*	See note [2]
CE7+P	6.78 *±1.63*	6.53 *±1.8*	5.80 *±1.1*	See note [2]
CE7+P+Ce	6.32 *±1.31*	7.22 *±1.58*	3.92 *±0.67*	See note [2]
CE7+Sr	0.91 *±0.03*	0.28 *±0.01*	0.54 *±0.48*	See note [2]

Notes

[1] Sandvik-Osprey material was HIPed under previously optimised proprietary conditions along with batch production work

[2] Under advice from Bodycote HIP two sets of HIP conditions were tried on Oxford spray formed material. It was not possible to HIP Oxford material in Sandvik-Osprey batch production because of contamination concerns.

[3] Maximum and minimum at different billet locations, scatter in an individual region is as indicated

[4] This was the %porosity in the most dense region of the billet. In some regions there was a maximum of ~30% porosity with considerable variation across the billet. Only the most dense regions of material are considered in this analysis and subsequent testing.

The Sandvik-Osprey HIPing conditions were previously optimised for CE7 and were thus effective in reducing porosity from 2 - 4 to <0.1area% in Sandvik-Osprey CE7 and from ~1.6 to 0.07% in Oxford CE7. It was not possible to HIP CE7+P or CE7+P+Ce using these conditions because of the presence of low melting point phases. A full HIP optimisation programme for the ternary alloys was not possible. However, two other sets of HIP conditions were investigated as shown in Table 6.2 and designated as 'Specified HIP' and 'Densal® HIP'. The specified HIP conditions were more effective in reducing porosity in CE7+B; whereas the Densal® conditions were more effective for CE7+Sr only. It should be noted that CE7+P and CE7+P+Ce both contained a large volume of intermetallic phases resulting from Cu, P and Ce additions, it is thought these

phases restricted the re-distribution of Al during HIPing and accounts for the high porosity. In addition the presence of intermetallic phases made porosity mapping more difficult owing to difficulty applying a binary threshold to the image and pull-out of brittle phases affecting the apparent porosity values measured, this is reflected in the errors attached to these data. In all cases the Densal® and specified HIP cycles were less effective than the Sandvik-Osprey conditions by virtue of the relatively high temperature and long times of the Sandvik-Osprey HIP conditions.

6.3 Phase fraction as a function of temperature

MTDATA was used to investigate the phase equilibria and solidification of the CE7 alloys modified with P(+Cu), B and Sr. The National Physical Laboratory updated Thermotech database (Saunders) for MTDATA did not include Ce or P interactions. Solidification conditions for both equilibrium and Scheil solidification conditions were considered where no solid diffusion and full mixing in the liquid were assumed, but only those for Scheil conditions are shown here. Figures 6.6(a) shows that for CE7+B primary Si liquidus temperature was 1220°C. AlB_2 formed at 1050°C constituting 2.25% at 560°C and there was a terminating 12.2% Al-Si eutectic reaction at 560°C. CE7+P(+Cu) in Figure 6.6(b) shows the liquidus temperature was 1239°C and no other phases appeared until a Cu suppressed Al-Si eutectic reaction between 531 and 510°C, and the final solidification of Cu enriched liquid Al in an α-Al/Al_2Cu eutectic between 510 and 504°C . Figure 6.6(c) shows that CE7+Sr had a liquidus temperature of 1216°C, an Al-Si eutectic reaction occurred at 560°C and was

complete at 550°C, and there was the formation of 0.23% Al_2Si_2Sr between 770 and 748°C.

MTDATA calculations of likely arrest temperatures for CE7+B and CE7+Sr broadly agreed with the billet cooling curves previously shown in Figure 6.5 and described in Section 6.1.4 that indicated a Al-Si eutectic reaction at ~567°C, compared with the MTDATA predicted temperature of 560°C in CE7+B and CE7+Sr. CE7+P(+Cu) arrests at 534 and 515°C compared well with MTDATA predictions of 531 and 510°C corresponding to the Al-Si eutectic reaction and the formation of Al_2Cu respectively. The temperature arrest seen in CE7+P+Ce(+Cu) at 554°C was attributed to the eutectic reaction predicted at 531°C; a second arrest at 511°C was attributed to the formation of Al_2Cu predicted by MTDATA at 510°C. The formation of other phases in this alloy could not be assessed by MTDATA due to the unusual alloy compositions which were not covered by the thermodynamic database associated with the program.

6.4 Physical characterisation

6.4.1 Bulk compositional analysis

The composition of modified CE7 alloys was assessed using fused bead X-ray fluorescence (XRF) and where appropriate, inductively coupled plasma (ICP) analysis by LSM (Rotherham, UK). In each case samples were taken from 50% of the billet height and the mid-point of the billet diameter. XRF was carried out on 0.2g samples and ICP on 5.0g samples. The measured and nominal bulk alloy compositions are shown in Table 6.3:

Table 6.3: Nominal and measured composition using XRF / ICP of modified CE7 alloys.

Analysis	Alloy	wt%		Addition (wt%)					Impurity (wt%)		
		Al	Si	Cu	P	Sr	B	Ce	Fe	Zr	Ti
Nominal	CE7+B	30.0	69.0	--	--	--	1.0	--	--	--	--
XRF	CE7+B	17.9	78.3	0.02	0.034	<0.01	1.06	--	0.34	0.01	0.42
Nominal	CE7+P	28.13	66.03	5.3	0.9	--	--	--	--	--	--
XRF	CE7+P	22.16	70.45	4.79	0.49	<0.01	--	--	0.35	0.01	0.34
Nominal	CE7+P+Ce	26.5	61.8	5.6	1.0	--	--	5.0	--	--	--
XRF	CE7+P+Ce	24.89	61.62	5.37	0.39	--	<0.01	--	0.19	<0.01	0.06
ICP		--	--	--	--	--	--	5.08	--	--	--
Nominal	CE7+Sr	29.85	69.65	--	--	0.25	--	--	--	--	--
XRF	CE7+Sr	26.79	72.03	0.01	0.03	0.23	<0.01	--	0.19	<0.01	0.05

As previously described in Section 4.3.1, the measured concentrations of Al and Si differed from the nominal composition because of peak overlapping. The intended concentrations of B, P(+Cu), P(+Cu)+Ce and Sr of 1, 0.9(+5.3), 1(+5.6)+5.0 and 0.25% were measured as 1.06, 0.49(+4.79), 0.39(+5.37)+5.08 and 0.23 respectively, showing good agreement for additions of B, Ce, Cu, and Sr. P concentration was lower because of the high vapour pressure of P (Shackelford 2001) and its evaporation from the melt prior to spray forming. Fe, Zr and Ti impurity elements were present in higher concentrations in CE7+B and CE7+P than in CE7+P+Ce and CE7+Sr, and were attributed to the use of different batches of Al-Si feedstock material in these first two spray forming experiments.

Fe concentrations in Oxford alloys were similar to those in Sandvik-Osprey CE7 of 0.26% measured by XRF. Concentrations of Zr were typically ~0.01% in Oxford alloys compared to 0.04% in Sandvik-Osprey CE7 and this difference

was attributed to contamination of the melt prior to spray forming by fragments of a ZrO_3 refractory furnace wash used by Sandvik-Osprey. Ti impurities were ~0.05% in CE7+P+Ce and CE7+Sr and comparable to 0.04% in Sandvik-Osprey CE7; higher concentrations of 0.42 and 0.34% Ti in CE7+B and CE7+P were again attributed to use of a less pure batch of feedstock in those earlier spray forming experiments.

6.4.2 Vickers indentation

Vickers indentation testing was carried out in order to estimate the fracture toughness of Oxford manufactured binary and modified CE7 alloys as described in Chapter 3.3.2. Table 6.4 shows K_{1c} toughness for Sandvik-Osprey and Oxford CE7-based alloys in the HIPed and as sprayed condition, percentage porosity after HIPing is indicated for reference:

Table 6.4: K_{1c} obtained from Vickers indentation.

Material	**As Sprayed**	**HIPed***	**Minimum post HIP Porosity (%)**
	K_{1c} (MPa $m^{1/2}$)	**K_{1c}** (MPa $m^{1/2}$)	
Ox CE7 (binary)	2.84 ±0.21	2.79 ±0.30 (S-O)	0.07
Ox CE7+B	2.45 ±0.18	2.87 ±0.22 (S)	0.37
Ox CE7+P	3.21 ±0.23	3.34 ±0.21 (S)	5.80
Ox CE7+P+Ce	2.28 ±0.36	2.21 ±0.31 (S)	3.92
Ox CE7+Sr	2.64 ±0.26	2.73 ±0.29 (D)	0.28
Sandvik-Osprey CE7	2.29 ±0.46	2.55 ±0.65 (S-O)	<0.1
Sandvik-Osprey CE9	Material not available	2.02 ±0.22 (S-O)	<0.1
Sandvik-Osprey CE11	Material not available	2.36 ±0.16 (S-O)	<0.1

*In each case the densest material as previously determined by image analysis was used for Vickers indentation, Sandvik-Osprey (S-O), Specified (S) or Densal® (D) HIP cycle is indicated and conditions defined in Table 6.2.

Modified HIPed CE alloys had K_{1c} values in the range 2.21 to 3.34MPa $m^{1/2}$ compared with 3.14MPa $m^{1/2}$ for Sandvik-Osprey CE7. Only CE7+P exhibited a small improvement in toughness of ~6% over the Sandvik-Osprey CE7. This alloy also provided the greatest improvement in toughness of~20% over Oxford CE7. In almost all cases there was apparently a small improvement in fracture toughness after HIPing, however this increase was small and typically fell within experimental scatter.

6.4.3 Hertzian indentation

Hertzian indentation testing was also used to determine the fracture toughness of Oxford manufactured binary and modified CE7 alloys as previously described in Section 3.3.3 and shown in Table 6.5, percentage porosity after HIPing is indicated for reference:

Table 6.5: K_{1c} obtained from Herzian indentation data.

Material	As Sprayed	HIPed*	Minimum post HIP Porosity (%)
	K_{1c} (MPa $m^{1/2}$)	K_{1c} (MPa $m^{1/2}$)	
Ox CE7 (binary)	1.27	1.44 (S-O)	0.07
Ox CE7+B	1.13	1.44 (S)	0.37
Ox CE7+P	1.45	2.39 (S)	5.80
Ox CE7+P+Ce	0.89	1.87(S)	3.92
Ox CE7+Sr	0.94	0.98 (D)	0.28
Sandvik-Osprey CE7	1.35	1.68 (S-O)	<0.1

*In each case the densest material as previously determined by image analysis was used for Hertzian indentation , Sandvik-Osprey (S-O), Specified (S) or Densal® (D) HIP cycle is indicated and conditions defined in Table 6.2.

All alloys showed an increase in toughness following HIPing ranging from 109%, for CE7+P+Ce to a negligible increase of 4% for CE7+Sr. Once again CE7+P at 2.39MPa $m^{1/2}$ had a higher toughness than both Oxford and Sandvik-Osprey

CE7, at 1.44 and 1.68MPa $m^{1/2}$ respectively. CE7+Sr had a very low fracture toughness of 0.98 MPa $m^{1/2}$ after HIPing, approaching 0.94 MPa $m^{1/2}$ for pure polycrystalline Si (Ericson 1988).

The increase in fracture toughness after HIPing was due to the partial healing of porosity that is an unavoidable consequence of the spray forming process (Grant 1995a). However, overall there was no strong quantifiable correlation between the magnitude of the reduction in porosity after HIPing in Table 6.2 and the magnitude in the improvement in toughness in Tables 6.4 and 6.5 for Vickers and Hertzian indentation. The fracture toughness determined by Hertzian indentation and Vickers indentation showed a considerable discrepancy with the Vickers technique giving higher and more consistent fracture toughness values than the Hertzian technique. It is thought that the ring-crack fracture criteria in CE alloys was not satisfied due to the presence of the interpenetrating ductile Al phase. The presence of the Al phase is thought to account for the large scatter in Hertzian fracture toughness results and the lack of correlation with the Vickers technique, this effect will be discussed further in section 7.4.3.

6.4.4 Impulse excitation

The Young's modulus of CE based alloys was determined by impulse excitation are shown in Table 6.6, the material measured was that with the lowest available porosity in the HIPed condition.

Table 6.6: Young's modulus of Oxford manufactured modified CE7 determined by impulse excitation.

Alloy	Young's Modulus E (GPa)	Optimum HIP Cycle	Minimum post HIP Porosity (%)
Oxford CE7+B	128.7	Specified HIP	0.37
Oxford CE7+P	121.1	Specified HIP	5.80
Oxford CE7+P+Ce	98.9	Specified HIP	3.92
Oxford CE7 + Sr	123.9	Densal HIP	0.28
Sandvik-Osprey CE7	129.8	Sandvik-Osprey	<0.1

All the CE7-based alloys had similar Young's moduli in the range 121 to 128GPa and comparable to that of Sandvik-Osprey CE7 of 129.8GPa, except CE7+P+Ce that had a significantly lower modulus of 98.9GPa. In general, it appears that with increasing area fraction of porosity, there was a corresponding decrease in Young's modulus. This effect was attributed to the a change in the resonant frequency of the material resulting from the presence of pores and discontinuous intermetallic particles. This effect is particularly apparent in CE7+P+Ce with ~10.8wt% additions of Ce, Cu and P present predominantly as intermetallic phases and porosity of 3.9%.

6.4.5 Optical emission spectroscopy (OES) macrosegregation mapping

Optical emission spectroscopy was used to assess the distribution of solute (Al) and alloy addition (Sr) through the cross section of Oxford manufactured CE7+Sr billet. Other billets were not assessed due to equipment failure. Analysis was conducted on a longitudinal slice through the billet diameter, as shown in Figure 6.7(a). Regions of high porosity at the billet top were not suitable for analysis. Figure 6.7(b) shows a contour map of the concentration of

Al across the CE7+Sr billet with discrete data points indicated by the black dots. There were strong Al gradients between both edge and centre and top and bottom, with Al enrichment at billet periphery and top. At 50% of the billet height, Al concentration varied from ~29% at the periphery to ~26% at the billet centre, while at the mid-radius the Al concentration varied vertically from ~29% at the base to ~31% Al at the top. Sr levels were above the calibrated limit of the machine and could not be mapped. The segregation of Al closely resembled the macrosegregation pattern previously seen in Sandvik-Osprey CE7, Figure 4.4(a) and (b).

6.4.6 Coefficient of thermal expansion (CTE) measurements

Figure 6.8 shows the CTE of Oxford CE7-based alloys and Sandvik-Osprey CE7 in the Y (axial) and X (radial) billet orientations between 25 and 500°C. As previously discussed in Section 4.2.5, Sandvik-Osprey CE7 exhibited a CTE that was ~0.7x10^{-6} °C^{-1} greater in the X orientation when compared to the Y orientation. CE7+Sr also cut in the radial orientation closely followed the Sandvik-Osprey X-axis CTE curve, with a CTE increasing from ~7x10^{-6} °C^{-1} at 100°C to ~9x10^{-6} °C^{-1} at 400°C. The CTE of CE7+B was consistently lower than CE7+Sr or Sandvik-Osprey CE7 with a CTE of ~6x10^{-6} °C^{-1} at 100°C increasing to a maximum of ~7.5x10^{-6} °C^{-1} at 300°C. CE7+P and CE7+P+Ce both had an approximately linear CTE of ~6x10^{-6} °C^{-1} throughout the 25 – 500°C temperature range. In all cases the measured CTE of the alloys was less than that predicted by the rule of mixtures (ROM), as shown on Table 6.7 below. This was attributed to the fine scale of the interpenetrating Si network

microstructure and low thermal expansion of the Si primary phase, whereby the bulk CTE was reduced by the presence of the low CTE, high modulus primary Si phase, which restricted the expansion of the higher CTE Al phase. This effect was evidently enhanced by the presence of intermetallic phases which further reduced the CTE, presumably by the further pinning and inhibiting the thermal expansion of the Al phase

Table 6.7, Summary of the measured and predicted CTE for binary and modified CE alloys.

Alloy	**Measured CTE, x10^{-6} °C^{-1} (in temp range 25 – 400°C)**	**CTE predicted from rule of mixtures*$^{¥}$, x10^{-6} °C^{-1}**
Sandvik-Osprey Binary CE7	X-axis 4 – 9 Y-axis 6 – 10	8.71
CE7+B	6 – 7.5	8.75
CE7+P	6	9.08
CE7+P+Ce	6	9.10
CE7+Sr	7 – 9	8.92

*Elemental CTE data from Smithells, 1978, calculation based on nominal alloy composition
¥Composition from XRF and ICP analysis shown in Table 6.3

6.4.7 Four point bend testing

When a sample is subjected to bending as shown in Figure 3.6(b) a compressive stress is generated in the upper surface and a tensile stress in the lower surface. As the tensile strength of brittle materials is less than the compressive strength, fracture commences at the tensile surface. The modulus of rupture (MOR) is higher than the true tensile strength because only one face of the sample is under tension and due to the limited volume of material under load. The breaking force, modulus of rupture (MOR), estimated true tensile strength (from Equation 4.1) and the Weibull modulus for Oxford HIPed CE7-based alloys and HIPed CE7 Sandvik-Osprey CE7 is shown in Table 6.8.

Table 6.8 Summary of bend tests results indicating the average breaking force, modulus of rupture, estimated true UTS and the Weibull modulus

Alloy	Breaking force (N)	Modulus of rupture (MOR) (MPa)	*Tensile strength (MPa)	Weibull Modulus
CE7+B	534.4	122.4	94.4	16
CE7+P	446.6	100.5	76.5	15
CE7+P+Ce	329.5	74.1	48.0	8
CE7+Sr	555.4	124.6	101.6	22
Sandvik-Osprey CE7	783.1	167.5	135.2	21

*Calculated from Equation 4.1

Table 6.8 shows that the mean breaking force, modulus of rupture and calculated tensile strength of HIPed CE7-based alloys were in every case less than that of Sandvik-Osprey CE7. The best performance was measured for CE7+B and CE7+Sr, the lowest strengths were measured in CE7+P+Ce.

Figure 6.9 presents the bend test data summarised in Table 6.8 as a Weibull plot and indicates significant differences in the bend strength and 'predictability' behaviour of CE7-based alloys. A lower Weibull modulus (the gradient of a best-fit line to the data) indicated more scatter in the data, i.e. a less predictable fracture behaviour, while the position of the data set relative to the X-axis indicated the mean MOR of the material. Sandvik-Osprey CE7 had the highest strength with a similar Weibull modulus to CE7+Sr, being 21 and 22 respectively; CE7+B, and CE7+P were similar at 16 and 15; while CE7+P+Ce had the lowest Weibull modulus of 8. The mean MOR were those previously shown in Table 6.8. Table 6.9 summarises the data in Table 6.8 and Figure 6.9 in terms of total wt% alloying addition (excluding Al and Si).

Table 6.9 Weibull data indicating the Weibull modulus, MOR, Weibull strength ranking for Sandvik-Osprey CE7 and Oxford CE7-based materials measured by 4-point bend testing.

Alloy	Weibull modulus	MOR (MPa)	Weibull strength ranking*	Total wt% alloy addition
CE7+P+Ce	8	74.1	5	11.6
CE7+P	15	100.5	4	6.2
CE7+B	16	122.4	3	1.0
Sandvik-Osprey CE7	21	167.5	1	0.42†
CE7+Sr	22	124.6	2	0.5

* based on curve position against the X axis (relative MOR) in Figure 6.9.
† From Table 4.1, Gravimetric / ICP (solid) analysis of impurities

Further discussion of the influence of the intermetallic phase fraction and alloy additions on the Weibull modulus can be found in section 9.4.5.

6.4.8 Fractography

Scanning electron microscopy (SEM) was used to investigate the fracture surfaces of failed (HIPed) bend test specimens. Figure 6.10(a) shows a typical fracture surface of CE7+B with apparently transgranular cracking of the Si phase (failure through grains following certain crystallographic planes). The Al-rich phase displayed ductile tearing with some plastic deformation. Figure 6.10(b) shows the ductile failure of Al at higher magnification along with cracks in the primary Si phase. The fracture path passed through a ~30μm pore in the material, and again significant plastic deformation of the Al phase was evident.

Figure 6.11(a) shows a typical fracture surface of CE7+P, again showing a brittle transgranular fracture path through the Si phase. The inset Figure 6.11(b) shows a faceted fracture in primary Si, where the crack has apparently

progressed along a macroscopic defect rather than along <110> or <111> cleavage planes as is commonly observed (Brodie 2002, Perez 2000). Again the Al-rich phase failed with significant ductile character. While very fine AlP (1-2μm) particles may be expected for this alloy, they show no phase contrast in SE or BSE images. Figure 6.11(c) shows a BSE image with a fine distribution of 5-10μm Al_2Cu particles identified by EPMA. The multiple crack paths passing through θ-Al_2Cu particles as shown in Figure 6.11(c) suggests that θ-Al_2Cu particles were involved in Si with cracking and failure.

CE7+P+Ce indicating the similar fracture behaviour as CE7+P. However, Figure 6.12(b) shows a BSE image where the crack path passed through blocky ~15 x 60μm intermetallic particles identified as Al-Ce-Cu-Si rich by EPMA, as well as further θ-Al_2Cu particles.

Figure 6.12(b) shows a BSE image indicating a distribution of ~35μm particles that were ascribed to Al_2Si_2Sr on the basis of MTDATA calculations and EPMA measurements. Results for Oxford CE7-based alloys were consistent with brittle transgranular cracking Si and ductile failure of Al seen in Sandvik-Osprey CE7. In every case, stress raising features such as porosity and intermetallic particles were apparently associated with failure.

6.5 Microstructural characterisation

6.5.1 Optical microscopy

Initial microstructural characterisation revealed a dramatic difference in the scale of microstructure exhibited by the Sandvik-Osprey CE7 when compared with all of the Oxford CE alloys. Figure 6.13(a) shows the microstructure of Sandvik-Osprey CE7 with a fine, interpenetrating network of primary Si and divorced Al eutectic. The microstructure is such that the primary Si network is permeated and delineated by a sinuous network of Al, with neither phase having isolated regions larger than ~ 30μm, and interconnectivity with adjacent particles apparent throughout both phases. Oxford binary CE7 was sprayed under conditions designed to replicate Sandvik Osprey CE7 as described in Section 3.5.1. The resultant microstructure shown in Figure 6.13(b) resembles Sandvik-Osprey CE7 in all aspects except for the scale of the particles which constitute the interpenetrating network. Al regions are larger and there is apparently reduced connectivity of the Al 'islands', regions of primary Si are larger, often >70μm. Alloy additions of B, P, P+Ce and Sr had little effect on refining the scale of the network structure as shown in Figures 6.13(c) – (f) respectively. The scale of the microstructure was quantified using image analysis as described in Section 6.5.2. The most apparent effect of the alloy additions was to form intermetallic phases of varying size and morphology.

Figure 6.14(a) shows that the microstructure of CE7+B resembled Sandvik-Osprey CE7 shown in Figure 4.13 (a-c). Borides of a hexagonal morphology, typically 6 – 10μm diameter were distributed through the Al and Si networks.

Contrast in optical microscopy suggested two boride stoichiometries of similar morphology and the Al-B phase diagram in Figure 6.14(b) indicates these to be AlB_2 (lighter) and AlB_{12} (darker), and as shown in Figure 6.14(c) and 6.14(d) respectively. The boride compositions were later confirmed by EPMA. Intermetallic Al-Fe-Si phases with an acicular morphology were distributed throughout the Al phase as shown in Figure 6.14(c) and 6.14(d).

Figure 6.15(a) & (b) shows the microstructure of CE7+P resembled Sandvik-Osprey CE7 shown in Figure 6.13(a) and consisted of an interpenetrating network of primary Si and an Al-rich phase. Figure 6.15(a) shows AlP particles were present in the Si network but in many cases appeared to have 'pulled out' of the matrix during preparation leaving pits in the Si surface, suggesting poor adherence to the Si matrix. Figure 6.15(b) shows the Al-rich phase was interspersed with regions of α-Al / Al_2Cu eutectic lamellae. Figure 6.15(c) & (d) shows the microstructure of CE7+P+Ce resembled Sandvik-Osprey CE7 shown in Figure 6.13(a). The Al-rich network contained regions of α-Al / Al_2Cu eutectic, and was also interspersed with mixed morphology Al-Ce-Cu-Si phases, often with cracks initiating in the Ce containing phases and propagating into the surrounding Si matrix. As previously observed in CE7+P, there was evidence of AlP in the primary Si network and 'pull out' of AlP during sample preparation. Figure 6.15(e), (f) & (g) shows the primary microstructure of CE7+Sr resembled Sandvik-Osprey CE7 shown in Figure 6.13(a) but throughout the Al-rich network there were intermetallic phases of plate and script morphology ascribed to Al_2Si_2Sr and shown in Figure 6.15(f) and 6.15(g) respectively. In all cases the

phases indicated in Figures 6.14(a), (c) & (d) and 6.15(a-g) were identified by EPMA, although in some cases it was not possible to identify an exact stoichiometry because of interaction volumes, as described in Section 3.2.5.

6.5.2 Image analysis - interface length

Image analysis previously described in Section 3.2.3 was used to determine the interface length of Oxford CE7-based alloys. Representative micrographs, typical of those used in image analysis are shown in Figure 6.13(a) – (f). CE7+P+Ce could not be analysed due to the problems of grey-level thresholding the large number of phases of differing contrast. Additional information regarding the distribution of phases was obtained and included the number of discrete Al sites / unit area and a shape factor for the Si phases where 1 represented a perfect circle and 0 represented a line. Calculated from Equation 4.2 the data from image analysis are summarised in Table 6.10 below:

Table 6.10: Inter-phase interface length and Al phase distribution determined by image analysis for Oxford CE7-based alloys and Sandvik-Osprey CE7.

Alloy	Average number of discrete Al sites/mm^2	Interface length (mm/mm^2)	Average circularity
Oxford CE7	84.3	8.3	0.46 ±0.03
CE7 + B	121.6	7.6	0.61 ±0.02
CE7 + P	101.3	6.1	0.47 ±0.03
CE7 + Sr	83.0	6.3	0.56 ±0.02
CE7+P+Ce	Not measured due to difficulty applying binary threshold		
Sandvik-Osprey CE7	168.6	14.6	0.55 ±0.02

Sandvik-Osprey CE7 has an interface length of ~14.6mm/mm^2 compared to 6.1 - 8.3mm/mm^2 for Oxford CE7 and CE7-based alloys. Sandvik-Osprey material

also had a significantly larger number of discrete Al sites being ~168/mm^2 compared with 83 – 121/mm^2 for Oxford CE7 and CE7-based alloys. The larger inter-phase interface length in Sandvik-Osprey material was attributed to the use of a particle injector during manufacture of the Sandvik-Osprey alloy. The effect of particle injection is discussed further in Section 7.1.

Differences between Oxford manufactured alloys were attributed largely to experimental scatter with no clearly discernible effect of alloy additions on interface length or number of discrete Al sites. A circularity of 0.61 for CE7+B showed it had the least faceted Si morphology followed by CE7+Sr, Sandvik-Osprey CE7, CE7+P and Oxford CE7 with circularities of 0.56, 0.55, 0.47 and 0.46 respectively.

6.5.3 Electron Probe Micro Analysis (EPMA)

Electron probe micro analysis (EPMA) showed that similarly to the Sandvik-Osprey CE7, CE7-based alloys show no evidence of α-Al / Si eutectic, or fine scale Si precipitation. Typically the Al-rich phase contained approximately 0.23wt% Si compared with a maximum solid solubility of 0.05wt% at 300°C (Murray 1984). Assuming all the Si was in solid-solution (small precipitates below the resolution of EPMA cannot be discounted), then the relatively high Si concentration may be attributed to the non-equilibrium solidification conditions and Si electron beam interaction volume effects whereby the incident electron beam stimulated emission from adjacent or underlying regions of Si phase (beam interaction volume was ~2μm^3 compared with a Al regions of ~5-15μm). As expected and previously seen in optical microscopy a variety of intermetallic

phases, resulting from deliberate additions and impurity elements, were interspersed through the Al-rich and primary Si networks. The small size of many of the intermetallic particles made quantitative analysis difficult because of beam interaction volume effects. Where stoichiometry is given, sufficient numbers of large particles were analysed to give confidence in the result, where phases were small or of low volume fraction they are ascribed a label based on their primary constituents. X-ray diffraction (XRD) and wet chemical methods for intermetallic phase extraction were explored but the low volume fraction of intermetallics and difficulty in extracting particles from a Si matrix made accurate quantitative analysis difficult.

Figure 6.16(a) shows a typical BSE image of CE7+B showing acicular Al_4FeSi and AlB_2 (ringed) and AlB_{12} (arrowed). Figure 6.16(a) shows borides distributed throughout the microstructure, predominantly in the Si phase. The Al-8B master alloy added to the Si-Al melt consisted primarily of Al and AlB_{12}. At ~1350°C AlB_{12}+liquid transformed to AlB_2+liquid by a quasi-peritectic reaction as shown in the phase diagram in Figure 6.14(b). However this reaction is slow and results here suggest that it did not proceed to completion. Figures 6.16(b)-(f) show WDX elemental concentration maps corresponding to Al, B, Si, Zr and Ti respectively. Figures 6.16(b)-(d) show the borides were distributed throughout the primary Si and Al-rich phases. The addition of B appeared to have a beneficial effect on the Zr and Ti impurities which did not form large intermetallic particles as previously seen in the Sandvik-Osprey binary CE7 but were present as a finer dispersion, as indicated in Figures 6.16(e) and 6.16(f) respectively.

Figure 6.17(a) shows a BSE image of CE7+P with suggested stoichiometries of all major phases indicated and corresponding Al, Fe, Si, P and AlP WDX elemental concentration maps in Figures 6.17(b)-(f) respectively. Figure 6.17(b) implies that Cu was present in the Al-rich phase as lamellar eutectic structure consisting of Al_2Cu and Al ~0.9%Cu copper solid solution. There were large intermetallic phases with the approximate stoichiometry Al_4FeSi_2, as shown in Figure 6.17(c) that were often ~1mm in length and penetrated the Si phase. Figures 6.17(d)-(f) show the fine distribution of AlP throughout the primary Si network. Figure 6.18(a) shows a region of primary Si with several high angle Si-Si grain boundaries, Figure 6.18(b) shows the corresponding X-ray intensity map for P and with the location of grain boundaries overlaid in Figure 6.18(c). These images together suggest a ~2μm AlP particle at a Si-Si triple point and perhaps implicated in the nucleation of two or more primary Si grains. This is supported by subsequent EBSD results in Figure 6.24(f) showing AlP at Si-Si grain boundaries and Si grain centres.

Figure 6.19 shows a BSE image of CE7+P+Ce with a now more complicated microstructure consisting of interpenetrating primary Si and Al-rich phase interspersed with a range of phases determined approximately by EPMA to be Al_4Cu_2CeSi, $AlCuCe_6Si_{11}$, $Al_6Cu_3Ce_4Si_6$ Al_8Fe_2Si, Al_2Cu, TiC and TiN. Figure 6.20(a) shows a backscattered electron image of CE7+P+Ce with corresponding Si, Al, Ce, Cu, Fe, Ca, P, Zr and Ti WDX elemental concentration maps in Figures 6.20(b)-(j) respectively. Figures 6.20(b)-(e) show blocky, acicular Al-Cu-Ce-Si rich phases with suggested stoichiometries based

on repeated analysis of multiple samples of Al_4Cu_2CeSi, $AlCuCe_6Si_{11}$, $Al_6Cu_3Ce_4Si_6$ dispersed through the Al-rich and primary Si network. Figures 6.20(f) and 6.20(g) show trace impurities of ~0.1wt% Fe and Ca associated with Al-Cu-Ce-Si phases and occasional Al_8Fe_2Si intermetallics of varying size and morphologies. Figure 6.20(h) shows 2 – 6μm P particles present as AlP finely distributed through the primary Si network. Figure 6.20(h) shows Zr finely dispersed with no evidence of Si-Ti-Zr intermetallic phases previously observed in the Sandvik-Osprey CE7, shown in Figure 4.19(d & e). Figure 6.20(j) shows Ti was present as small (~2μm) particles of blocky morphology attributed to TiN formed with N_2 atomising gas. Figure 6.21(a) shows a BSE image of Al-Cu-Ce-Si particles, that had a banded composition with ~70%Ce at the centre, 50%Ce in the intermediate regions and 35%Ce at the periphery. Figure 6.21(b) shows a WDX Ce concentration map showing the typical blocky, faceted morphology of a banded particle. Figure 6.21(c) indicates the three bands of composition more clearly.

Figure 6.22(a) shows a BSE image of CE7+Sr with suggested stoichiometries of major phases indicated and corresponding Si, Al, Sr and Fe WDX elemental concentration maps in Figures 6.22(b)-(e) respectively. The Al-rich phase was interspersed with 10-20μm blocky, faceted Sr containing phases of suggested stoichiometry Al_2Si_2Sr as shown in Figures 6.22(a)-(d) and previously predicted by MTDATA in Section 6.3. The inset in Figure 6.22(a) shows a cracking, typical of this phase, suggesting the phase is brittle. Figure 6.22(c) and 6.22(e) show the Al-rich phase also contained numerous acicular Fe containing intermetallics

of typical size 2 x 20μm and ascribed to Al_5FeSi. There was no evidence of the Al-Ti-Zr intermetallic phases or Ti rich particles previously observed in the Sandvik-Osprey CE7 and shown in Figure 4.19(d & e).

6.5.4 Electron backscatter diffraction (EBSD)

EBSD orientation data for CE7+B was partitioned into Al and Si maps using concurrently collected EDS data. The Al orientation map and corresponding pole figure are shown in Figures 6.23(a) and (b) respectively indicating that the analysis area consisted primarily of two large Al grains, interpenetrated by primary Si. Figure 6.23(b) shows strong texture, indicating the analysis area consisted of two grains delineated by high angle grain boundaries. It was not possible to deduce an Al grain size from this data, although inspection of orientation maps suggests grains >200μm. Figures 6.23(c) and (d) are the Si orientation map and corresponding pole figure respectively for the same data set and show that the primary Si phase consisted of a fine (4.8μm excluding twin boundaries and 4.3μm including twin boundaries), random, equiaxed grain structure. The orientation key corresponding to 6.23(a) and (c) is given in 6.23(e)

The Al orientation map and corresponding pole figure for CE7+P are shown in Figures 6.24(a) and (b) respectively. The analysis area consisted of approximately three large Al grains interpenetrated by Si, with occasional dendritic patterns in the Al phase because of the lamellar eutectic growth of α-Al / Al_2Cu. Figure 6.24(c) shows the same data set partitioned for Si showing a

large number of fine, twinned equiaxed grains with an average grain size of 9.1μm excluding twin boundaries and 7.6μm including twin boundaries. The corresponding pole figure given in Figure 6.24(d) shows the distribution of fine, randomly orientated Si grains. The orientation key corresponding to 6.24(a) and (c) is given in 6.24(e). Figure 6.24(f) shows an EDS combination map for Si (blue) and P (green) concentration, with high angle (>15°) Si grain boundaries superimposed in white showing AlP particles (identified by EPMA) in the centre of Si grains and at many Si-Si grain boundaries and triple points suggesting that P was successful in nucleating primary Si.

The Al orientation map for CE7+P+Ce and corresponding pole figure are shown in Figures 6.25(a) and 6.25(b) respectively. The analysis area consisted of approximately six large (75 - 100μm) Al grains interpenetrated by Si, and approximate Al-Al grain boundaries are indicated in white. Figure 6.25(c) shows the same data set partitioned for Si showing a large number of fine, equiaxed grains with an average grain size of 7.3μm excluding twin boundaries and 5.1μm including twin boundaries. The corresponding Si pole figure in Figure 6.25(d) again shows the random distribution of grain orientations. Figure 6.25(e) shows a portion of an EBSD orientation map for P showing the random orientation and fine distribution of AlP particles. The orientation key corresponding to 6.25(a), (c) and (e) is given in 6.25(f).

The Al orientation map for CE7+Sr and corresponding pole figure are shown in Figures 6.26(a) and 6.26(b) respectively, showing one large Al grain continuously interpenetrated by primary Si. Figure 6.26(b) shows very strong

texture, indicating the analysis area consisted of one large grain with little sub-structure. The Al-rich phase was investigated further investigated using a larger scan area with a coarser 5μm step. Figure 6.26(c) shows that the second analysis area also consisted of one large Al grain estimated to be >1.25mm diameter. Figure 6.26(d) shows the same data set as 26.26(a) partitioned for Si showing a large number of fine, equiaxed grains with an average grain size of 6.4μm excluding twin boundaries and 5.6μm including twin boundaries. The corresponding Si pole figure is given in Figure 6.26(e) and again shows the random distribution of Si grain orientations. The orientation key corresponding to 6.26(a), (c) and (d) is given in 6.26(f)

6.5.4.1 Si grain size

EBSD was the only effective method of measuring the Si grain size distribution (GSD) since chemical etches for Si-Si grain boundaries proved unsuccessful as described in Section 3.2.2. The Si GSD for Sandvik-Osprey CE7 and Oxford CE7-based materials is shown in Figure 6.27, where twins boundaries were treated as high angle grain boundaries, and a probe step size of 1.5μm (as described in Section 3.2.6) was used in each case. All Oxford material showed a similar GSD with modal Si size of ~5-9μm, summarised in Table 6.11 below. Sandvik-Osprey CE7 material showed a broader GSD and an average grain size of 4.1μm, with a larger population of small grains and few grains >10μm. This difference was attributed to particle injection used at Sandvik-Osprey during manufacture providing a large number of additional nucleation sites. The full GSD could not be obtained as grain size measurement was limited by the

step size of the EBSD analysis giving a minimum grain resolution of ~2.3μm as described in Section 3.2.6.

6.5.4.2 Al grain size

It was not possible to obtain an accurate indication of the Al grain size from EBSD measurements as the analysis areas typically only incorporated a few (1-5) Al grains. Nevertheless an indication of length scale can be estimated B and P modified CE7 appeared to have Al grains >200μm whereas P-Ce modified CE7 appeared relatively refined with an Al grain size of ~75-100μm, Al grains in CE7+Sr were >1.25mm.

Table 6.11 Summary of grain size data for primary Si and Al in Sandvik-Osprey CE7 and all Oxford modified CE7 alloys.

Alloy	**Si Grain Size***	**Al Grain Size (estimated)**
Sandvik-Osprey CE7	4.1	300μm
CE7+B	5.0	>200μm
CE7+P	7.1	>200μm
CE7+P+Ce	6.8	75-100μm
CE7+Sr	9.7	>1250μm

*Including twin boundaries as high angle grain boundaries

6.6 Summary

- Spray formed Al-Si alloys modified with B, P, P & Ce and Sr were successfully produced at Oxford university.
- Controlled post-spray cooling and solidification of billets was achieved in order to replicate the Sandvik-Osprey processing conditions.
- Solidification profiles of the spray formed alloys broadly agreed with MTDATA predictions the equilibrium solidification.

- HIPing at non-optimised conditions yielded only a small decrease in billet porosity.
- A fracture toughness of 2.2 – 3.3MPa $m^{1/2}$ was measured on modified CE7 alloys using Vickers indentation. Hertzian indentation yielded results ~50% lower than the Vickers technique.
- Young's modulus was broadly similar to Sandvik-Osprey CE7, but decreased with increasing porosity and increasing intermetallic fraction.
- CTE of modified CE alloys does not obey the rule of mixtures.
- The Weibull modulus of modified CE alloys ranged from 8 to 22 and decreased with increasing intermetallic phase content.
- Intermetallic particles appear to be associated with crack initiation and fracture.
- The inter-phase interface length of all modified CE alloys is around half that of Sandvik-Osprey CE7.
- EPMA shows cracking within intermetallics, sometimes propagating to matrix Si.
- EPMA shows AlP successfully nucleating primary Si.
- EBSD shows a fine equiaxed Si grain size interpenetrated by large Al grains.
- Al grain size is 75 – 1250μm, Si grain size is 5 – 10μm in modified CE alloys

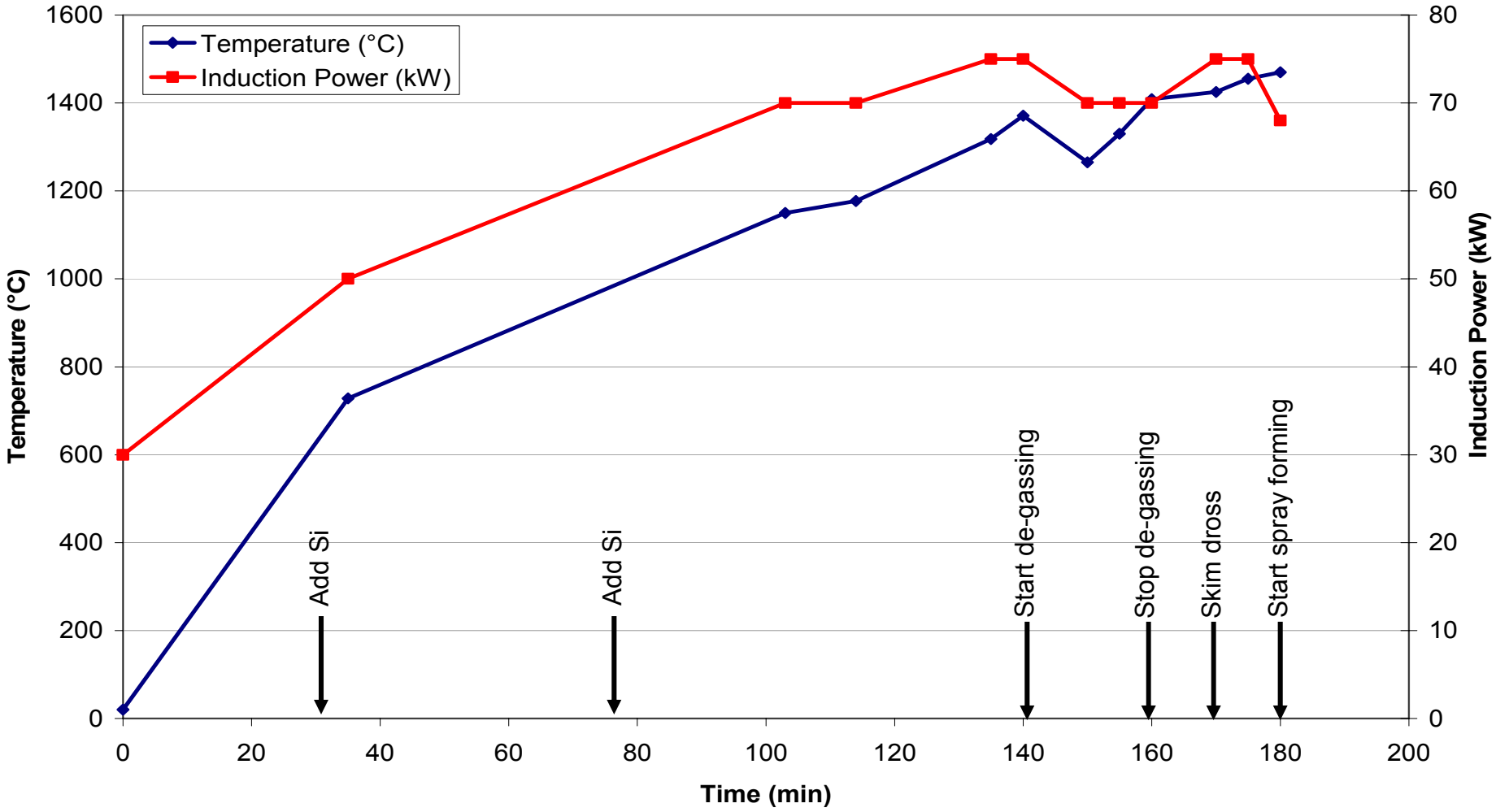

Figure 6.1

Typical charge melting profile and corresponding induction furnace power. Key operations (de-gassing, dross skimming, alloy additions) are indicated.

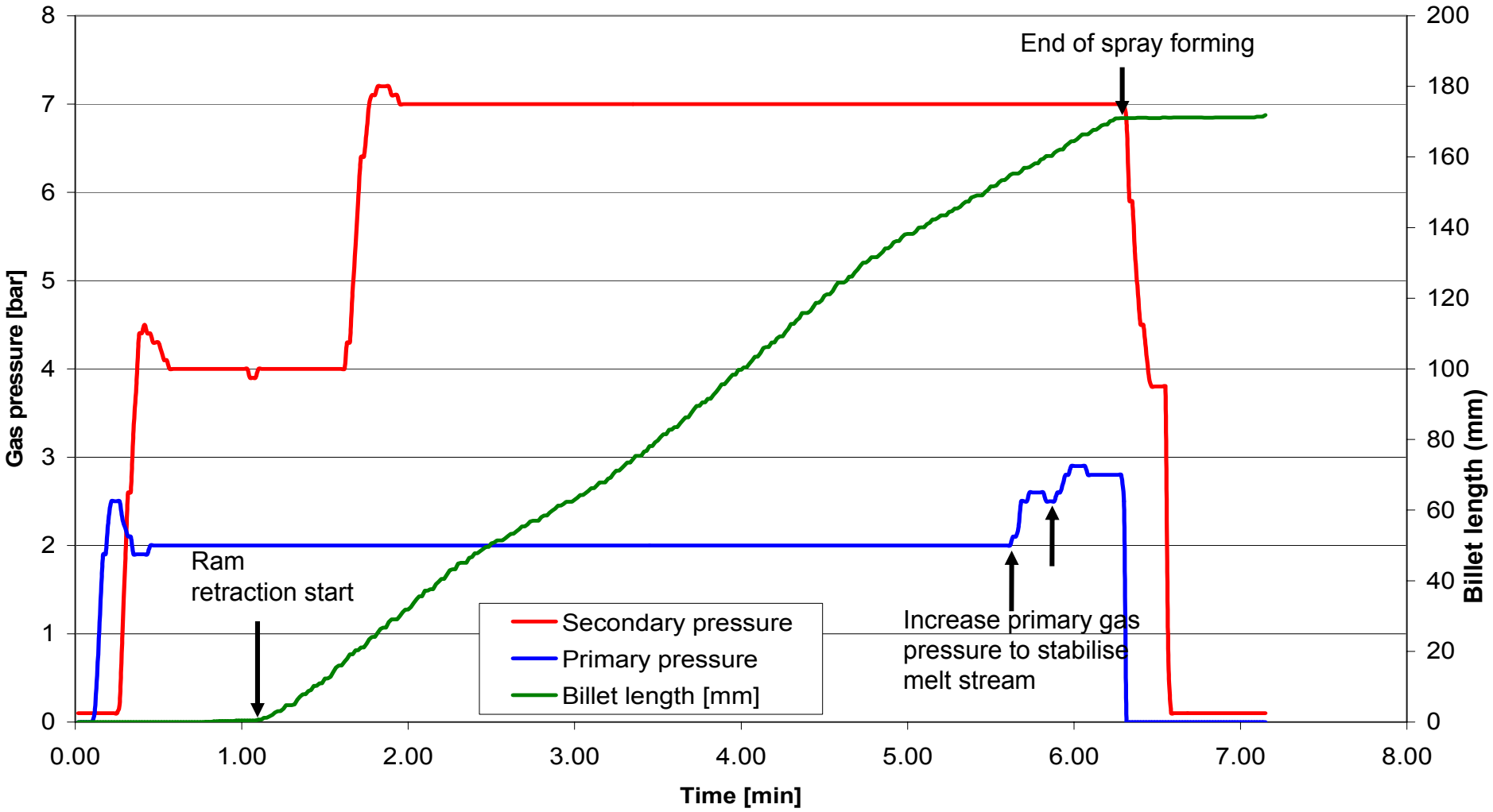

Figure 6.2

Typical primary and secondary gas pressures and billet growth during a spray forming experiment as a function of time.

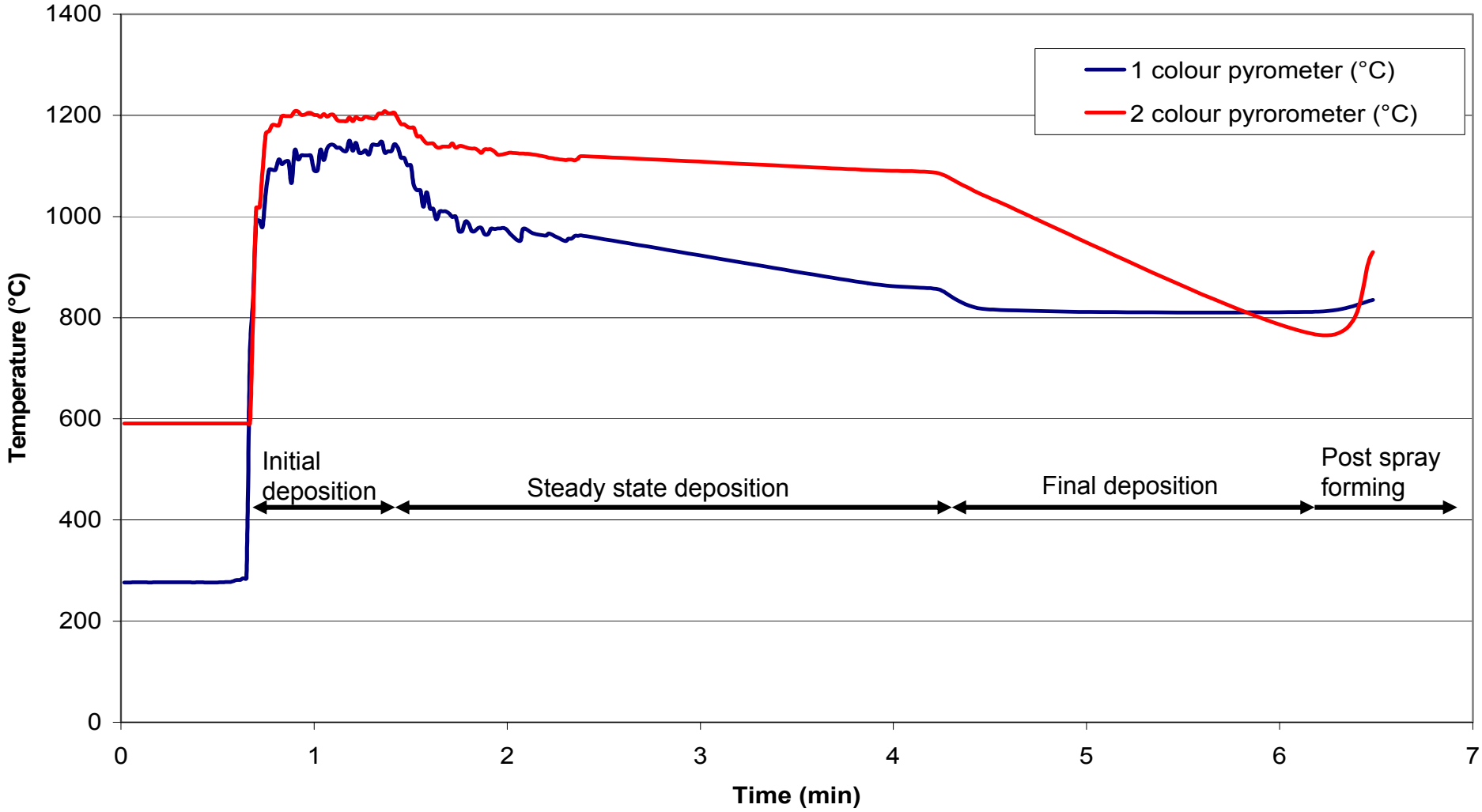

Figures 6.3

Manually filtered one and two colour pyrometer data with obscuration by overspray powder removed, indicating the temperature during initial, steady state and final deposition and post spray temperature.

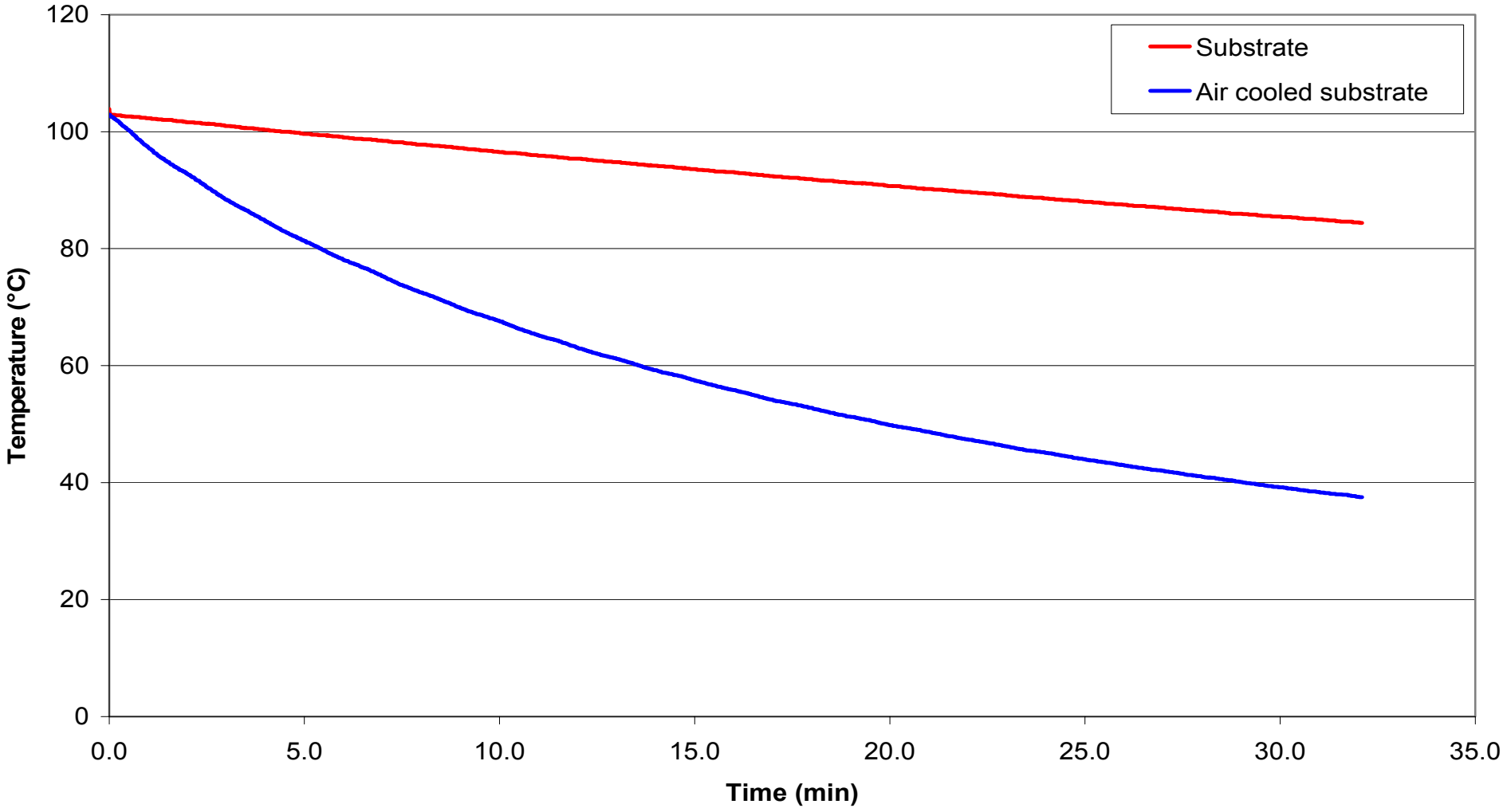

Figures 6.4

the temperature of the modified Oxford collector plate with and without the effect of a forced air cool as a function of time

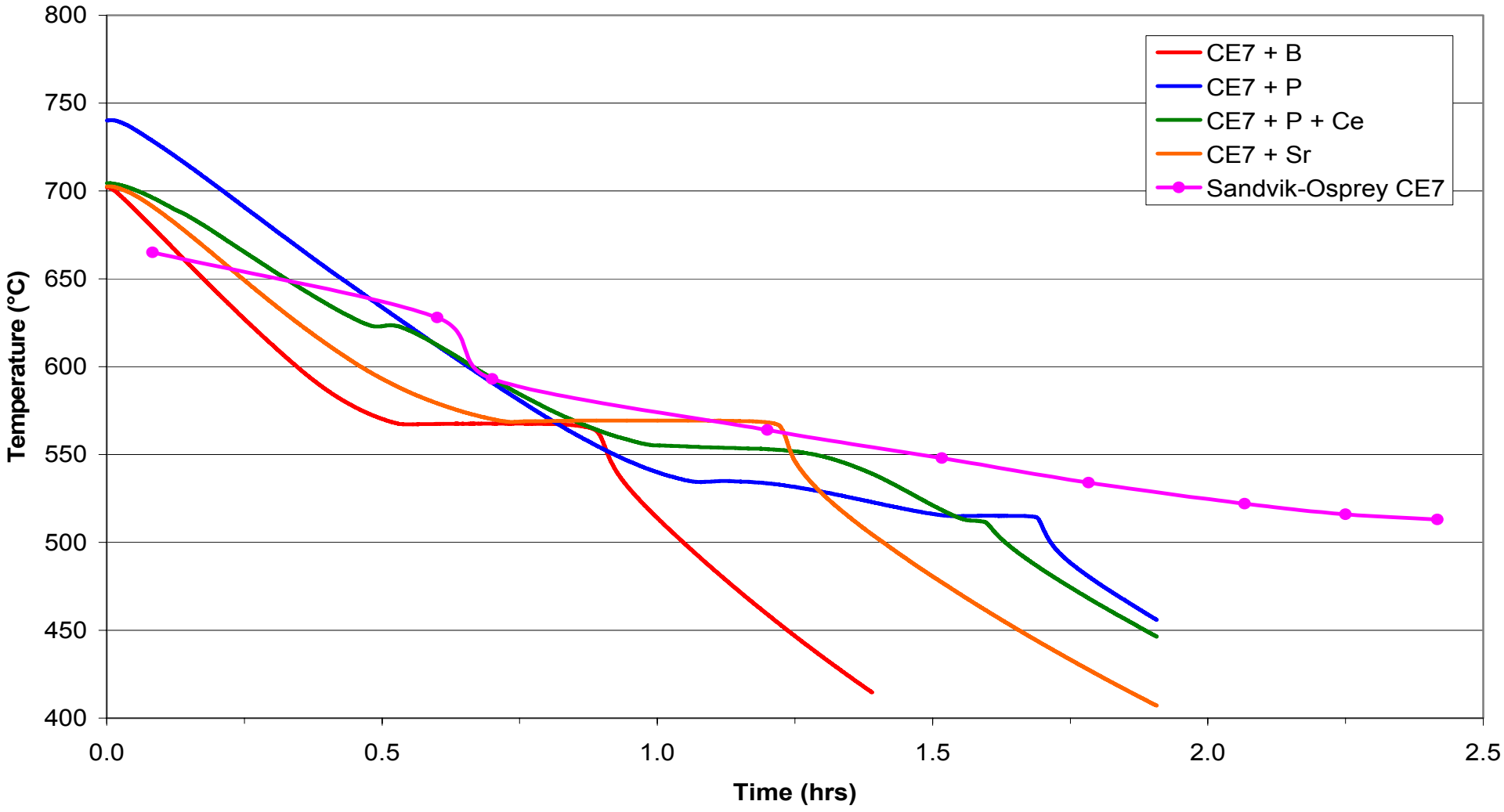

Figures 6.5

The temperature of modified CE7 billets sprayed at Oxford and the binary CE7 billet spray formed at Sandvik-Osprey as a function of time

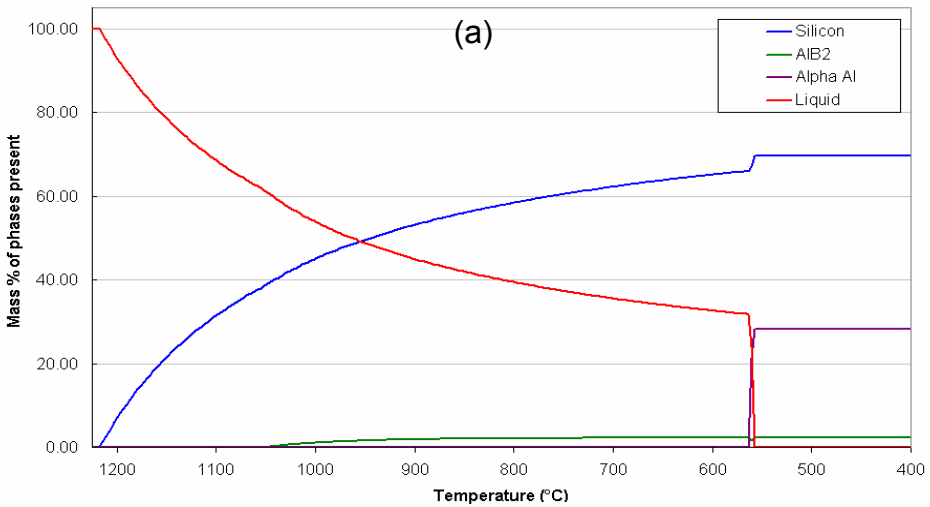

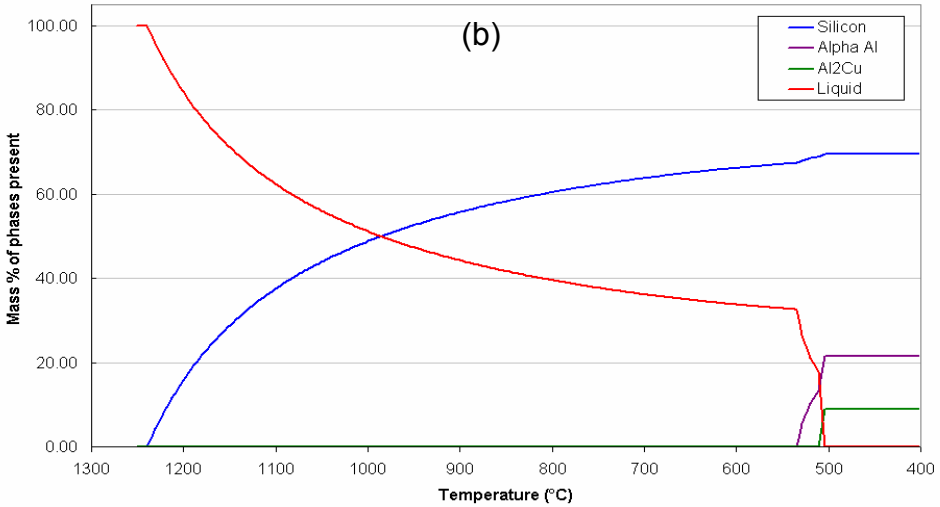

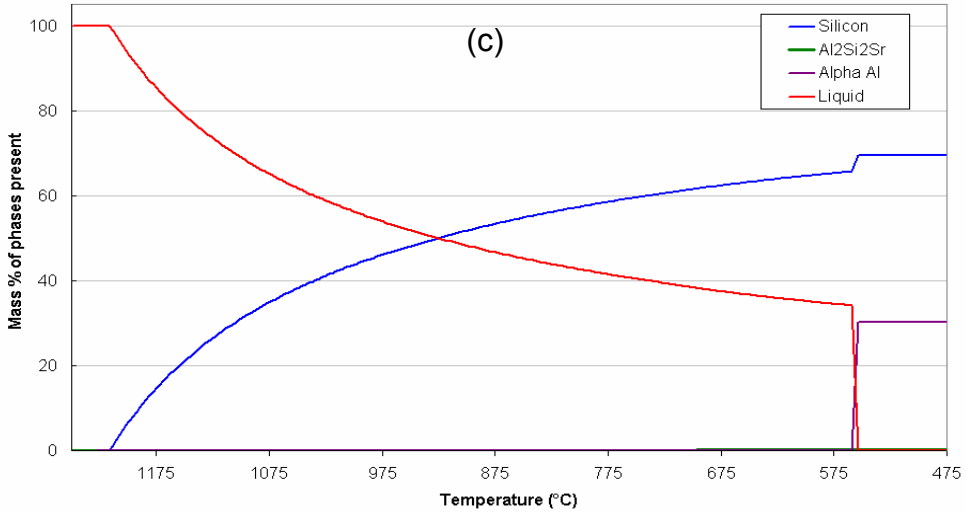

Figures 6.6
MTDATA plot of mass% of phases as a function of temperature assuming Scheil solidification conditions for (a)CE7+1%B, (b) CE7+5% Cu, (c) CE7+1% Sr

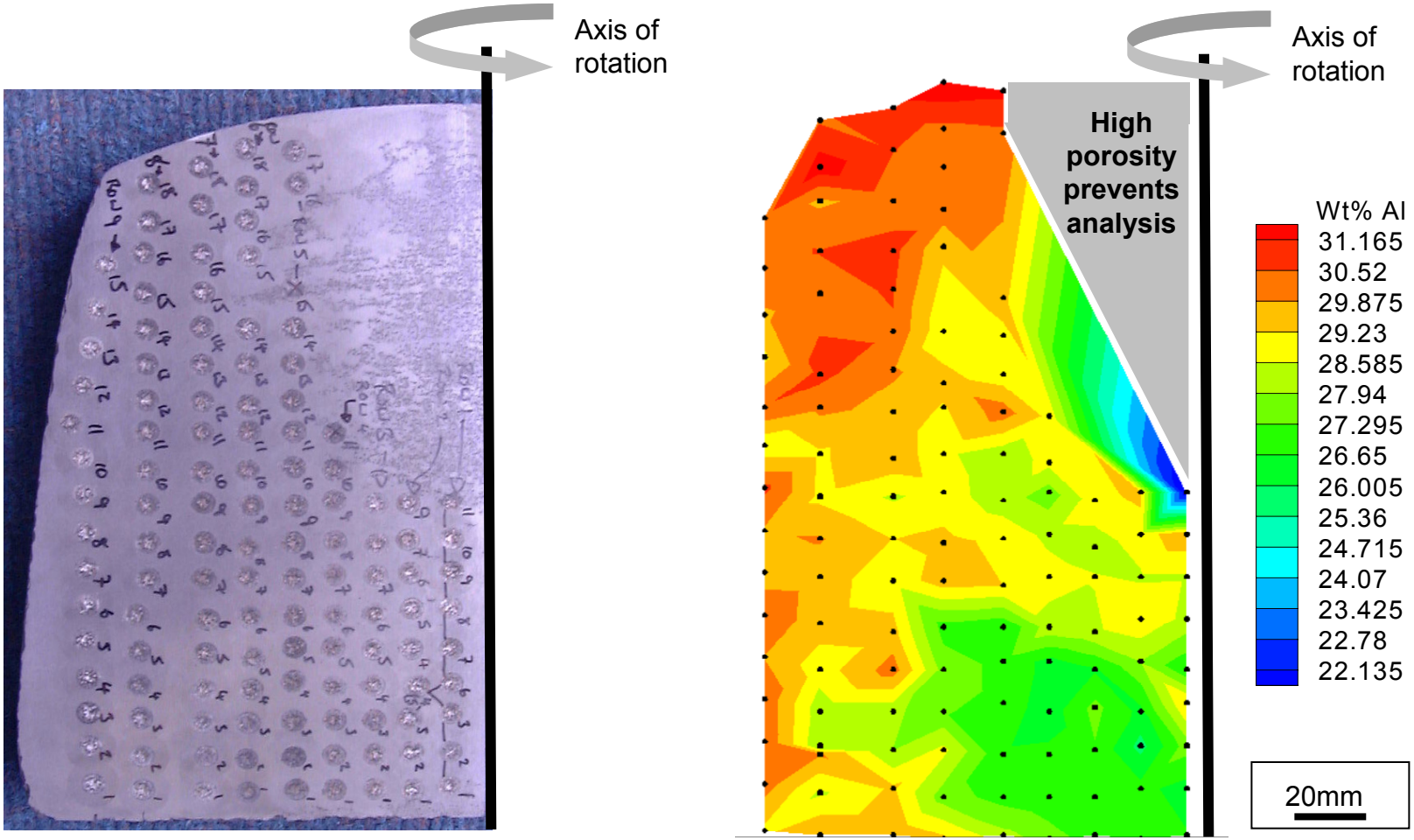

Figures 6.7(a) and 6.7(b)
(a) CE7+Sr showing OES analysis sites a and region of high porosity at the billet top centre and (b) a contour plot of Al concentration as a function of billet position for Oxford CE7+Sr.

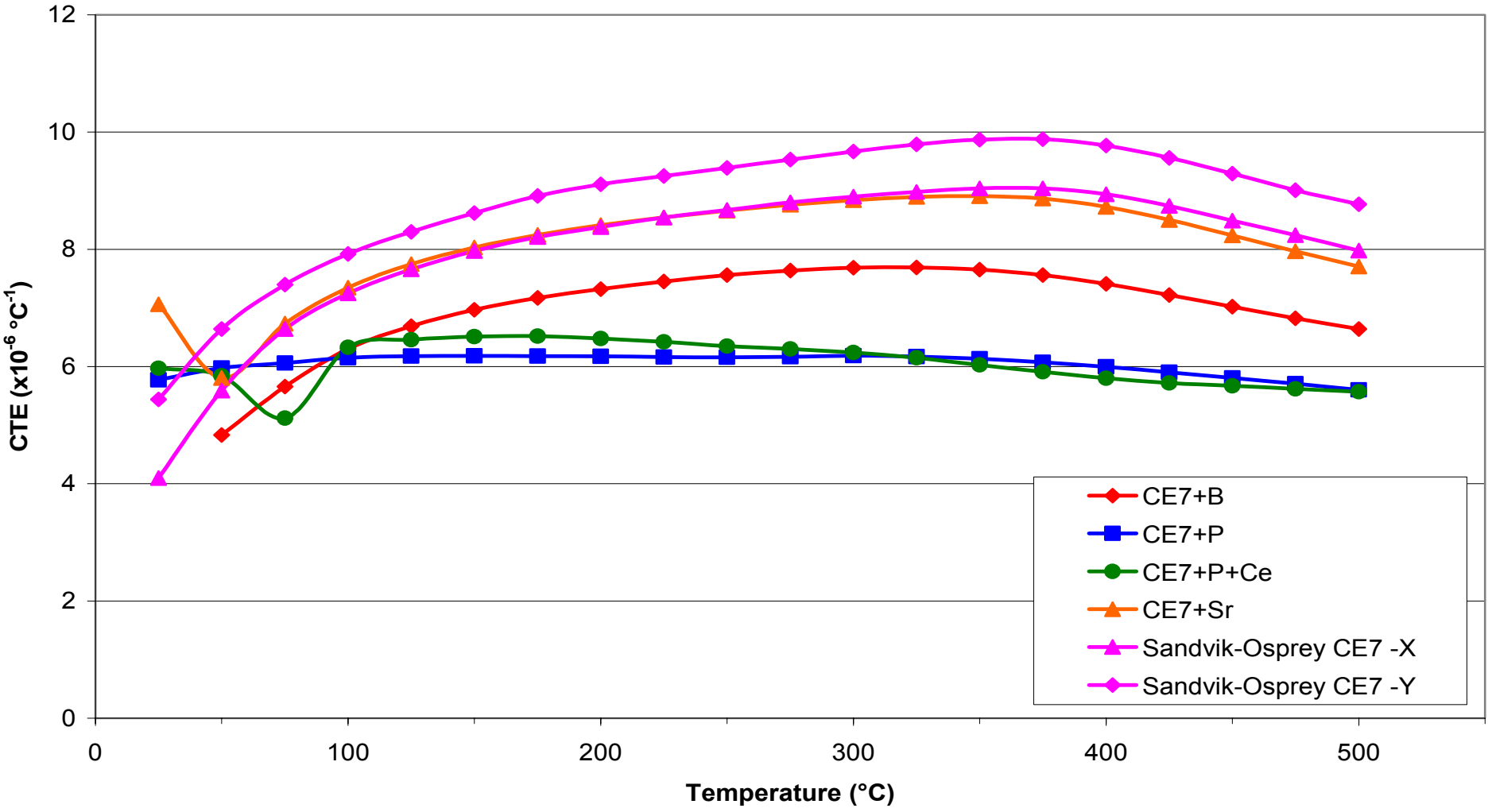

Figure 6.8

Coefficient of thermal expansion (CTE) of Oxford CE7-based alloys and Sandvik-Osprey CE7 in X (radial) and Y (axial) billet orientations as a function of temperature

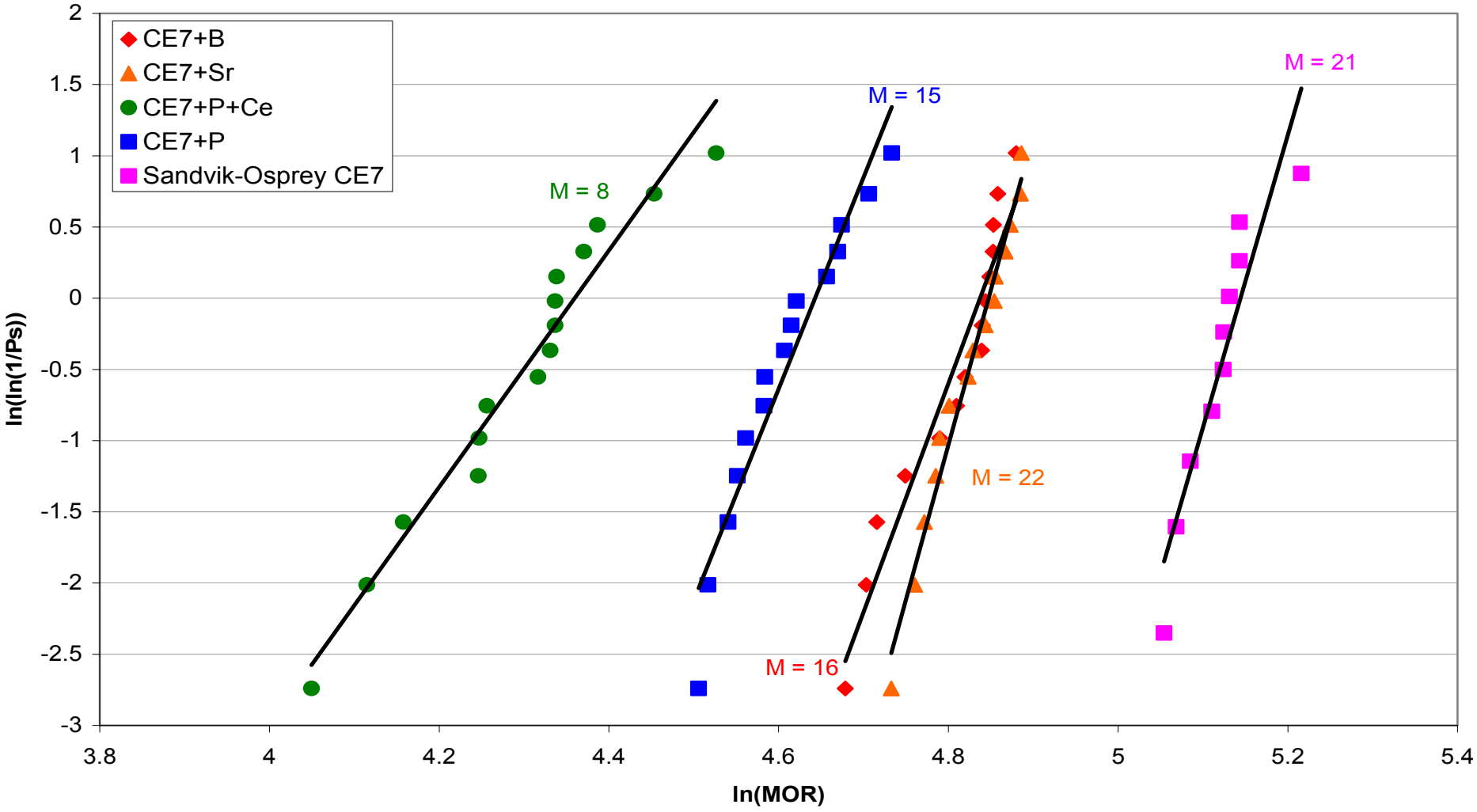

Figure 6.9

Bend test data presented as a Weibull modulus plots for HIPed Oxford CE7-based alloys and Sandvik-Osprey CE7

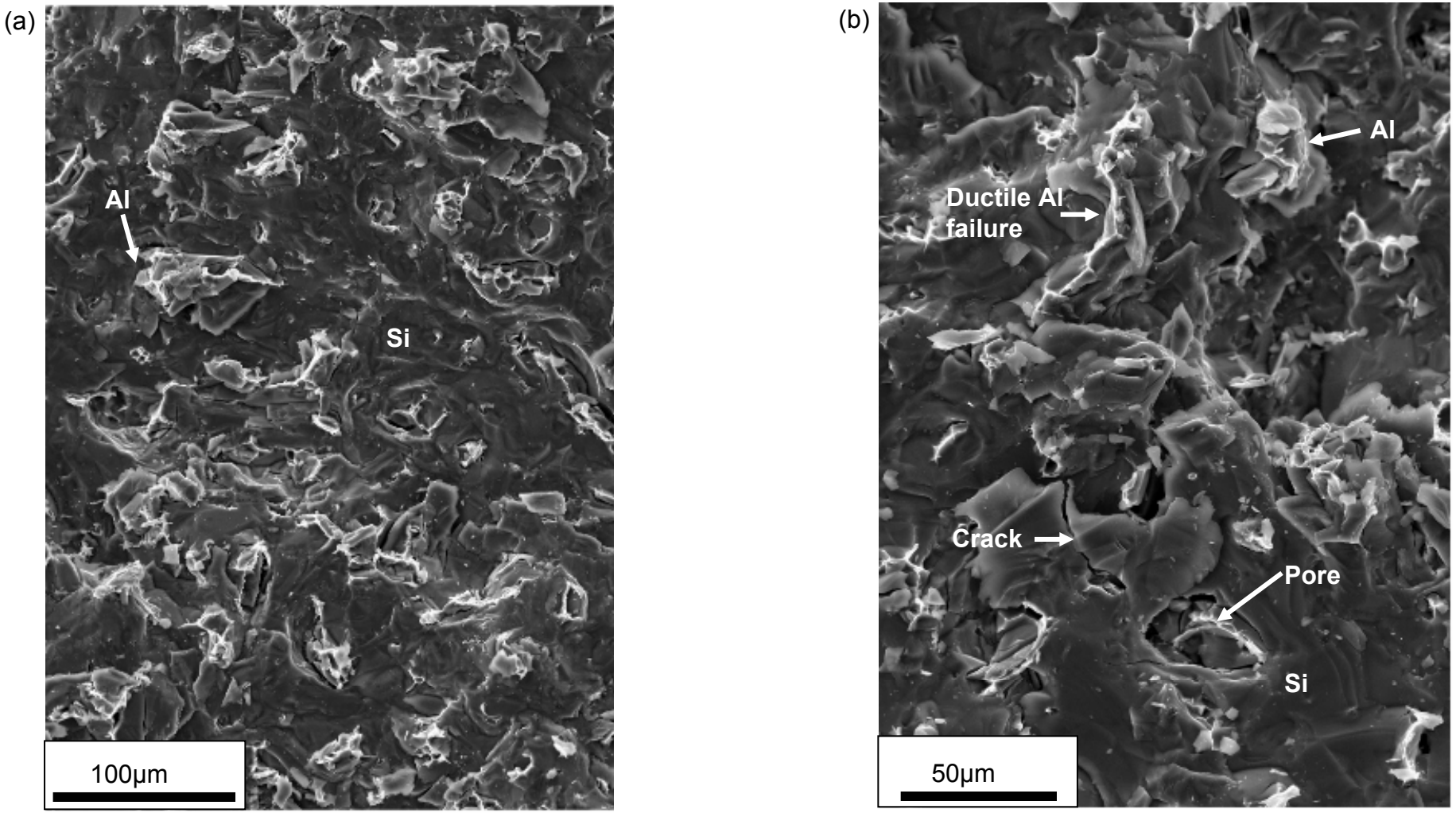

Figures 6.10(a) and 6.10(b)

CE7+B SEM secondary electron micrographs of bend test specimen fracture surfaces (a) low magnification showing brittle Si failure and ductile Al failure, and (b) high magnification showing cracks in the Si phase and pores.

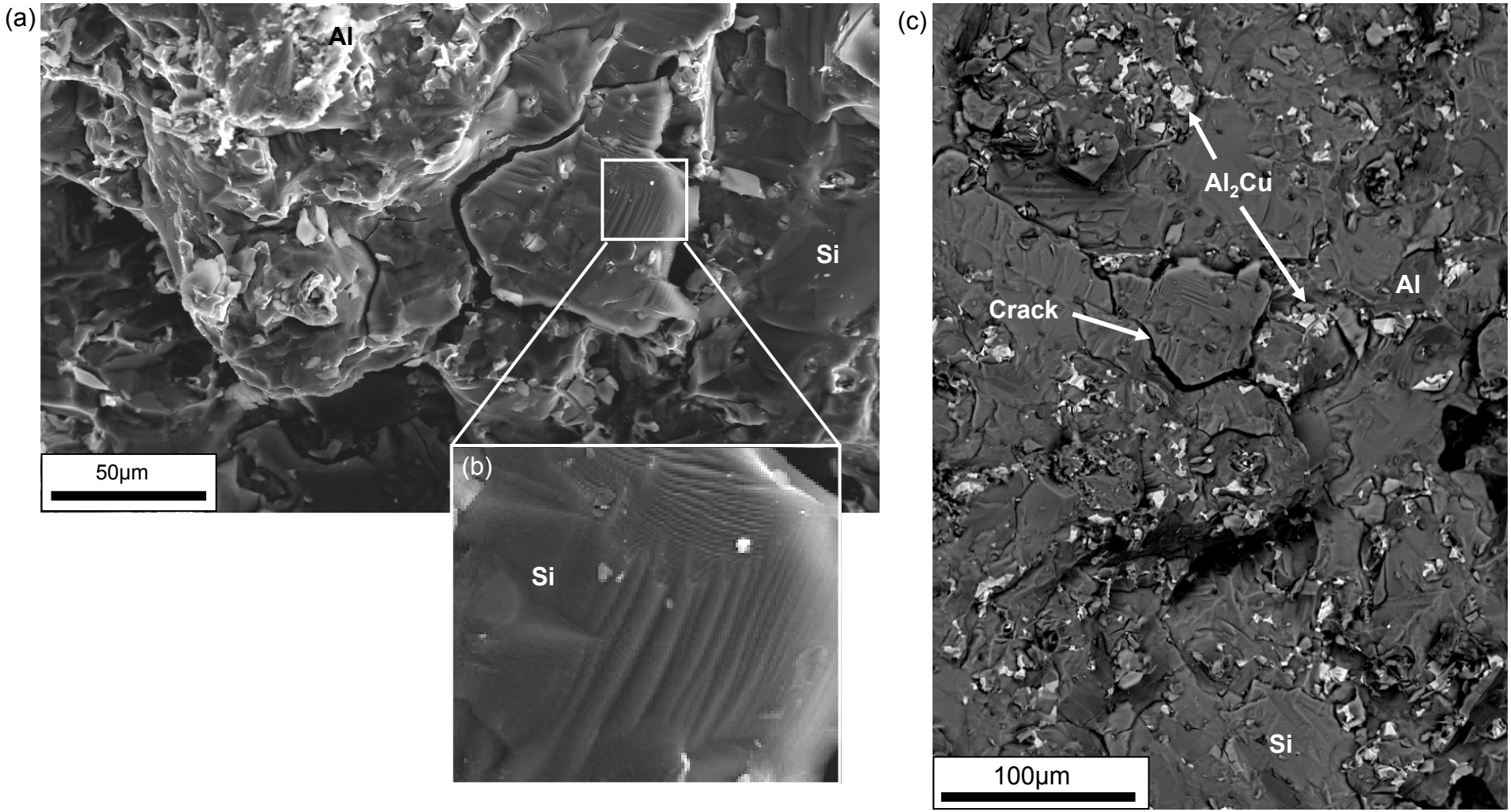

Figures 6.11(a) – 6.11(c)

CE7+P SEM micrographs of (HIPed) bend test specimen fracture surfaces (a) secondary electron image showing brittle Si fracture (b) inset showing steps in Si (c) back scattered electron image showing distribution of Al_2Cu.

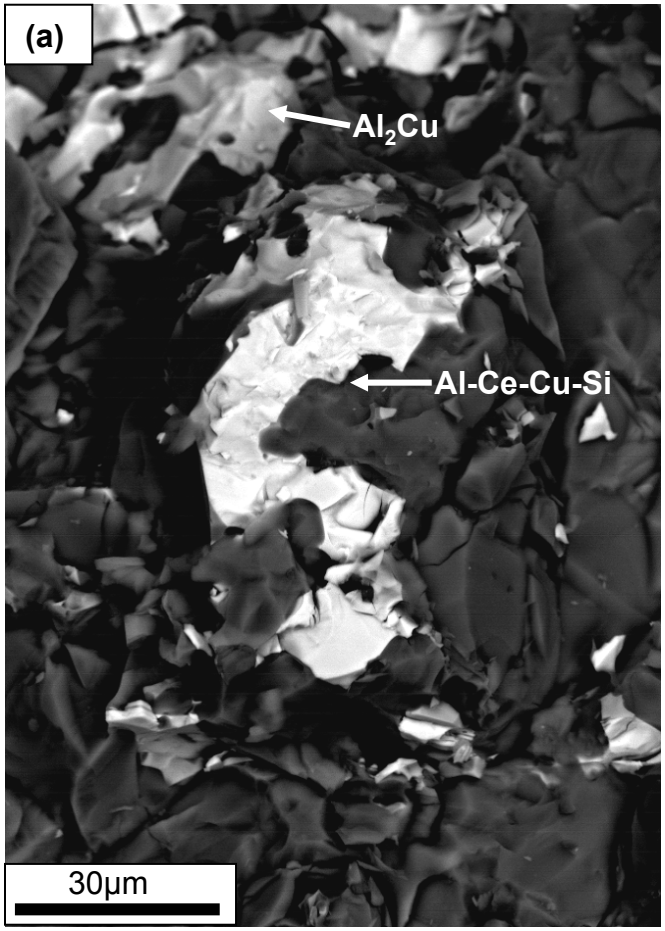

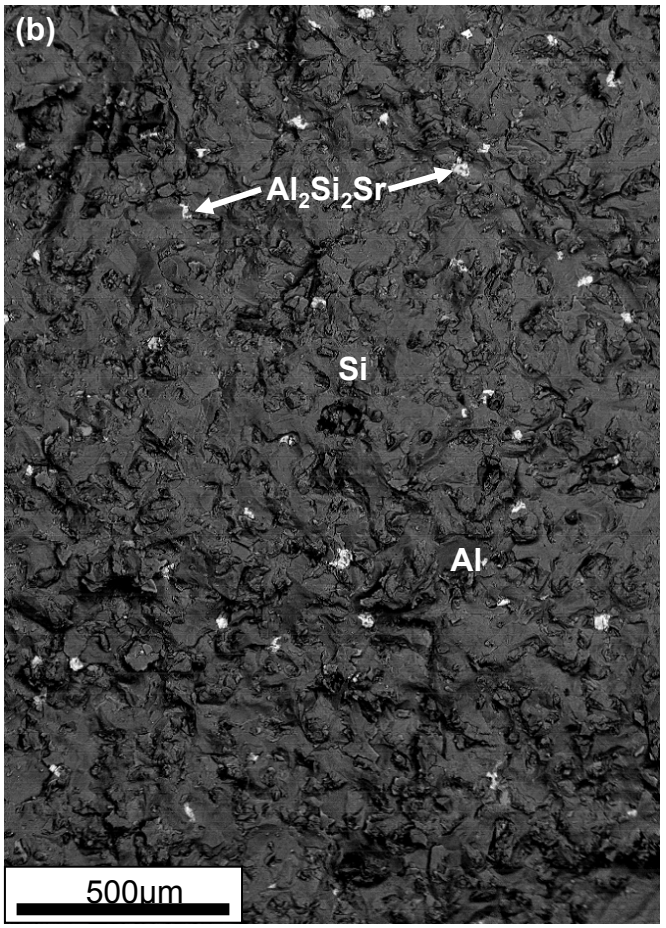

Figures 6.12(a) and 6.12(b)

SEM micrographs of (HIPed) bend test specimen fracture surfaces (a) CE7+P+Ce back scattered electron image showing a large Al-Ce-Cu-Si intermetallic phase in a Si matrix crack path, (b) CE7+Sr back scattered electron image showing distribution of Sr containing intermetallics on the fracture surface

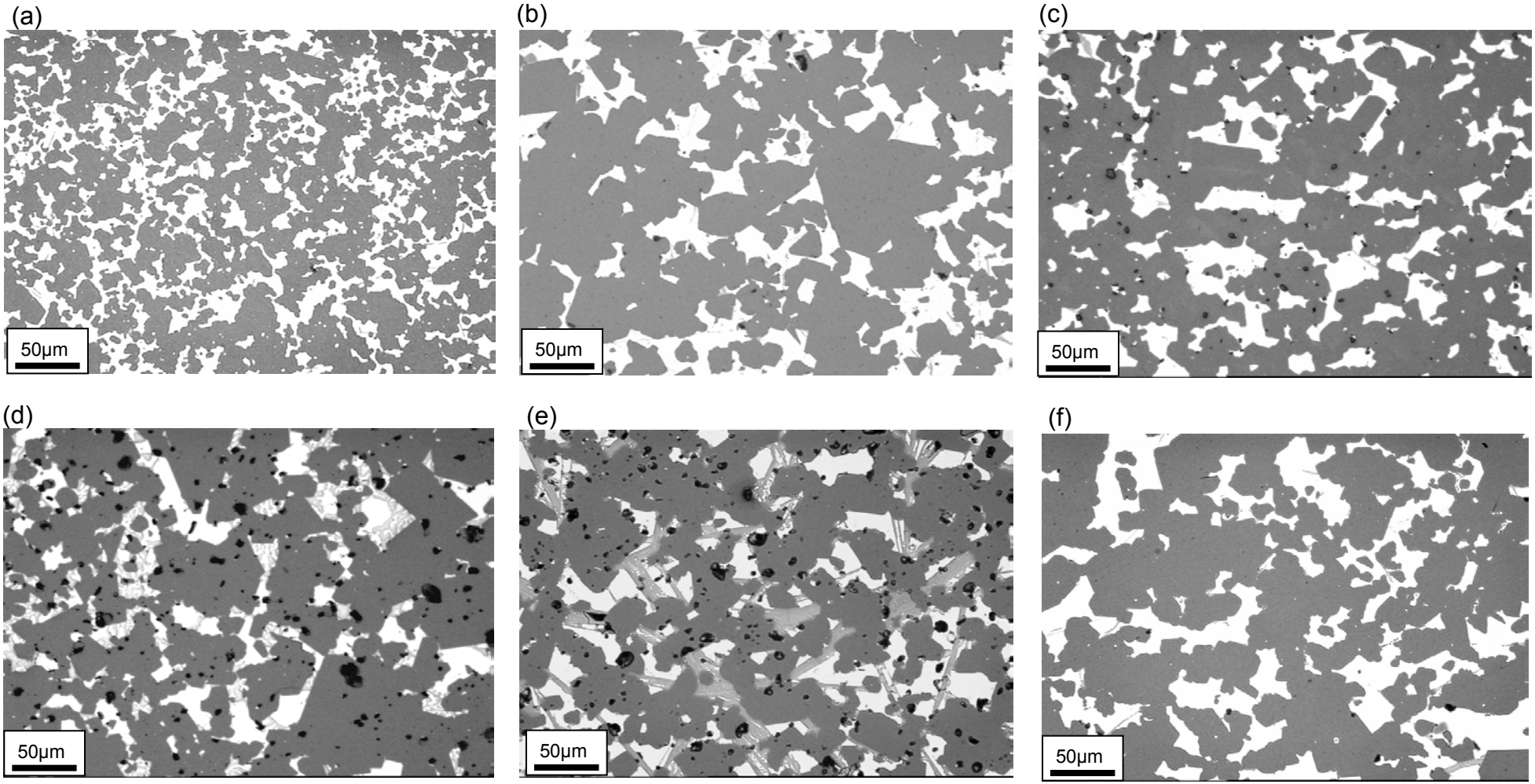

Figures 6.13(a) – 6.13(f)

Reflected light optical micrographs of (a) Sandvik Osprey CE7, (b) Oxford Binary CE7, (c) CE7+B, (d) CE7+P, (e) CE7+P+Ce, (f) CE7+Sr, at the same magnification showing the scale of the primary microstructure in each case.

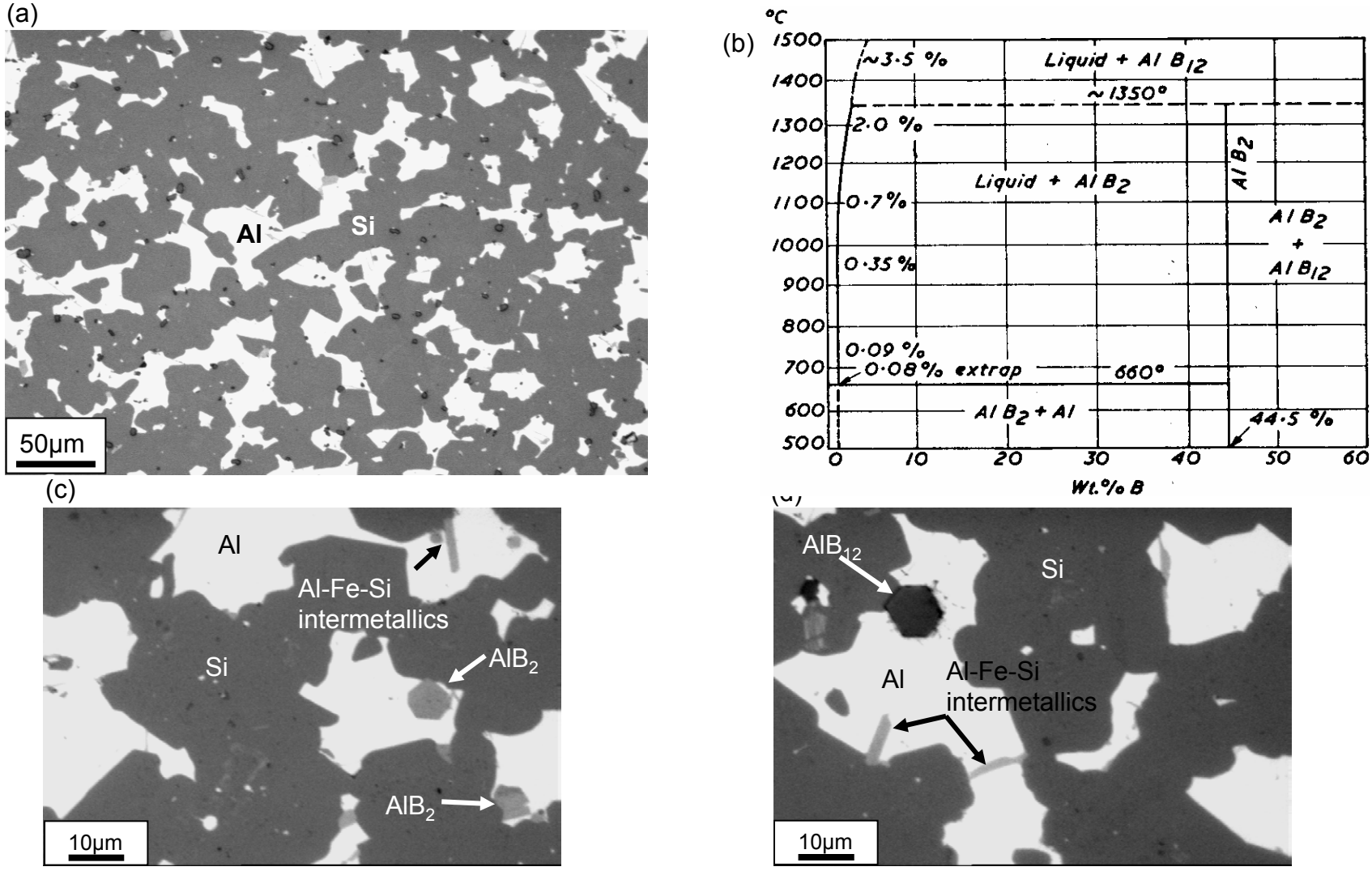

Figures 6.14(a) – 6.14(d)

Reflected light optical micrograph of CE7+B showing (a) the interpenetrating Al –Si network structure, (b) the Al-B phase diagram, (c) AlB_2 and Al-Fe-Si acicular intermetallics, (d) AlB_{12} and Al-Fe-Si acicular intermetallics,

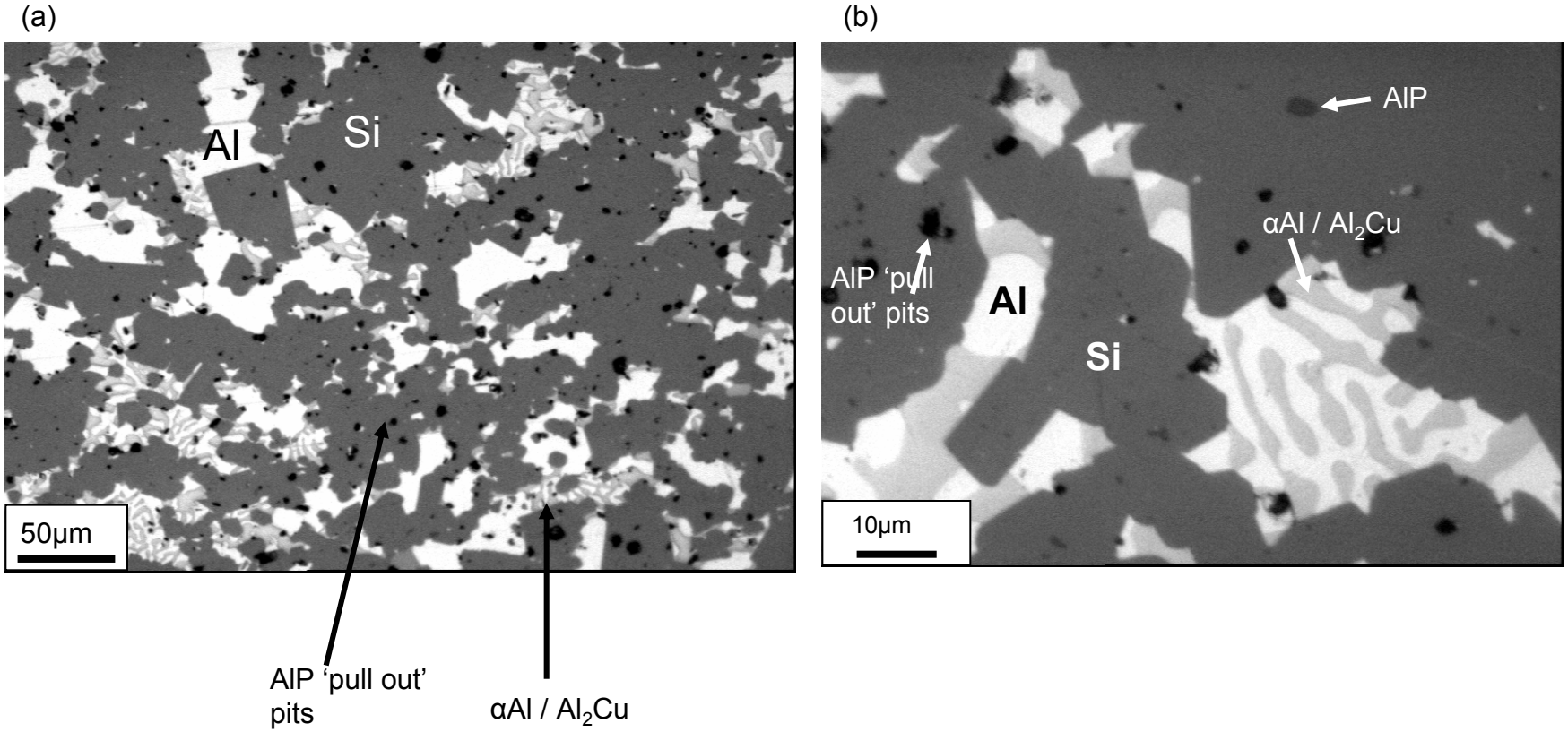

Figures 6.15(a) – 6.15(b)

Reflected light optical micrographs of CE7+P showing AlP 'pull out' and Al_2Cu phases , at; (a) low magnification and (b) high magnification

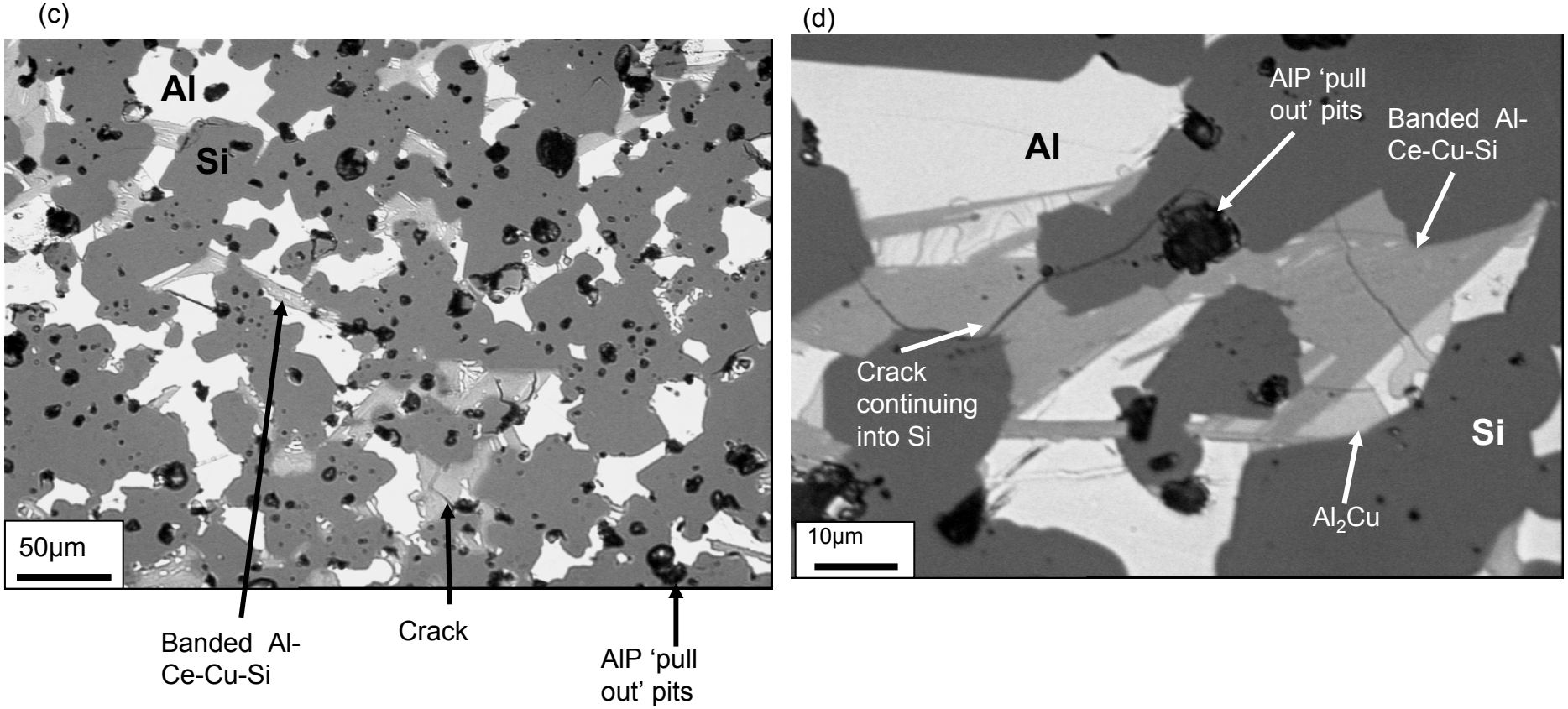

Figures 6.15(c) – 6.15(d)

Reflected light optical micrographs of CE7+P+Ce, showing banded Ce-Cu-Si phases AlP 'pull out' and cracking at; (c) low magnification and (d) high magnification

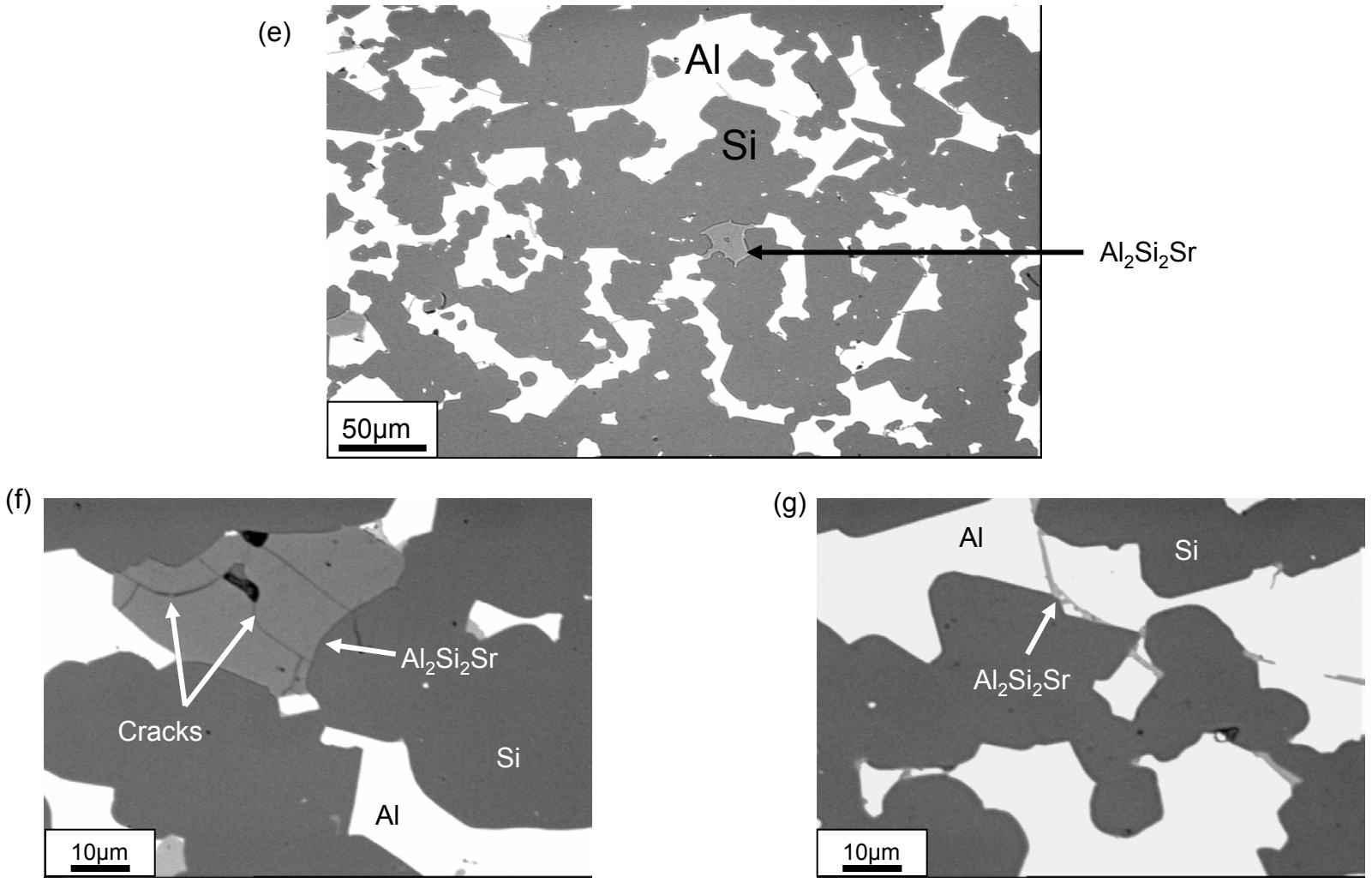

Figures 6.15(e) – 6.15(g)

Reflected light optical micrographs of CE7+Sr at; (e) low magnification, (f) high magnification showing plate morphology Al_2Si_2Sr particles and (g) low magnification showing script morphology Al_2Si_2Sr particles

.

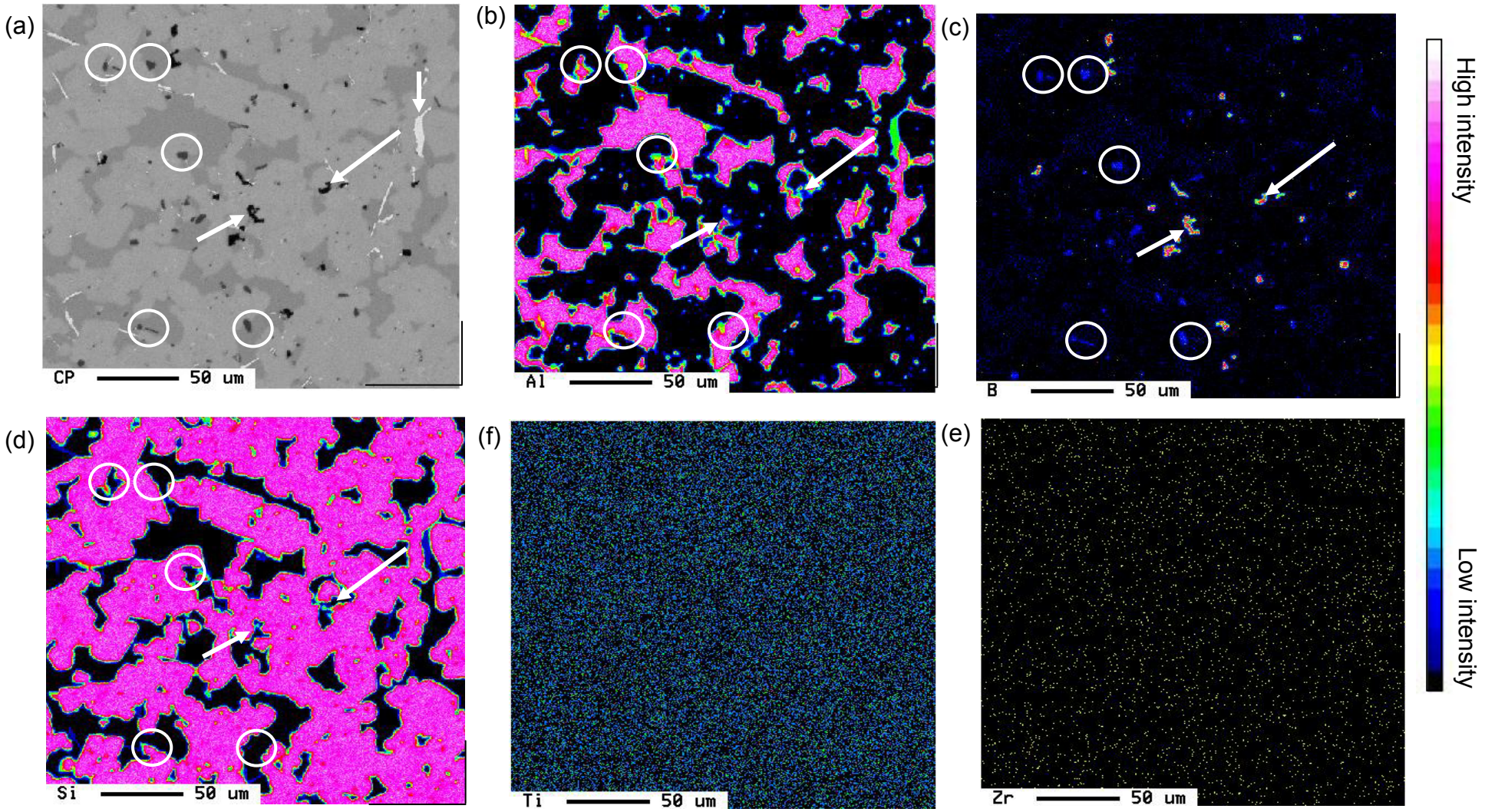

Figures 6.16(a) – 6.16(f)
(a) Backscattered electron image for CE7+B and corresponding concentration WDX map for, (b) Al, (c) B, (d) Si, (e) Zr, (f) Ti. (a) – (d) show the presence of AlB_2 (ringed) and AlB_{12} (arrowed). (e) and (f) show a fine dispersion of Ti and Zr and the absence of coarse Zr-Ti-Si intermetallics

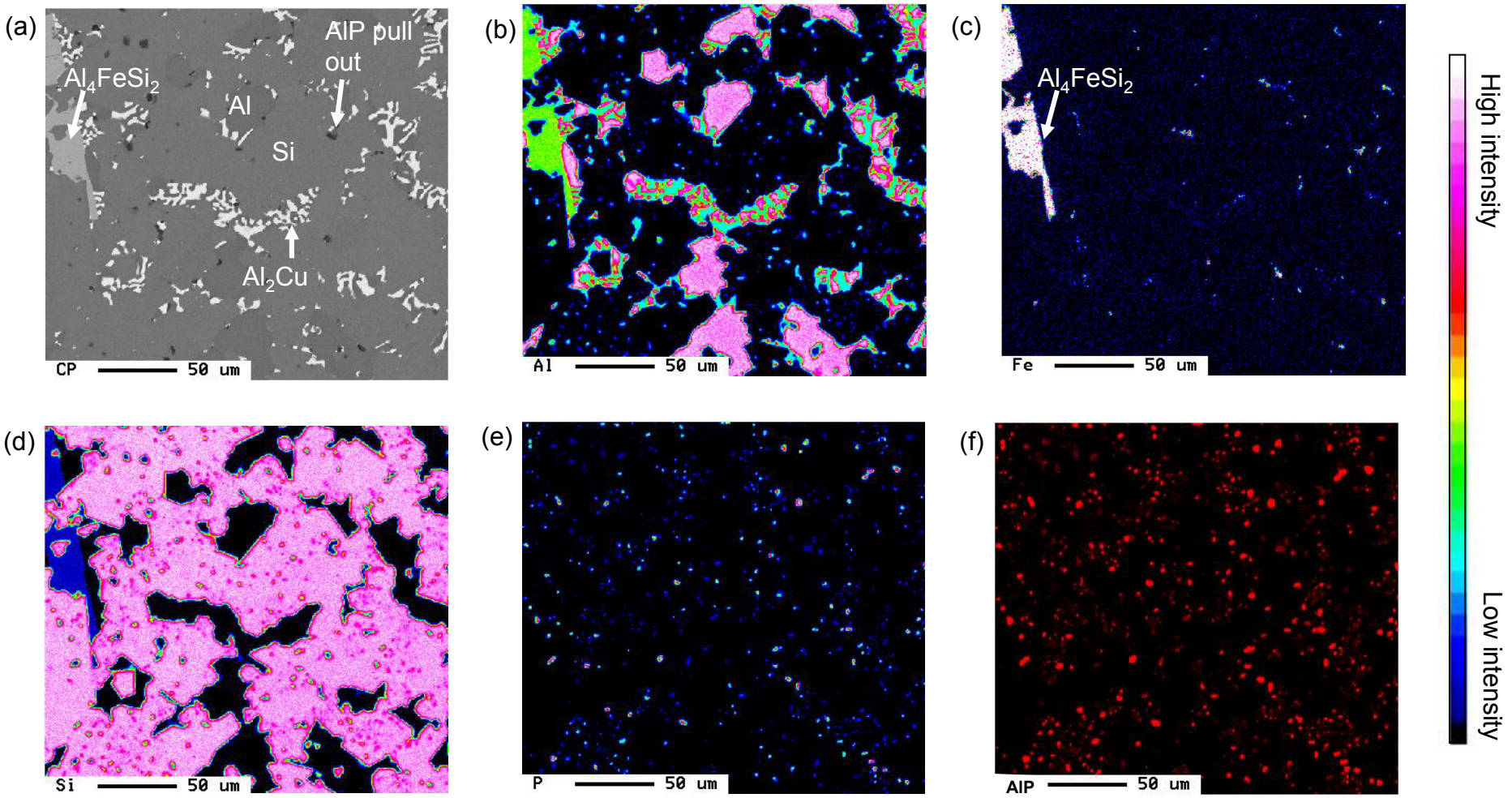

Figures 6.17(a) – 6.17(f)

(a) Backscattered electron image for CE7+P and corresponding WDX concentration maps for (b) Al, (c) Fe, (d) Si, (e) P, (f) combination P+Al (AlP) showing a fine dispersion AlP throughout the primary Si phase.

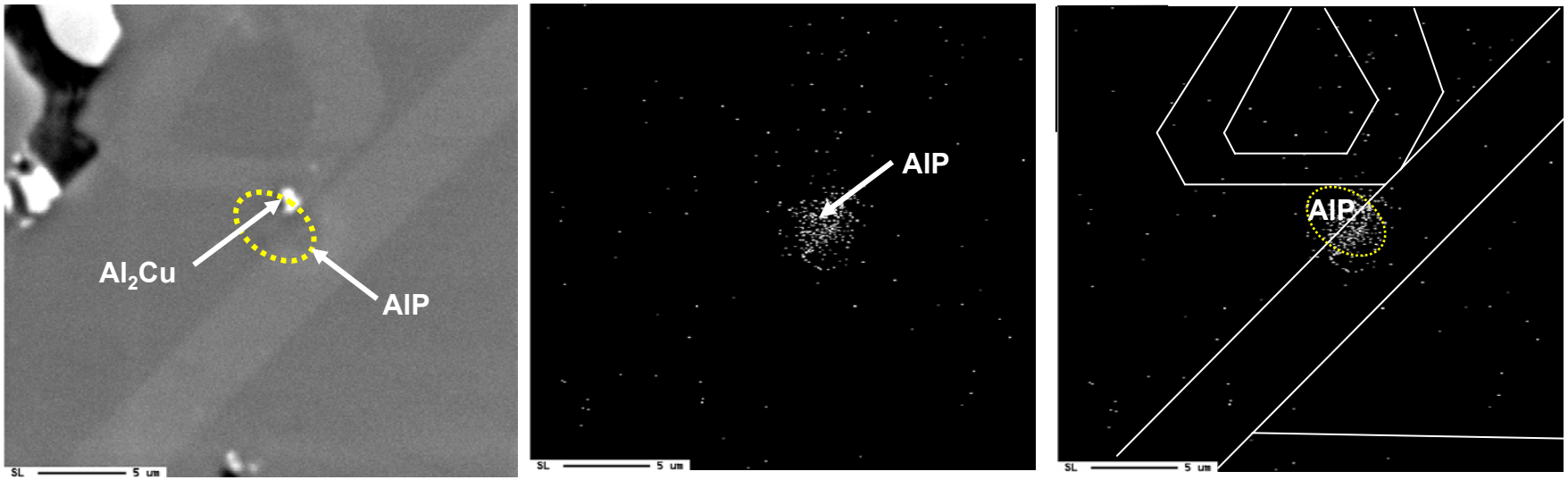

(a) (b) (c)

Figures 6.18(a) – 6.18(c)

(a) Backscattered electron image of the primary Si phase in CE7+P, showing high angle grain boundaries, (b) X-ray intensity map for P corresponding to (a) and (c) High angle grain boundaries superimposed over the X-ray P map showing AlP at a Si-Si grain boundary.

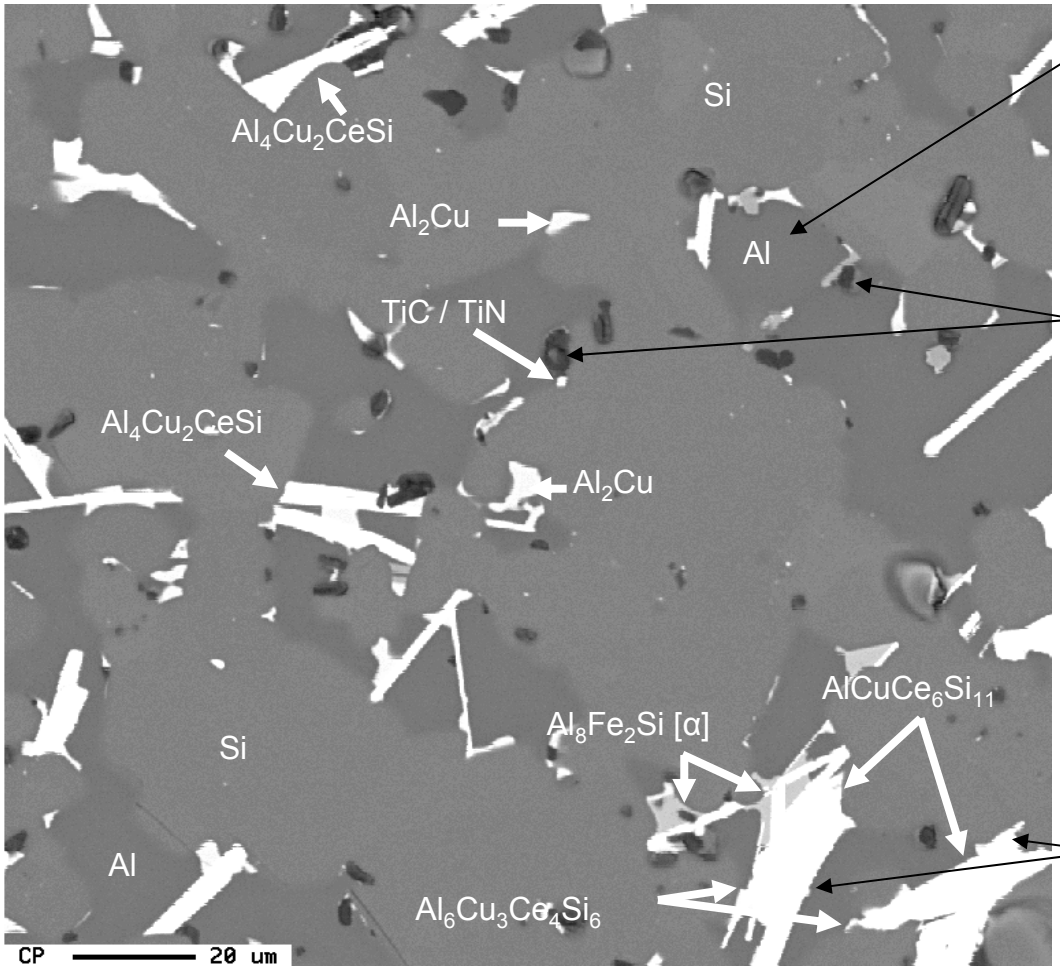

Figure 6.19

Backscattered electron image for CE7+P+Ce with major phases and particles indicated from EPMA stoichiometry.

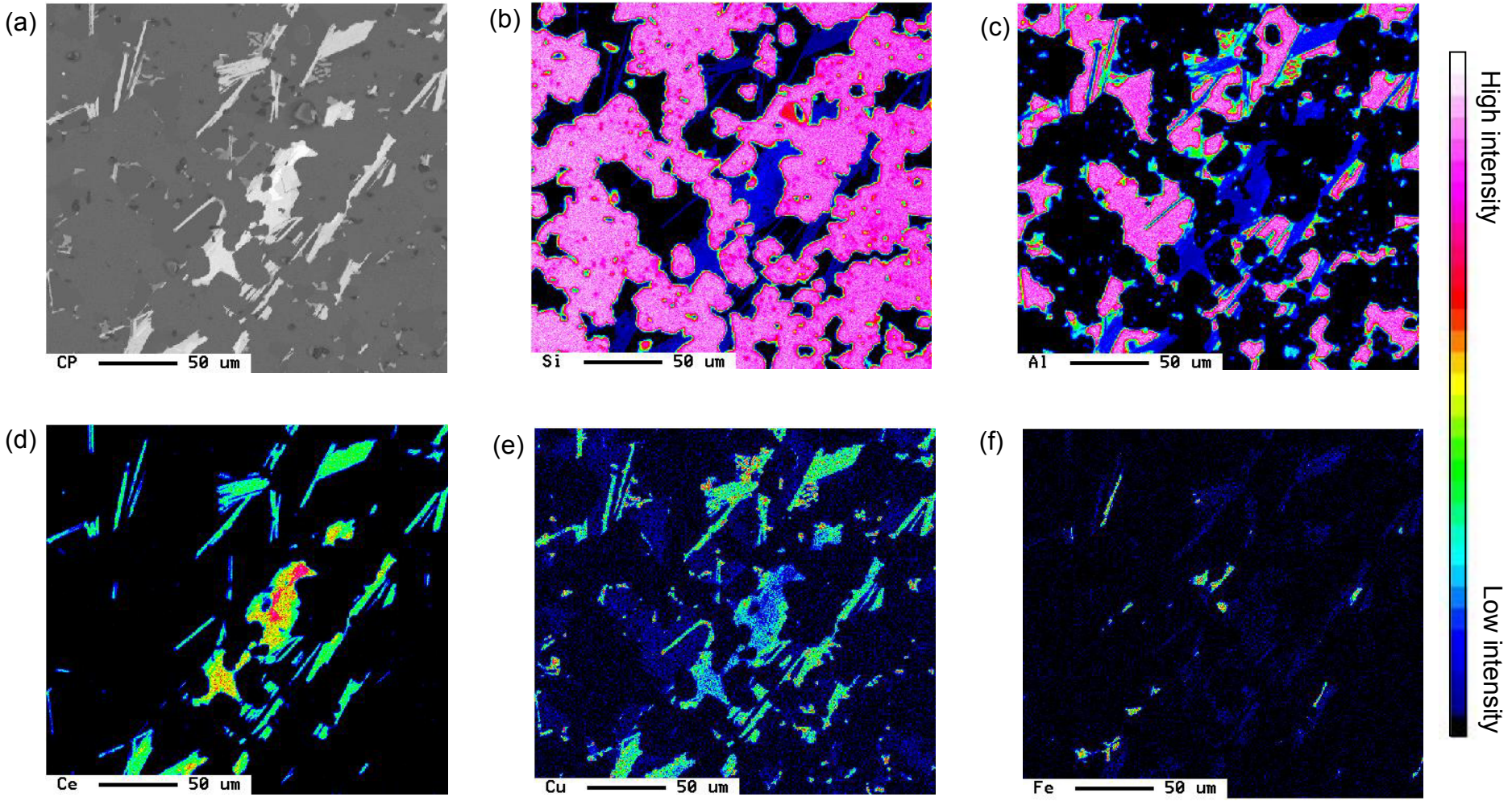

Figures 6.20(a) – 6.20(f)

(a) Backscattered electron image of CE7+P+Ce, with corresponding WDX concentrations map for (b) Si, (c) Al, (d) Ce, (e) Cu, (f) Fe, showing Fe based intermetallics

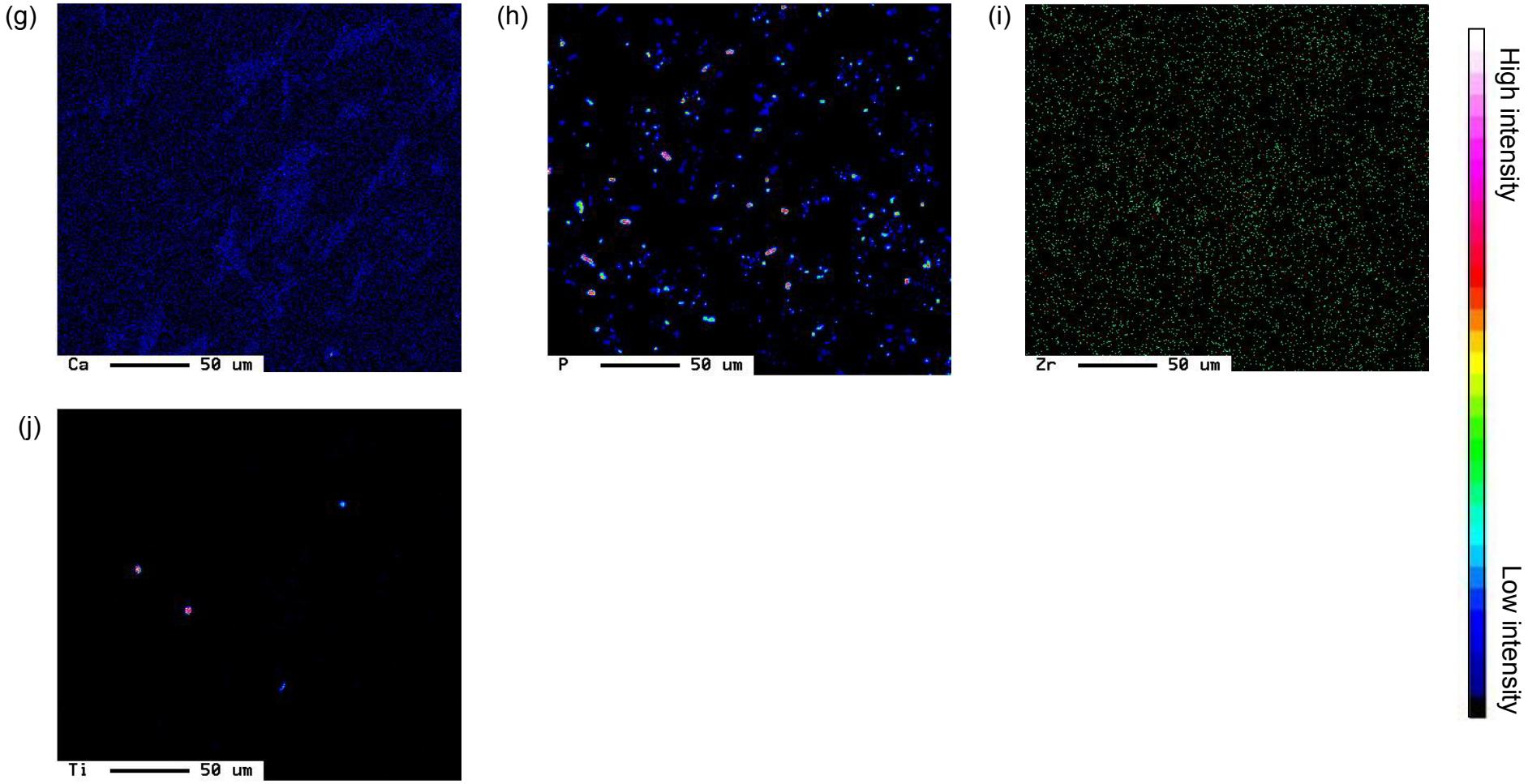

Figures 6.20(g) – 6.20(j)

WDX concentration maps corresponding to 6.20(a) showing (g) Ca, (h) P, (i) Zr (j) Ti

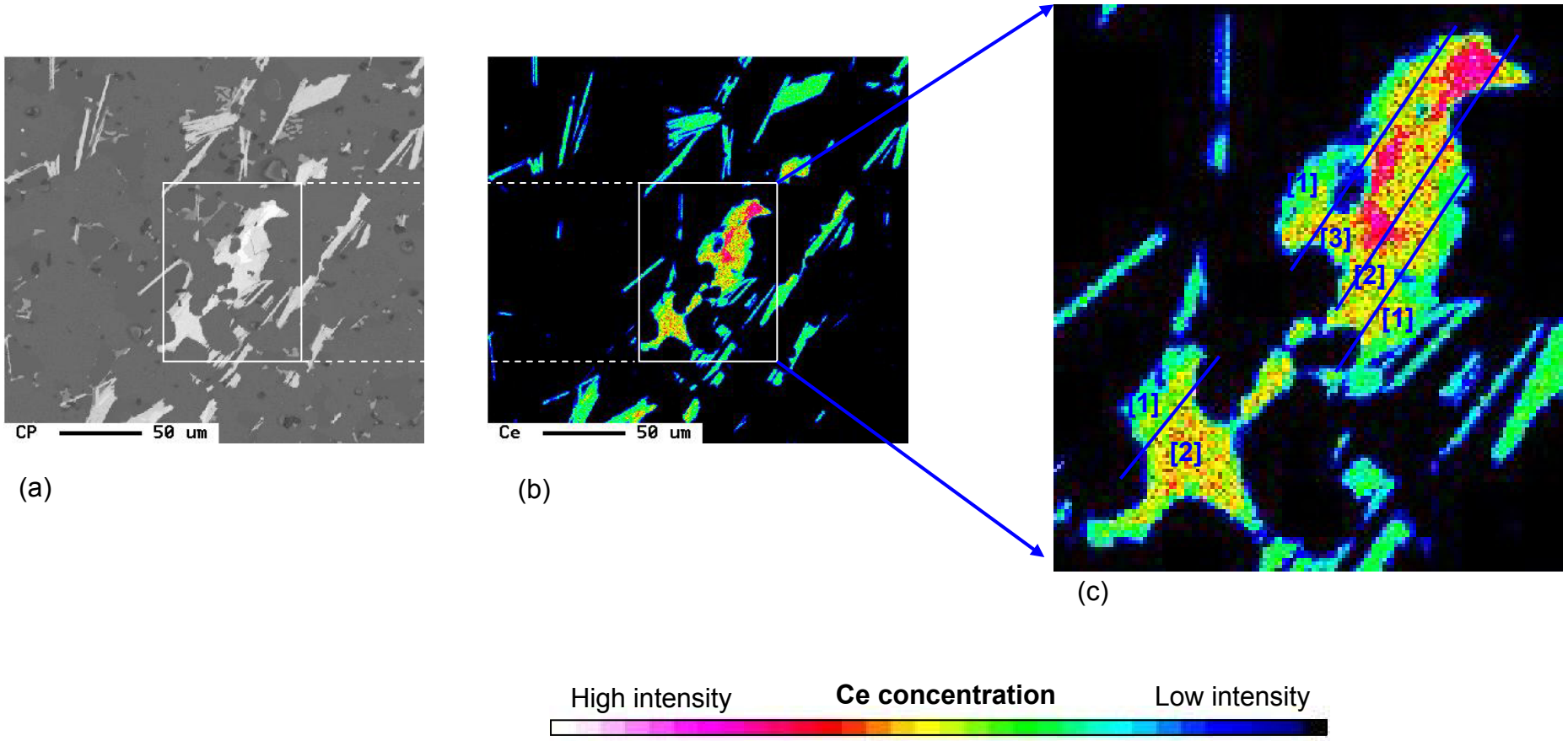

Figures 6.21(a) – 6.21(c)

(a) Backscattered electron image of CE7+P+Ce with (b) corresponding WDX Ce concentration map and (c) detail of one Ce containing particle showing the banded Al-Ce-Cu-Si particle consisted of three composition zones of 70wt% Ce at centre[3], 50wt% Ce intermediate[2] , 35wt% Ce at periphery[1]

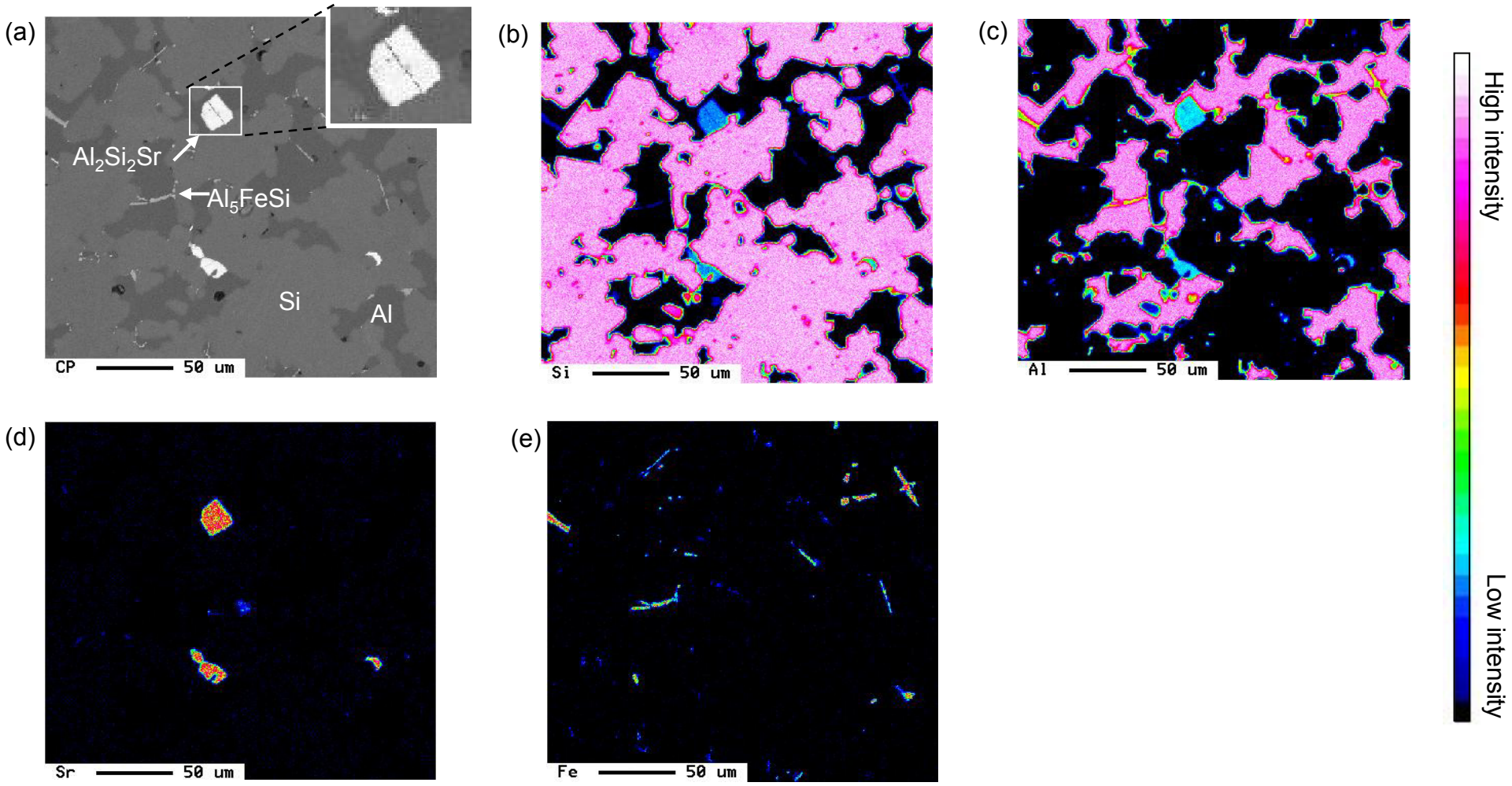

Figures 6.22(a) – 6.22(g)

(a) Backscatter electron image of CE7+Sr, with corresponding WDX concentration maps for (b) Si, (c) Al c, (d) Sr, (e) Fe, (f) Ti and (g) Zr

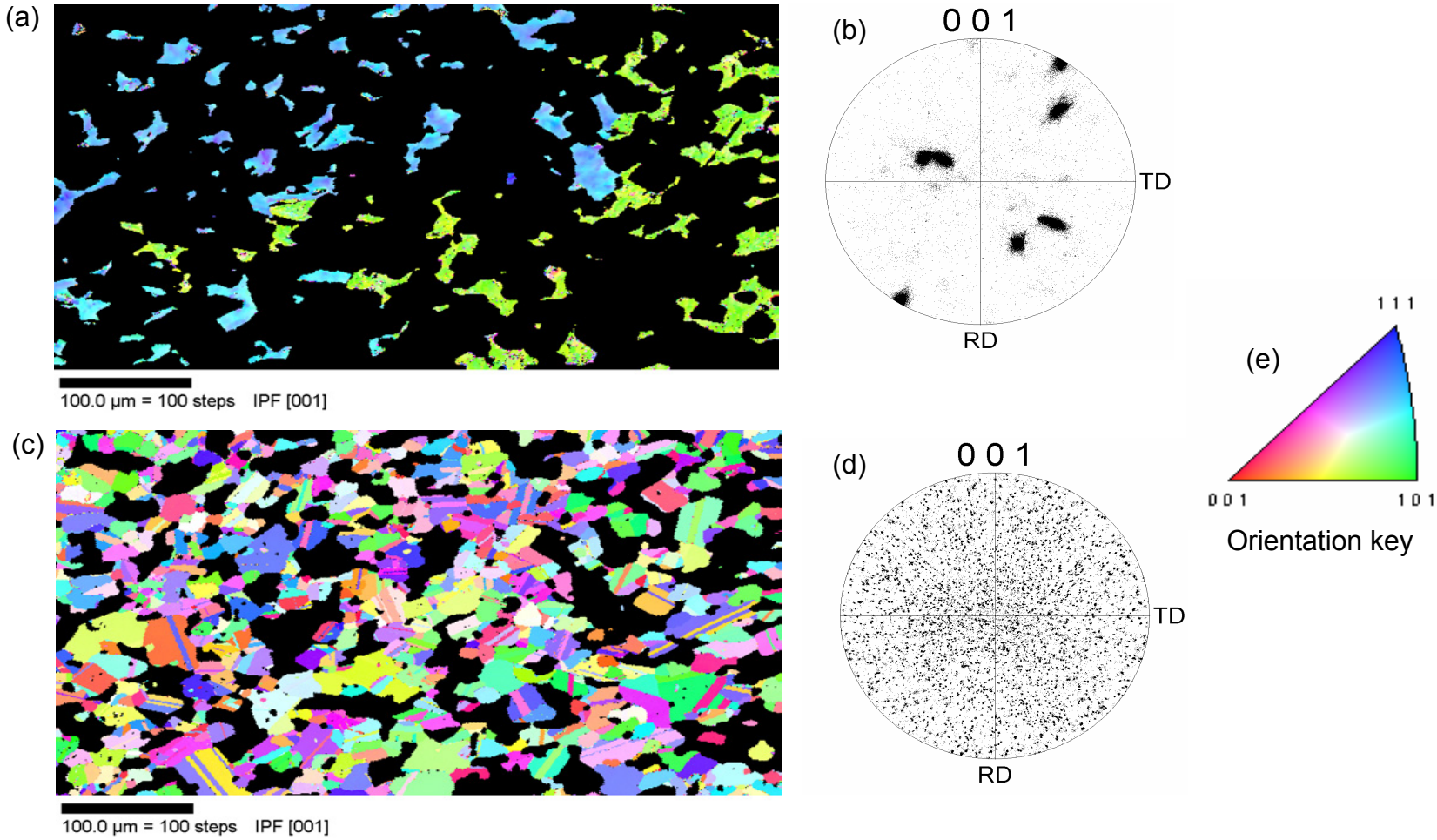

Figures 6.23(a) – 6.23(e)

EBSD results for CE7+B, (a) partitioned to show Al orientation, (b) Al pole figure, (c) partitioned to show Si orientation, (d) Si pole figure, (e) orientation key corresponding to (a) and (c).

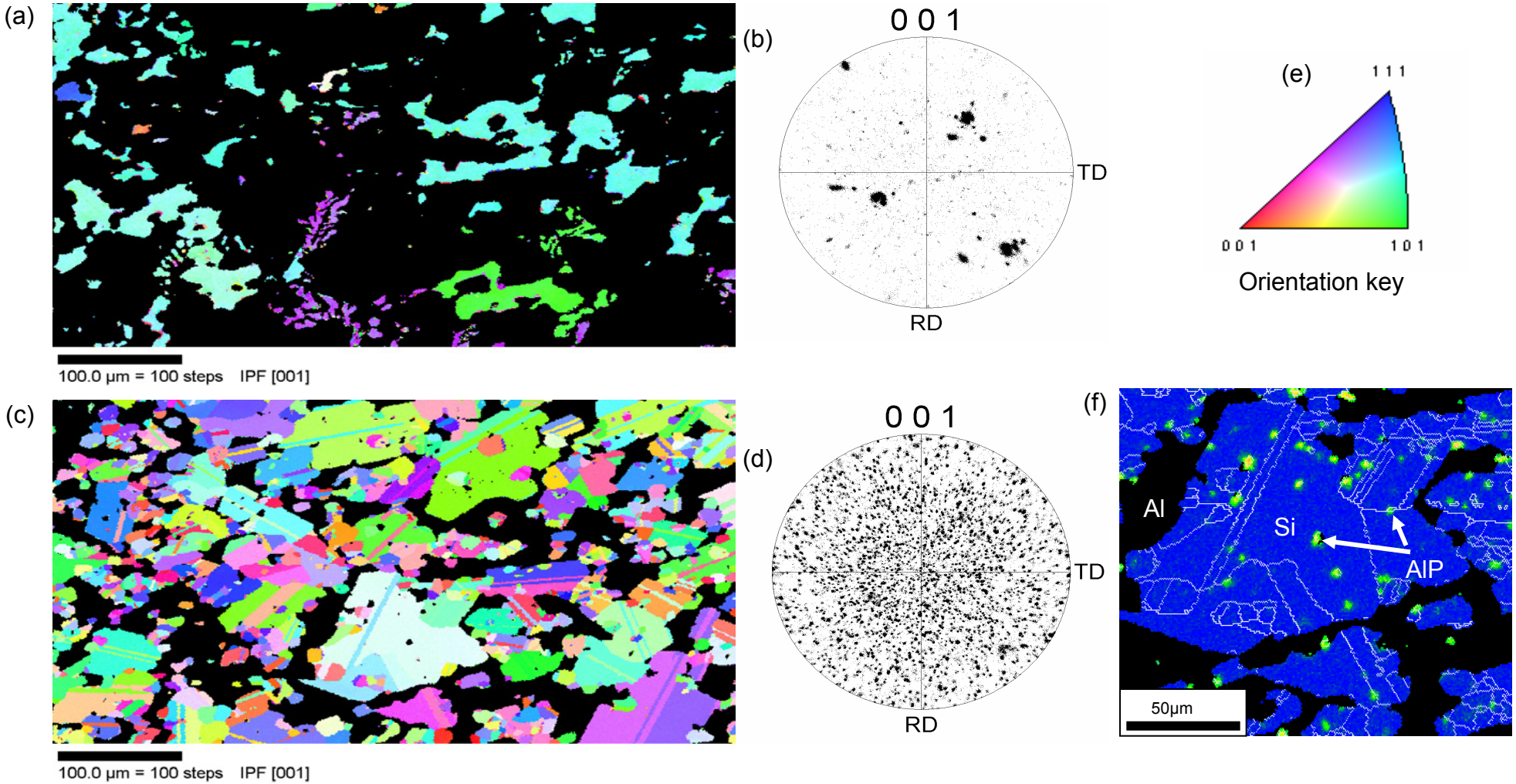

Figures 6.24(a) – 6.24(f)

EBSD results for CE7+P, (a) partitioned to show Al orientation, (b) Al pole figure, (c) partitioned to show Si orientation, (d) Si pole figure, (e) orientation key corresponding to (a) and (c), (f) Combination map showing Si (blue) P (green) and Si high angle grain boundaries (white)

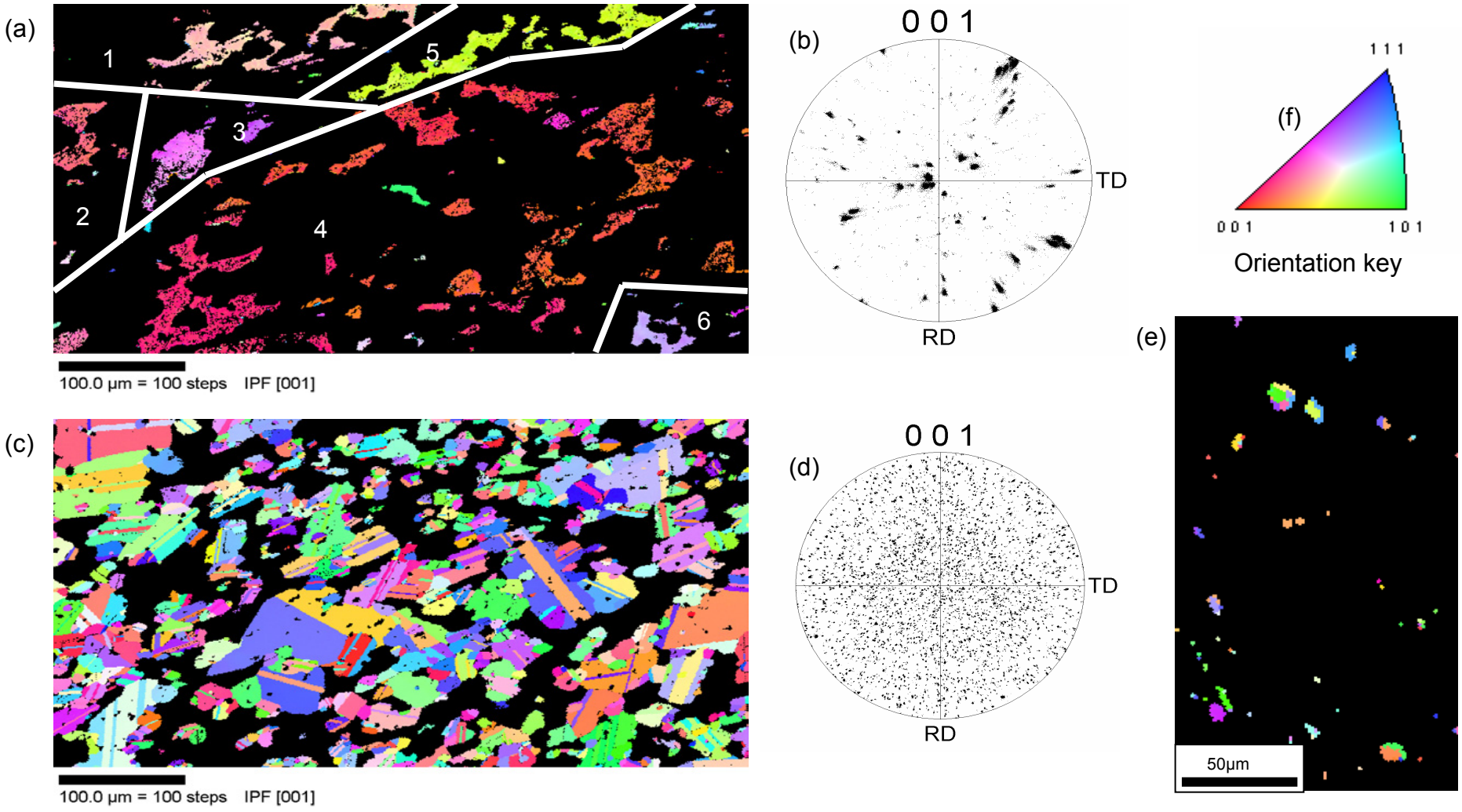

Figures 6.25(a) – 6.25(f)

EBSD results for CE7+P+Ce, (a) partitioned to show Al orientation, (b) Al pole figure, (c) partitioned to show Si orientation, (d) Si pole figure, (e) partitioned to show P orientation (f) orientation key corresponding to (a), (c) and (e).

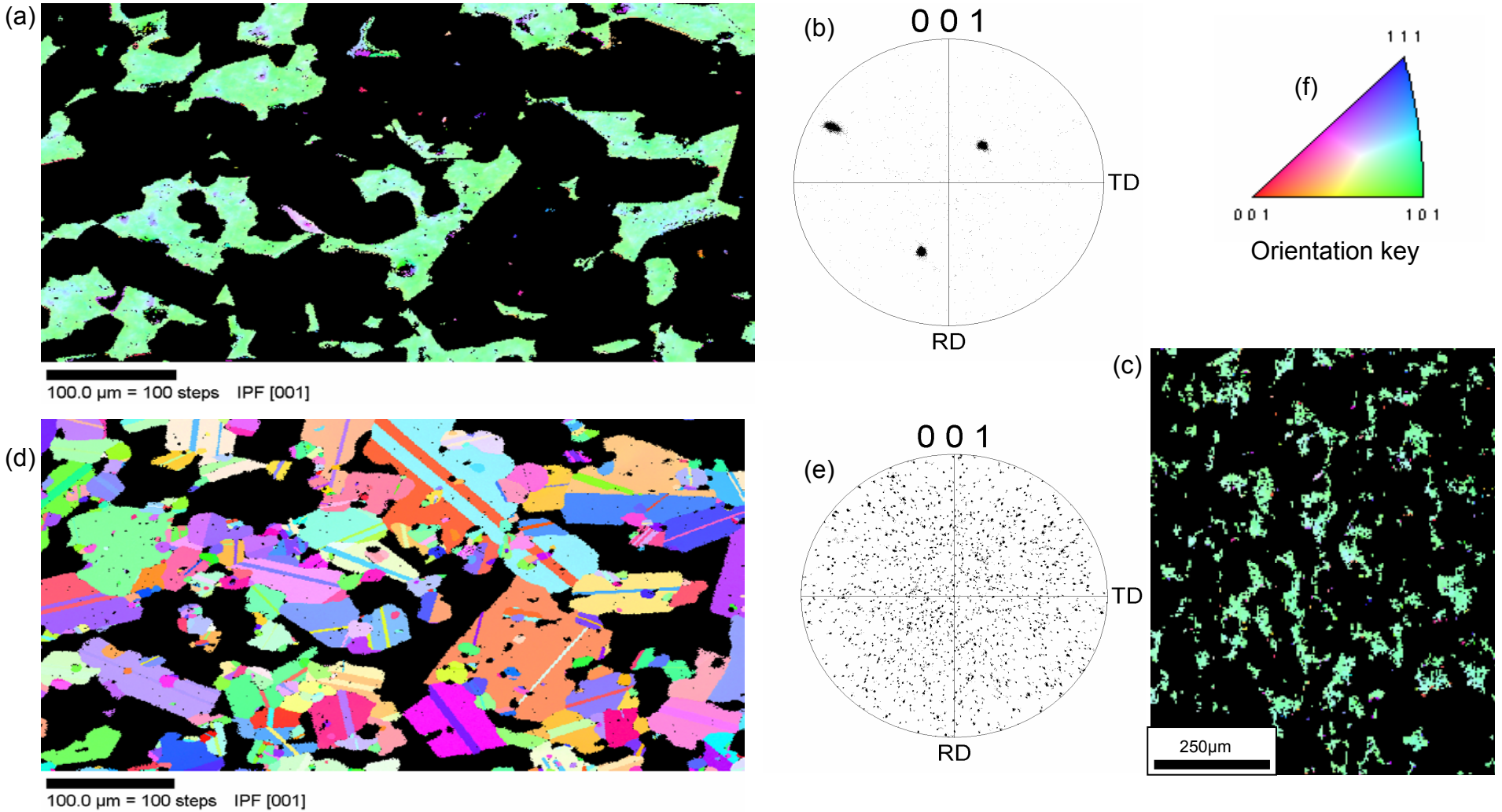

Figures 6.26(a) – 6.26(f)

EBSD results for CE7+Sr, (a) partitioned to show Al orientation, (b) Al pole figure, (c) Al orientation coarse scan, large area, (d) partitioned to show Si orientation, (e) Si pole figure, (f) orientation key corresponding to (a), (c) and (d).

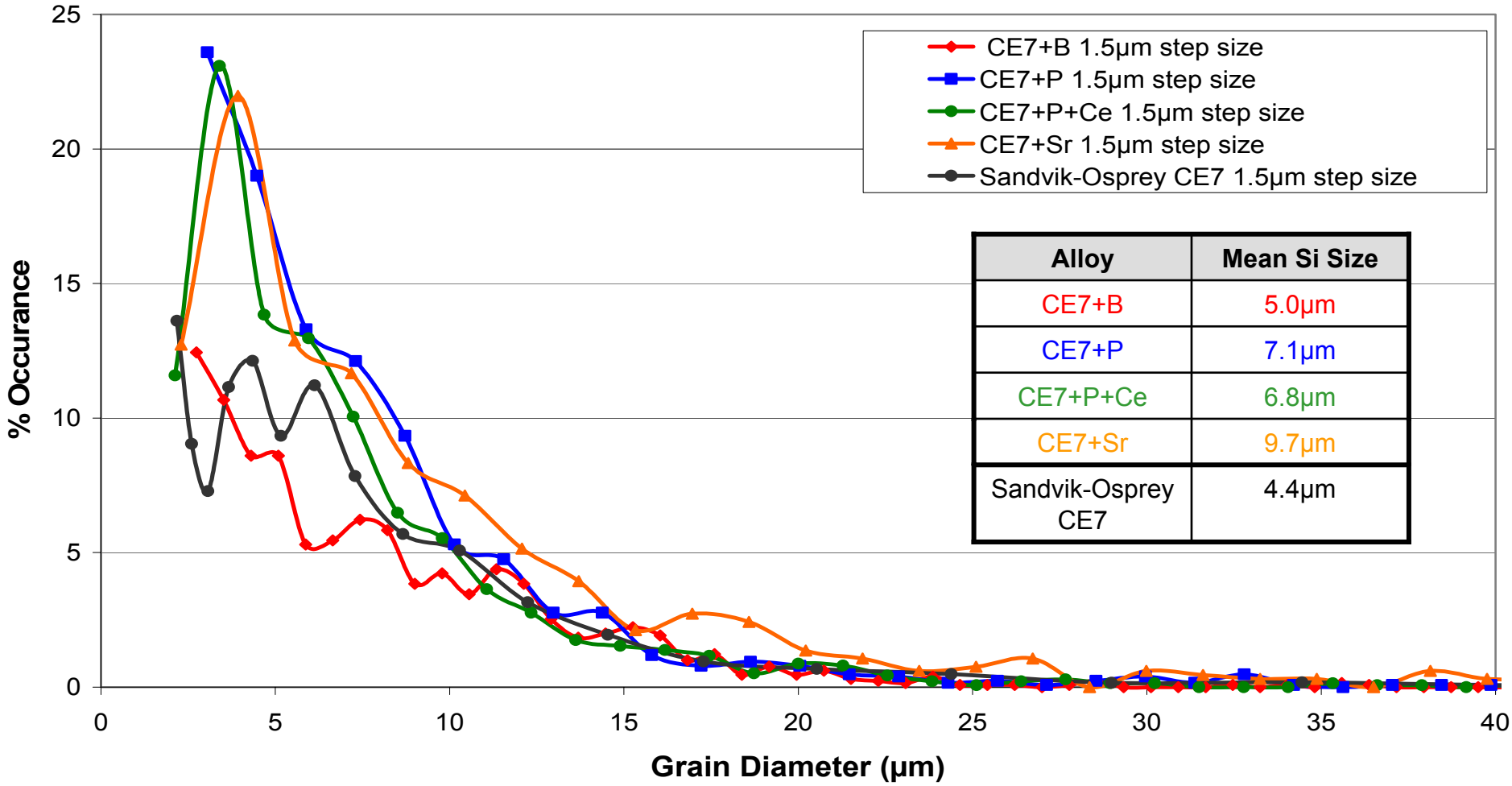

Alloy	Mean Si Size
CE7+B	5.0µm
CE7+P	7.1µm
CE7+P+Ce	6.8µm
CE7+Sr	9.7µm
Sandvik-Osprey CE7	4.4µm

Figure 6.27

Si grain size distribution in Oxford CE7-based alloys and Sandvik-Osprey CE7. Measurement including twin boundaries as high angle grain boundaries. All EBSD grain size measurements taken at a 1.5µm step size. The table indicates the mean primary Si grain size

7.0 Discussion - Sandvik-Osprey CE7

The industrial scale processing and resultant microstructure of Sandvik-Osprey CE7 is discussed in Section 7.1 and 7.2. The microstructure of CE7 has several interesting and unusual features including; a divorced eutectic with an absence of eutectic Si, macrosegregation of the Al rich phase, differing grain orientation (texture) in the Si and Al phases, and a variety of intermetallic particles, these are discussed in more detail in Sections 7.2.1 to 7.2.5 respectively. The post-spray forming HIPing of billets is discussed in relation to both porosity and the effect on Si microstructure and coarsening in Section 7.3. The microstructural observations are then considered in conjunction with physical characterisation in Section 7.4. The Young's Modulus and CTE are considered and compared with a rule of mixtures approach in Sections 7.4.1 and 7.4.2. The problems, processes and results from fracture toughness measurements are presented in Section 7.4.3, and in combination with Weibull modulus and bend test data from Section 7.4.4 is used to calculate the typical flaw size in CE7. The deleterious influence of thermal cycling on mechanical properties is discussed in Section 7.4.5.

7.1 Spray Forming

7.1.1 Particle injection

The importance of particle injection in controlling the alloy microstructure and process yield has been demonstrated. By recycling the overspray powder and re-injecting it via a particle injector a significant material saving was made, contributing significantly to the financial viability of the process by allowing

Sandvik-Osprey to obtain yields of ~80% during commercial manufacture of CE7 (Ogilvy 2003). As shown in Figure 4.14 the particle injection ratio also has a strong effect on the inter-phase interface length, which is implicated in controlling toughness. For an increase in particle injection ratio from 27 to 46% where: injection ratio is given by powder flow rate / melt flow rate x 100, the interface length increased from 13 to 21 mm/mm^2 as shown in Figure 7.1. The effect of injection ratio must have an upper limit, which occurs when the liquid fraction at the billet top surface is reduced by the presence of solid particles so much that it can no longer ensure that the impacting solid particles stick and become incorporated in the billet with the attendant re-melting required to remove any remnant of the overspray structure. Indeed a remarkable feature of Sandvik-Osprey CE7 is how completely the re-injected solid is partially re-melted and homogenised into the billet, consistent with the observations of Hogg (2001). Mathur (1991a) demonstrates the criticality of top surface liquid fraction in controlling yield, described by Equations 2.1 and 2.2 in Section 2.2.5.2. Figure 7.1 re-plots the relationship between injection ratio and interface length together with a tentative suggested relationship interpolated between points and extended beyond the region of measurement. Oxford binary CE7, that was manufactured with no particle injection, does not safely fit the variation given by the Sandvik-Osprey alloys because of the differences in the processing and solidification conditions previously detailed in section 3.5.1. In order to explore the range of interface lengths that may be achievable, Sandvik-Osprey were asked to manufacture a series of well-controlled billets using different injection ratios. However this was not possible due to the heavy

schedule of commercial production work on Sandvik-Osprey plants. The possibility of integrating a particle injector into the Oxford spray forming plant was also investigated. Integration of a particle injector with the Oxford control system and design of a powder injector that met current explosive powder regulations was considered too complex, costly and would not be available on the timescales compatible with this study. It is clear from Figure 7.1 and the microstructures presented in Figure 6.13(a) – (f) that particle injection is a key parameter in optimising microstructure, and represents a more effective refining mechanism than the alloy additions used at Oxford. This is discussed further in Section 9.3 & 9.4

7.1.2 Post spray forming solidification

The slow, directional post-spray cooling procedure developed by Sandvik-Osprey (Osprey 2001) was implemented at Oxford to reduce gross defects and porosity in conventionally cooled CE7 billets. These defects result from the exceptionally large freezing range (~640°C) and substantial (~30%) liquid content after spray forming and associated severe difficulty in feeding the solidification shrinkage of residual Al-rich liquid. Controlling the final stages of solidification by insulating the billet and force cooling from the base had the effect of concentrating porosity at the top of the billet, by driving the solidification front from the base to the top of the billet. While controlled cooling was effective in managing macrostructural defects, microstructural effects have been hitherto neglected. Investigations by EBSD and OES elemental mapping revealed for the first time that the combination of large freezing range and directional cooling

caused micro and macrostructural effects, and associated physical effects that are discussed later.

7.2 Microstructural Evolution

Microstructural refinement of CE7 results from the myriad of solid and semi-solid droplets which form during melt atomisation (Grant 1995a); these particles of varying solid fraction impact the semi-solid surface of the billet and undergo-partial re-melting and recalescence to primary Si and liquid. The remaining solid particles provide an abundance of nucleation sites for the nucleation of primary Si, resulting in a network structure of fine polygonal Si. Immediately after deposition is complete the billet temperature is ~700°C and consists of interconnected primary Si interpenetrated by Al-22%Si liquid (Murray 1984). The liquid composition rapidly homogenises by rapid diffusion of Si in liquid Al-Si (Petrescu 1970).

Insulation of the billet allows temperature equilibration, aided by the high latent heat of fusion of Si of 50.6kJmol^{-1} (Smithells 1978), and partially re-melts some previously solid regions (e.g. the top surface where comparable Oxford pyrometer data in Figure 6.3 shows an increase in temperature after spraying is complete, and the Sandvik-Osprey cooling curve in Figure 6.5 shows a billet surface temperature above the liquidus).

Sandvik-Osprey CE7 microstructure shown in Figure 4.13(a) shows no eutectic Si. This is attributed to the slow cooling and small inter-Si spacing between primary Si particles leading to epitaxial growth of rejected Si solute onto the

surrounding primary Si, as discussed in Section 7.2.1. As the temperature decreases to the eutectic temperature the pre-existing Si network coarsens and solidifies, probably by a ledge attachment mechanism (Hogg 2001).
Silicon undergoes a volume increase on solidification of ~ 7.9% (Shackelford 2001) compressing liquid in the inter Si regions and frequently resulting in Al-Si liquid being exuded at the billet surface, (Ogilvy 2003). Between 710 and 582°C a range of Al-Fe-Si intermetallic phases are formed with various stoichiometries and morphologies (Mondolfo 1979). During subsequent cooling it is postulated that acicular intermetallic particles of different CTE to the surrounding Al and Si initiate cracks in the primary Si phase as shown in Figure 4.16, which have been shown in Section 4.2.10 to grow during thermal cycling. Al-Si liquid becomes progressively enriched in Al as the billet temperature approaches the eutectic temperature of 577°C and upon solidification the liquid exhibits a volume decrease of 2.7% providing the driving force for inverse segregation as discussed in Section 7.2.2. Cooling data in Figure 6.5 indicates a eutectic temperature arrest during post spray cooling, however no α-Al / Si eutectic lamellae were observed, and a divorced eutectic was apparent in all areas of the billet.

7.2.1 Divorced Eutectic

Figure 7.2(a) and (b) show the typical microstructure of a cast, unmodified hypereutectic Al-70Si alloy consisting of coarse primary Si and a eutectic lamellae of α-Al and Si, and the same composition alloy after spray forming

comprising equiaxed primary Si continuously penetrated by an Al-rich phase devoid of eutectic microstructure.

As the billet temperature reaches the eutectic temperature and the Al-12.2%Si liquid becomes unstable, it must undergo phase separation and solidification. In a conventional casting this occurs by the nucleation of α-Al / Si eutectic, of various morphologies dependent on composition, the presence of modifiers, temperature gradient G and growth rate V (Day 1968). However, in spray formed CE7 growth of Si from the liquid is on the pre-existing Si, as this acts as effective nuclei for Si, diffusion distances are small, and there is extended time at an elevated temperature. This is consistent with Day (1968) who suggested that with low temperature gradients and low growth rates the inter-lamellae spacing increases, approaching the inter-primary Si distances seen in spray formed CE7. Furthermore with low growth rates and large inter-lamellae spacing, the solidification front undergoes catastrophic breakdown (Fisher 1979) allowing Si to grow either epitaxially on the pre-existing Si network or form new grains at the primary Si / liquid interface which are indistinguishable from the primary Si network. This is supported by EBSD results shown in Figure 4.21(a) showing agglomerations of fine, equiaxed Si grains and by calculations of Si diffusion rates in liquid Al-Si. The diffusion coefficient of Si in liquid Al-Si can be estimated using the standard form of the diffusion equation:

$$D = D_0 \exp\left(\frac{-Q}{RT}\right)$$

Equation 7.1

where T is the absolute temperature, R is the gas constant ($Jmol^{-1} K^{-1}$), Q is the activation energy for diffusion of Si in liquid Al-Si eutectic of 25.7 kJ mol^{-1} (Petrescu 1970), D is the diffusion coefficient ($m^2 sec^{-1}$) and D_0 is the corresponding frequency factor of $2.08x10^{-7}$ $m^2 sec^{-1}$ (Petrescu 1970). The time t required for Si diffuse a distance *x* can be approximated in Equation 7.2:

$$t = \frac{x^2}{D}$$

Equation 7.2

Table 7.1 shows the time required for Si to diffuse various distances as a function of temperature using Equations 7.1 and 7.2. Even just above the eutectic temperature at 578°C, Si can diffuse >30μm in <1s.

Table 7.1 Diffusion times (s) for Si in liquid Al-Si as a function of temperature and time from Equations 7.1 and 7.2.

Distance (μm)	**Diffusion times (s) at different Temperatures (°C)**			
	1100	**900**	**700**	**578**
5	0.001	0.002	0.003	0.005
10	0.005	0.007	0.012	0.018
20	0.018	0.027	0.046	0.073
30	0.041	0.061	0.104	0.163

The diffusion process is likely to be further enhanced by turbulent liquid flow on the surface of the billet induced by impingement of the turbulent atomising gas causing redistribution of solute (Doherty 1984). Consequently the resulting Al-rich inter-primary Si regions are essentially devoid of Si as subsequently confirmed by EPMA and shown in Figure 4.19(a-c).

7.2.2 Macrosegregation

Elemental mapping of Sandvik-Osprey material, shown in Figure 4.4(a) demonstrated segregation of Al with an ~5% concentration gradient across the billet radius, the centre of the billet being relatively denuded of Al at 30wt% compared with the periphery that contained 35wt% Al. Material spray formed at Oxford demonstrated similar segregation patterns e.g. the CE7+Sr billet shown in Figure 6.7(b).

This type of solute variation is commonly termed 'inverse segregation' (Flemings 1974) where solute is present in the chilled exterior regions of a casting rather than at the centre as might be expected if solute rejection during solidification were ahead of the solid / liquid interface and for a partition coefficient k <1. The 'inverse' solute enrichment results from the shrinking of Al-rich liquid as it transforms to solid which induces interdendritic flow of the remaining solute rich liquid from the centre to feed the solidification shrinkage. Until comparatively recently macrosegregation in spray formed materials was assumed to be slight because of the low liquid fraction and the relatively high cooling rates in the billet (Doherty 1997). However more recent studies have demonstrated significant macrosegregation can occur in large ~200kg billets (Mingard 2000). In this case and as in conventionally cast billets, macrosegregation was driven by heat flow outwards towards the gas chilled surfaces, and to a lesser extent, by vertical heat flow via conduction to the cool substrate. This is a process whereby the cooler external surfaces solidify first and solidification shrinkage to these areas is fed by increasingly Al-rich liquid

from the semi-solid region in the billet core. Mingard (2000) suggested that macrosegregation was further exaggerated by the centrifugal forces due to the rotation of the billet, although centrifugal contributions to macrosegregation in CE7 are questionable since rotation of the billet ceases ~1 hour before solidification is complete.

The partition coefficient $k = C_s/C_l$ where C_s is the composition of the solid and C_l is the composition of the liquid of Al in Si was calculated by Drapala (1993) as 0.019 for the primary Si liquidus. *k* can also be obtained from the phase diagram (Murray 1984), and a constant value of *k* with temperature can be estimated if it is assumed that the liquidus and the solidus are straight lines. At the eutectic temperature 577°C, C_s the solid solubility of Al in Si is 0.001% and C_l the composition of the eutectic liquid is 12.2%, so $k = 8.1 \times 10^{-5}$. Because CE7 has $k << 1$, a large freezing range of ~640°C and relatively high latent heat of solidification of 38.6 kJ mol^{-1}(calculated using the rule of mixtures from Smithells 1978) , it is certain liquid was present in the billet for a considerable time after spraying was complete. Figure 6.5 shows that the final solidification times may be up to 1 hour in Sandvik-Osprey CE7. One manifestation of these conditions is the presence of solidification shrinkage in the billet centre unless the final stages of solidification are controlled, as described in Section 7.2.2.
The CE7 heat flow during solidification comprises two components:
(i) Predominantly radial heat flow during spray forming where the billet surfaces are cooled by convection to the atomising gas and radiation.

(ii) Predominantly axial heat flow during post spray cooling where the surfaces of the billet are insulated and cooling is downward through the billet to the cooled substrate.

This combination of slow cooling, low partition coefficient, high latent heat of solidification, and Al volume change on solidification provides conditions suited to inverse segregation of Al. The resulting compositional variations in the billet resulted in variations in the CTE in different areas of the billet as described in Section 7.4.2

7.2.3 Si texture

Figure 4.21(a) showed that the Si grain size was entirely randomly oriented, equiaxed, polygonal and strongly refined to a diameter of typically ~5μm.
Si was usually observed as agglomerations of grains with grain boundaries only observable by EBSD. EBSD showed that within Si agglomerations Si grains were not delineated by grain boundary Al, indicating that high angle Si-Si grain boundaries are not wetted by Al, consistent with the findings of Hogg (2005). The abundance of solid nucleants from both the spray and the injected overspray in Sandvik-Osprey CE7 provide an excess of Si nucleation sites resulting in tremendously refined, equiaxed Si grain size. Indeed it should be noted there are no other examples of an essentially 200kg cast ingot with an unvarying primary grain size of <5μm. While the Si grains are randomly oriented as expected from a excess of heterogeneous nucleation sites, this was not the case for the terminating Al-rich phase.

7.2.4 Al texture

Grant (1995a) reported that spray forming under optimum conditions is a process that produces a refined, relatively homogeneous and isotropic microstructure. However, several aspects of spray formed CE7 microstructure show significant inhomogeneity. The Al-rich secondary phase comprises large (>300μm) strongly oriented grains that form within the Si network and appear oblivious of the Si grains, as previously observed by Hogg (2005). The large Al grains are interpenetrated the Si network structure, with no evidence of heterogeneous nucleation on the surrounding Si matrix presumably due in part to the large difference in lattice parameter of Al=4.05Å and Si=5.43Å (Smithells 1978). The results described in Section 4.3.5 suggest that the Al-rich phase is columnar and aligned in the billet growth direction, although this has not been shown conclusively. In some instances, small regions of equiaxed, refined Al were observed, as shown in Figure 4.22(d). In these regions it is probable that the Al rich liquid was isolated or connected to the residual Al by a tortuous path, to alter locally the solidification conditions from growth of existing grains to favour the heterogeneous nucleation of α-Al on minority phases or impurities.

In combination, the CTE measurements (discussed in Section 7.4.2) and EBSD micro-texture investigations show that spray forming of Al-70Si yields a product that is inhomogeneous and anisotropic. These effects result from the nature of the spray forming process, the long freezing range, characteristics of the Al-70Si system, and necessary post-deposition methods to manipulate final solidification. While spray forming has allowed the production of billets on a

commercial scale in otherwise 'un-processable' materials, it is evident that the arising material presents challenges for scale up to full commercial manufacture with respect to porosity, macrosegregation, anisotropic CTE, low toughness and intermetallic and thermal crack initiation and growth.

7.2.5 Intermetallic particles

Gravimetric and ICP analyses of CE7 showed impurities of Fe, Cu, Ti and Zr of 0.37, 0.02, 0.02 and 0.03% respectively, as shown in Table 4.1. EPMA shows that these elements are present in the form of complex intermetallic phases with the range of morphologies and stoichiometries described in section 4.3.4. X-ray diffraction (XRD) analysis of these phases proved difficult because of their low volume fraction. Electron microscopy showed that many acicular intermetallic phases appear to initiate cracking of the adjacent primary Si. This is attributed largely to geometric effects of stress concentration around the tip of the particles, and in part to CTE mis-match between the intermetallic particles and adjacent Si shown in Figure 4.16. Subsequent discussion in sections 7.4.4 and 7.4.5 describes the effect of these intermetallic phases on bend strength and Weibull modulus before and after thermal cycling.

7.3 Hot isostatic pressing

Spray formed materials always have some residual porosity in the as-sprayed condition because of atomising gas entrapment, solidification shrinkage and gas evolution (Grant 1995a). In some alloy systems porosity can be reduced by de-gassing the melt with Ar to reduce the dissolved hydrogen content, by careful

control of the thermal conditions, or the use of reduced pressure operating environments. However shrinkage porosity and gas entrapment remain inherent in the spray forming process. Porosity can be removed by downstream HIP and / or forging operations but in some cases this can lead to deleterious texture and anisotropy (Grant 1995a). However, in CE7 the brittle Si network makes forging operations impossible and it is necessary to control porosity by primary processing and subsequent HIPing. In thermal management applications the electronic packages must often be hermetic, and for many space and aerospace applications, materials must exhibit no He transmission over a 24hr period (Jacobson 1998). Sandvik-Osprey use optimised HIPing conditions for CE7 of 565°C for 16 hours at 140MPa. The applied HIP pressure causes any pores to shrink and the entrapped gas in will either dissolve and diffuse away, or become compressed to a smaller pore. If the pore can be fully closed, the internal surfaces of the pore diffusion bond.

Experimental observations suggest that there is little growth of the primary Si during HIPing in Oxford CE7-based alloys. Because Sandvik-Osprey CE7 used higher HIP temperatures, it is conceivable that some coarsening of the primary Si occurs during HIPing. Assuming that Si coarsening in the solid state is diffusion controlled since the Si phase is frequently interpenetrated by the Al phase (continuous phases usually coarsen according to interface control and following parabolic kinetics), the isothermal coarsening behaviour was approximated (Martin 1997):

$$K = (r_t^3 - r_0^3)/t$$

Equation 7.3

where K is the isothermal coarsening constant at the given temperature, r_t is the Si radius after time t, r_0 is the initial Si radius, and t is the time at coarsening temperature. A coarsening constant of ~24000nm^3 s^{-1} was taken from a plot of coarsening constant versus Si concentration in the range 7 to 22% in Al-Si alloys (Jones 2004), and a linear extrapolation to 70% Si. While 22% to 70% Si is a large extrapolation, the Jones (2004) data is linear with r^2=0.96, this value of coarsening constant should therefore be regarded as a best estimate based on available data. Using Equation 7.3 a HIP cycle of 16 hours at 565°C will cause a 20μm Si particle to coarsen to 20.008μm, or a 5μm Si particle, suggested to be typical by EBSD results to coarsen to 5.1μm. Any Si coarsening during HIPing can therefore be concluded to be negligible both for Sandvik-Osprey CE7 and Oxford CE7-based materials.

7.4 Properties

7.4.1 Young's modulus

The CE7 Young's modulus (E) and Poisson's ratio (μ) were required to calculate K_{1c} from Herzian and Vickers indentation. Measurement of E by tensile test was problematic because of the brittle nature of the material. On the other hand impulse excitation measurements required a simple rectangular bar geometry and is a non-destructive test, allowing samples to be re-used for subsequent 4-point bend and CTE testing. Comparison of impulse excitation measurements of modulus at Oxford with measurements carried out at CERAM

by impulse excitation showed agreement to within ±3%. Sandvik-Osprey CE7 had a Young's Modulus of 129MPa and a Poisson's ratio of 0.36 as detailed in section 4.2.3. This compares with 168MPa for pure, polycrystalline Si (Ericson 1988) and 70MPa for annealed polycrystalline Al (Askeland 1993). Using a rule of mixtures (ROM) approach where $E_{Al\text{-}Si} = Vf\ E_{Si} + (1\text{-}Vf)\ E_{Al}$, E was estimated for Al-70Si as 138GPa. From the data presented in Figure 4.3 a ROM approach over-predicts the measured Young's modulus of CE alloys. A best-fit linear trend line fitted to the measured impulse excitation data showed the divergence increased with increasing Si content. While extrapolation of the best fit linear trend through the impulse excitation data gave excellent agreement with the modulus of pure Al of 70GPa, it did not correctly predict agree with the modulus for pure Si.

Measured moduli consistently below ROM can be explained by consideration of ASTM E1876-01 which is the testing standard for the determination of Young's modulus by impulse excitation of vibration (ASTM 2002). The standard states that the relationship between resonant frequency and Young's modulus is specifically applicable to homogeneous, isotropic materials. Figure 2.20 showed the inhomogeneous microstructure of CE7 consisting of an interpenetrating network of Al and primary Si. In the case of multi-phase or composite materials, the standard states that the resonant frequency behaviour is altered by the size, morphology, distribution, interfacial bonding and elastic properties of the second phase particles and is not dependent only on the volume fraction. From Figure 4.3 it would appear that the inhomogeneous, two phase microstructure of CE

alloys causes attenuation of the resonant response of the material, causing it to deviate from the ROM prediction in proportion to the Si content of the spray formed alloy. Methods of understanding and overcoming the attenuation of frequency in composite materials have been investigated by finite element modeling (Nisitani 1998), but are not considered within the scope of this thesis.

7.4.2 Coefficient of thermal expansion

In the temperature range 20 – 150°C the CTE of CE7 (cut in the X-axis, as shown in Figure 7.3(a) increased from ~4.0 to 8.0 $x10^{-6}$ $°C^{-1}$ and above 200°C is approximately constant at around 8.5 $x10^{-6}$ $°C^{-1}$. A CTE of ~8.5 is in good agreement with a rule of mixtures calculation for CE7 which predicts a CTE of 8.7 $x10^{-6}$ $°C^{-1}$ (Smithells, 1978). This indicates that the high modulus, low CTE Si phase is forced to expand beyond its own CTE by the lower modulus, higher CTE Al phase. The internal stresses associated with this process may cause cracking of the Si phase and undermine properties as discussed in Section 7.4.5.

Figure 4.5 showed a difference in the CTE in the X (radial) and Y (axial) billet orientations, with Y-axis samples having a CTE 0.6 to 0.9 $x10^{-6}$ $°C^{-1}$ greater than X-axis samples. Figure 7.3(a) shows the location of the samples in the billet and the Al macrosegregation map is shown in Figure 7.3(b). A previously determined relationship between CTE and composition for a range CE alloys is shown in Figure 7.3(c) (Osprey 2001). In the range Al-40Si to Al-30Si, the variation of CTE with composition in this range is ~0.2$x10^{-6}$ $°C^{-1}$ per 1% Si. The

macrosegregation map indicates the composition of the Y-axis and X-axis samples were Si-34Al and Si-30.5Al corresponding to a $0.7x10^{-6}$ $°C^{-1}$ difference in CTE and is consistent with measured differences shown in Figure 4.5.

7.4.3 Fracture Toughness

The fracture toughness of CE7 material is of primary consideration for Sandvik-Osprey in their manufacturing, handling and design of thermal management components. The most commonly recognised method for fracture toughness determination is the compact tensile test in which a fatigue pre-crack in a sample of known geometry is extended by tensile loading of the sample, the crack opening displacement (COD) is then measured by a clip gauge and the fracture toughness calculated as a function of load and COD (ASTM 1997). However, for CE7 the specialised machining and the complex sample geometry made this test prohibitively expensive and low ductility of CE7 necessitates many tests to generate confidence in the data.

Two alternative techniques were suggested (Roberts 2003), both techniques operating on the micro-scale and not requiring large volumes of material or complex and costly sample preparation. The Vickers indentation technique has been investigated by a variety of workers who showed the accuracy of the technique is strongly dependent on cracking mechanism and selection of the appropriate equation to process results (Ponton 1989a, 1989b). Results presented in Figure 4.1 and discussed in Section 4.2.1 showed that CE7 did not conform to either the Palmqvist or halfpenny cracking mechanisms.

The data for CE7 presented in Figure 4.1(a) at different indenter loads shows $P/c^{3/2}$ was not a constant, and behaved in a similar way to Knoop indentations in Lube (2001). This indicated that the point force model was not an appropriate description of the fracture behaviour of CE7 under Vickers indentation. Lube (2001) proposed several reasons why materials may deviate from the relationship in Equation 3.1 that assumes that K_{1c}, E and H are constants (Ponton 1989a). Lube (2001) simplified Equation 3.1 by combining E and H into a single parameter χ, where χ is a residual stress factor dependant on the elastic plastic deformation behaviour of the material as a function of indenter geometry. Lube (2001) is consistent with Ponton (1989a) in suggesting that if χ and K_{1c} are constant then $P/c^{3/2}$ is a constant independent of load. Lube (2001) stated that deviations from this behaviour may be explained by two main effects: (i) the deformation fields are not self similar for different indentation loads and thus lead to crack driving stress fields (characterised by changes in χ) that vary with indentation load; and (ii) the material exhibits an R-curve i.e. fracture toughness increases with crack extension

Plotting crack length c against K_{1c}, R-curve behaviour can clearly be seen for Sandvik-Osprey CE7 material as shown in Figure 4.1(b), and Equation 3.1 is not satisfied. Wegner 2001, Travitzky 1992, Rodel 1995 and Knechtel 1994 support the assertions by Lube (2001) and suggest that R-curve fracture behaviour is typical of two-phase ceramics and interpenetrating phase composite materials, such as CE7.

It is suggested that the fracture behaviour of CE7 in Figure 4.1(a) and 4.1(b) results from the very different fracture behaviour of the interpenetrating Al and Si phases. The ductile Al phase acts as a toughening mechanism in CE7 during Vickers indentation and the crack path does not conform to the Palmqvist or halfpenny models (Ponton 1989a, 1989b). As the crack propagates from the indent, bridging occurs in the Al phase leaving ductile metal ligaments which shield the crack tip and dissipate energy as they stretch plastically (in some cases) to failure. The extent of this bridging behaviour is dependant on several factors: ligament size associated with the scale of the microstructure (Rodel 1995); volume fraction of Al (Rodel 1995); and interfacial bonding (Knechtel 1994).

Therefore the Vickers indentation technique does not give a valid measure of fracture toughness in CE7 as calculated by Equation 3.1. Some attempts have been made to account for rising R-curve behaviour for Vickers determinations of fracture toughness in cermet materials (Tancret 2000). However further work to resolve this complex problem is not considered within the scope of this thesis. Nonetheless Vickers measurements add weight to the argument that the scale and distribution of the Al phase within the Si matrix is a key factor in controlling the fracture toughness of CE alloys. It should be understood that where Vickers K_{1c} is quoted, this is not an absolute value or a valid measure of fracture toughness, rather the Vickers indentation technique is used at a fixed load (5Kg) to rank and compare the fracture behaviour of Sandvik-Osprey CE alloys and Oxford modified CE7.

The Hertzian indentation test relies on the extension of pre-existing surface flaws under an applied load. This technique requires that there is suitable defect, of the optimum size / aspect ratio and in the optimum orientation with respect to the indenter (Warren 1995a). This criterion is rarely fulfilled and Warren (1995a) suggests a coarse polish prior to testing to increase the population of surface flaws and this was done in the current study using a 9μm diamond polish.

Vickers and Hertzian K_{1c} determination are described in Section 4.2.1 and 4.2.2 respectively and show Vickers K_{1c} value of 2.55 MPa $m^{1/2}$ compared with a Hertzian K_{1c} of 0.96 MPa $m^{1/2}$. This large discrepancy may be explained by the nature of the fracture in a 2-phase microstructure such as CE7, containing both brittle (Si) and ductile (Al) phases. The schematic of Vickers indentation in Figure 7.4(a) shows cracks propagating from the corners of the indentation. Cracks penetrate both Al and Si phases before being ultimately arrested by the more ductile Al phase. A schematic of a typical Hertzian indent is shown in 7.4(b) and consists of cracking only in the Si phase, showing that several crack nuclei have propagated forming a discontinuous ring-crack in the Si, broken by regions of more ductile Al. Thus it can be seen that the Vickers technique is propagating a crack through both phases, and providing a measure of the resistance to crack propagation of the bulk material. However, it is not a true measure of fracture toughness of CE7 as discussed above. Hertzian indentation is effectively measuring only the fracture toughness of Si, with no cracks propagating through the Al phase. This was supported by the results which showed that using Hertzian indentation the measured fracture toughness of

CE7 is 0.96MPa $m^{1/2}$ approaching literature values of 0.94MPa $m^{1/2}$ for pure polycrystalline Si (Ericson 1988). Thus it is considered that for CE alloys, neither the Vickers or Hertzian indentation techniques provide a valid measure of fracture toughness.

7.4.4 Bend testing

Figure 7.5 presents the bend test data as a Weibull plot comparing the difference in behaviour between the as-sprayed and HIPed material. The as-sprayed material exhibited a larger scatter of bend test results and correspondingly low Weibull modulus (M) of 12.6 indicating a low reliability and reproducibility under load. HIPed CE7 exhibited a significant improvement in reliability and reproducibility as well as UTS, after HIPing M=20.6. The low Weibull modulus of as-sprayed material is attributed to the residual porosity of 2 to 4area% in the as-sprayed microstructure that dominated failure behaviour so that micro-flaws were redundant in the failure process.

The HIPed material bend strengths fitted more readily to a Weibull distribution as shown in Figure 7.5, giving a Weibull modulus of 20.6. Porosity was reduced to <0.1% by HIPing, and failure of HIPed CE7 was controlled by the remaining distribution of micro-flaws. The divorced eutectic plays a critical role here, since it is postulated that if the divorced eutectic did not form, then the material integrity would be further undermined – perhaps to unusable strengths. Because there is no α-Al / Si eutectic, and indeed the residual Al-rich phase is relatively denuded in Si at 0.27%, the Al phase maintains significant ductility

that is critical in blunting / deflecting the myriad of Si based micro-cracks. The Al crack blunting mechanism is shown in Figure 4.12 cracks (a) & (c), Figure 4.13(c) and Figure 4.16(a) & (b), whereby cracks propagate freely through the Si phase and are arrested in the Al phase, usually at the Al-Si interface.
CE7 fracture surfaces contained two different fracture modes corresponding to the Al-rich and Si phases. The brittle Si phase failed by transgranular cracking, probably following certain crystallographic planes, typically <110> or <111> cleavage planes (Perez 2000); while failure of the Al-rich phase was by a ductile tearing mechanism. Figure 4.6(a) showed an example of a crack on a Fe-rich intermetallic particle, and together with the EPMA results shown in Figure 4.16(a) and (b), strongly suggests intermetallic particle involvement in inducing Si cracking. It is postulated that cracking is initiated by geometric effects arising from stress concentration around acicular intermetallic phases in combination with CTE mis-match between intermetallic particles and surrounding Si. The CTE of $FeAl_3$ is estimated at ~$1.8x10^{-6}$ $°C^{-1}$ (Reddy 2000) compared to 23.5 and $7.6x10^{-6}$ $°C^{-1}$ for Al and Si respectively (Smithells 1978). Consequently, during cooling from an elevated temperature $FeAl_3$ will be placed in compression by the greater contraction of surrounding Al-rich phases; by corollary, the brittle Si phase will be placed in tension, exacerbated in local regions of stress concentrating angular morphologies.

On the basis of the bend strengths the estimated tensile strength of HIPed Sandvik-Osprey CE7 was estimated at ~135MPa in Table 4.5(b). This low strength supports the observed cracking shown in Figures 4.6(a), 4.13(a) and

4.16(a) & (b) demonstrating a high population of flaws undermining material strength. From the empirical relationship given in Equation 7.4, the flaw size for fracture can be calculated:

$$K_{1c} \approx \sigma_F \cdot \sqrt{\pi c}$$

Equation 7.4

where K_{1c} is the fracture toughness (estimated as 2.55MPa $m^{1/2}$ from Section 4.2.1, but not an accurate value as discussed in Section 7.4.3), σ_F is the calculated UTS of 135MPa from Table 4.5(b)), and c is the flaw size. Rearranged to:

$$c = \left(\frac{K_{1c}}{\sigma_F} \right)^2 . \frac{1}{\pi}$$

Equation 7.5

this relationship indicates an average flaw size of ~114μm for HIPed material. This appears to be a disproportionately large defect for a bend test specimen of 60.0 x 8.0 x 4.0mm, however it should be noted that this calculation of flaw size is based on a K_{1c} which has only limited validity in those materials, as discussed in Section 7.4.3. No defects of this scale were ever observed in either optical microscopy shown in Figure 4.13(a) or electron microscopy shown in 4.16(a) & (b) where typical crack sizes are 10 – 20μm. It is speculated that in some cases the flaws in Si observed during 2D during microscopy must extend considerably further in 3D until arrested by the more ductile Al phase. It is therefore suggested that ~114μm^3 is the maximum volume of a region of cracked Si bounded by Al, and in many cases these Si regions will contain a 3D network of micro-cracks. However this is only supposition and X-ray micro-tomography would be required to investigate this.

7.4.5 Thermal cycling

Figure 7.6 shows that after thermal cycling, there is a reduction in the calculated UTS from 135 to 123MPa, but Weibull moduli remain unchanged at ~20 as shown in Figure 7.6. This indicates a step change in the flaw population where the reliability behaviour of the material remains similar after thermal cycling, but failure occurs at lower stresses.

Figure 4.12 showed that away from the fracture surfaces the population of micro-cracks induced in the Si was increased by thermal cycling. It is postulated that pre-existing cracks were propagated during thermal cycling by CTE mis-match between Si and intermetallic particles and / or Al-rich phase, with cracks propagating through Si by a ratchet mechanism during each temperature cycle (Brodie 2002). Optimising strength must therefore begin with minimising the occurrence of intermetallic particles, achieved by selection and control of feedstock materials with minimal impurities. In many thermal management applications CTE-graded packages are required to match the CTE of different electronic components. Packages often require welding or joining. Jacobson (1998) showed it was possible to EB weld and diffusion bond similar and dis-similar CE alloys, however the effect of thermal cycling on the joints was not reported. Figures 4.8 and 4.9 showed CE7-CE11 and CE7-CE11-CE7 diffusion bonded laminates after thermal cycling from -50 to +150°C. In both cases an Al foil interlayer was used to improve bonding and minimise interfacial CTE mismatch. There was no macroscopic delamination after 53 and 106 cycles and vacuum dye penetrant inspection showed no evidence of surface or interfacial micro-cracking. Results show that while thermal cycling is deleterious to the

bulk strength and Weibull modulus of CE7, there was no microstructural effect on the interface of graded materials.

7.5 Summary

- By recycling the overspray powder and re-injecting it via a particle injector Sandvik-Osprey obtain yields of ~80% during commercial manufacture of CE7. The particle injection ratio also had a strong effect on the inter-phase interface length, which is implicated in controlling toughness.
- The microstructure of CE7 consists of a network of agglomerated, randomly orientated, fine scale Si grains of ~5μm interpenetrated by large, orientated Al grains often >300μm. The Al phase is devoid of Al-Si lamellae eutectic and exhibits a divorced eutectic, due to slow cooling, low temperature gradient and growth velocity, high mobility of Si in liquid Al-Si and small inter-primary Si distances.
- CE7 exhibits significant radial macrosegregation of Al with consequent measurable effect on CTE. This segregation is driven by convective cooling from the billet edge during manufacture as reported by Mingard (2000) but is augmented by the post-spray directional cooling developed to manage gross defect formation in CE alloys
- Intermetallic particles result from the presence of impurity elements such as Fe, Cu, Zr, Ti in feedstock or picked up from foundry materials and are strongly implicated in crack initiation in the brittle primary Si phase

because of stress-concentrating morphologies and differences in CTE with the surrounding Al-rich phases.

- Cracks initiating from intermetallic particles undermine the bend strength of CE7
- Bend strengths in the as-sprayed condition are limited by porosity. After HIPing, porosity reduces dramatically and strength is controlled by the micro-flaws in the primary Si, many of which have been introduced by intermetallic phases.
- Cracks in the Si around acicular intermetallic particles are propagated during thermal cycling because of CTE mis-match at stress raising features, resulting in a loss of average bend strength.
- While spray forming has allowed the production of billets on a commercial scale in otherwise ‘un-processable’ materials, it is evident that the arising material present challenges of low toughness, in-service crack growth, and macrosegregation which need to be understood prior to full manufacture.

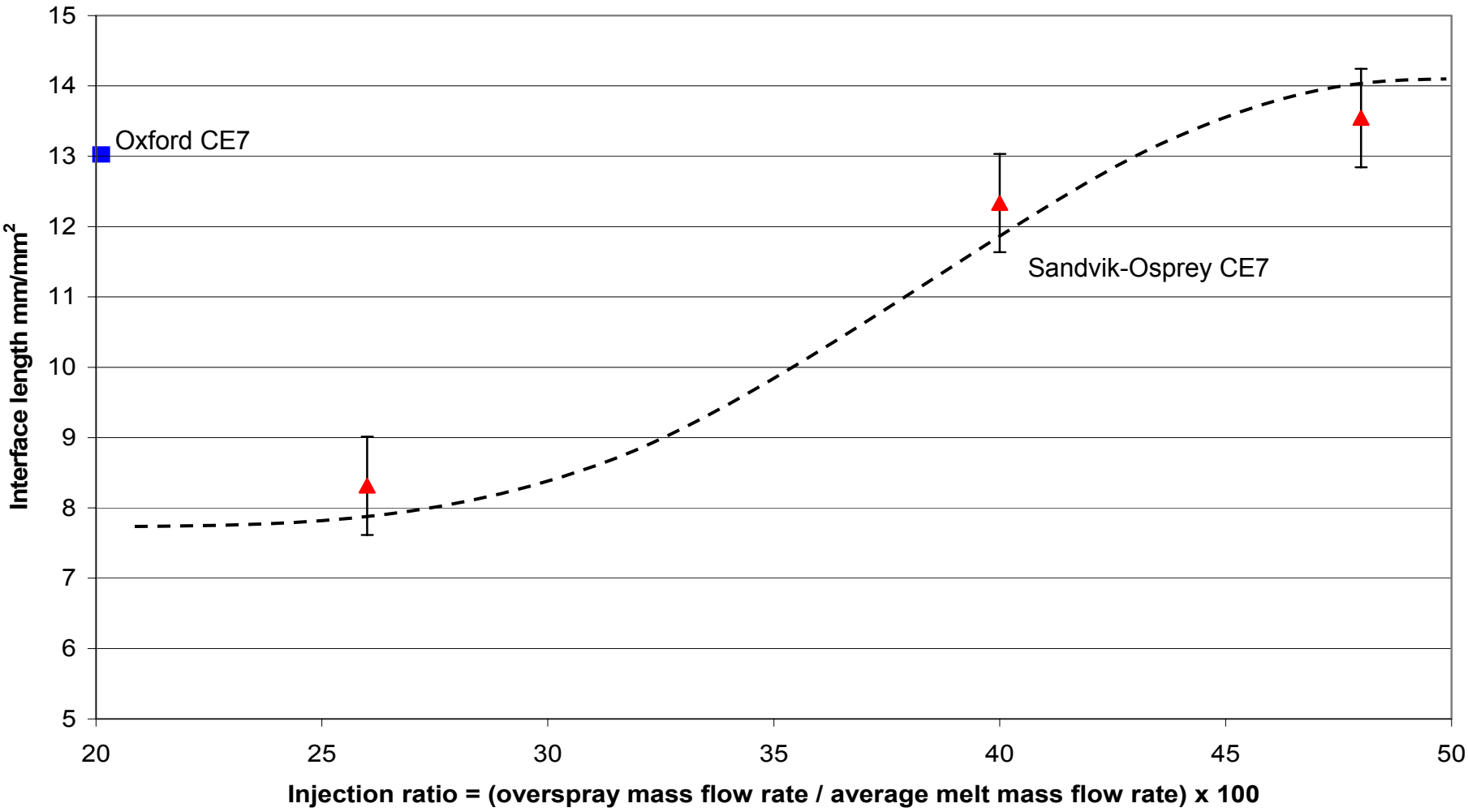

Figure 7.1

Plot suggesting the relationship between injection ratio and interface length

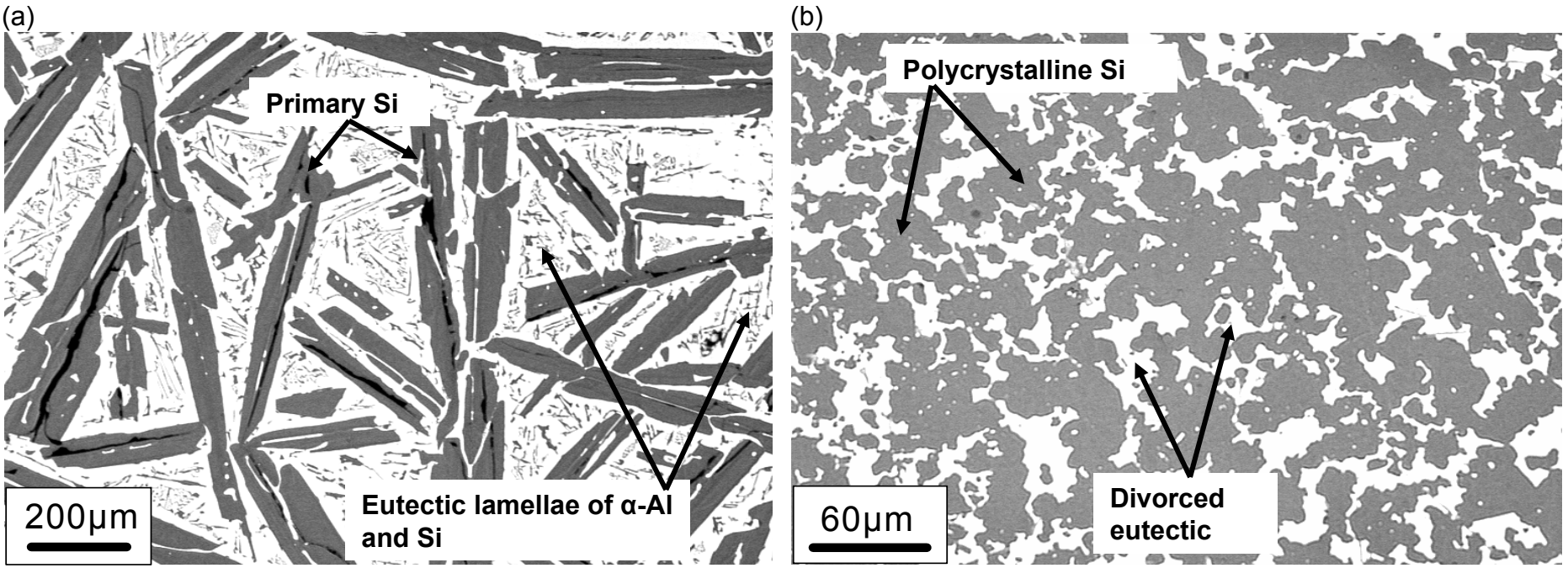

Figure 7.2

Optical micrographs of (a) cast Al-70Si, (b) spray formed Al-70Si (CE7)

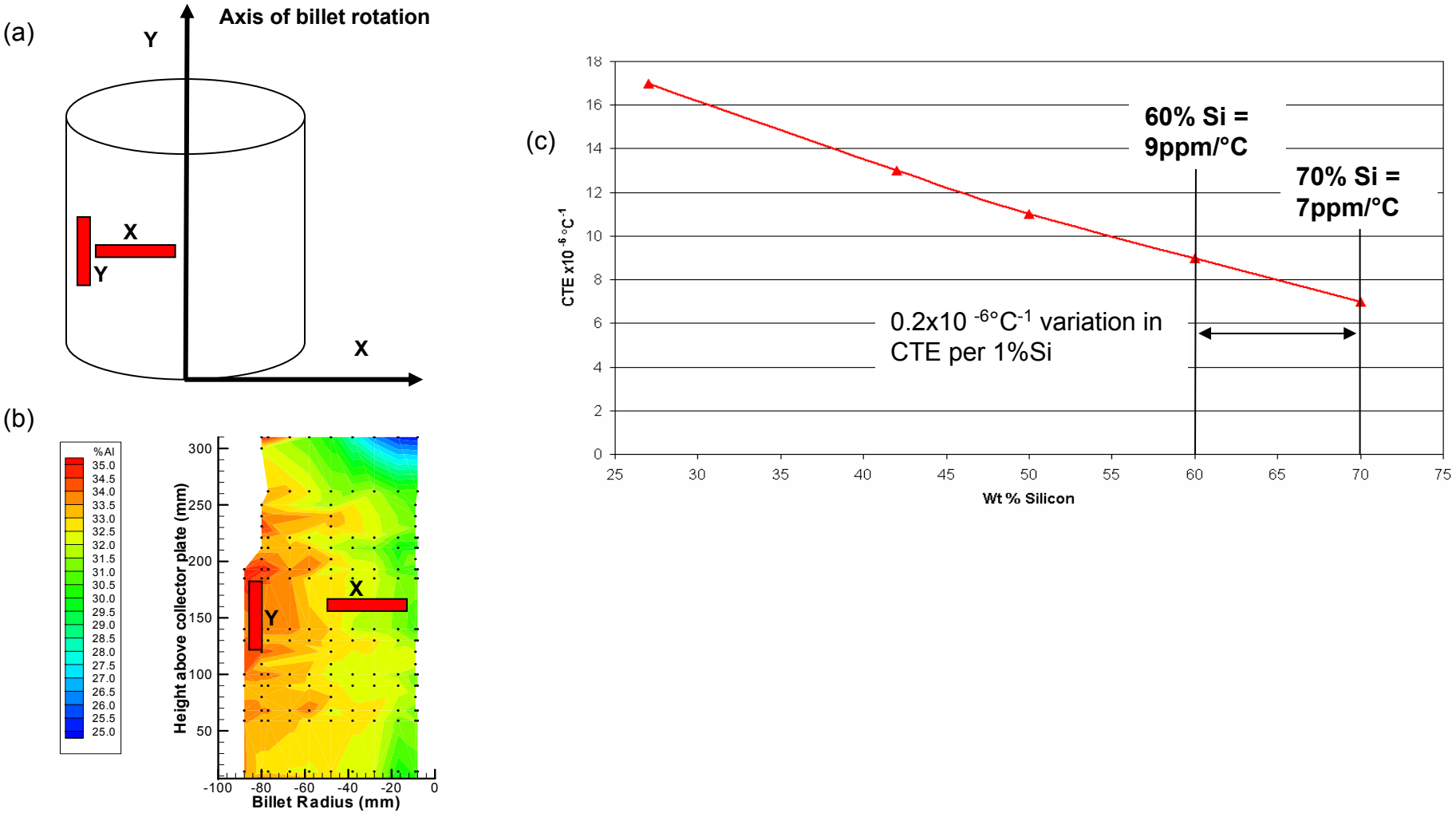

Figure 7.3

(a) Location of CTE test pieces within Osprey CE7 baseline billet, (b) location of CTE test pieces with relation to billet macrosegregation, (c) relationship between CTE and composition in spray formed CE alloys

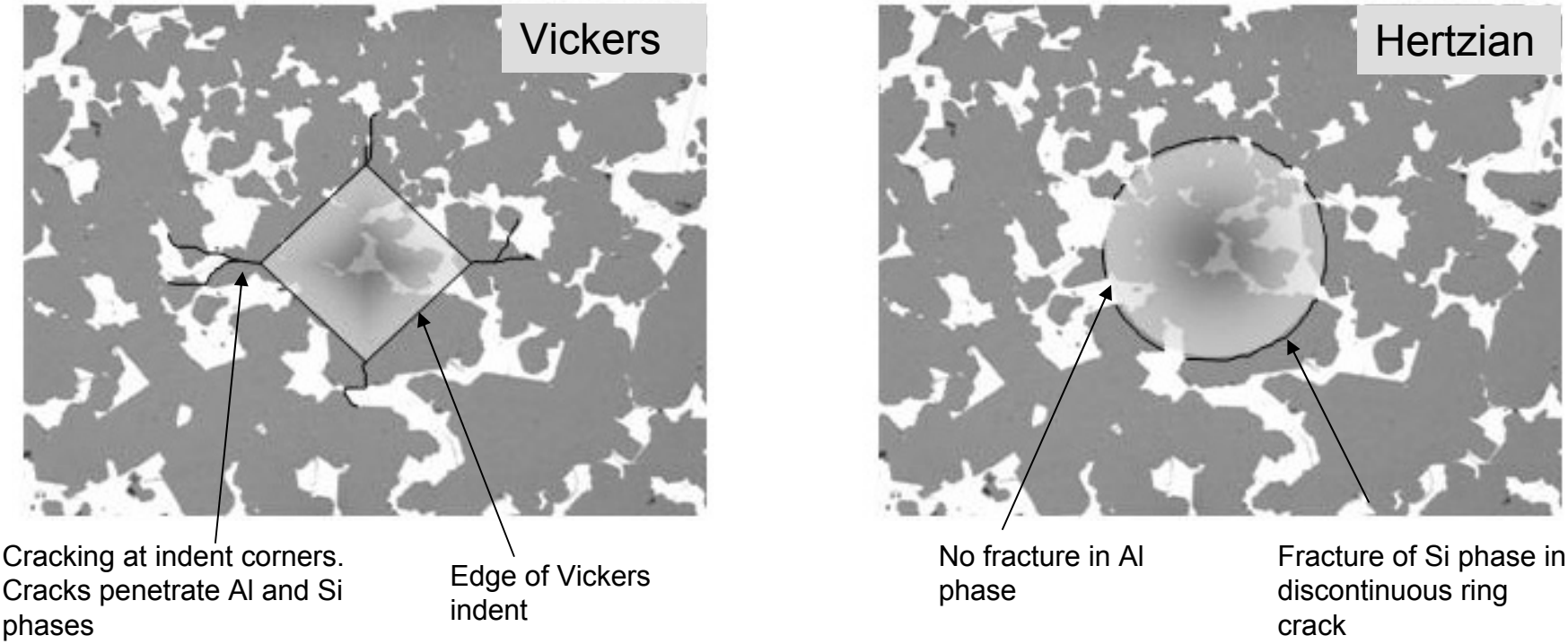

Figure 7.4

(a) Schematic of Vickers indentation fracture, (b) Schematic of Hertzian indentation fracture

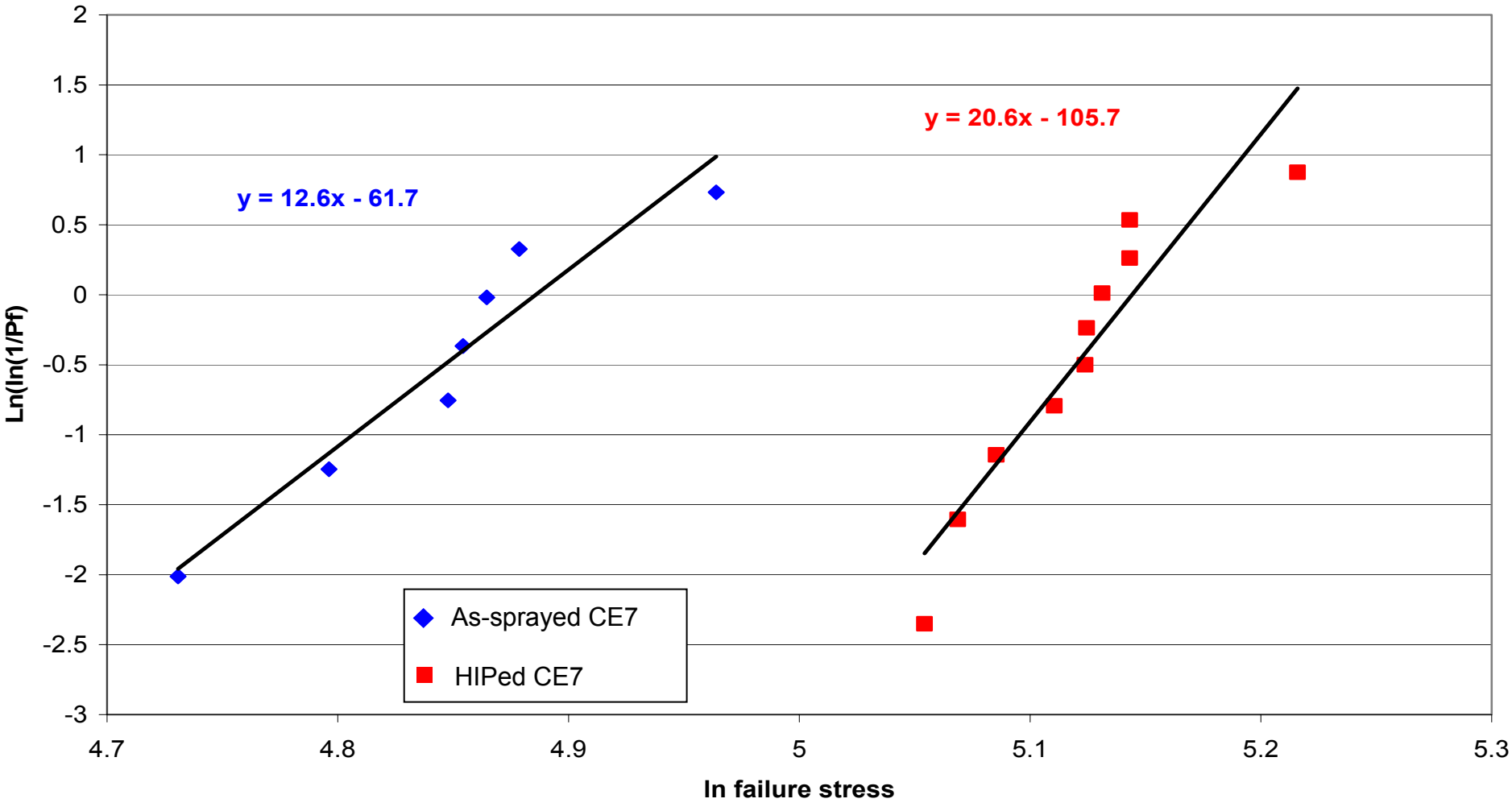

Figure 7.5
Weibull modulus plot of bend test data for as-sprayed and HIPed Sandvik-Osprey CE7

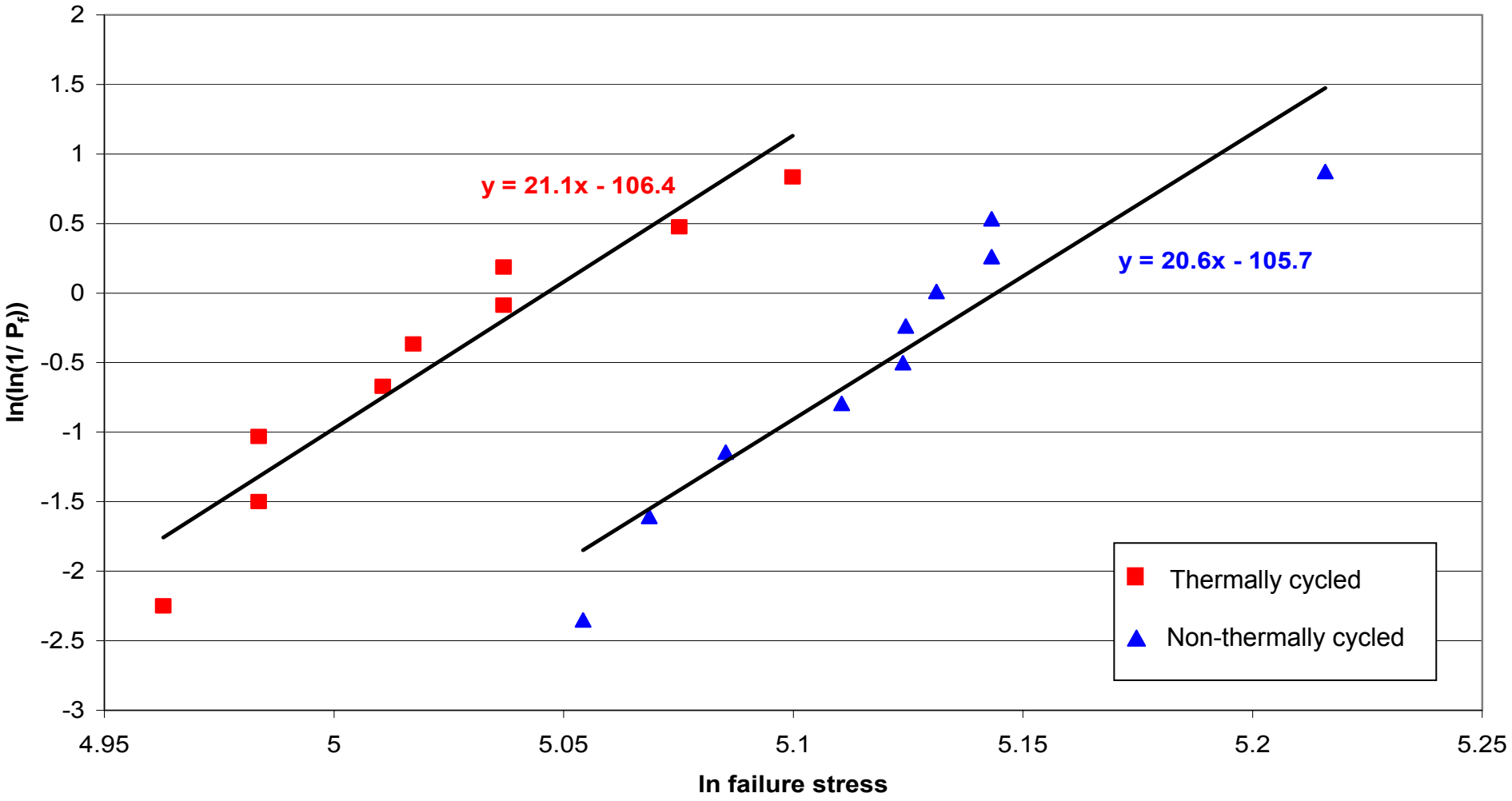

Figure 7.6

Weibull modulus plot of bend test data for HIPed Sandvik-Osprey CE7 before and after thermal cycling

8.0 Discussion - Al-50Si Chill Casting

The modification and inoculation of Al-high Si castings is discussed in Section 8.1, with the resultant microstructures being discussed in Section 8.2. Specific features of interest in the cast microstructure are discussed in more depth including; Si crystal morphology, Star morphology, Al halo, and the Al-Si eutectic structure, in Sections 8.2.1 – 8.2.4 respectively. The alloy additions selected for subsequent spray forming trials are reviewed in Section 8.3, with individual descriptions of the effect of B, P, Ce and Sr in Sections 8.3.1 – 8.3.4 respectively.

8.1 Alloy modification

Al-Si alloys containing ~6 to 25%Si encompass a large number of commercial alloys designed for strength and wear resistant applications (ASTM 1988) and have been the subject of review articles e.g. Lu (1995) and Tenekedjiev (1990). Above ~25% Si, there has been little research into inoculation and modification due to the lack of applications resulting from the low toughness of these alloys. In Chapter 5 various modifiers and inoculants representing those commonly used in industry (P, Sr, Sb), and other less common additions (Mg, Ce, Ce-P, B, Bi, Ti), were investigated for their possible benefit in reducing and refining microstructural scale in Si-Al alloys by a variety of possible mechanisms (ASTM 1988). In each case the melting, casting and cooling conditions of model Al-50Si were standardized to enable comparison.

8.2 Microstructure

The large freezing range of ~460°C in Al-50Si led to the formation of significant shrinkage porosity in all chill cast samples. Porosity, various intermetallic particles and the varying scale of the Al-Si eutectic made quantification of microstructures using image analysis difficult. Chapter 5, Figures 5.3 – 5.13, showed representative microstructures at a range of magnifications and estimates of the primary Si size and inter-eutectic lamellae spacing were made and are summarised in Table 8.2.

8.2.1 Si crystal morphology

Primary Si can form with a wide variety of morphologies depending on nucleation and growth conditions (Elliot 1983). In general there is a strong trend towards the growth of octahedral Si crystals with {111} facets (Wang 1997). Wang (1997 & 1999b), suggested limits to the growth velocity $V_{<111>}$ normal to the {111} facet plane, outside of which the Si crystal adopted other morphologies as shown in Figure 8.1 and where outgrowths from pyramidal corners formed from {111} planes resulted in the formation of hollow 'hopper' crystals (Wilcox 1977). Stage 1 in Figure 8.1 consists of radial, non-faceted, isotropic growth from nuclei typical of high undercoolings; during stage 2, growth becomes strongly faceted and the predominance of {111} surfaces imposes an octahedral morphology, often modified by twinning. Perfect octahedral growth requires that $V_{<111>}$ is equal for all facets and this was possibly not the case in the directionally cooled chill castings. During stage 3, at large Si crystal sizes of >50μm, stable growth at edges and corners is lost: in

the chill casting the rejection of Al from the growth region causes Al enrichment of the liquid adjacent to facets, reducing the Si supersaturation and hence reducing the driving force for growth. However at the corners and edges, rejected Al diffuses into the melt maintaining a relatively high Si concentration. Growth is therefore more rapid at edges and corners and leads to an acicular, often hollow crystal with dendritic outgrowths.

'Hopper crystals' occur where growth from certain crystallographic planes is greater than others resulting in particles with a trough or hopper type morphology. Wang (1997) produced solidification diagrams indicating the ratio of growth velocities (V) of different crystallographic planes which will impose equiaxed, octahedral or linear growth of Si crystals. Figure 8.1 shows a schematic of Si crystal growth (after Wang 1999b), indicating that at high undercoolings with directional cooling the octahedral morphology can not be sustained. In this case growth will proceed rapidly in the preferred <211> plane rather than the <111> plane, resulting in depressions in the <111> planes and ultimately resulting in long, linear hopper crystals.

Hopper crystals were observed in the unmodified Al-50Si alloy and also those with additions of 5.0%Ce, 0.5% B and 1.0% Bi. These additions were those that showed the least effective refinement of primary Si crystal size, suggesting larger Si particles had an increased tendency to form hopper crystals, consistent with arguments presented by Wang (1999b). Figure 8.2 shows chill cast CE7+5%Ce with examples of castellated, dendritic outgrowths at the periphery of hopper crystals.

The low volume fraction of effective nucleants in binary Al-50Si and Ce, B, and Bi modified alloys results in large primary Si crystals formed at high growth velocities, since for a given rate of heat exchange, poorly nucleated Si will grow at a relatively high velocity. Under these conditions, the microstructures suggest growth is unstable and results in breakdown of stable Si morphologies leading to dendritic outgrowths, branching and hopper crystals. When compared with spray forming, with an abundance of nuclei derived from the very large number of solid and semi-solid droplets introduced into the growing billet, the Si / liquid growth velocity is correspondingly lower and facilitates the stable growth of equiaxed, polygonal Si grains.

8.2.2 Si star morphology

P+Ce, Ti and Sb modified Al-Si alloys, shown in Figures 5.7, 5.12 and 5.13 respectively exhibited primary Si with a star morphology typically with 5 or 6 points, as previously observed by Napolitano (2004) and Kobayasi (1985 & 1979). The star morphology occurs because of the growth of multiple Si crystals from a single, multiply twinned decahedral nucleus (Kobayasi 1979). Kobayasi (1979) showed that certain combinations of local growth velocity (V) and thermal gradient (G), as well as local constitutional factors, enhance the development of Si star morphologies. As the G/V ratio is increased above ~10^3 sKmm^{-2}, a randomly orientated plate morphology is replaced with connected angular Si particles in a star configuration. Much of the relevant literature concerns un-modified alloys and lower Si contents than those investigated here, yielding a simpler microstructure and making features such as the star

morphology more readily observable, Napolitano (2004) being a typical example. Figures 8.3(a) and 8.3(b) after Napolitano (2004) show the formation of primary Si stars in Al-13Si at G=7.5°Cmm^{-1} and V=5μms^{-1} and 0.5μms^{-1} respectively. Star morphology Si in chill cast alloys modified with Sb and Ti respectively are shown in Figure 8.3(c) and 8.3(d). The Si star morphology is much less distinct because of the more uncontrolled solidification conditions, the microstructural scale is coarser and the primary Si more defective.

8.2.3 Al halo

In faceted / non-faceted alloy systems such as Al-Si, solidification conditions can give rise to eutectic microstructures over a range of compositions. The 'coupled zone' is the term used to express the range of liquid compositions and undercoolings and growth conditions that permit a fully eutectic microstructure (Hellawell 1970). Solidification under conditions outside the coupled zone leads to microstructural features in hypereutectic alloys such as an Al halo around primary Si and dendritic α-Al surrounded by eutectic (Fisher 1979). The boundaries of the coupled zone represent the locus of temperatures at which primary crystals grow at the same rate as a fine scale duplex front, and are dependent upon the temperature gradient G and growth velocity V (Fisher 1979).

After primary Si phase nucleation, the liquid composition moves down the liquidus until the terminating eutectic reaction is reached and phase separation and solidification occur. The liquid adjacent to primary Si will be enriched in Al and if the liquid composition is outside the coupled zone Al may grow epitaxially

as a halo on the primary Si as previously observed by Thangaraj (1992). Section 5.1 showed that a halo of Al devoid of eutectic Si was present at the periphery of all primary Si crystals. Examples shown in Figure 8.4 indicate that Al has grown epitaxially on the adjacent pre-existing primary Si, rather than nucleating and growing an α-Al / Si lamellar eutectic by conventional coupled growth. As the halo grows, the surrounding liquid becomes enriched in Si until a point where the liquid composition satisfies coupled growth conditions and α-Al / Si eutectic forms.

The growth of the Al is often dendritic (Fisher 1979) as shown in Figure 8.4(a), (b) and (d). Cracking in the primary Si is attributed to thermal contraction stresses from the mis-match of Si and intermetallic particles during cooling to room temperature and many of the cracks were arrested by the relatively ductile Al halo as shown in Figure 8.4(d).

8.2.4 Eutectic structure

It is well documented that the addition of elements such as Sr and Sb to hypoeutectic Al-Si alloys result in a finer lamellar (fibrous) eutectic microstructure (Elliot 1983). A review by StJohn (1999) states that Sr modified Si eutectic exhibits a high twin density with micro-faceted Si which promotes epitaxial growth of Al. Optical micrographs of Al-50Si +Sr in Figures 5.9(a-c) show significant eutectic refinement compared with the unmodified alloy shown in Figure 5.3. Additions of Bi, Mg and Ti were also demonstrated in Sections 5..2.8, 5.2.9 and 5.2.10 respectively to be effective in the refinement of the

eutectic microstructure and are shown in Figures 5.10, 5.11 and 5.12 respectively, but are less commonly used in conventional Al-Si alloys. There is no general agreement on the refinement mechanisms of these additions, (Dahle 2001, ASTM 1988). Common explanations suggest that these additions suppress the growth of Si within the eutectic, yielding a finer lamellar spacing. The microstructural scale also depends upon the cooling conditions (Jenkinson 1975) with increased solidification rates leading to a similar refinement of the inter-lamellar eutectic spacing (ASTM 1988). Since the casting conditions were nominally constant, microstructural changes due to ternary additions have been ascribed to the effects of nucleation and growth only.

8.3 Alloy screening and selection

The Key features of the chill cast microstructures are summarised in Table 8.2 below. Shaded cells indicate those alloy additions used in subsequent spray forming experiments.

Table 8.2, Summary of modified Al-Si chill cast microstructures, and corresponding Figures

Alloy (wt%) Figures	**Primary Si** Key Features	**Eutectic** Key Features
Al-50Si Fig 5.3	Si rods >1mm x 70µm Hopper crystals	Coarse irregular flake Indistinct Al halo ~15µm wide
Al-50Si+0.5%P (slow cool) Fig 5.14(a)	Fine, equiaxed and short rods >800µm and equiaxed, & short rods ~50 – 100µm	Fine lamellae ~2µm spacing Weak Al halo, dendritic Al
Al-50Si+0.5%P Fig 5.4 & 5.14(b)	Fine, equiaxed, & short rods, ~50 – 100µm	Fine lamellae ~2µm spacing Weak Al halo, dendritic Al
Al-50Si+1.0%P Fig 5.5, 5.14(c) & 8.3(c)	Fine, equiaxed ~30 – 50µm Hexagonal, curved faces	Fine lamellae, 0.5µm spacing Strong, interacting Al halos
Al-50Si+5.0%Ce Fig 5.6 & 8.2	Si rods >1mm length Hopper crystals Curved, castellated surfaces	Script morphology ~7µm lamellae spacing Intermittent Al halo
Al-50Si+ 1.0%P+5.0%Ce Fig 5.7	Si rods >500µm length Star morphology Hopper crystals	Script morphology ~5 µm lamellae spacing Indistinct Al Halo
Al-50Si+0.5%B Fig 5.8	Rods (200x20µm) and clusters / colonies Interpenetrated by Al	Coarse flake morphology Intermittent Al halo
Al-50Si+0.05%Sr Fig 5.9 & 8.3(d)	Si rods 300 - 1000 x 90µm Rounded rod ends	V. fine script morphology Dendritic Al, narrow Al halo
Al-50Si+1.0%Bi Fig 5.10 & 8.3(a)	Si rods 500 - 800µm length Hopper crystals Angular rods	Fibrous 'wheat sheaf' ~3µm lamellae spacing Defined 10µm Al halo
Al-50Si+2.0%Mg Fig 5.11	Cracked Si rods >1mm Hopper crystals	Feather morphology Mg_2Si Fine eutectic Dendritic Al, strong Al Halo
Al-50Si+0.5%Ti Fig 5.12, 8.3(d) & 8.3(b)	Cracked Si rods 500 – 1000µm x 100µm Star morphology	Varied lamellae spacing Al Halo, dendritic Al
Al-50Si+0.4%Sb Fig 5.13 & 8.4(c)	Si rods 200 - 400µm length Star morphology	Fibrous flake morphology Al-Sb hexagonal intermetallics
N.B. Shaded cells indicate those additions used in subsequent spray forming experiments		

Based on the study of chill cast modified Al-50Si microstructures and related literature, a selection was made of four alloy additions deemed to be most

effective in refining primary Si. The selected alloy additions were B, P, Ce and Sr, and typical micrographs of the chill cast microstructure are shown in Figure 8.5 together with an unmodified Al-50Si chill casting for comparison. The selection of P, B & Sr modifier elements is supported by Elkem (1994) who used additions of ~0.1%B, 0.05%P and 0.5%Sr to modify Al >35Si alloys manufactured by powder metallurgy and hot consolidation.

8.3.1 Boron

B was observed to be effective in both refining the primary Si and producing a less faceted morphology of many fragmented hopper crystals as shown in Figure 5.8. Nogita (2003) demonstrated successful refinement of Al-10Si hypoeutectic alloys with 720ppm of B. Maintaining this B:Si ratio gives ~0.5%B for Al-70Si. Due to concerns about sedimentation of AlB_{12} particles (Mohanty 1996), this was increased to an addition of 1%B for subsequent spray formed CE7-based alloys.

8.3.2 Phosphorus

Chill cast microstructures showed that P was extremely effective in refining primary and eutectic Si at high Si contents as shown in Figure 5.4, 5.5 & 5.14. Refinement occurred because of a progressively higher AlP nucleation density and an increase in cooling rate. Figure 5.14 shows increasing refinement with increasing P addition and decreasing cooling rate. As the primary Si size decreased, the interface length increased and produced a corresponding increase in fracture toughness as shown in Figure 5.15, supporting the

hypothesis that interface length is important in controlling toughness. Despite considerable refinement compared to unmodified chill cast Al-50Si, the degree of microstructural refinement remains small compared to spray formed material. Sandvik-Osprey CE7 had an interface length an order of magnitude greater of ~14mm/mm^2 with a corresponding K_{1c} measured by Vickers indentation of 3.14MPa m$^{1/2}$, resulting from the large number of nucleation sites from solid and semi-solid droplets and the re-injected overspray powder.

Typical P additions to a hypoeutectic Al-20Si alloy are 200 – 500ppm, with additions made as Fe-P or Cu-P, added to the melt at ~800°C prior to casting (Kyffin 2001, Heshmatpour 1996, Arnold 1961). Owing to the higher pour temperature for spray formed CE7 of ~1450°C, the increased crucible residence time and the high vapour pressure of P, an excess of P was added to the melt in an attempt to ensure sufficient P remained for effective modification. Unlike Na and Sr (Arnold 1961), no reports were found in the literature of deleterious effects due to over modification with P, therefore 0.9% P was added, with the expectation that a large proportion would be lost in evaporation. In practice ~54% was lost through evaporation giving ~0.49%P in the spray formed alloy as shown in Table 6.3.

8.3.3 Cerium

Ce had a strong effect on the growth mechanism of Si in chill castings, with a marked decrease in the length scale of the primary Si as shown in Figure 5.6. Jirattiticharoean (2004) and Xian (1993) suggested that co-inoculation with Ce

and P can be effective by the combination of refinement mechanisms: P to nucleate Si and Ce to inhibit Si growth. Based on the literature, and evidence from chill casting experiments, an addition of 1.0%P and 5.0% Ce was selected.

8.3.4 Strontium

Fjellstedt (2001) demonstrated the efficacy of Sr in refining the length scale of the primary Si in Al-25Si with additions of 250ppm Sr, noting that the refining effect of Sr increased with increasing cooling rate. Sr is widely used in hypoeutectic and hypereutectic Al-Si alloys, and in chill cast Al-50Si was demonstrated to be effective in refining the Al-Si eutectic structure, as described in section 5.2.7. There is a wealth of literature relating to the modification of Si in Al-Si alloys using Sr, however the majority of these do not consider alloys with a Si content greater than ~20% (Dahle 2001, StJohn 1999, Haque 1995, Yilmaz 1992, Tenekedjiev 1989 and Jenkinson 1975). The modifying effect of Sr was plotted as a function of Sr:Si in an effort to extrapolate likely required Sr concentrations to the high Si concentrations typical of CE alloys, as shown in Figure 8.6. Based on Figure 8.6, at a concentration of 70% Si, the addition of 0.25%Sr to Al-70Si was chosen.

8.4 Summary

- Chill cast Al-50Si consisted of large primary Si rods of <1mm, delineated by regions of coarse flake-like α-Al / Si eutectic.
- Additions of P, B and Sb produced refinement of the primary Si size, with the most significant effect from additions of P. Additions of P, P+Ce, Sr, Bi, Mg and Ti refined the inter-lamellae spacing of the eutectic, with Sr showing the strongest effect.
- Microstructural features such as Si hopper crystals and star morphology primary Si resulted from faceted growth of Si, twinning and conditions of temperature gradient (G), and growth rate (V).
- Conditions of G and V and local compositional factors result in eutectic solidification outside the coupled zone resulting in dendritic Al and Al halo regions surrounding primary Si.
- Progressively more refined primary Si was observed in Al-50Si +P with increasing P addition and increasing cooling rate. Refinement resulted in an increase in inter-phase interface length with a corresponding increase in toughness
- Based on observations from chill cast microstructures, additions of 1%B, 0.9%P, 1%P+5%Ce and 0.25%Sr were selected as suitable additions for modification of spray formed Al-70Si.

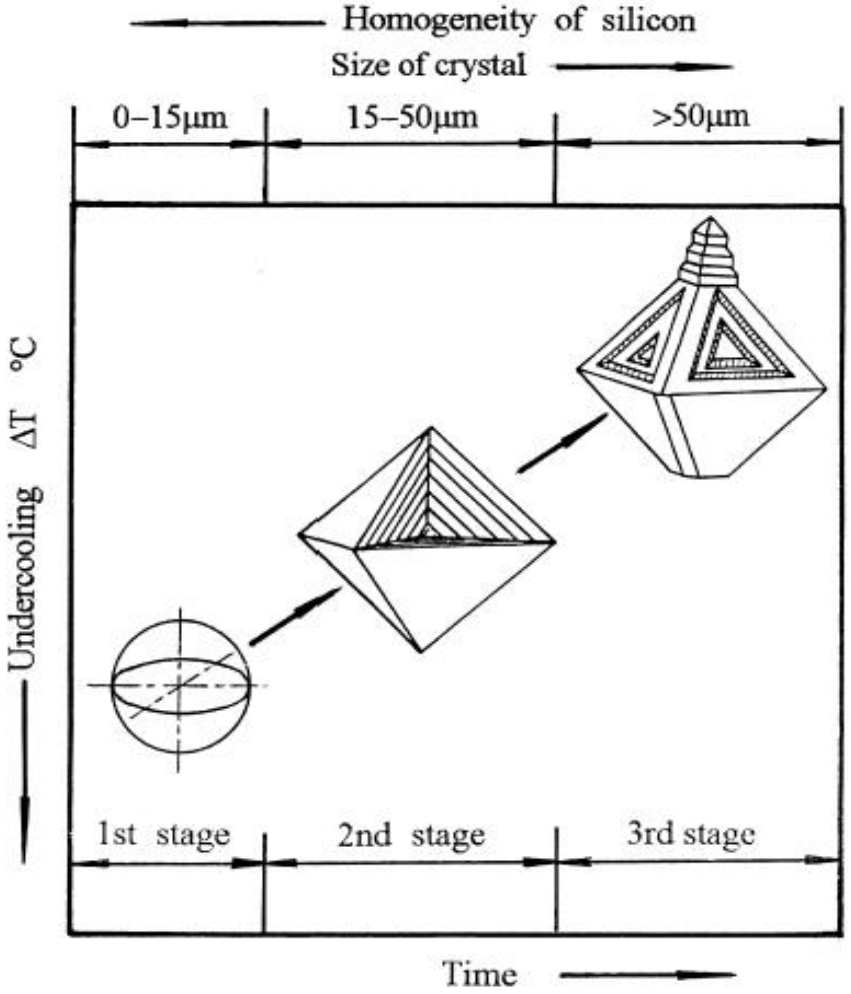

Stage 1

Radial, non-faceted, isotropic growth from nucleus. Typical at high undercooling.

Stage 2

Strongly faceted and the {111} impose an octahedral shape, often modified by twinning. Perfect octahedral growth requires that $V_{<111>}$ (the growth velocity normal to each {111} facet) is equal for all facets. This is not the case in a directionally cooled chill casting. Stable growth occurs at moderate to low undercooling.

Stage 3

At large Si crystal sizes stable growth at edges and corners is lost. Rejection of Al from the growth region causes Al enrichment of the liquid adjacent to facets, reducing the Si supersaturation hence reducing the driving force for growth. Adjacent to corners, rejected Al diffuses into a larger body of melt, permitting a higher Si concentration to be maintained. Growth is more rapid at edges and corners leading to acicular, often hollow crystals or dendritic outgrowths at corners.

Figure 8.1

The 3 stages of growth in primary Si, showing [1] isotropic nucleus [2] stable octahedral growth, [3] unstable, acicular crystal growth of hollow crystals (after Wang 1999b).

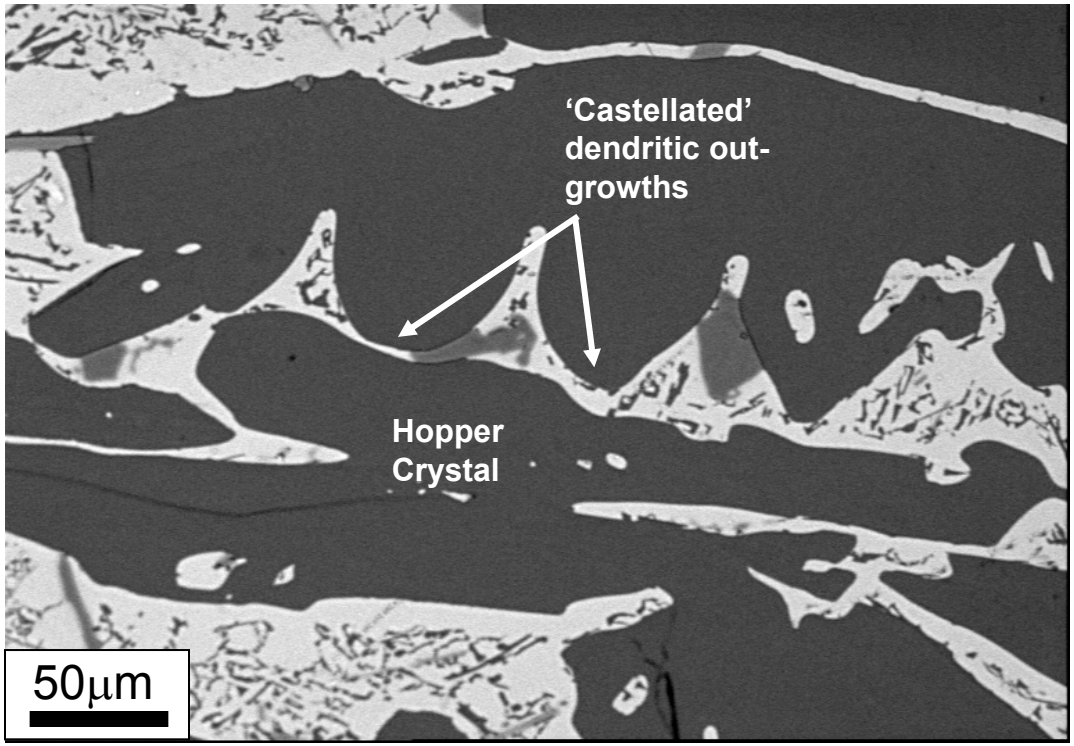

Figure 8.2

Chill cast Al-50Si modified with 5%Ce showing castellated dendritic out-growths and hollow 'hopper' crystals.

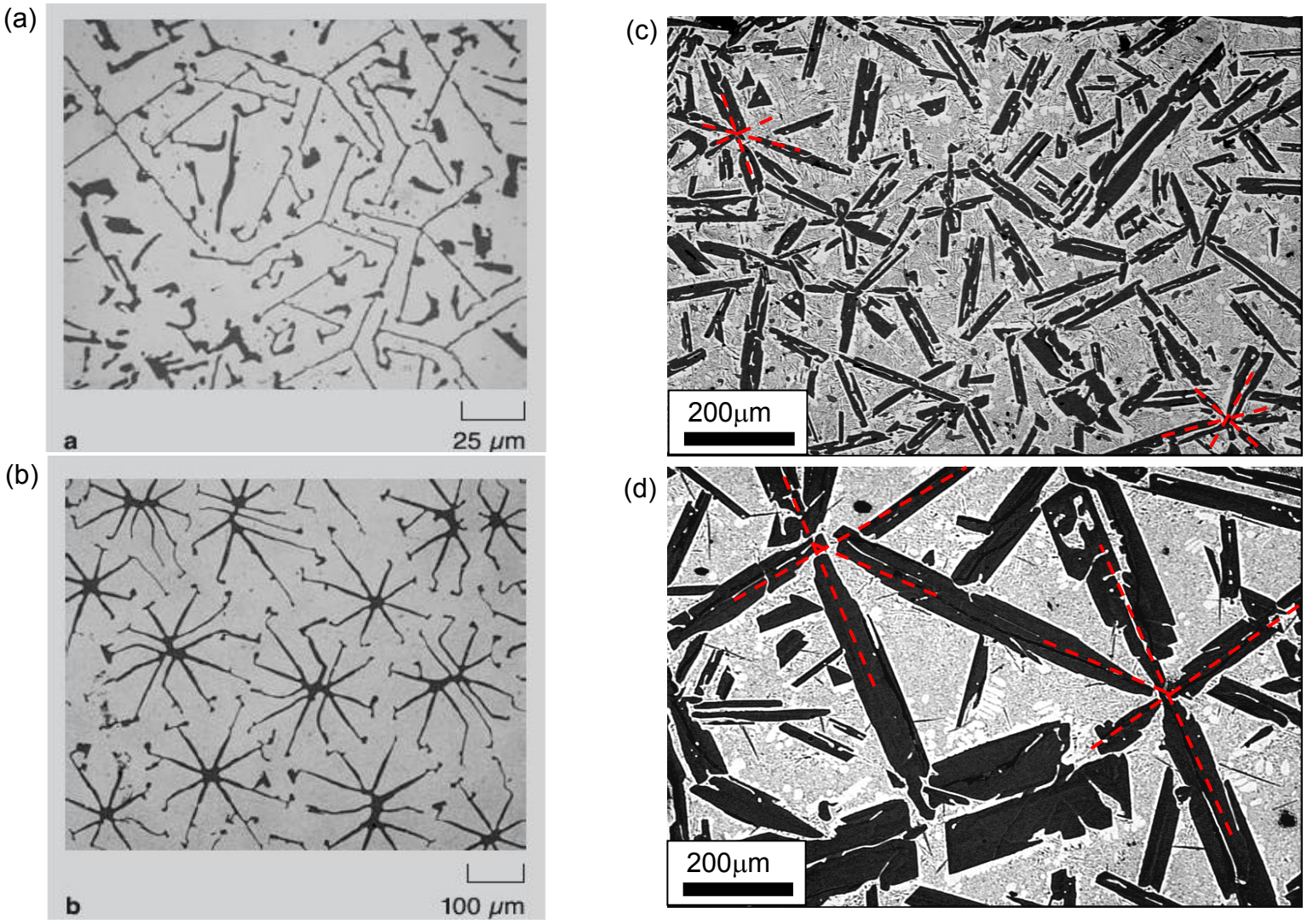

Figure 8.3 (a) – (d)

Star morphology Si observed in Al-13Si directionally solidified with a thermal gradient of G=7.5°C/mm and a growth velocity of (a) 5μm/s and (b) 0.5μm/s (after Napolitano 2004). Star morphologies observed in chill cast Al-50Si with additions of (c) 0.4% Sb and (d) 0.5%Ti. Star morphology Si is highlighted with yellow dashed lines.

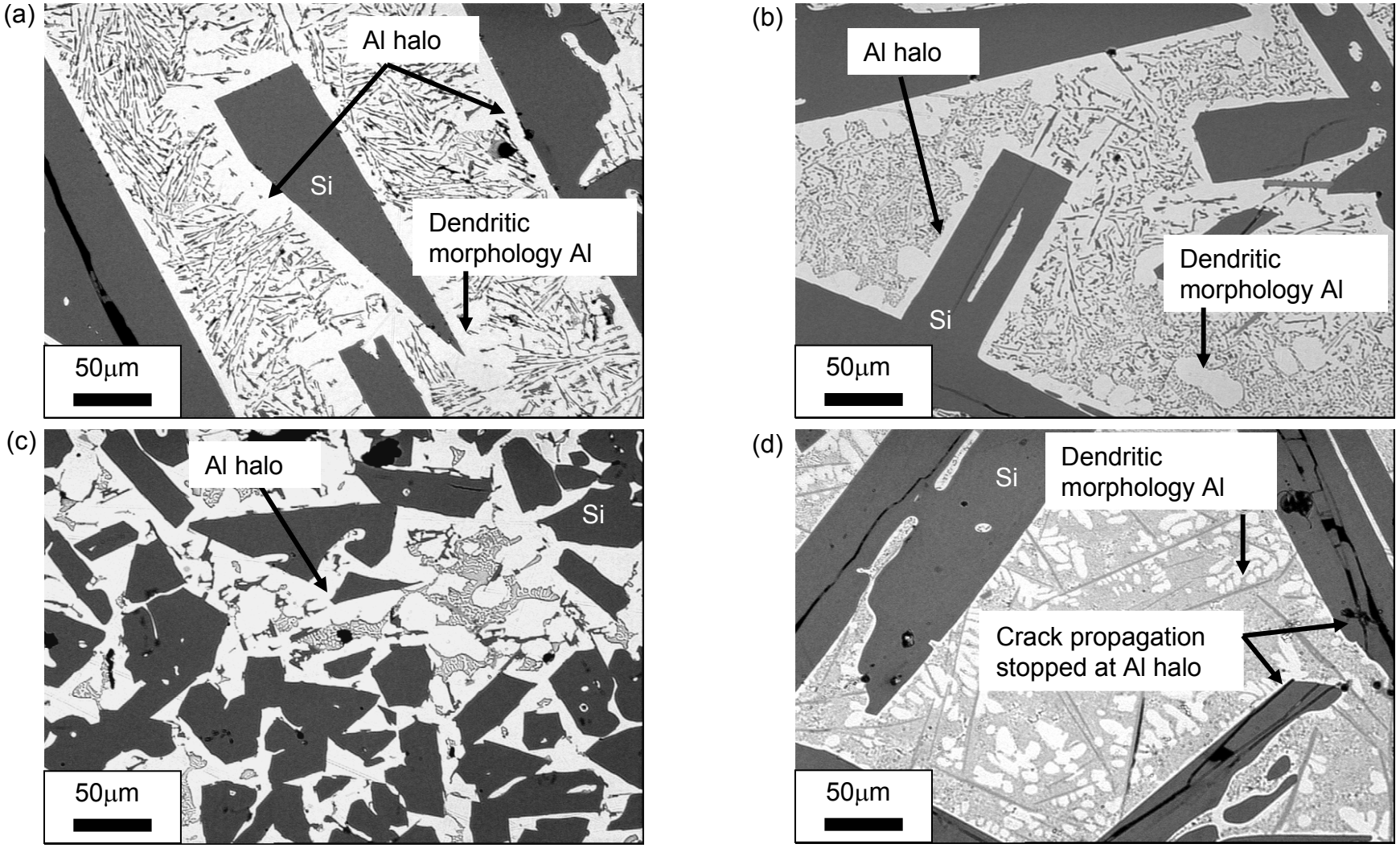

Figure 8.4 (a) – (d)

Examples of Al halo observed around primary Si in chill cast Al-50Si modified with (a) 1.0%Bi, (b) 0.5%Ti, (c) 1.0%P and (d) 0.05%Sr.

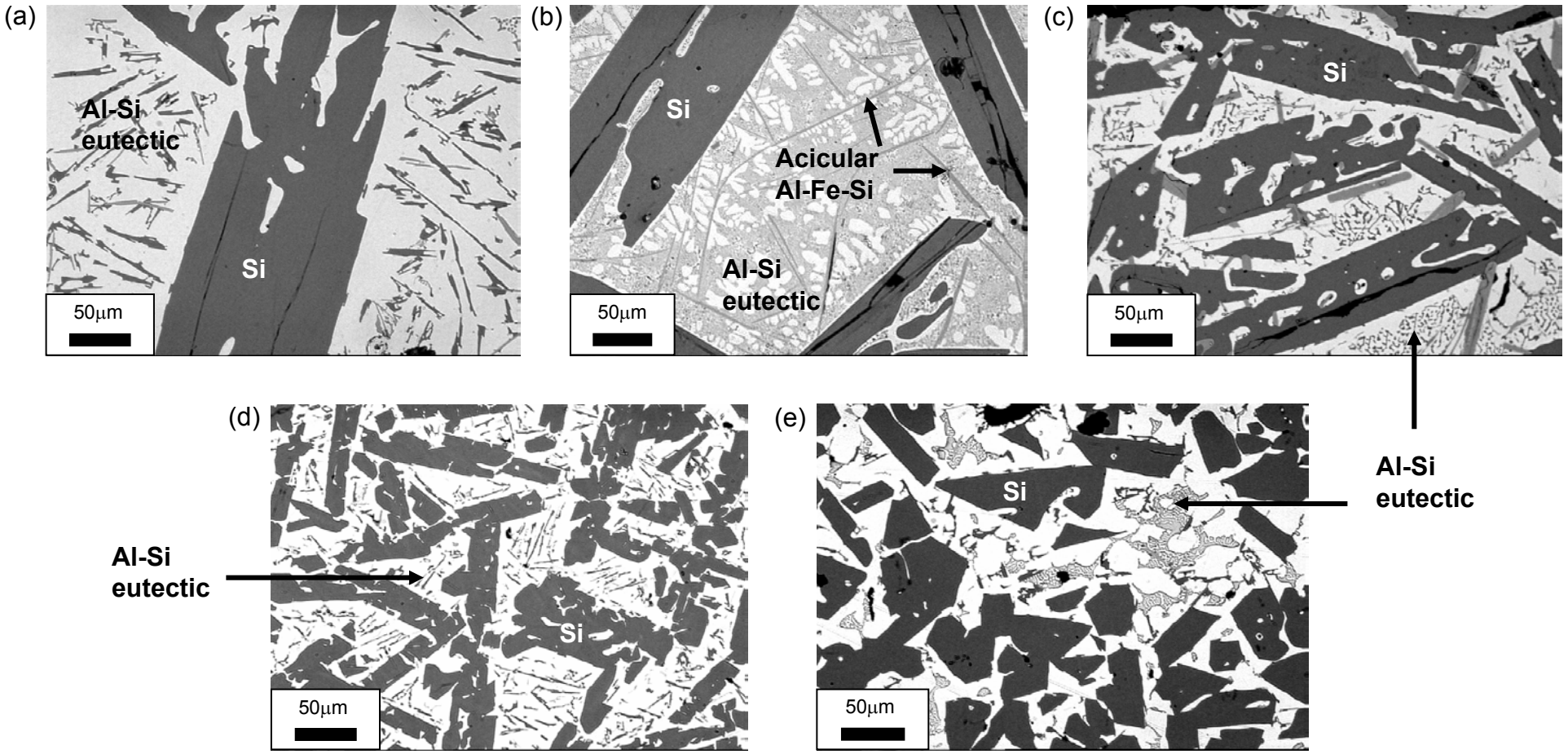

Figure 8.5 (a) – (e)

Optical micrographs of chill cast microstructure: (a) unmodified Al-50Si, (b) Sr modified Al-50Si, (c) P-Ce modified Al-50Si, (d) B modified Al-50Si, and (e) P modified Al-50Si.

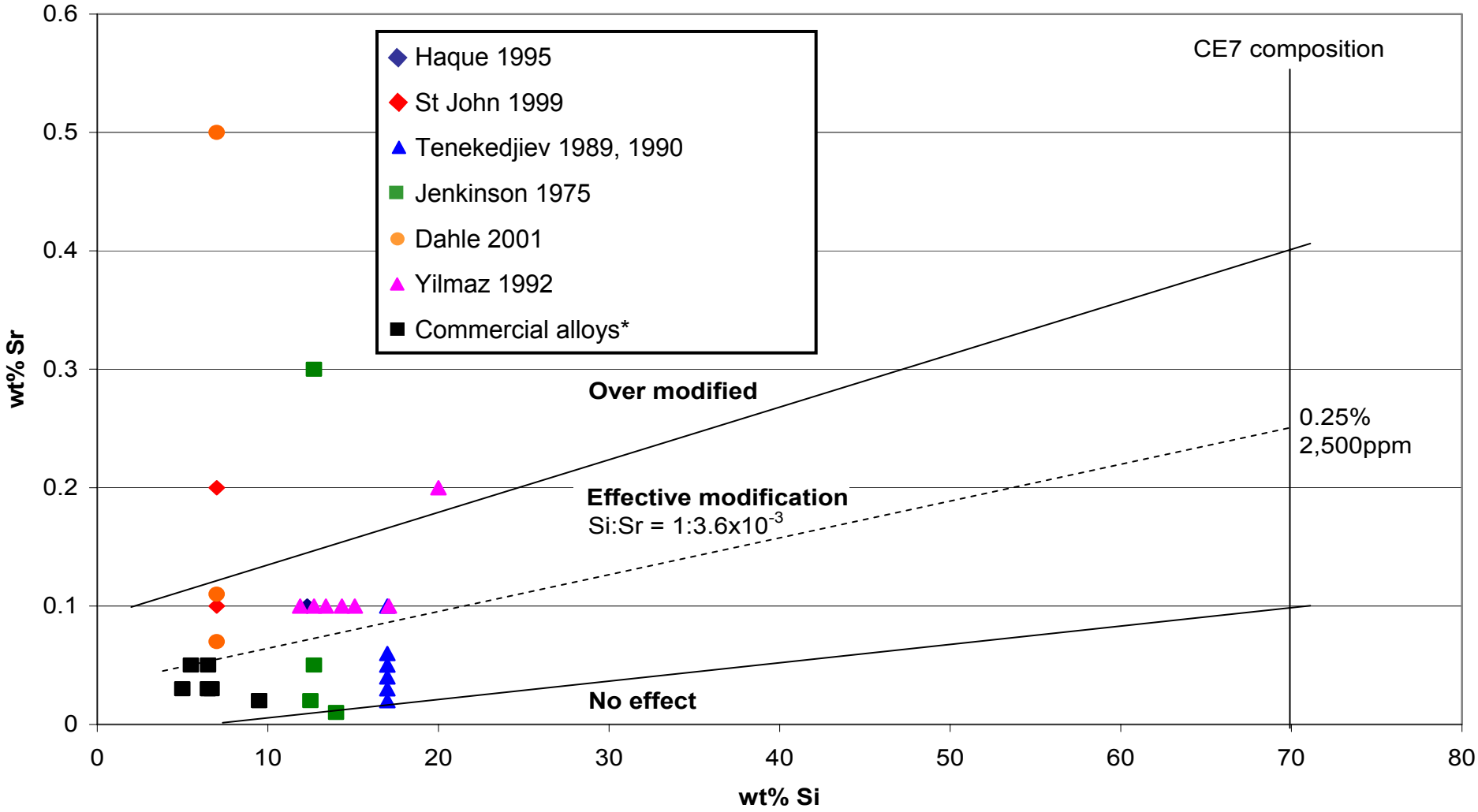

Figure 8.6

Map of Sr and Si concentrations in Al-Si-Sr alloys showing regions of relative efficacy of refinement.

(* Commercial alloy designations: 356.2M, 357, a356.2m, a356.2r, 365.1)

9.0 Discussion - CE alloys manufactured at Oxford University.

The processing of modified CE7 is discussed in Section 9.1, pyrometry was used as a measure of process repeatability during billet manufacture and is discussed in Section 9.1.1. Immediately after spray forming was complete the billet was insulated and directionally cooled, this procedure and its effect are described in Section 9.1.2. Post spray forming HIPing to reduce porosity is discussed in Section 9.2. The resultant microstructure for B, P P+Ce and Sr modified CE7 is discussed in Sections 9.3.1 – 9.3.4 respectively, and texture and grain size compared in Section 9.3.5. The resultant mechanical properties are discussed in the context of the microstructure in Section 9.4. Inter-phase interface length is considered and the influence on fracture toughness discussed in Section 9.4.1. Macrosegregation is considered in Section 9.4.2 and compared with Sandvik-Osprey results in Section 7.2.2. The dramatic effect of intermetallic phase fraction on CTE, Young's modulus and Weibull modulus is considered in Section 9.4.3 – 9.4.5 respectively.

9.1 Processing

Spray forming was conducted using equipment comparable with only two other research facilities world-wide: Pennsylvania State University, USA and Bremen University, Germany. The Oxford spray forming plant is a pilot-scale facility with instrumentation, data logging and remote process control largely superior to the other two facilities. The operation of the Oxford facility for CE alloys was one of the first applications of the equipment, and its safe operation, working practices and process protocols were an integral part of the research in this thesis.

Furthermore as previously described, the largely un-researched Si-Al alloys present particular processing challenges – even by spray forming – and consequently some of the key aspects of the processing itself are now discussed briefly.

National Instruments™ 'Lookout' software provided the user interface for the control of spray parameters allowing direct manual control over key spray forming parameters via a touch screen. This aspect was critical so that the equipment could be operated entirely remotely from a separate room for health and safety reasons, and so that only a reasonably small team of four was required for experiments. The system software provided:

- Logically ordered process steps with key operator prompts;
- Safety interlocks prevented unsafe operation e.g. chamber O_2 concentration;
- Automated emergency shutdown procedures;
- Real-time recording of process parameters; and
- Interfacing of additional monitoring equipment.

Operation of the spray forming plant was divided into four specific roles, operated by a minimum of four individuals: (i) *furnace operator* – charging furnace, skimming dross, de-gassing; (ii) *furnace monitor* – logging, monitoring, communication with control office; (iii) *process control* – operation of control PC during pre-spray and spray forming; and (iv) *process safety* – safety check lists, communication with furnace monitor.

The processing parameters used at Oxford were based on those used by Sandvik-Osprey for the commercial manufacture of billets. However as each of the CE7-based alloys at Oxford contained different alloy additions that altered the flow and solidification characteristics, the processing conditions were probably not optimised to the same extent as those used daily at Sandvik-Osprey. In a commercial environment, the shape evolution of the billet should be predictable and reproducible in order to minimise the amount of material removed prior to downstream processing, and to maintain a constant material quality. The Oxford plant used manual control, based on CCTV monitoring of billet growth to maintain a slightly domed, parallel sided billet. The as-sprayed billets in Figures 9.1(a-d) show that accumulated expertise in manual control provided approximately cylindrical, flat topped billets.

Poor process yield and the corresponding undermining effect on overall spray forming costs has been one of the major factors preventing the widespread commercialisation of spray forming, and attempts to increase yield have been reported (Aumund-Kopp 2002, Baker 1993, Mingard 1993). Yield can be increased by: (i) increasing the mass fraction of the spray impacting the substrate, which is related to the spray footprint size relative to the substrate; and (ii) increasing the 'sticking' or deposition efficiency of impacting droplets which is related to the angle of impingement of the spray relative to the billet, the liquid fraction in the spray and the liquid fraction in the billet top surface (Mathur 1991a). In the experiments performed at Oxford, the alloy composition was different for each experiment and although considerable care was taken to

set-up and run the plant identically for each experiment, losses from each experiment varied as shown in Table 6.1, with yields of 31-46%. If overspray powder was recycled and re-injected, as conducted by Sandvik-Osprey in commercial manufacture of billets, then yields of 53-73% should be achievable at Oxford. Nonetheless, sufficient alloy was manufactured to give representative bulk material produced under near steady-state deposition conditions.

9.1.1 Pyrometry

Controlling the liquid fraction of the spray and on the surface of the growing billet is of paramount importance for the production of a high integrity billet (Annavarapu 1993). Intrusive methods of measuring the billet top surface temperature were problematic owing to the rotation and retraction of the billet and the harsh operating environment. Accurate non-intrusive measurement e.g. via pyrometry or thermal imaging, was no less problematic because of problems of calibration for alloy emissivity, obscuration by overspray powder, infrared absorption by glass in viewing ports and geometric constraints. Although thermal data presented here cannot be considered as absolute, it was used to indicate relative billet temperature, and give an indication of the stability of intended steady-state conditions. Figure 9.2 shows manually filtered two colour pyrometer temperature data during CE7+P, CE7+P+Ce and CE7+Sr spray forming experiments, indicating an underlying downward temperature trend during nominally steady-state deposition. This is attributed to cooling of the melt in the tundish and crucible prior to atomisation. Future process optimisation steps should consider adjustments in atomiser pressure / gas flow rate and / or

ram withdrawal rate to compensate for this effect. In the current study, stability of atomisation – also continuously monitored by CCTV – was considered paramount and in the absence of sufficient operator experience, adjustment of key primary processing parameters was kept to an absolute minimum.

9.1.2 Post spray cooling and solidification

The top surface temperature of the billet derives from a balance of energy input rate from the impinging spray and energy output rate via convection, conduction and radiation (Grant 1995a). At ~1000°C under typical spray forming conditions, convection is the dominant component of cooling, which is dependent on the heat transfer coefficient between the billet and the N_2 atomising gas (Mayer 2001). Once spraying was complete and the chamber clear of re-circulating overspray, pyrometry measurements showed billet surface temperatures of ~700°C, although as the external surfaces of the billet were chilled by the atomising gas, the core of the billet was expected to be considerably hotter (~850°C). The application of an insulated ceramic jacket eliminated the convective component of cooling and the billet was cooled by conduction through the substrate and ram. The air-cooled Cu plate was inserted between the substrate and the top of the ram to increase this cooling component. Although broadly similar, this cooling arrangement differed in detail from that used at Sandvik-Osprey (Osprey 2001), and was adopted to minimise the time between the end of spraying and the start of controlled cooling.

Inspection of the billets showed macro-cracking in the CE7+P billet, shown in Figures 9.3(a+b). The reason for cracking in this billet but not in the others is uncertain. However as Figure 9.3(b) shows porosity was relatively high, possible causes include: too rapid cooling that failed to consolidate solidification shrinkage in the billet top; high liquid fraction immediately after deposition; or even P gas evolution at this relatively high P concentration (ASTM 1988).

9.2 Hot isostatic pressing (HIPing)

The four CE7-based materials spray formed at Oxford all exhibited porosity inherent to the spray forming process (Grant 1995a). Prior to mechanical testing, HIPing was conducted by Bodycote HIP, Chesterfield, UK. The presence of low melting phases in CE7+P and CE7+P+Ce dictated that HIP conditions differed from the optimised Sandvik-Osprey cycle for CE7 of 16 hours at 140 MPa and 565°C. Optical microscopy and image analysis in Table 6.2 showed the optimised Sandvik-Osprey HIPing conditions worked well on the Oxford CE7 material as expected. Results for the CE7-based alloys under non-optimised HIP conditions were more varied. B and Sr billets contained relatively low porosity in the as sprayed condition of 1.94 and 0.91 area% respectively, and this was reduced after HIPing to 0.37 and 0.28 area% respectively. The P and P-Ce modified alloys contained much higher porosity in the as-sprayed condition of 6.78 and 6.32 area% respectively, and HIPing was less effective on these alloys with post-HIP porosity levels of 5.8 and 3.92 area% respectively. Porosity before and after HIPing, the most effective HIPing cycle and the percentage of intermetallic phases is summarised in Table 9.1 below:

Table 9.1 Summary of Porosity before and after HIPing and corresponding % of intermetallics in each alloy

Alloy	As sprayed % porosity	Minimum HIPed Porosity[1]	HIPing cycle	Analysed % intermetallic
Osprey CE7	2.0 – 4.0 *±0.24 – ±0.62*	0.1 ±*0.03*	Sandvik-Osprey HIP[2]	0.42[5]
Oxford CE7	1.62 ±*0.16*	0.07 ±*0.02*	Sandvik-Osprey HIP[2]	0.24[6]
CE7+B	1.94 ±*0.14*	0.37 ±*0.01*	Specified HIP[3]	1.88[7]
CE7+P	6.78 ±*1.63*	5.80 ±*1.1*	Specified HIP[3]	5.98[7]
CE7+P+Ce	6.32 ±*1.31*	3.92 ±*0.67*	Specified HIP[3]	11.09[7]
CE7+Sr	0.91 ±*0.03*	0.28 ±*0.01*	Densal® [4]	0.51[7]

Notes
[1] This was the %porosity in the most dense region of the billet. In some regions there was a maximum of ~30% porosity with considerable variation across the billet. Only the most dense regions of material are considered in this analysis and subsequent testing.
[2] Sandvik-Osprey material was HIPed under previously optimised conditions along with batch production work. 565°C /140 MPa, 16hr
[3] Specified HIP conditions: 500°C/140MPa, 4h
[4] Densal® : Proprietary conditions
[5] From Table 4.1, Gravimetric / ICP (solid) analysis of all impurities elements
[6] Calculated from feedstock certification
[7] Data from XRF and ICP analysis in Table 6.3 – alloy additions + impurity elements

Porosity in the primary Si phase was attributed to pull-out and / or dissolution of AlP phases (Nogita 2004b) during sample preparation making assessment of the porosity difficult. During HIPing the primary Si phase does not coarsen significantly, as shown in Section 7.3, or significantly deform, but must move as the Al phase flows to fill porosity during HIPing. It is postulated that Al_2Cu, AlB_{12}, AlB_2, Al-Ce-Cu-Si and impurity-based intermetallic phases inhibited the healing of porosity by inhibiting grain boundary movement in the Al-rich phase (Atkinson 2000) and physical movement of primary Si grains / particles. The presence of intermetallic particles is detrimental to the HIPing characteristics of CE7-based alloys and therefore should be minimised.

Table 9.2 below summarises the % decrease in porosity and the corresponding percentage of intermetallic particles. Although there is no direct correlation between the volume of intermetallics in the alloy and the ability to effectively HIP the material, it is clear that with increasing intermetallic content the percentage decrease in porosity during HIPing is reduced.

Table 9.2 Summary of the intermetallic content compared to the percentage change in porosity after HIPing for each Oxford alloy. Sandvik-Osprey CE7 included for comparison

Analysed % intermetallic	**Alloy**	**% decrease in Porosity** (Δ porosity / as sprayed porosity) x100
(minimum) 0.24	Oxford CE7	96
0.42	Sandvik-Osprey CE7	97
0.51	CE7+Sr	69
1.88	CE7+B	81
5.98	CE7+P	14
(maximum) 11.09	CE7+P+Ce	38

9.3 Microstructure

Similarly to Sandvik-Osprey CE7, shown in Figure 4.13(a) and 6.13(a), the microstructure of all the CE7-based alloys at Oxford shown in Figure 6.13(b-f) consisted of an interpenetrating network of Al and primary Si with little or no Al-Si eutectic structure. In all cases the scale of the Oxford modified CE alloys was coarser than the Sandvik-Osprey alloy, as shown in Figure 6.13(a) – (f) and described in Section 6.5.2. Optical microscopy showed intermetallic particles in all CE7-based alloys, usually concentrated within the Al network. EPMA was used to help clarify the stoichiometry of intermetallic phases although particle

sizes of 1-3μm for some of the intermetallics presented problems during EPMA because they are similar to the likely electron beam interaction volumes. MTDATA calculations for CE7-based alloys involved much higher Si concentrations than recommended by the underlying database suppliers (Saunders). The MTDATA calculations of phase fractions should be considered indicative (at best) and in combination with microstructural / EPMA / EBSD / cooling data. The Al-data database of elements did not include Ce or P, therefore only additions of Cu, B and Sr could be assessed. The 'Scheil' solidification conditions used in the MTDATA calculations assumed no back diffusion in the solid state but complete mixing in the liquid state. The MTDATA predicted solidification profile has been compared to the solidification profiles obtained during post-spray controlled cooling and was discussed in Sections 6.1.4 and 6.3. Table 9.3 shows a summary of MTDATA predicted and observed temperature arrests due to phase formation in each alloy, and suggests the corresponding phases either identified or proposed, while footnotes indicate sources of supporting data.

Table 9.3 MTDATA predicted and experimentally observed temperature arrests during post-spray cooling with phases identified or proposed for each arrest

Alloy	Temperature arrest	MTDATA prediction (°C)	Observed (°C)	Phase
CE7+B	Arrest 1	560	567	α-Al / Si eutectic*
CE7+P	Arrest 1	531	534	Suppressed α-Al / Si eutectic*
	Arrest 2	510	515	Al_2Cu‡
CE7+P+Ce	Arrest 1	Not predicted	623	Al-Ce-Cu-Si ??¥ $\alpha Al_{11}Ce_3$?† $\beta AlCe_3$?†
	Arrest 2	531	554	α-Al / Si eutectic*
	Arrest 3	510	511	Al_2Cu‡
CE7+Sr	Arrest 1	727	--	Al_2Si_2Sr§
	Arrest 2	560	569	α-Al / Si eutectic*

* Eutectic solidifying as a divorced eutectic as previously described.
‡ Predicted by MTDATA and literature (Mondolfo 1979), confirmed by EPMA
† Suggested by Al-Ce phase diagram but unable to confirm by EPMA.
¥ Suggested by EPMA but not predicted by MTDATA, phase diagrams or literature.
§ Predicted by MTDATA, observed by EPMA, but not observed in cooling curve due to low volume fraction.

9.3.1 CE7+B

In CE7+B intermetallic particles were observed in the primary Si network, identified by EPMA as AlB_{12} and AlB_2. At equilibrium, α-AlB_{12} should transform to β-AlB_2 via a quasi-peritectic reaction, α-AlB_{12}+liquid →β-AlB_2 (Fjellstedt 1999), but it is commonly observed that some AlB_{12} is retained due to the sluggishness of this reaction (Fjellstedt 1999). The quasi-peritectic reaction nucleates at the α-AlB_{12}/liquid interface and the β-AlB_2 phase then grows along the interface to envelop the α-AlB_{12}, isolating it from the liquid. Once the α-AlB_{12} is surrounded by β-AlB_2 , further growth can only occur by diffusion of B through β-AlB_2 and this impedes the peritectic transformation and can lead to retained α-AlB_{12} (Howe 2000). CE7+B contains a fine distribution of AlB_2 and AlB_{12} throughout

the Al and primary Si network as shown in Figure 6.14. Typically, there was no evidence of crack initiation around these particles although bend test data in Table 6.8 and Weibull modulus data in Figure 6.9 indicated that borides do undermine bulk mechanical properties, probably by stress concentration and CTE mis-match effects. In contrast to Sandvik-Osprey CE7, Zr and Ti were present only as a relatively fine dispersion throughout the microstructure, and did not form the large acicular intermetallic phases seen in Sandvik-Osprey CE7 and as shown in Figures 4.16(a) and (b). Figures 6.13(b) and (c) compare Oxford Binary CE7 with CE7+B, showing little refining effect from the addition of B. Figure 6.13(a) shows Sandvik-Osprey CE7 manufactured with particle injection which exhibits a considerably more refined microstructure compared with binary or B modified CE7.

9.3.2 CE7+P

CE7+P also exhibited intermetallic phases distributed through the primary Si phase. EBSD and EPMA results in Figure 6.24(f) show nucleation of Si on particles of AlP and optical micrographs in Figure 16.15(a) and (b) showed AlP pull-out and dissolution during sample preparation (Nogita 2004). The primary Si grain size distribution shown in Figure 6.27 shows ~23% of Si grains had a diameter of ~4.5μm in CE7+P compared with ~17% in CE7+B. The P additions were effective in the nucleation of Si grains via the formation of AlP which is isomorphous to Si (Nogita 2004, Ghost 1964). However Figure 6.27 also shows that Sandvik-Osprey CE7 without P had a smaller primary Si grain size of ~2μm compared with all the modified CE7 alloys. Once again this suggests that

particle injection is more effective in promoting primary Si nucleation than alloy additions. Cu was present in CE7+P and CE7+P+Ce alloys because P could only be added as Cu-P or Fe-P master alloys. Fe had been previously demonstrated to be detrimental to the mechanical properties because of the formation of acicular Al-Fe-Si intermetallic particles, and Cu-P was therefore chosen. The Cu additions unsurprisingly resulted in an α-Al / Al_2Cu eutectic reaction in the Al rich network, identified by EPMA. Again Figures 6.13(b) and (d) compare Oxford Binary CE7 with CE7+P, showing little refining effect from the addition of P, and is further discussed in Section 9.4.1.

9.3.3 CE7+P+Ce

CE7+P+Ce exhibited a variety of complex Ce containing phases that were typically faceted and often cracked. In many cases cracks propagated from the Ce containing phase into the surrounding Si matrix, resulting in a loss of mechanical strength in the bulk material as shown in Figure 6.15(b). Al-Cu-Ce-Si phase morphology resembled Al_2Si_2Ce phases identified by Jirattiticharoean (2004) in a Al-20Si+Ce alloy. While P was successful in nucleating primary Si, there was little evidence that Ce inhibited the growth of primary Si as previously suggested by Jirattiticharoean (2004), Chang (1998a) and Xian (1993). The mechanism proposed by Chang (1998a) suggested that Ce poisoned TPRE attachment sites inducing polyhedral rather than star Si morphology. However the findings in this thesis are consistent with Nogita (2004) who showed that Ce had no refining effect on eutectic Si in Al-7Si. Despite 2 potential mechanisms of refinement (nucleation and inhibited Si growth) Figures 6.13(b) and (e)

compare Oxford Binary CE7 with CE7+P+Ce, and show no refining effect from the addition of P+Ce

9.3.4 CE7+Sr

CE7+Sr formed an intermetallic phase with rod morphology consistent with over-modification of the alloy. XRF analysis showed that 0.23% Sr was retained in the billet representing a Sr loss of only 8% and lower than forecast when choosing Sr concentration. The high concentration of Sr resulted in the presence of Al_2Si_2Sr of similar morphology to over modified phases observed by Jenkinson (1975). Sr is thought to refine eutectic Si by poisoning Si attachment sites, promoting impurity induced twinning (Lu 1987, 1989) although this mechanism is still debated (McDonald 2004). Impurity induced twinning is a mechanism whereby atoms of large atomic radii collect at the solid-liquid growth front and 'poison' Si attachment sites. This has the effect of locally increasing the undercooling which promotes twinning in the advancing solid Si growth front (Elliot 1983). However no evidence of refinement was observed, Figures 6.13(b) and (f) compare Oxford Binary CE7 with CE7+Sr, and show no refining effect from the addition of Sr

As this alloy was devoid of eutectic Si, Sr could have refined the primary Si by the TPRE mechanism (Jenkinson 1974). The TPRE model was originally conceived for Ge crystals (Wagner 1960) and refers to growth of crystals nucleated in the re-entrant angle formed between adjacent twins. This results in rapid, preferred growth in the centre line of the groove created between the

twins. In a singly twinned nucleus these planes rapidly grow out resulting in a trigonal particle. However in a nucleus with 2 or more twin planes, growth is sustained in the <112> directions in the 109.5° groves between the twins (Hamilton 1960). This often results in long plates or hexagonal plate-like Si (Kobayashi 1985). This mechanism can be disrupted by the addition of Na or Sr which are known to refine Si and operate by the same mechanism. The effect of Sr was investigated by Yimmaz (1992) which showed that additions of Sr poisoned TPRE grove sites, preventing (or reducing) preferred <112> growth and reducing the occurrence of long hexagonal plates and star morphology Si.

However in Sr modified CE7 there is little evidence of significant Si refinement from the EBSD grain size measurements shown in (Figure 6.27). This lack of TPRE refinement probably results from the initially high cooling rate in the droplets and the large number of Si nucleants that solid and semi-solid droplets create. This is consistent with Atasoy (1984) who showed that the TPRE mechanism was dominant at low cooling rates.

9.3.5 Texture and grain size

EBSD proved an effective tool in the investigation of the structure of CE7 alloys providing the only practical method for measuring Al and Si grain size. The Si phase consisted of small, equiaxed randomly oriented grains, with a mean grain size of ~5 - 10μm in the CE7-based materials and ~4.4μm in Sandvik-Osprey CE7. This refinement of primary Si in Sandvik-Osprey CE7 was attributed to the use of overspray re-injection providing a greater population of nucleation sites

and decreasing the mean temperature at the billet surface. The Al rich phase consisted of large grains of 250μm – 1250μm, however an accurate grain size could not be resolved due to the limited analysis area in EBSD. The discovery that the microstructure of CE7 consists of a combination of large, Al grains interpenetrated by a Si network of refined, equiaxed grains represents a hitherto un-observed phenomenon and builds towards a fuller understanding of the processing – microstructure – property relationship in this class of materials.

9.4 Properties

9.4.1 Interface length and fracture toughness

As previously discussed in section 7.4.3, Hertzian and Vickers K_{1c} measurements showed considerable discrepancy and neither technique provided a satisfactory measure of fracture toughness as discussed in Section 7.4.1. The Vickers toughness measurements showed some sensitivity to interface length and Al phase distribution and were used to rank and compare modified CE alloys. Data showed that CE7+P had the highest fracture toughness followed by CE7+B, Oxford CE7, CE7+Sr and CE7+P+Ce in decreasing order of estimated K_{1c}. Cracks propagate through the Si network, often initiated at intermetallic particles, pores and driven by thermal expansion or external stress (such as preparation techniques or service loads). The ductile Al phase is effective in deflecting, blunting and stopping cracks as shown in Figure 4.13(c) and 4.16(a) & (b), and consequently the blunting effect of the Al phase has been considered throughout as an important microstructure parameter, as discussed in Section 7.4.4. A relationship between the inter-

phase interface length between the Al and Si phases and the fracture toughness estimated from Vickers indentation is proposed in Figure 9.4. This relationship indicates that with increasing inter-phase interface length the toughness of the material increases, due to the reduced distance a crack can propagate through the Si before being blunted or deflected by the Al phase. Figure 9.4 shows an approximate linear relationship, with considerable scatter, between Vickers estimate of K_{1c} and interface length for chill cast Al-50Si+P, Sandvik-Osprey CE7 and Oxford modified CE7. Figure 9.4 shows that an interface length of ~3.3mm/mm^2 gave a K_{1c} value of ~1.5MPa.m$^{1/2}$ increasing to 3.4MPa.m$^{1/2}$ at an interface length of ~14.5mm/mm^2. However it is recognised that this relationship has been proved to be approximate, based on a poor measure of fracture toughness as discussed in Section 7.4.3, and with considerable scatter, further work - particularly in producing a wide range of interface lengths - is required on carefully controlled material.

Two factors affect the interface length in spray formed CE7:

Nucleation density.

As shown in Figure 7.1, increasing the nucleation density by particle injection had a significant effect on increasing interphase interface length. Tables 4.7, 6.10 and Figures 6.13 (a) – (f) show that the interface length of all the CE7-based alloys was significantly less than the Sandvik-Osprey CE7 that utilised particle injection.

Particle injection has been shown to be much more effective in controlling interface length than any alloying approaches. Indeed the Oxford CE7+P

showed that the nucleation density and subsequent interface length was rather insensitive to alloying additions, despite contrary findings in the chill-cast alloys. Table 6.10 shows that P inoculated CE7 had an interface length less than B, Sr and P+Ce modified Oxford CE7, despite the strong grain refining effect of P shown in chill castings and detailed in the literature (Kyffin 2001, Heshmatpour, 1996, Arnold 1961). Consequently the intrinsic self-grain refining effect of spray forming produces an excess of nuclei for the solidification of residual liquid, irrespective of the compositions investigated.

Solidification and growth conditions.

Chill casting experiments described in Chapter 5 demonstrated that under the same cooling conditions, some alloy additions were effective in altering the scale and morphology of primary Si. It was hoped that the additions of Ce to inhibit Si growth would increase the interface length in spray formed alloys. However Ce had little effect on interface length, probably because of the high nucleation density swamping any growth effects. At first consideration, it might be expected that growth of Si in spray formed billets may be faster than the chill cast alloys – not least because of the misconception that spray forming is a rapid solidification process. It is worth emphasising that because of the huge number of nuclei generated by the injected powder partially re-melting on the billet surface, and the solid and mushy droplets from melt atomisation, the local primary Si growth conditions are much slower than the chill castings – hence the relative absence of defective Si grain morphologies.

9.4.2 Macrosegregation

Elemental mapping in the Sandvik-Osprey CE7 billet shows significant macrosegregation of Al as discussed in Section 7.2.2. This pattern was replicated in the CE7+Sr alloy shown in Figure 9.5. Sandvik-Osprey CE7 and CE7+Sr both exhibited a ~5% Al concentration gradient from the edge to centre of the billet. Macrosegregation has already been demonstrated here to lead to anisotropy in the CTE as discussed in section 7.4.2.

9.4.3 CTE and Intermetallic phase fraction

Figure 6.8 shows the CTE of Sandvik-Osprey CE7 and Oxford CE7-based alloys. CE7-based materials had a range of CTEs at ~100°C: ranging from 7 $x10^{-6}°C^{-1}$ for CE7+Sr to $6.2x10^{-6}°C^{-1}$ for CE7+P, compared with 7.0 and 8.0 $x10^{-6}°C^{-1}$ in the Sandvik-Osprey CE7 X and Y orientations respectively. Table 9.4 compares these data with a rule of mixtures approach for the measured alloy composition (composition taken from analysis in Tables 4.1 and 6.3).

Table 9.4, Summary of the measured and predicted CTE and corresponding intermetallic phase fraction for Oxford modified CE alloys.

Alloy	**Measured CTE‡, $x10^{-6}$ °C^{-1} (25 – 400°C)**	**CTE from ROM* Measured composition¥ $x10^{-6}$ °C^{-1}**	**Total alloy addition (wt%)****
Sandvik-Osprey CE7	X-axis 4 – 9 Y-axis 6 – 10	8.71	0.42*‡
CE7+B	6 – 7.5	8.75	1.88
CE7+P	6	9.08	5.98
CE7+P+Ce	6	9.10	11.09
CE7+Sr	7 – 9	8.92	0.51

*ROM – Rule of Mixtures, Elemental CTE data from Smithells, 1978,
¥Composition from XRF and ICP analysis shown in Table 6.3
** Total including deliberate alloy additions and impurity elements (from table 6.3)
‡ From Figure 6.8
*‡ ICP measurements of Impurity elements from Table 4.1

The CTE for Sandvik-Osprey CE7 was a close match to a ROM approach, with a closer match at higher temperatures of ~300°C, as discussed in Section 7.4.2 and shown in Figure 6.8. Table 9.4 shows that the measured CTE for modified CE alloys does not closely conform to a rule of mixtures (ROM) calculation, although it must be noted that this calculation is based on elemental CTE and not the CTE of the many intermetallic phases which form in these alloys as described in Section 6.5.3. In all cases the measured CTE is less than that predicted by the ROM. It is assumed that the interpenetrating network microstructure results in the higher CTE of the Al phase (23.1×10^{-6} °C^{-1}) being retarded the intermetallic phases and to a lesser extent by the surrounding low CTE (2.6×10^{-6} °C^{-1}), high modulus Si. This effect is increased with increasing alloy addition as the thermal expansion of the Al phase was increasingly inhibited by the presence of intermetallics. Table 9.4 shows that CTE decreases with increasing alloy addition and intermetallic content, indicating that the intermetallic phases have a pinning effect on the thermal expansion of the higher CTE Al phase, causing a discrepancy between measured and predicted results.

9.4.4 Young's Modulus and Intermetallic phase fraction

Young's modulus measurements showed similarly that with increasing alloy addition, the modulus was progressively reduced from ~130GPa in Sandvik-Osprey CE7 to ~99GPa in CE7+P+Ce as shown in Table 9.5 below. A rule of mixtures approach using Young's modulus data for elemental Al, Si, Cu, and Ce is shown in Table 9.5; the measured Young's modulus was in every case lower

than the calculated modulus, however both followed the same trend, with modulus decreasing with increasing alloy addition. The discrepancy between the ROM calculation and measured moduli was attributed to the inhomogeneous microstructure of modified CE7 alloys, consisting of an interpenetrating network of Al and primary Si interspersed with intermetallic phases. In the case of multi-phase or composite materials the testing standard (ASTM 2002) states that the resonant frequency behaviour is altered by the size, morphology, distribution, interfacial bonding and elastic properties of the second phase particles and is not dependent only on the volume fraction of alloy additions. Frequency attenuation is also altered by residual porosity which remained despite HIPing, as detailed in paragraph 6.2. and shown in Table 9.5. The residual porosity after HIPing also increased with alloy addition, due to the increased intermetallic fraction which inhibited Al flow during HIPing, as discussed in Section 9.2. Cracking and delamination of intermetallic particles from the bulk material will also add discontinuity to the material and contribute to altered resonant properties of modified CE7 in a similar way to porosity.

Table 9.5, Summary of the measured and predicted Young's Modulus (E), residual porosity and corresponding Intermetallic phase fraction for Oxford modified CE alloys and Sandvik-Osprey CE7

Alloy	Young's Modulus* (E) (GPa)	Young's Modulus from ROM[¥] (GPa)	% Residual porosity (post-HIP) [‡]	Total alloy addition (wt%)[†]
CE7+B	128.7	131.3	0.37	1.88
CE7+P	121.1	132.3	5.80	5.98
CE7+P+Ce	98.9	127.3	3.92	11.09
CE7+Sr	123.9	132.7	0.54	0.51
Sandvik-Osprey CE7	129.8	133.7	<0.1	0.42**

* From Impulse excitation measurements in Figure 6.6
[¥] ROM – Rule of Mixtures, Elemental CTE data from Smithells, 1978,
[†] Total including deliberate alloy additions and impurity elements (from table 6.3)
[‡] From Table 6.2
** ICP measurements of Impurity elements from Table 4.1

9.4.5 Weibull modulus and Intermetallic phase fraction

Bend test data shows differences between CE7-based alloys, both in the UTS and the Weibull modulus as shown in Table 6.8 and Figure 6.9. EPMA analysis in Section 6.5.3 and Figures 6.16 to 6.22 has shown ternary alloying elements formed generally complex stoichiometry intermetallic phases, and these particles are frequently implicated in crack initiation. It is the presence of these brittle, stress concentrating phases that is thought to be responsible for the systematic reduction in reducing both the strength (MOR) of the material reliability and predictability (Weibull modulus). This effect is exacerbated by the increase in porosity associated with alloying addition as shown in Table 9.5. The combined effect is to systematically undermine the calculated UTS from 135 to 48MPa and the Weibull modulus from 22 to 8 by raising the alloy addition from ~0.42% (in Sandvik-Osprey CE7 with Fe, Zr and Ti impurities) to 11.1% in

P+Ce(+Cu) modified CE7. It is thought that cracks leading ultimately to fracture will propagate readily through the Si phase from crack nuclei at intermetallic phases and at residual porosity, until the catastrophic failure of the sample. Using the Equation 7.5 in Section 7.4.4 the critical flaw size for fracture can be estimated from the fracture toughness (from Vickers indentation) and the UTS (calculated from Equation 4.1). The calculated flaw size, UTS and K_{1c} and calculated critical flaw size are shown in Table 9.6 below.

Table 9.6, Summary of the relationship between fracture toughness, UTS, and the critical flaw size at fracture, compared with the total deliberate and impurity alloying elements.

Alloy (HIPed)	**K_{1c} * (Mpa $m^{1/2}$)**	**UTS‡ (MPa)**	**Calculated flaw size¥ (μm)**	**Total alloy addition (wt%)†**
CE7+B	2.87	94.4	294	1.88
CE7+P	3.34	76.5	606	5.98
CE7+P+Ce	2.21	48.0	674	11.09
CE7+Sr	2.73	101.6	290	0.51
Sandvik-Osprey CE7	2.55	135.2	114	0.41**

** Impurity elements from Table 4.1
* Data from Table 6.4, based on estimates from Vickers indentation testing
‡ Data from Table 6.8
† Total including deliberate alloy additions and impurity elements (from table 6.3)
¥ Calculated from Equation 7.5

Table 9.6 shows the flaw size increasing from 114μm in Sandvik-Osprey material up to >600μm in highly alloyed CE7+P+Ce and CE7+P. The increase in flaw size resulted from residual porosity and from stress raising intermetallic phases which both delaminated from the matrix Si and initiated cracking, and these defect types are increased by increasing alloy addition.

Figure 9.6 shows the bend test Weibull modulus plotted as a function of ternary alloying concentration (deliberate and impurity additions) regardless of which

element is added. In all cases, the greater the alloying content and consequently intermetallic particle volume fraction, the greater the reduction in Weibull modulus. SEM analysis of fracture surfaces after bend testing (Figures 6.10 – 6.12) supported the undermining of strength and Weibull modulus by intermetallic particles showing cracks passing through and initiating from intermetallic particles. A consequence of Figure 9.6 is that melt cleanliness and good control over feedstock alloy composition is important in maintaining useful properties in CE7-based materials. It should also be noted that because CE7+P and CE7+P+Ce alloys exhibited pull-out and dissolution of brittle AlP phases (Nogita 2004), resulting in increased surface defect density which may have undermined Weibull modulus and bend strengths further.

9.5 Summary

- In CE7-based alloys, the primary Si phase is fine grained, random and equiaxed; while the Al-rich phase is coarse grained and textured, closely resembling binary CE7 manufactured by Sandvik-Osprey.
- Increased inter-phase interface length results in an increase in fracture toughness, by increasing the frequency of a crack blunting by the more ductile, Al-rich phase.
- Alloy additions of B, P(+Cu), P+Ce(+Cu) and Sr were not effective in refining the interphase interface length in spray formed CE7-based alloys compared with the extent of refinement from particle injection used by Sandvik-Osprey.

- CE7 appears insensitive to conventional Al-Si alloy grain refinement, no significant refinement was observed in modified CE7 alloys compared with Oxford Binary CE7.
- Ternary additions to CE7 formed a range of intermetallic phases that were often implicated in the cracking of primary Si, and consequently undermined toughness, bend strength and Weibull modulus.
- HIPing of CE7-based alloys was not as effective as HIPing binary CE7 because of necessarily non-optimised HIPing conditions and the presence of intermetallic phases.
- CTE decreased with increasing alloy addition in CE7-based alloys because of the lower CTE of intermetallic phases, and their pinning and inhibiting effect on the CTE of the Al phase.
- Weibull modulus decreased with increasing alloy addition because of an increased tendency for crack initiation and stress concentration around intermetallic particles.
- Young's modulus measured by impulse excitation decreased with increasing alloy addition because of altered resonant frequencies resulting from porosity, intermetallic particles and cracking in the primary Si.

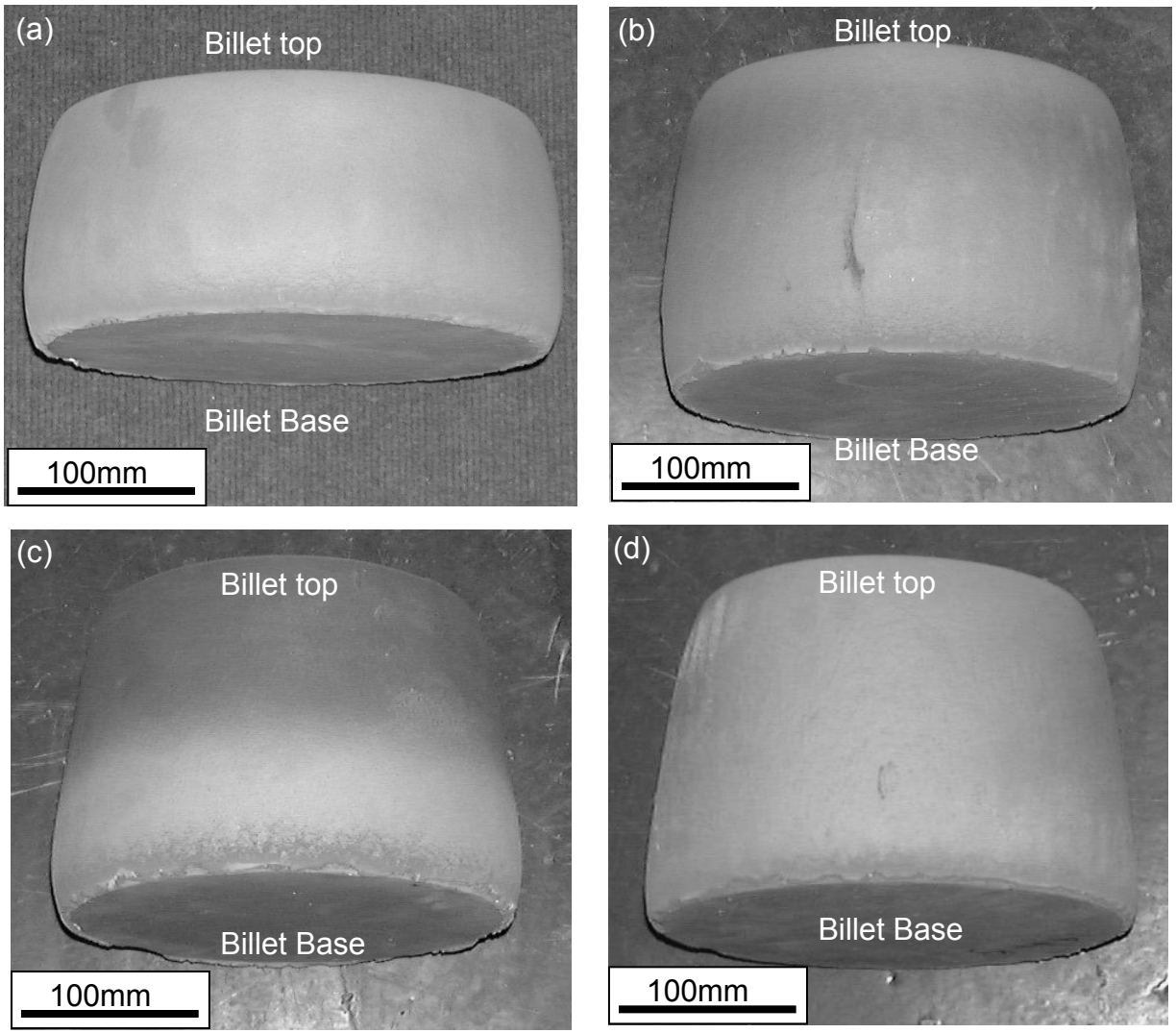

Figure 9.1(a) – 9.1(d)

Billets spray formed at Oxford, (a) CE7+B, (b) CE7+P, (c) CE7+P+Ce, (d) CE7+Sr

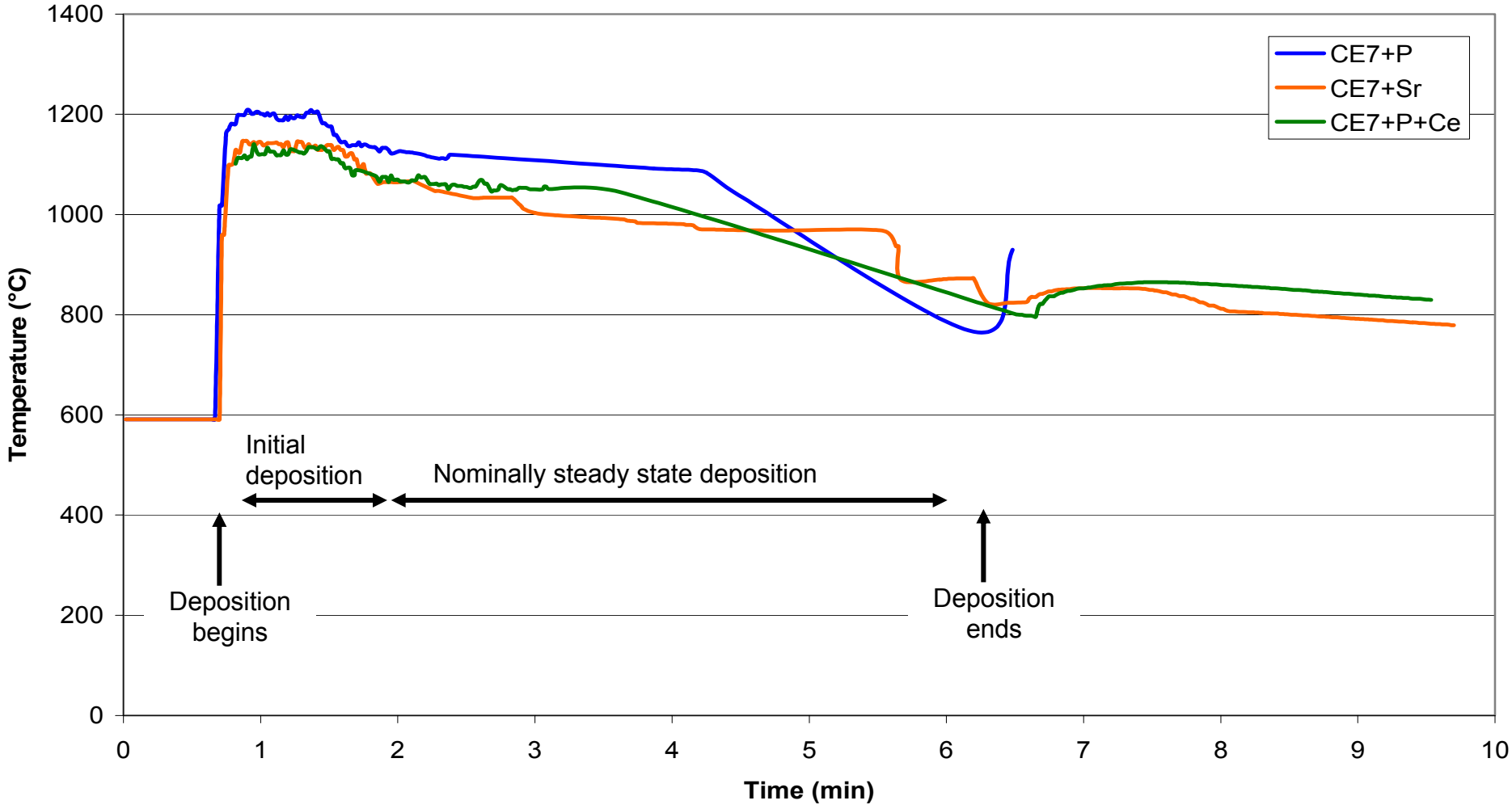

Figure 9.2

Billet top surface temperature measured by two-colour pyrometer as a function of time during spray forming of CE7+P, CE7+P+Ce and CE7+Sr

(a)

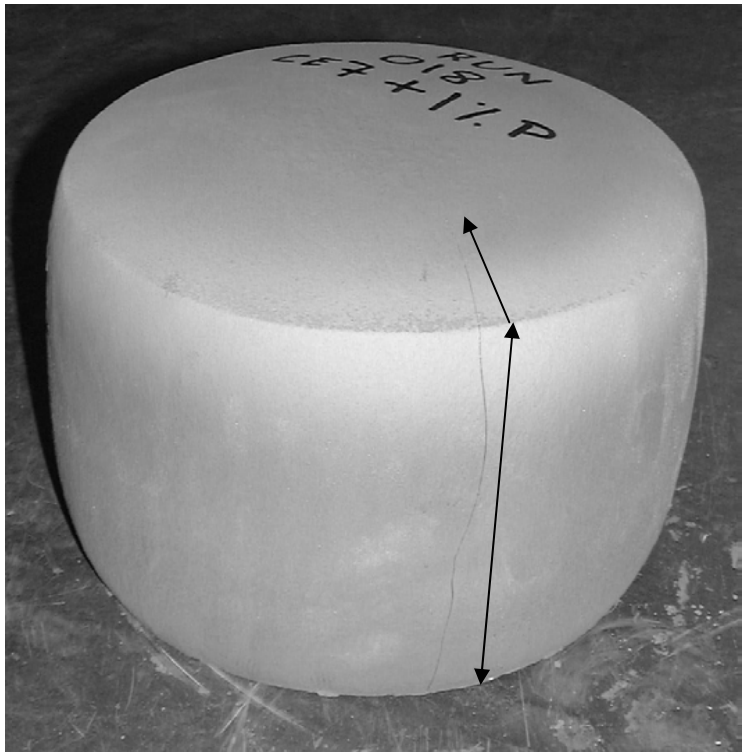

(b)

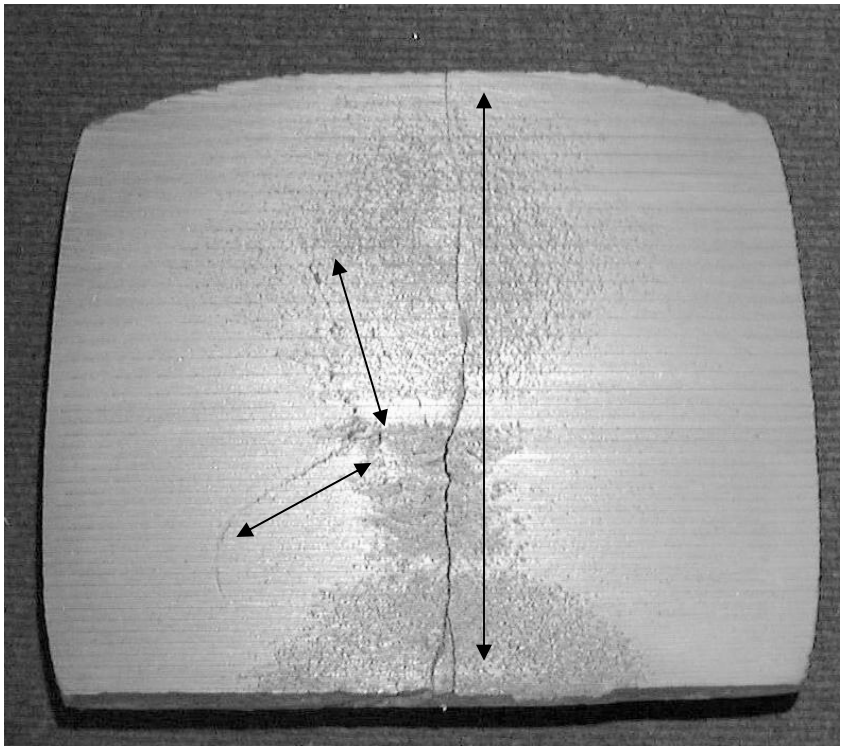

Figure 9.3(a) – 9.3(b)

Gross cracking in Oxford manufactured CE7+P billet. Cracks are highlighted by arrows running parallel to the crack: (a) cracks in the as-sprayed billet; and (b) cracks in the billet cross section,

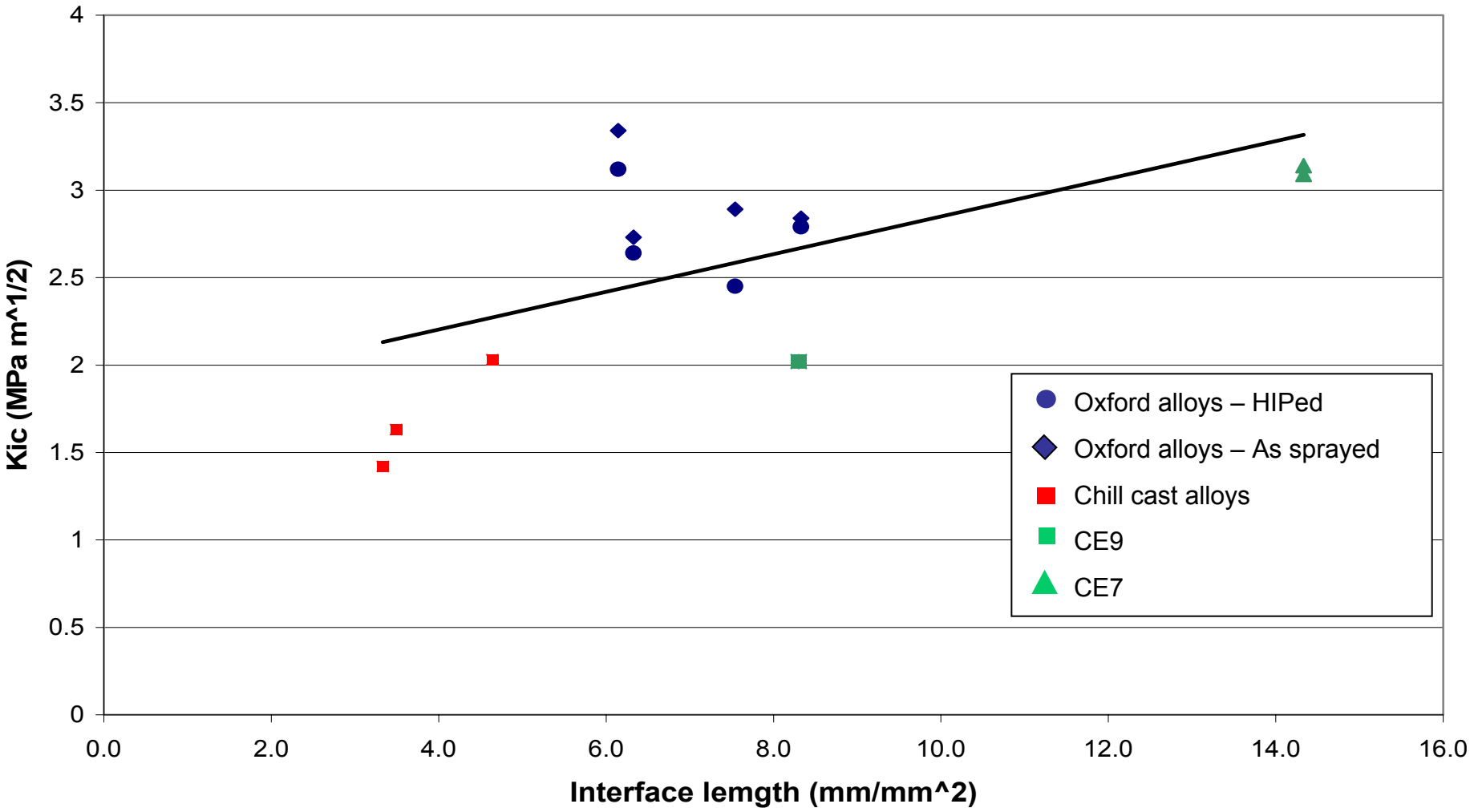

Figure 9.4

Vickers Indentation fracture toughness as a function of interface length in chill cast Al-50Si + P, Sandvik-Osprey CE7 & CE9 and Oxford modified CE7 alloys

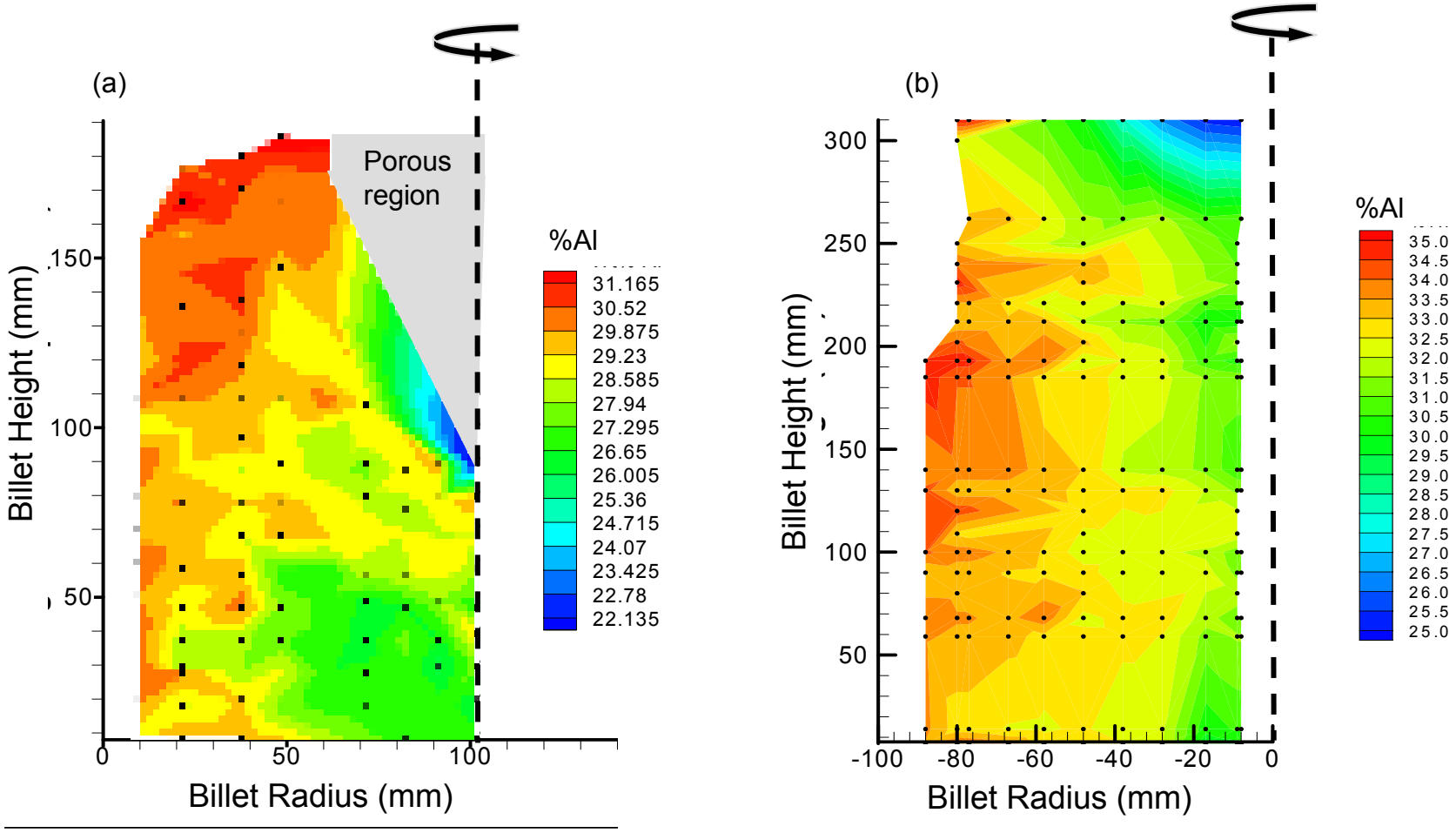

Figure 9.5

OES map of Al concentration across the cross section of (a) spray formed CE7+Sr, and (b) CE7 manufactured at Sandvik-Osprey.

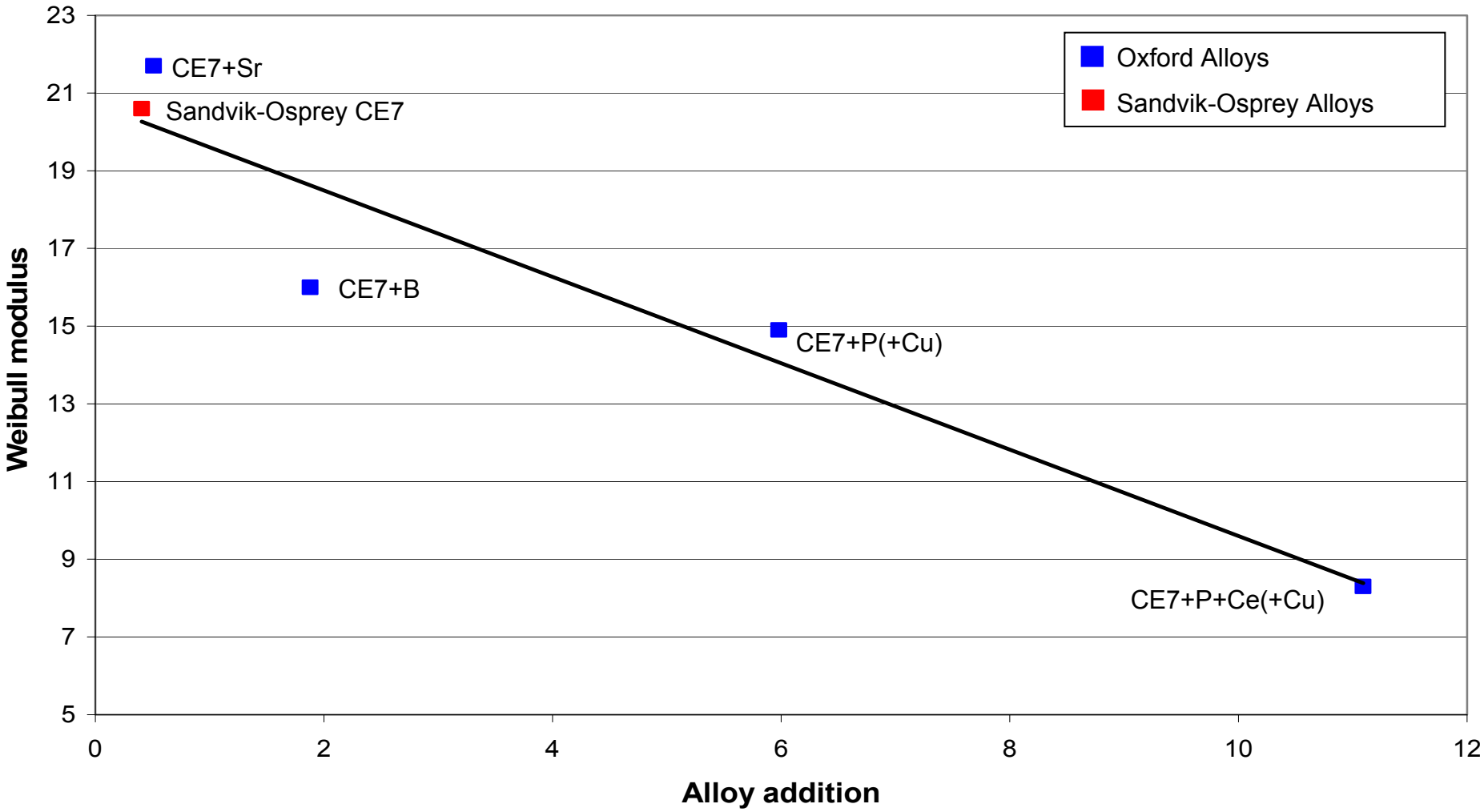

Figure 9.6

Variation in Weibull modulus determined by 4-point bend testing as a function of total alloy addition (deliberate and impurity), measured by fused bead XRF and ICP.

10.0 Conclusions

The discussion section(s) relevant to each conclusion are indicated in square brackets after each statement.

- By recycling the overspray powder and re-injecting it via a particle injector, Sandvik-Osprey obtain yields of ~80% during commercial manufacture of CE7. The particle injection ratio also has a strong effect on the inter-phase interface length, which is implicated in controlling toughness. For an increase in particle injection ratio from 27 to 46% where injection ratio is given by powder flow rate / melt flow rate x 100, the interface length increased from 13 to 21 mm/mm^2. [Figure 7.1.1]
- The microstructure of CE7 consists of a network of agglomerated, randomly orientated, fine scale Si grains of ~5μm diameter interpenetrated by large, orientated Al grains often >300μm in length [Section 7.2]. The Al phase is devoid of a Al-Si lamellar eutectic and exhibits a divorced eutectic, due to slow cooling, low temperature gradient and growth velocity, high mobility of Si in liquid Al-Si and small inter-primary Si distances [Section 7.2.1].
- CE7 exhibits significant radial macrosegregation of Al [Section 7.2.2] with a consequent measurable effect on CTE of ±10% [Section 7.4.2]. This segregation is driven by convective cooling from the billet edge during manufacture as reported by Mingard (2000) but is augmented by the post-spray directional cooling developed to manage gross defect formation in CE alloys.

- Intermetallic particles result from the presence of impurity elements such as Fe, Cu, Zr, Ti or picked up from foundry materials, and are strongly implicated in crack initiation in the brittle primary Si phase because of stress-concentrating morphologies and differences in CTE with the surrounding Al-rich phases [Section 7.4.4 & 7.2.5].
- Cracks initiating from intermetallic particles undermine the Weibull modulus, bend strength and fracture toughness of CE7 [Section 7.4.4 & 7.2.5].
- Bend strength of CE7 in the as-sprayed condition is controlled by porosity. After HIPing, porosity reduces dramatically and strength is controlled by the micro-flaws in the primary Si, many of which have been introduced by intermetallic phases [Sections 7.2 & 7.4.4].
- Cracks in the Si around acicular intermetallic particles are propagated during thermal cycling because of CTE mis-match at stress raising features, resulting in a loss of average bend strength and a reduction in Weibull modulus [Sections 7.4.5].
- While spray forming has allowed the production of billets on a commercial scale in otherwise ‘un-processable’ materials, it is evident that the arising material presents challenges of macrosegregation [Section 7.2.2], intermetallic crack initiation and growth [Sections 7.2.5 & 7.4.5], and anisotropy [Section 7.4.2] which need to be understood and controlled for scale up to full commercial manufacture.
- Chill cast Al-50Si consisted of large primary Si rods of <1mm, delineated by regions of coarse flake-like α-Al / Si eutectic [Section 8.2.1 & 8.2.4].

- Microstructural features such as Si hopper crystals and star morphology primary Si resulted from faceted growth of Si, twinning and the local temperature gradient (G), and growth rate (V) [Section 8.2.1, 8.2.2].
- Conditions of G and V and local compositional factors result in eutectic solidification outside the coupled zone yielding in dendritic Al and Al halo regions surrounding the primary Si [Section 8.2.3].
- Progressively more refined primary Si was observed in Al-50Si +P with increasing P addition and increasing cooling rate. Refinement results in an increase in inter-phase interface length with a corresponding increase in toughness [Section 8.3.2].
- Additions of P, B and Sb produced refinement of the primary Si size, with the most significant effect from additions of P. Additions of P, P+Ce, Sr, Bi, Mg and Ti refined the inter-lamellae spacing of the eutectic, with Sr showing the strongest effect [Section 8.4,Table 8.2].
- Based on observations from chill cast microstructures, additions of 1%B, 0.9%P, 1%P+5%Ce and 0.25%Sr were selected as suitable additions for modification of spray formed Al-70Si [Section 8.4].
- In CE7-based alloys manufactured at Oxford University, the primary Si phase is again fine grained, random and equiaxed; while the Al-rich phase is coarse grained and textured, closely resembling binary CE7 manufactured by Sandvik-Osprey [Section 9.3].
- Oxford CE7 material exhibited lower interface length than Sandvik-Osprey material due to the absence of particle injection [Section 9.4.1].

- Increased inter-phase interface length results in a slight increase in fracture toughness, by increasing the frequency of a crack blunting by the more ductile, Al-rich phase [Section 9.4.1].
- Alloy additions of B, P(+Cu), P+Ce(+Cu) and Sr are not effective in refining the interphase interface length in spray formed CE7-based alloys compared with the extent of refinement from particle injection used by Sandvik-Osprey [Section 9.4.1].
- Ternary additions to CE7 form a range of intermetallic phases that are often implicated in the cracking of primary Si, and consequently undermined, bend strength and Weibull modulus [Sections 9.4.3 & 9.4.4].
- HIPing of CE7-based alloys was not as effective as HIPing of binary CE7 because of necessarily non-optimised HIPing conditions and the presence of intermetallic phases [Section 9.2].
- CTE decreased with increasing alloy addition in CE7-based alloys because of the inhibiting effect of intermetallic phases on the expansion of the Al phase [Section 9.4.3].
- Weibull modulus decreased with increasing alloy addition because of an increased tendency for crack initiation and stress concentration around intermetallic particles [Section 9.4.5].

11.0 Further work

Areas for further research include:

[1] Additional effort is required to further optimise the many process variables in the spray forming process including melt superheat, melt delivery nozzle diameter, spray distance, ram withdrawal, etc. to produce more consistent billets in terms of higher yield, lower levels of porosity and more consistent billet shape. Precise control of substrate withdrawal rate in relation to deposited metal mass flow rate and evolving billet shape using a real-time billet shape measurement system, as implemented commercially at PEAK, Germany should be considered.

[2] Despite difficulties encountered in the use of non-contact measurement of preform temperature by pyrometry, this technique remains the only practical means to investigate preform surface temperature that has been shown to be important in controlling preform microstructure. Equipment modifications should be made to reduce obscuration and interference from the glass in the viewing ports, allowing more reliable, continuous on-line temperature measurements.

[3] This research has highlighted the significance of overspray injection on final microstructure. Installation of a particle injector at Oxford would facilitate an in-depth investigation of particle injection ratio on spray formed microstructure and mechanical properties. Particle injection of a conventional Al grain refiner

such as TiB_2 is also of interest as it could reduce the extraordinarily large Al grain size in CE7, potentially improving the toughness and isotropy of the material.

[4] It has been shown that management of post-spray cooling of billets is key in controlling final microstructure. Modelling of billet heat flow, cooling and solidification may provide a greater insight to the controlling phenomena occurring within the billet after deposition.

[5] Options for ternary alloying additions in CE7 have been shown to be extremely limited since nucleation and growth conditions differ so much from castings and Si concentrations are so high application of conventional approaches are unlikely to help increase the Si/Al interface length. Furthermore any ternary phases undermine the toughness and presumably thermal conductivity. Reactive spray forming has been previously cited as a novel technique for the in-situ formation of dispersed phases. Reactive spray forming of CE7+Ti to form TiN may help pin Si grain growth in the mushy zone and provide the desired microstructural refinement.

[6] X-ray micro-tomography of CE7 may allow crack initiation from intermetallic phases to be visualised in 3D. If this were combined with thermal cycling experiments it would give a significant insight into the prevalent failure mechanisms and allow the deleterious effects of intermetallics to be quantified.

[7] The fracture toughness measurements were presented herein were all conducted on the micro scale using Hertzian and Vickers indentation. It was not possible to validate these results using conventional measurement techniques due to the cost of sample preparation and the high cost of external testing. Ideally this should be done using crack opening displacement K_{1c} measurements for bulk fracture toughness measurements as prescribed in ASTM E399.

[8] If possible, further thermal cycling experiments with concurrent acoustic emission would allow investigation of the on-set of cracking and allow crack development to be monitored as a function of time and temperature, and may provide insights into the balance of crack initiation and propagation during CE7 failure.

12.0 References.

The cited references in this study are given in the form of first authors surname and year, with the references listed below in alphabetical order by primary author's surname. Where papers by the same author are published in the same year, the text will read (Surname Year a, Year b), etc. Patents are referred to in the text using the name of the company and year of application, the full reference is listed alphabetically by company name. ASTM standards are listed under A, and by year of issue.

References are in the form:

Initial. Surname, Initial. Surname, etc. *Journal name,* **Vol(number)**, Beginning on page, Year

---

A

Aegis Inc, Patent document, US Patent Specification, publication number US US5 111 277, Filed 1992

C.M. Allen, K.A.Q. O'Reilly, B. Cantor, P.V. Evans. *Prog. Mat. Sci.*, **43(2)**, p.89, 1998

S. Annavarapu, R. D. Doherty. *Powder Met*., **29(4)**, p.331, 1993

S. Annavarapu, R.D. Doherty, D. Apelian, A. Lawley, P. Mathur. ICSF 1, Paper 31, Proceedings of the Second International Conference on Spray Forming, Published Osprey Metals, Neath, UK, 1990

G.R. Anstis, P. Chantikul, B.R. Lawn, D.B. Marshall. *J. Am. Ceram. Soc*., **64(9)**, p.553, 1981

F.L. Arnold, J.S. Prestley. *AFS Trans.*, **69**, p.129, 1961

D.R. Askeland. The Science and Engineering of Materials, 2nd SI edition, Publ. Chapmen and Hall, London, 1993

ASTM standard E-1876-01, Standard test for Young's modulus, Shear modulus and Poison's ratio by impulse excitation of vibration, 2002

ASTM E-399 (90), Standard Test Method for Plane-Strain Fracture Toughness of Metallic Materials, 1997

ASTM Handbook, Castings, Vol 15. Publ. ASTM International, 1988

ASTM1239-94a Standard Practice for Reporting Uniaxial Strength Data and Estimating Weibull Distribution Parameters for Advanced Ceramics, 1995

O.A. Atasoy, F. Yilmaz and R. Elliott, J. Cryst. Growth, **66**, p.137, 1984

H.V. Atkinson, S. Davis. *Met. and Mater.Trans. A*, **31A**, p.2981, 2000

C. Aumund-Kopp., D.H. Muller. *Mater. Sci. Eng. A*, **A326**, p.176, 2002

B

F.W. Baker, R.L. Kozarek, G.J. Hilderman. ICSF 2, p.395, proceedings of the second International Conference on Spray Forming, Neath, UK, Published Osprey Metals, Neath, UK,1993

A.P. Bewlay, B. Cantor, *JOM. Res*., **6(7)**, p.1433, July 1991

A.P. Bewlay, B. Cantor, *Met. and Mater. Trans. B*, **21B**, p.899, 1990

A.P. Bewlay, B. Cantor. *Mater. Sci. Eng*., **118**, p.207, 1989

L. Bing, E.J. Lavernia, *Acta Mater*., **45(12)** p.5015, 1997

D. Bradley, *J. Appl. Phys. D,* **6**, p.1724, 1973a

D. Bradley, *J. Appl. Phys. D*, **6**, p.2267, 1973b

R.H. Bricknell. *Met. Trans. A,* **17A**, p.583, 1986

BRITE-EURAM Project number BE-5095-93, Fabrication of semiconductor device packages using metal matrix composites, final technical report, issued August 1997

R.C. Brodie, D.F.Bahr. *Mater. Sci. Eng. A*, **A351**, p.166, 2002

G. F. Brooks, Proceedings of TMS Annual Meeting, Las Vegas, The Minerals, Metals & Materials Society, Feb. 1995

M.G. Brown, P.J. Brown. *Acta Cryst.*, **9**, p.911, 1956

G. A. Butzer, K. Bowen, T. Tom, T. Cabral, *Foundry Management and Technology*, **20**, p.20, 1998

C

W. Cai, E. J. Lavernia. *Met. and Mat. Trans. B,* **29(B),** p.1085, 1998

J. Campbell. Castings, Publ. Butterworth-Heinemann, 1993

B. Cantor, K-H. Baik, P. S. Grant, *Prog. Mat. Sci.,* **42**, p.373, 1997

W.T. Carter, R. M. Forbes. *Advanced Materials Processing*, p.27, July 2002

J.Y. Chang, G.H. Kim, I.G. Moon, C.S. Choi. *Scripta Mater.*, **39(3)**, p.307,1998a

J.Y. Chang, I.G. Moon. *JOM*, **33**, p.5015, 1998b

Y. Chen and D.D.L. Chung, *JOM,* **29**, p.6069 1994

P. Chesney, ICSF 5, p.5-3 Proceedings of the Fourth International Conference on Spray Forming, Bremen, Germany, 2003.

Y-M Chiang, D.B. Birnie III, W.D. Kingery, Physical ceramics: Principles for Ceramic Science and Engineering. Publ: John Wiley & Sons Inc, 1996

M. G. Chu. ICSF 3, p.27, Proceedings of the Third International Conference on Spray Forming, Neath, UK, Published Osprey Metals, Neath, UK, 1996

B. Commandeur, P. Krug, R. Loos, G. Sinha. ICSF 5, p.5-37 Proceedings of the Fourth International Conference on Spray Forming, Bremen, Germany, 2003.

D

A.K. Dahle, K. Nogita, J.W. Zindel, S.D. McDonald, L.M. Hogan, *Met. and Mat. Trans. A,* **32(A)**, p.949, 2001

S.L. Dai, J-P. Delplanque, E.J. Lavernia. *Met. and Mat. Trans A*, **(29A),** p.2597, October 1998

M.S. Dargusch, A.L. Bowles, K. Petterson, P. Blake, G.I. Dunlop. *Met. and Mat. Trans. A*, **35(A),** p.1905, 2004

W.C. Dash, *J. Appl. Phys*., **27**, p.1193, 1956

S.K. Datta, S.N. Tewari, J.E. Gatica, W. Shih, L. Bentsen. *Met. and Mat. Trans. A,* **30(A)**, p.175, Jan 1999

M.G. Day, A. Hellawell. *Proc. Roy. Soc*., **305(A)**, p.473, 1968

DGM. (Deutsche Gesellschaft für materialkunde eV), working group discussion documents, Oxford assembly, November 2001

I. Diewwanit, M.C. Flemmings. TMS Annual meeting proceedings, p.787, Light Metals,1996

R.D. Doherty, C. Cai, L.K. Warner-Kohler. *Int. J. Powder Metall*., **33(3)**, p.50, 1997

R.D. Doherty, H-I. Lee, E.A. Feest. *Mater. Sci. En*g., **65**, p.181, 1984

J. Drapala, J. Lunacek, L. Kuchar, L. Kuxchar Jr. *Mater. Sci. En*g A, **A173 (1&2)**, p.73, 1993

A. Durrant, P.S. Grant, *Key Eng. Mater.,* **104-107**, p.155, 1995

E

Elkem (Norway) Patent document, World patent publication number WO 94/11138, Filed 1994

R. Elliott. Eutectic Solidification Processing, Publ. Butterworth, London, 1983.

F. Ericson. *Mat. Sci. Eng. A*, **105/106**, p.131, 1988

R. W. Evans, A.G. Leatham, G. R. Brooks. *Powder Met.* **28(1),** p.13, 1995

F

M. Fandel, W. Hagar, W. Schafer, K-H. Wichmann. Proceedings of the 3rd International Conference on Micro Materials, Berlin, p.265, 2000.

H. C. Fielder, T. F. Sawyer, R. W. Kop. Proc. 1986 Vacuum Metallurgy Conf. On speciality metals melting and processing. Publ. Iron and Steel Soc. Inc. USA p.157, 1987

D.J. Fisher, W. Kurtz. Proc. Conf. 'Solidification and Casting of Metals', Sheffield, England, Publ. The Metals Society, London, p.57, 1979

J. Fjellstedt. Doctoral Thesis, Dept. of Production Engineering, The Royal Institute of Technology, Stockholm, 2001

J. Fjellstedt, A.E.W. Jarfors, L. Svendsen. *Journal of Alloys and Compounds*, **283**, p.192, 1999

M.C. Flemings, Solidification Processing, McGraw-Hill, New York, 1974

A. Franco Jr, S.G. Roberts. *Cerâmica*, **50**, p.94, 2004

S-I. Fujikawa, K-I. Hirano, Y. Fukushima. *Met. Trans. A*, **9A**, p.1811, 1978

G

N.V. German, V.E. Zavodnik, T.I. Yanson, O.S. Zarechnyuk. *Kristallografiya*, **34**, p.738,1989

S. Ghost, W. J. Mott. *Modern casting*, **64(6)**, p.721, 1964

M.F.X. Gigliotti, G.A. Colligan, G.L.F Powell. *Met. Trans.*, **1**, p.891, 1970

P. S. Grant. *Prog. Mat. Sci*., **39**, p.947 1995a

P. S. Grant, I. T. H. Chang, B. Cantor, *Journal of Microscopy* **177(3)**, p.337, 1995b

P. S. Grant, B. Cantor, L. Katgerman. *Acta. Metal. Mater*, **41(11)**, p.3109, 1993

P. S. Grant, B. Cantor, *Powder Met*. **33(2)**, p.144, 1990

A.A. Griffith. *Phil. Trans. Roy. Soc.*, **A221**, p.163, 1920

C. Gueneau, C. Servant, F. d'Yvoire, N. Rodier. *Acta Cryst. C*, **C51**, p.177, 1995

H

R.R Hamilton and R.G Siedensticker, *J. Appl. Phys*., **32**, p.1165, 1960

W. Han, D. Feng, M. Yin, W. J. Ye. *Mat. Sci. Eng.,* **A225**, p.204, 1997

S.C. Hansen, C.R. Loper Jr. *Calphad*, **24(3)**, p.339, 2000

V, Hansen, B.C. Hauback, M. Sundberg, C. Rommings, J. Gjonnes. *Acta Cryst. B*, **54**, p.315, 1998

J. S. Harris, AGARD (Advisory Group for Aerospace Research & Development), Light Alloys meeting, Mierlo, Metherlands, Publ. North Atlantic Treaty Organisation, 1988

M. Haque. *J. Mater. Processing Tech.*, **55**, p.193, 1995

J. H. Hattel. *Mater. Eng. Sci.*, **7(3)**, p.413, 1999

A. Hellawell. *Prog. Mat. Sci.*, **15(1)**, p.3 1970

B. Heshmatpour. *Light Metals*, TMS Annual Meeting Orlando, Florida, February 9-13, p.801, 1997

B. Heshmatpour. *Light Metals,* TMS Annual Meeting Anaheim, California, February 4-8, p.687, 1996

S.C. Hogg, H.V. Atkinson. *Met. and Mat. Trans. A*, **36A(1)**, p.149, 2005

S.C. Hogg. Unpublished work, EPSRC grant number GR/R51100/01, 2004

S. C. Hogg, H.V. Atkinson, P. Kapranos. *Met. and Mat. Trans. A*, **34A**, p.899, 2004

S.C. Hogg PhD thesis, University of Sheffield, 2001

S. C. Hogg, C. J. D. Hetherington, H. V. Atkinson, *Phil. Mag. Lett.*, **80(7)**, p.477, 2000

A.A. Howe, D.H. Kirkwood. *Mat. Sci. Tech.*, **16**, p.961, 2000

I

A. Ibraham, F. A. Mohamed, E. J. Lavernia. *J. Mat. Sci.,* **26**, p.2597, 1991

J

D.M. Jacobson, S. P. S. Sangha*. Microelectronics International*, **15(3)**, p.17, 1998

D.M. Jacobson, S.P.S. Sangha. *GEC Journal of Technology*, **14(1)**, p.27, 1997

S.C. Jain, S.K. Agarwal, W.N. Borle, S. Tata. *Journal of Physics D*, **4(8)**, p.1207, 1971

D.C. Jenkinson, L.M Hogan. *Journal of Crystal Growth*, **28**, p.117, 1975

W. Jirattiticharoean, S.C. Hogg, C.A. Kirk, H. Jones, TMS Annual meeting, North Carolina, p.269, 2004

V. John. Testing of Materials, Publ. Macmillan Education Ltd, London, 1992

C. Johnson, Private Communication, 2003

C. Johnson, R. Young, A. Crossley. Proceedings of the 3rd International Conference on Micro Materials, Berlin, p.350, 2000.

T.P. Johnson, K. Stevens, M. Young, M.H. Jacobs. Proc. 3rd Int. Conf. Aerospace Defence and Demanding Applications. Ed. F. H. Froes. Publ. MPIF Princeton, p.157, 1993

H. Jones, W.M. Rainforth. *Mat. Sci. Tech.*, **20**, p.1223, 2004

K

A. Kahveci, *Science and Technology of Rapid Solidification Processing,* (Edited M.A. Otooni), p.249, Kluwer Academic Publishers, Dordrecht, The Netherlands, 1995

K.M. Kelkar, Z. Hou, S.V. Patankar, R.S. Minisandram, R.M. Forbes, W.T. Carter, S.K. Strivatsa, C. Madden. ICSF 4, session 4, paper 1, proceedings of the Fourth International Conference on Spray Forming, Baltimore, USA, 1999.

M. Knechtel, H. Prielipp, H. Mullejans, N. Claussen, J. Rodel. *Scripta Metallurgica et Materialia*, **31(8)**, p.1085, 1994

K.F. Kobayasi, L.M. Hogan. *J. Mat. Sci.*, **20**, p.1961, 1985

K.F. Kobayasi, L.M. Hogan. *Phil. Mag. A*, **40(3)**, p.339, 1979

B. Kocdemir, H-J Frcht, K-H Wichmann. Proceedings of the 3rd International Conference on Micro Materials, Berlin, p.251, 2000.

M. Krauss, D. Bergmann, U. Fritsching, K, Bauckhage. *Mater. Sci. Eng. A*, **A326**, p.154, 2002

M. Kunes. *Electronics and Communications Journal,* p.28 Feb, 1998

W.J. Kyffin. W.M. Rainforth, H.Jones. *Mater. Sci. Tech.*, **17**, p.901, 2001

L

A. Lambourne, P.S. Grant, S.C Hogg, A. Ogilvy, Inzynieria Materialowa **3(140)** p.616, 2004

A. Lambourne, Unpublished work, 2003
J. Lankford, *J. Mater. Sci. Lett.*, **1**, p.493, 1982

A. Lawley, D. Apelian. *Powder Met*., **37**, p.123, 1994

A. Lawley, *Journal of Metals,* **38(8)**, p.15, August 1986

A. Lawley, *Journal of Metals*, **33(1)**, p.13, January 1981

B.R. Lawn, A.G. Evans, D.B. Marshall. *J. Am. Ceram. Soc.,* **63(9-10)**, p.574, 1980

A.G. Leatham, Sandvik-Osprey Ltd, Neath UK, Private Communication, 2004

A.G. Leatham. *JOM-e* (e-Journal), **51(4)**, 1999
http://www.tms.org/pubs/journals/JOM/9904/Leatham/Leatham-9904.html

A.G. Leatham, J.S. Coombs, J.B. Forest, S. Ahn. Proceedings of the 2nd Pacific Rim International Conference on Advanced Materials Processing, Korea, 1995

D.D. Leon, R.L. Kozarek. *Advances in Powder Metallurgy and Particulate Materials,* **2**, p.7/3, 1995

Q. Liu. *Scripta Mat.*, **38(7)**, p.1083, 1998

S-Z. Lu, A. Hellawell. *JOM*, **47**, p.14, 1995

S-Z. Lu, A. Hellawell. *Met. Trans. A*, **20A**, p.1286, 1989

S-Z. Lu, A. Hellawell. *Met. Trans. A*, **18A**, p.1721, 1987

T. Lube. *Journal of the European Ceramic Society*, **21**, p.211, 2001

H. Lubanska. *J. Metals*, **32**, p.45, 1970

M

E.D. Manson-Whitton, I.C. Stone, J. R. Jones, P. S. Grant, B. Cantor. *Acta Mat.* **50**, p.2517, 2002

J.W. Martin, R.D. Doherty, B. Cantor. Stability of Microstructure in Metallic Systems, 2nd edition, Published Cambridge Univ. Press,1997

M.A. Martinez, A.J. Criado, J.A. Martinez. *Praktischen Metallopraphie*, **28**, p.25, 1991

C. Mascare. *Foundry Trade Journal*, **94**, p.725, 1953.

P. Mathur, D. Apelian, A. Lawley. *Powder Met*., **34(2)**, p.109, 1991a
P Mathur, S Annavarapu, D Apelian, A Lawley. *Mat. Sci, Engng.,* **A142,** p.261 1991b

P. Mathur, D. Apelian, A. Lawley, *Acta Met.*, **37(2)**, p.429, 1989

H. Mavoori, S Jin. *JOM*, **50(6)**, p.70, June 1998

O. Mayer, A. Schneider, V. Unlenwinkel, U. Fritsching, *Convective heat transfer from a billet due to an oblique impinging circular jet within the spray forming process, Colloquium of SFB372*, University of Bremen, Spray Forming Research Centre, Badgasteiner Str.3, D28359, Bremen, Germany, 2001.

S.D. McDonald, A.K. Dahle, J.A. Taylor, D.H. StJohn. *Met. and Mat. Trans. A*, **35A(6)**, p.1829, 2004

R. Mehrabian, R.G. Riek, M.C. Flemmings, *Met. Trans*., **5**, p.1899, 1974

K.P. Mingard, B. Cantor, I.G. Palmer, I.R. Hughes, P.W. Alexander, T.C. Willis, J. White. *Acta Mat*., **48**, p.2435, 2000

K.P. Mingard, J.J. Myerscough, J. Heath, P.W. Alexander. ICSF 2, p.399, Proceedings of the Second International Conference on Spray Forming, Neath, UK, 1993

P.S. Mohanty, J.E. Gruzleski. *Acta Mat.*, **44(9)**, p.3749, 1996

L.F. Mondolfo. Aluminium Alloys Structure and Properties, Publ. Butterworths, Second edition, 1979

M. H. Mulazimoglu, J. E. Gruzleski. *Forschung Aluminium*, **69(11)**, p.1014, 1993

H.R. Muller, K. Ohla, R. Zauter, M. Ebner. ICSF 5, p.5-9, Proceedings of the Fourth International Conference on Spray Forming, Bremen, Germany, 2003.

J. Mullers, M. Knuwer, K-H. Wichmann, W. Hagar. Proceedings of the 3rd International Conference on Micro Materials, Berlin, p.232, 2000.

J.L. Murray, A.J. McAlister. *Bulletin of Alloy Phase Diagrams*, **5(1)**, p.74 1984

N

R.E. Napolitano, H. Meco, C. Jung. *JOM*, **56(4)**, p.16, April 2004

Narumi China Corporation, Patent document, US Patent Specification, publication number 4680618, Filed 1987

M.D. Nave, A.K. Dahle, D.H. St John. *Acta Mat.*, **50**, p.2837, 2002

A.P. Newbury, P.S. Grant. *Journal of Thermal Spray Technology*, **9(2)**, p.250, 2000

H. Nisitani, Y. Takase, N. Noda
Transactions on Engineering and Science, **19**, p.688, 1998

K. Nogita, S.D. McDonald, K. Tsujimoto, K. Yasuda, A.K. Dahle. *Journal of Electron Microscopy*, **53(4)**, p.361, 2004a

K. Nogita, S.D. McDonald, A.K. Dahle. *Mat. Trans.*, **45(2)**, p.323, 2004b

K. Nogita, A.K. Dahle. *Scripta Mat.*, **48**, p.307, 2003

O

A. Ogilvy, Sandvik-Osprey Ltd, Neath, UK, private communication, 2003

Olin Corporation, Patent document, US Patent Specification, publication number US 5 650 592, Filed 1997

Osprey CE alloy machining data, courtesy of Osprey Metals Ltd , Neath, South Wales, 2004

Osprey Metals Ltd, Patent document, US Patent Specification, publication number US 6 312 535 B1, Filed 2001

Osprey Metals Ltd, Patent document, World Patent International publication number WO 97/03775, Filed 1997

Osprey Metals Ltd, Patent document, UK Patent Specification, publication number GB 2 317 900, Filed 1996

Osprey Metals Ltd, Patent document, UK Patent Specification, publication number GB 1,472,939, Filed 1974

Osprey Metals Ltd, Patent document, UK Patent Specification, publication number GB 1,397,261, Filed 1971

P

X. Peng, Z. Fan, J. R. G. Evans. *Mat. Sci. and Tech*., **16,** p.903, July / Aug 2000

R. Perez, P. Gumbsch. *Phys. Rev. Lett.*, **84(23)**, p.5347, 2000

M. Petrescu. *Z. Metallkde.*, **61**, p.14, 1970

C.B. Ponton, R.D.Rawlings. *Mat. Sci. and Tech*., **5**, p.865, 1989a

C.B. Ponton, R.D.Rawlings. *Mat. Sci. and Tech*., **5**, p.961, 1989b

C.B. Ponton, R.D. Rawlings. *Brit. Ceram. Trans. J.,* **88**, p.83, 1989c

R

S. Rawel. *JOM*, **53(4)**, p.14, April 2001

B.V. Reddy, S.C. Deevi. *Intermetallics*, **8**, p.1369, 2000

F. Rehme, R. Dolp, M. Kuffer, W. Hagar. Proceedings of the 3rd International Conference on Micro Materials, Berlin, p.311, 2000.

A. Rentsch and J. Wilde. Proceedings of the 3rd International Conference on Micro Materials, Berlin, p.259, 2000.

S.G. Roberts. Materials Department, Oxford, private communication, 2003

J. Rodel, H. Prielipp, N. Claussen, M. Sternitzke, K.B. Alexander. *Scripta Metallurgica et Materialia*, **33(5)**, p.843, 1995

E.L. Rooey. *Trans AFS.*, **72(44)**, p.421, 1972

S

N. Saunders. *Thermotech Al-Data Information*, Publ. Thermotech Ltd, Surrey Technology centre, 40 Occam Road, The Surrey Research Park, Guildford, Surrey, GU2 5YG, UK

S.J. Savage, F.H. Froes. *J. Met.*, **36**, p.20, April 1984

F. Secco d'Aragona. *J. Electrochem. Soc*., **119,** p.948, 1972

J.B. See, G. H. Johnson. *Powder Tech*., **21**, p.119, 1978

H. Seiter. Semiconductor Silicon, ed. H. Huff, E. Sirtl; Publ. Electrochem. Soc. Proc. Series, p.187, 1977

R. Senden. RSP Technology, Holland. Private communication, 2004

J.F. Shackelford, W. Alexander. Materials Science and Engineering Handbook 3rd Edition. Publ. CRC Press London, 2001

L.H. Shaw. *Powder Met*. **40(1),** p.28, 1997

A.R.E. Singer, D.J. Hodkin, P.W. Sutcliffe, P.G. Mardon. *Met. Tech.*, **10**, p.105, 1983.

A.R.E. Singer. *J. Metals*, **100**, p.185, 1972
A. R. E. Singer. *Metals and Materials*, **4**, p.246, 1970

E. Sirtl, A. Adler. *Z. Metallkde.*, **52,** p.529, 1961

C.J. Smithells. Metals reference book, 5th edition, Publ. Butterworths & Co, 1978

D.H. StJohn, A.K. Dahle, M.A. Easton, J.E.C. Hutt, N.L.M. Veldman. *Materials Science Forum*, **23**, p.137, 1999

T. S. Strivatsan, T. S. Sudarshan, E. J. Lavernia. *Prog. Mat. Sci.,* **39**, p.317, 1995

Sumitomo Electric Industries Ltd. US Patent number 4,926,242. Filed 1990a

Sumitomo Electric Industries Ltd. European Patent number 0 411 577, Filed 1990b

Sumitomo Electric Industries Ltd. US Patent number 4,830,820. Filed 1989

T

K. Tanaka, K Nawata, H. Inui, M. Yamaguchi, M. Koiwa. *Materials Research Symposia Proceedings*, **646**, p.N4.3, 2001

K. Tanaka. *J. Mater. Sci*., **22**, p.1501, 1987

F. Tancret. *Scripta Materialia*, **43**, p.9, 2000

N. Tenekedjiev and J.E Gruzleski. *Cast metals*, **3(2)**, p.96, 1990

N. Tenekedjiev, D. Argo J.E. Gruzleski. *Trans. AFS*, **97**, p.127, 1989

N. Thangaraj, K.H.Westmacott, U. Dahman. *Appl. Phys. Lett*., **61(8),** 1992

J. Tillwick, V. Uhlenwinkel, K.Baukhage. *International Journal of Heat and Fluid Flow*, **20**, p. 530, 1999

J-M. Ting and M. L. Lake. *JOM,* **46(3)**, p.23, March 1994

N. Tokizane, Y. Ohkubo, K. Shibue. p.37 ICSF 3, Proceedings of the Third International Conference on Spray Forming, Neath, UK, 1996

N.A. Travitzky, N. Claussen. *Journal of the European Ceramic Society*, **9**, p.61, 1992

E. Tzimas, A. Zavaliangos, *Mat. Sci. Eng A*, **A289**, p.217, 2000.

U

J. Ulrich, M. Berg, K. Bauckhage. *Minerals, Metals & Materials Society,* AIME, EPD Congress, p.105, March 1999

A. Unal. *Mat. Sci. Tech.*, **3**, p.1029, 1987

R.P. Underhill, P.S. Grant, B. Cantor, D.J. Bryant. *Int. Journal of Non-Equilibrium Processing,* **10**, p.201, 1997

R.P Underhill, D.Phil thesis, Oxford University, 1995

W

R.S. Wagner, *Acta Met.*, **8**. p.57, 1960

I. Wang, X.F. Bian, S.J. Yuan. Acta *Metall Sincia Lett (English Letters)*, **12**, p.611, 1999a

R. Wang, W. Lu, L.M. Hogan. *Journal of Crystal Growth*, **207**, p.43, 1999b

R. Wang, W. Lu, L.M. Hogan. *Met. and Mat. Trans. A*, **28A**, p.1233, 1997

P.J. Ward, H.V.Atkinson, P.R.G. Anderson, L.G. Elias, B. Garcia, L. Kahlen, J-M. Rodriguez-Ibabe. *Acta. Mater.*, **44(5)**, p.1717, 1996

P.D. Warren. *J. Euro. Ceram. Soc.,* **15**, p.201, 1995a

P.D. Warren. *J. Euro. Ceram. Soc.,* **15**, p.385, 1995b

L.D. Wegner, L.J. Gibson. *International Journal of Mechanical Sciences*, **43**, p.1771, 2001

A. White, S. Keck, I Smith, A. Silzars. *Hybrid Circuit Technology*, **12(1)** p.14, 1990

J. White, I.G. Palmer I.R. Hughes, S.A. Court. Conf. Proc. 5th International Al-Li conference, Williamsberg, 1989a

J. White, TC Willis. *Materials & Design*, **10(3)**, p.121, 1989b.

W.A. Wilcox. *Journal of Crystal Growth*, **38**, p.73, 1977

T. C. Willis, *Powder Met.,* **8**, p.485, Aug 1998

T. C. Willis, J. White, R. M. Jorden, I.R. Hughes. International conference on Powder Metallurgy and Aerospace Materials, Luzeren, 1987

M. J. Wright. *J. Electrochem. Soc.*, **124**, p.757, 1977

Y. Wu, E. J. Lavernia. *Met. Trans. A,* **23A**, p.2923, 1992

X

Z.H. Xian, C. Jun. *JOM*, **46**, p.42, 1994

Z.H. Xian, X.C. Man, H.F. Xun, C. Jun. 'Light Metals 1993', TMS, Warrendale, Published by The Minerals Metals and Materials Society p.825, 1993

X. Xiang, E. J. Lavernia. *Mat. Sci. Eng.,* **A161**, p.221, 1993

Y

F. Yilmaz, A.O. Atasoy. *Journal of Crystal Growth*, **118**, p.377, 1992

M. Yilmaz, S. Altinas. *J. Mat. Sci. Letters*, **15**, p.2093, 1996a

M. Yilmaz, S. Altinas. *Materials Science Forum*, **217,** p.1853, 1996b

M. Yilmaz, R. Elliott. *Metal. Science*, **18**, p.362, 1984

Z

G.M. Zatorska, G.S. Dmytriv, V.V. Pavlyuk, A. Bartzokas, A. Jaskolski. *Journal of Alloys and Compounds*, **346**, p.154, 2002

A. Zhou, J. Duszczyk, B.M. Korevaar. *J. Mat. Sci.*, **26**, p.5275, 1991

C. Zweben. *JOM,* **50(6)**, p.47, 1998